Multi-scale Nanoparticle Contrast Agents

Submited by Ahmed Obaid M. Alzahrani, to the University of Exeter

as a thesis for the degree of Doctor of Philosophy in Physics,

May 2015

I certify that all material in this thesis which is not my own work has been identified and that no material has previously been submitted and approved for the award of a degree by this or any other University.

.....Ahmed Obaid M. Alzahrani

Abstract

Nanoparticles have potential biomedical applications because of their special physical properties. Multi-scale nanoparticles contrast agents are those particles that provide contrast in different scale imaging modalities. Such particles are of great interest for monitoring anti-cancer drug delivery, allowing investigations of whole body drug distribution as well as that at the microscopic level. Magnetic nanoparticles in particular have been used as contrast agents in MRI and optical techniques such as confocal microscopy and two photon fluorescence (TPF) microscopy to achieve multiple scale imaging. However, confocal microscopy has a limited optical penetration in biological tissue. Moreover, both techniques, confocal microscopy and TPF microscopy, require labelling of the biological tissue which alters the particle distribution and complicates the biological system under-investigation.

Coherent Raman scattering (CRS) imaging techniques are label-free with chemical contrast and relatively large optical penetration. To the best of the authors knowledge, only one study was carried out to image magnetic particles with such an imaging system using a four wave mixing (FWM) process. However, micro-sized particles were used and such size is not typical for drug delivery applications.

The aim of this thesis is to develop techniques to combine the two scales imaging modalities, MRI and CRS in order to image the well-established MRI contrast agents, iron oxide and gadolinium oxide nanoparticles in a biological context. Moreover, the thesis examines the label-free ability of MRI and CRS to determine tumour boundaries through ex-vivo imaging of a mouse brain tumour.

In MRI, it was found that the optimal contrast between healthy tissue and tumour for formalin fixed mouse brain is achieved when a spin echo (SE) sequence with TE/TR = 3000/110 ms is applied. The tumour edges were extracted at high resolution ($0.125 \times 0.125 \times 0.150$ mm^3) which allows measuring the tumour volume in a clinically available 1.5 T MRI scanner with such resolution for the first time. The high resolution label-free volumetry data was used as a gold standard to estimate experimental error in conventional histology tumour volume measurements and it was found that 20 % average error results from tumour shape irregularity. A mosaic CARS image of a tumour slice was produced with a novel technique that compensates for phase curvature.

The magnetic nanparticles were synthesised with homogeneous precipitation and hydrothermal methods and a tuneable mono-disperse sizes were achieved. It was found that the Er doped gadolinium oxide nanoparticles pose a strong upconversion when excited with a 816 nm laser. Doped gadolinium oxide nanoparticles were imaged in CRS system with four wave mixing (FWM) and UC photoluminescence in a biological model. Also, Iron oxide nanoparticles were imaged using FWM and two photon photothermal lensing (TPPL).

It can be concluded that MRI and CRS are capable of determining tumour edges in a label-free manner. Moreover, CRS system can be utilised to image nanoparticles contrast agents in a biological tissue with a number of potential optical techniques.

Dedication

To my mum, dad ,my wife Amirah

my lovely children

Maha

Wejdan

Hatim

and my newly born baby

Battal

Acknowledgments

I would like to thank the people who have helped me to accomplish this thesis. First of all, many thanks to my supervisors Dr. Julian Moger and Dr. Ian Summers for all the support they have been providing thought the period of the study. I would like to thank Julian for the weekly group meeting which helped me develop the critical discussion skills, and for the open door policy providing very effective advice when needed. Thanks are due to Ian who worked even after his retirement to provide me with very useful feedback about the MRI aspects of my research. Also, many thanks to Prof Yanqiu Zhu for allowing me to work in his material engineering laboratories to fabricate the magnetic nanoparticles needed for the study and for his advice in regard to particle fabrication. In addition, I want to thank Dr. Eva Hemmer who inspired me to synthesise and investigate doped gadolinium oxide nanoparticles by sending me a test sample. Many thanks to Ellen Green for helping me in the labs whenever required and to Malik who helped me regarding the MRI experiments. Finally, thanks are also due to Natalie and Jessica for helping me in the laser lab and to all the biophysics group members.

List of Abbreviations

MRI - Magnetic resonance imaging

TPF - Two photon fluorescence

CRS - Coherent Raman scattering

FWM - Four wave mixing

SE - Spin Echo

TE - Echo time

TR - Repetition time

CARS - Coherent anti-Stokes Raman scattering

UC - Upconversion

TPPL - Two photon photothermal lensing

CT - Computational tomography

RF - Radio frequency

NMV - Net magnetisation vector

FID - Free induction decay

GE - Gradient echo

MR - Magnetic resonance

TI - Inversion time

CA - Contrast agents

OPO - Optical parametric oscillator

SRL - Stimulated Raman loss

SRG- Stimulated Raman gain

PL - Photoluminescence

ESA - Excited state absorption

ETU - Energy transfer upconversion

PA - Photon avalanche

NA - Numerical aperture

PMT - Photomultiplier tube

SEM - Scanning electron microscope

EDS - Energy dispersive spectroscopy

TEM - Transmission electron microscope

XRD - X-ray diffraction

SNR - Signal to noise ratio

FOV - Field of view

FFE - Fast field echo

ROI - Region of interest

GONPs - Gadolinium oxide nanoparticles

UCPL - Upconversion photoluminescence

CW - Continuous wave

Contents

1 Introduction **11**

2 Background Theory **14**

2.1 Introduction 14

2.2 MRI 14

2.2.1 Introduction 14

2.2.2 Atomic structure 15

2.2.3 Active MRI nuclei 16

2.2.4 Alignment 17

2.2.5 Resonance and relaxation 19

2.2.6 Signal detection 22

2.2.7 Imaging sequences 24

2.2.8 The Bloch equations 27

2.2.9 Measuring relaxation time 30

2.2.10 MRI contrast agents 32

2.3 Optical spectroscopy and microscopy 35

2.3.1 Introduction 35

2.3.2 Confocal microscopy 35

2.3.3 Two photon fluorescence (TPF) microscopy 37

2.3.4 Spontaneous Raman scattering 38
2.3.5 Coherent anti-Stokes Raman Scattering (CARS) 40
2.3.6 Four wave mixing (FWM) 45
2.3.7 Stimulated Raman Scattering (SRS) 46
2.3.8 Two Photon Photothermal lensing (TPPL) 48
2.3.9 Photoluminescence (PL) 49
2.3.10 Upconversion Photoluminescence (UPL) 50

3 Method and Instrumentation 53

3.1 Introduction 53
3.2 Magnetic Resonance Imaging 53
3.3 Optical setup 54
3.3.1 Raman Spectroscopy and Photoluminescence 54
3.3.2 Confocal microscope 55
3.3.3 Coherent anti-Stokes Raman Scattering 56
3.3.4 Stimulated Raman Scattering 60
3.3.5 Two Photon Photothermal Lensing (TPPL) 61
3.3.6 Upconversion spectroscopy and imaging 61
3.4 Nanoparticles fabrication and Characterisation 63
3.4.1 Fabrication 63
3.4.2 Characterisation 65

4 Label-free Imaging of Tumours 67

4.1 Introduction 67
4.2 MRI of mouse brain tumour 69
4.2.1 Introduction 69
4.2.2 Whole animal MRI 75

4.2.3 T_1 and T_2 measurements of mouse brain . . . 77
4.2.4 High resolution MRI of tumour . . . 81
4.2.5 MR image processing . . . 85
4.3 Nonlinear optical microscopy of mouse brain tumour . . . 94
4.3.1 Introduction . . . 94
4.3.2 CARS imaging of tumour . . . 95
4.4 Summery . . . 102

5 Nanoparticle characterisation 104
5.1 Introduction . . . 104
5.2 Composition materials . . . 105
5.3 Morphology and size . . . 108
5.4 Crystalline structure . . . 114
5.5 Photoluminescence . . . 116
5.6 Upconversion Photoluminescence Spectroscopy . . . 122
5.7 Magnetic relaxivity . . . 137
5.8 Summary . . . 146

6 Nanoparticle optical imaging 148
6.1 Introduction . . . 148
6.2 Confocal imaging . . . 150
6.3 FWM imaging . . . 155
6.4 Upconversion imaging . . . 160
6.5 Two photon photothermal lensing (TPPL) imaging . . . 168
6.6 Summary . . . 177

7 Conclusion and future work 179

Appendices **184**

.1 Image processing 185

.1.1 3D MRI image normalisation against distance from coil 185

.1.2 Rename images as Tile grid of images 186

.2 Tumour volumetry data 187

List of Figures

2.1 Orientation of nuclear spins in the absence of a magnetic field. 17
2.2 Alignment of nuclear spins in an external field before and after an RF pulse. 17
2.3 Precession of a nuclear spin. 18
2.4 Illustration of the NMV and its components 21
2.5 Longitudinal component recovery and transverse component decay curves 22
2.6 The NMV orientation in the rotating frame just after a 90° pulse 23
2.7 Free induction decay (FID) 24
2.8 Spin-echo pulse sequence. 25
2.9 Gradient Echo pulse sequence. 26
2.10 The relaxation as seen from the lab frame. 30
2.11 The time dependence of M_z in the inversion recovery experiment 32
2.12 The principle of confocal microscopy. 36
2.13 The excitation volume of single photon excitation versus two photon excitation. 37
2.14 The energy digram of one photon and two photon fluorescence excitation. 38
2.15 Energy diagram of Raman scattering 39
2.16 Energy diagram of CARS. 41

2.17 Phase matching condition in CARS 42
2.18 Resonance and nonresonance CARS 44
2.19 Imaging iron oxide micro-particles, a) transmission light, b) on resonance , and c) off resonance FWM. 46
2.20 Stimulated and spontaneous Raman scattering 47
2.21 The loss and gain in the stimulated Raman scattering 48
2.22 Upconversion excitation processes 51

3.1 Image of the Raman spectrometer (RM1000). 54
3.2 Sketch of the optical setup of the Raman spectrometer (RM1000). 55
3.3 The optical setup of CARS microscopy. 57
3.4 The transparency of the dichroic 850nm long-pass mirror 58
3.5 The transmission profile of the 750/210 nm band pass filter 59
3.6 The cathode radiation sensitivity of the PMT (R3896, Hamamatsu) . . . 60
3.7 The additional setup required for UC spectroscopy and imaging. 62
3.8 The interior setup of the Andor spectrometer. 62
3.9 Teflonlined steel autoclaves used for hydrothermal synthesis method. . . 65

4.1 A slice of a 3D MRI image of a whole rat body showing anatomical details.The arrow indicates the heart. 76
4.2 A slice of a 3D MRI image of a whole rat body showing anatomical details. The arrows indicate brain and liver. 77
4.3 T_1 values for tumour and normal brain tissue measured with the inversion recovery method. 79
4.4 T_2 values for tumour and normal brain tissue measured by varying the echo time. 80
4.5 The optimum contrast between normal brain tissue and tumour. 81

4.6 High resolution T_2 weighted 3D image of two brains with FOV positioned to the tumour 84
4.7 A plot of grey scale line profile across the tumour 85
4.8 Normalised and unnormalised images of an MRI stack 87
4.9 Three example images from different brains before and after ROI selection 89
4.10 3D model of a tumour showing its irregular shape. 90
4.11 Tumour diameter measurements from a coronal cross- section of mouse brain, simulating histology measurements. 91
4.12 A plot of MRI (3D ROI) volume measurements vs simulated-histology measurements for 64 mouse brain tumours. 93
4.13 Percentage difference between MRI (3D ROI) volume measurements and simulated-histology measurements for 64 mouse brain tumours. 94
4.14 Detailed CARS image showing the different structures and features of brain tissue. 97
4.15 Large scale mosaic of CARS images of a whole brain slice. 99
4.16 The effect of coverslip curvature on CARS mosaic images. 100
4.17 Image normalisation of CARS mosaic of mouse brain tissue. 101

5.1 SEM image of Gd_2O_3: 5% Er^3+ nanoparticles with three rectangles indicating three areas where three EDS spectra were acquired. 107
5.2 The dispersive energy spectroscopy of Gd_2O_3: 5% Er^3+. 107
5.3 SEM image of doped Gd_2O_3 particles (Sample1). 109
5.4 SEM image of doped Gd_2O_3 particles showing the effect of changing nucleation time on particle size. 110
5.5 An illustration of the process of the statistical analysis of particle size monodispersity. 112

5.6 Histogram of size distribution of doped gadolinium oxide nanoparticles (S3a) . . . 113
5.7 Histogram of size distribution of Iron oxides nanoparticles (S21) . . . 113
5.8 XRD of doped gadolinium particles (sample 3a) (a)before and (b) after annealing at 950° for 30 min. . . . 115
5.9 PL spectrum of different percentages co-doped gadolinium oxide particles. 118
5.10 PL spectrum of gadolinium oxide particles (S1, S30, and S31) excited with 785 nm CW laser. . . . 119
5.11 PL spectrum of gadolinium oxide particles under 785 nm CW laser excitation. . . . 121
5.12 PL spectrum of doped gadolinium oxide particles(Sample2) as prepared (red) and annealed at 950° for 30min (blue). . . . 122
5.13 UCP of different doped/co-doped gadolinium oxide particles. . . . 124
5.14 The UCP and FWM spectrum of S31. . . . 126
5.15 UCP of S1 under the 1064 nm excitation at 100 mW. . . . 127
5.16 The effect of changing excitation wavelength on UC photoluminescence . 128
5.17 UCP power dependence of S1 under the 978 nm excitation. . . . 131
5.18 UCP power dependence of S1 under the 816 nm excitation of the range of powers (20 - 100 mW). . . . 132
5.19 UCP power dependence of S2 under the 816 nm excitation of the range of powers (20 - 100 mW). . . . 133
5.20 UCP of gadolinium oxide particles co-doped with 10% Yb and different Tm concentrations. . . . 134
5.21 The 811 nm UCP of S24 under constant 100 mW power and range of excitation wavelengths (971 nm - 984 nm). . . . 135
5.22 UCP of different doped/co-doped gadolinium oxide particles. . . . 136

5.23 The molecular structures of Magnevist and Vasovist. 138
5.24 The samples arrangements (a) and inversion recovery images (b-h) of different concentrations of the clinically used contrast agents Gadovist and Vasovist. 140
5.25 The longitudinal relaxivity measurements of Magnevist and Vasovist. . . 141
5.26 The signal intensity of a T_1-weighted image of different concentrations of gadolinium ions (Magnevist) in water and gel. 142
5.27 UCP of different doped/co-doped gadolinium oxide particles. 143
5.28 A replication of the data in Figure.5.27 with a better particle distribution and less aggregations. 145

6.1 SEM of sample 3a. 151
6.2 Confocal microscopy images of S2 particles at different zoom and detection spectra as labeled on the images. 153
6.3 The spectral ranges covered by the red and green channels of the Confocal microscope. 154
6.4 Confocal of sample 22b single particle green and transmission. 154
6.5 A FWM image of aggregation of gadolinium oxide nanoparticles 156
6.6 A FWM image of iron oxide particles suspended in agarose gel. 158
6.7 A FWM image of iron oxide nanoparticles (S21) spin coated on a glass coverslip. 159
6.8 UCP images of Gd_2O_3:1 % Yb, 1% Er particles taken with 816 nm excitation. 162
6.9 An illustration of the decay time effect on the image. 163
6.10 The effect of imaging speed on the upconverting nanoparticles image . . 165

6.11 Imaging the upconversion nanoparticles in a biological context model(starch). 167
6.12 The spectra range covered by the 660/40 nm band pass filter of the UCP and FWM. 167
6.13 FWM and TPPL of iron oxide nanoparticles (S20 and S21). 169
6.14 The z-confinement of the TPPL signal detected from iron oxide nanoparticles (S21). 170
6.15 The excitation wavelength sensitivity of TPPL of iron oxide nanoparticles 172
6.16 Isolating particle TPPL contrast from biological context via the desynchronisation of the two excitation pulse trains. 173
6.17 The signal intensities of SRS of starch and TPPL of iron oxide particles as functions in phase. 175
6.18 A composite of two images epi-CARS of starch (red) and TPPL of iron oxide nanoparticles recorded at phase of 160°. 176

7.1 Stimulated emission of Gd_2O_3 nanoparticles 182

Chapter 1

Introduction

Multi-scale nanoparticles contrast agents are nanoparticles that provide contrast in both large scale and microscopic imaging modalities. The development of such particles would lead to better understanding of the mechanism of uptake of anti-cancer drugs at the whole body and the cellular level. Cancer drug resistance in tumours is considered as one of the major obstacles toward an effective treatment due to the complicated tumour microenvironment that results in poor drug penetration and insufficient uniform drug distribution [1,2]. Tumour cells form pockets that resist chemotherapy and survival of a single cancer cell might reinitiate a new tumour. Nanomedicine has been used widely not only to overcome this obstacle, but also to reduce the side effects of drugs via targeted delivery where the medicine only kills tumour cells [3,4]. Magnetic nanoparticles in particular have received remarkable research attention for their targeted therapy potential provided either by magnetic targeting or with specific targeting ligands [5–8]. However, a considerable amount of effort is still required to engineer enhanced nano-therputic nanostrucures and multi-scale imaging techniques are required to assess efficiency of targeting and curing [9]. The imaging technique, on one hand, should comprehensively cover the overall large-scale drug distribution over the whole body volume to inspect

targeting a specific organs or tissue. On the other hand, it should provide microscopic details about drug distribution in tumours to allow investigation of its efficiency to overcome the drug resistance which occurs in the tumour microenvironment. Unfortunately, with the current available technologies these imaging scale specifications can not be provided by a single imaging modality. Magnetic resonance imaging (MRI) and X-ray computational tomography (CT) are capable of large scale imaging but the spatial resolution of both modalities is not at the level of probing the microscopic cellular details [10, 11]. Optical microscopy can image the microscopic details of biological tissue, but its imaging penetration and field of view are limited to several hundred micrometers depending on the specific utilised technique [12]. Accordingly, a considerable number of previous studies suggested dual-modality imaging combining two different scale imaging techniques with nano-contrast agents to achieve the comprehensive monitoring of drug distribution [13]. Regarding whole body imaging, MRI offers enhanced contrast when imaging soft tissue and greater contrast of magnetic nanoparticles in comparison to CT [14]. For this reason this thesis will be limited to those multi-modal imaging studies in which MRI was used for the large scale imaging. Several studies combined MRI with confocal microscopy to image fluorescent magnetic nanoparticles in biological tissues [15–21]. However, confocal microscopy has a limited optical penetration in scattering tissue and suffers from photobleaching since a single-photon fluorescence signal is generated above and below the focal plane [22]. Instead of confocal microscopy, a number of other previous studies utilised two-photon fluorescent (TPF) microscopy that benefits from nonlinear excitation to increase the optical penetration and to reduce photobleaching [23–26]. Nevertheless, both confocal and two-photon microscopies require labelling the biological tissue which complicates investigating the distribution of multi-scale nanoparticles at the cellular level. Raman microscopy provides label-free contrast of the biological tissue via molecular vibrational imaging, but it requires a

very long acquisition time (hours) [27]. Coherent Raman scattering (CRS) techniques provide label-free microscopy of biological tissues with chemical contrast, great optical penetration, and reasonable imaging time [28, 29]. To the best of the author's knowledge, there is only one previous study in which magnetic particles were imaged under a CRS system [30], however micro-particles were used which is considered as a limitation since such particle size is not suitable for tumour uptake.

The aim of this thesis is to investigate possible methods of using magnetic nanoparticles as multi-scale contrast agents in both MRI and CRS. The motivation as mentioned above is to propose these particles as delivery and tracking agents for anti-cancer drugs in the label-free imaging modalities. The thesis is structured in six chapters in addition to the current chapter. In chapter two, the theoretical background techniques required for spectroscopy, imaging, characterisation, and synthesis of the particles will be presented, while chapter three will cover the experimental specifications of these techniques. In chapter four, the label-free ability of MRI and CRS to determine tumour edges will be investigated. This will be accomplished by imaging mouse brain tumours with MRI and CARS in a collaborative study with the London School of Pharmacy to measure tumour volume as a response to different cancer medicines. Also, a technique will be developed to compare images of the two different scale imaging modalities. In Chapter five, the magnetic particles material, size, morphology, crystalline structure, optical and magnetic properties will be characterised. Chapter six demonstrates the optical contrast that can be obtained from particles in model biological samples. Finally, the conclusion and future work will be presented in chapter 7.

Chapter 2

Background Theory

2.1 Introduction

This thesis describes the application of multiple imaging modalities to characterise or image biological tissues, or nanoparticles within a biological model. The aim as stated in the introduction is to propose practical methods for imaging nanoparticles both in MRI and non-linear optical microscopies. This Chapter presents the theoretical background of these imaging techniques.

2.2 MRI

2.2.1 Introduction

In 1946 Felix Bloch and Edward Purcell discovered the magnetic resonance phenomenon independently. Both were awarded the Nobel Prize in 1952 for this. However, it was not until 1975 that Richard Emst proposed the frequency and phase coding method which takes advantage of the phenomenon for imaging.

Since then, magnetic resonance imaging (MRI) has been widely utilised for medical

diagnosis. It is a non-invasive imaging technique, based on the magnetic properties of nuclei. When a biological tissue is placed in a strong magnetic field the nuclei align parallel or anti-parallel to it. Applying an external radio source at an appropriate frequency the nuclei resonate and absorb energy. Accordingly, more nuclei align anti-parallel to the magnetic field. On switching off the radio source the biological tissue re-emits the energy as radio waves as a relaxation process to return to equilibrium. A 3D image of the biological tissue can be reconstructed from this signal.

2.2.2 Atomic structure

The atom consists of a nucleus surrounded by an electronic cloud. The nucleus contains positively charged nucleons (protons) and uncharged nucleons (neutrons). The atomic electrons occupy a set of energy levels. The transition of an electron between two energy levels (orbits) is caused by a loss in its energy via photonic emission, or an energy gain via absorbing a photon. For such a process to occur, the photonic energy should match the energy difference between the energy levels. Optical properties of atoms will be considered in more detail in Section(2.3). The physics of the atom on the microscopic scale is explained by quantum mechanics. However, it is sufficient for most of the topics of this chapter to apply a classical mechanical approach, although the quantum mechanical approach will be applied when it is necessary. According to a classical picture, electrons orbit the nucleus and spin on their own axes, while the nucleus also spins on its axis. Quantum mechanically, the electron, the proton and the neutron have spin of 1/2; the nuclear angular momentum is the vector sum of the angular momentum of the individual nucleon - spins plus orbital angular momentum within the nucleus. (In MRI of hydrogen, where the nucleus is a single proton, the nuclear spin is 1/2, with a component +1/2 or -1/2 in the direction of the applied magnetic field; the + and -

signs indicate spin up or spin down, the only two possible spin energy states.)

As stated by the Biot-Savart law, a moving charge generates a magnetic field. If this charge moves in a loop, there will be a magnetic moment associated with it. An orbiting charged particle can be considered as a current loop, with an associated magnetic moment. The spin of a charged particle on its axis can also be considered as a current loop, so the proton has an intrinsic magnetic moment associated with its spin (as does the neutron, although a classical model does not provide a simple explanation for this). The nucleus as a whole has a magnetic moment associated with its overall angular momentum.

2.2.3 Active MRI nuclei

As mentioned in the previous section, the spin of the nucleus results from the spin of its nucleons. The nucleons are organised in pairs in such a way that a nucleus with even mass number A (number of nucleons) and even atomic number Z (number of protons) exhibits no net spin. If A is even and Z is odd, the nucleus has integer spin values (1, 2, 3.). If A is odd, the nucleus has half-integer spin values (1/2, 3/2, 5/2.).

According to the above, not all nuclei are useful in the context of MRI, since non-zero nuclear spin is required to give the necessary non-zero magnetic moment. Examples of MRI active nuclei are ^{1}H (spin 1/2), ^{13}C (spin 1/2), ^{15}N (spin 1/2), ^{17}O (spin 5/2) and ^{19}F (spin 1/2). Among those nuclei, ^{1}H exists in abundance in biological tissue. This is because more than 70% of the human body consists of water (H_2O). Also, fat molecules, which exist in about 20% of the human body, have hydrogen atoms in their molecular structure.

2.2.4 Alignment

As discussed in the previous section, active MRI nuclei have a magnetic moment. The nuclei are orientated randomly in the absence of magnetic fields (Fig.2.1).

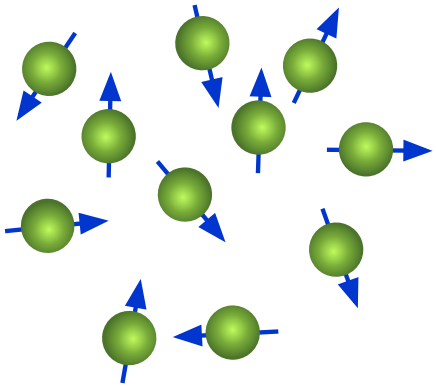

Figure 2.1: Orientation of nuclear spins in the absence of a magnetic field.

However, when they are placed in a strong magnetic field, the nuclear spins align either parallel or anti-parallel to the applied field (Fig.2.2).

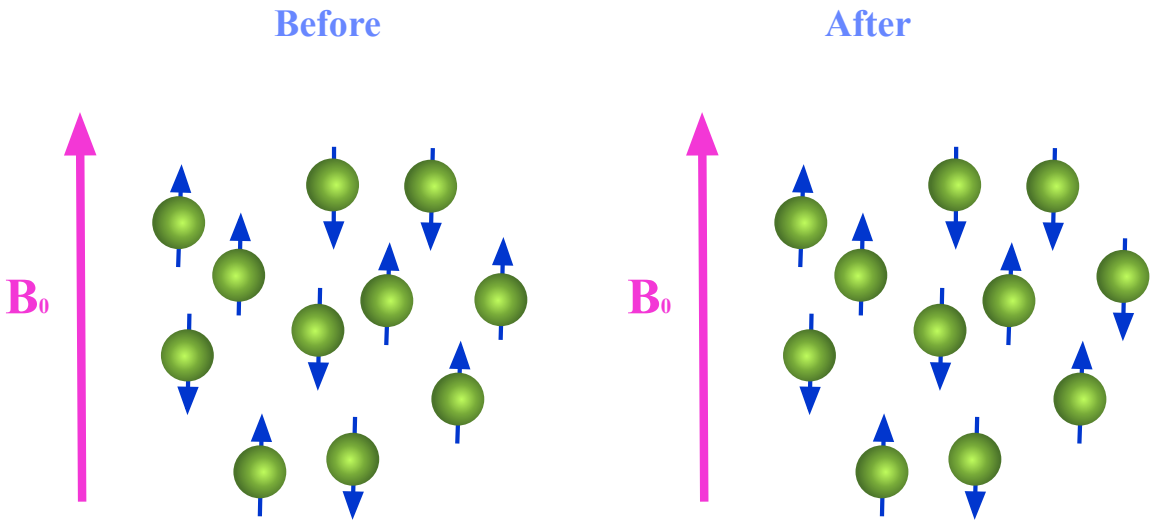

Figure 2.2: Alignment of nuclear spins in an external field before and after an RF pulse.

This corresponds to the only available energy states: spin up and down. (Note:

here we consider only the case of spin -1/2 nuclei, for simplicity.) This is a situation that can only be explained by quantum mechanics; classically one would expect that most of the nuclei would align with the magnetic field, and would not expect the anti-parallel alignment. However, classical physics provides an equivalent analysis: If the magnetic moment of a nucleus is directed at any non-zero angle with respect to an applied magnetic field, the magnetic moment moves around the direction of the magnetic field in a motion known as precession (Fig.2.3).

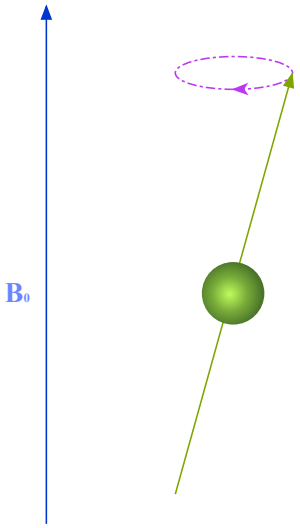

Figure 2.3: Precession of a nuclear spin.

The frequency at which the precession occurs depends on the nature of the nucleus and the strength of the applied magnetic field. This relationship is described by Equation(2.1)

$$\omega_0 = \gamma B_0 \tag{2.1}$$

where ω_0 is the precession (angular) frequency, also known as the Larmor frequency, γ is the gyro-magnetic ratio, which is determined by the type of nucleus and B_0 is the strength of the magnetic field. It might be relevant to mention that the hydrogen nucleus

(the proton) has a relatively high γ value. This results in greater sensitivity (higher signal) when using hydrogen nuclei in an imaging experiment, compared to nuclei with lower values of γ.

The nuclei that are aligned anti-parallel to the direction of the external magnetic field are in a higher energy state. In thermal equilibrium the number of nuclei with higher energy (anti-parallel alignment) is less than the number of parallel-aligned nuclei (lower energy) according to the Boltzmann distribution law.

$$\frac{N_{ap}}{N_p} = e^{-\Delta E/kT} \tag{2.2}$$

where N_{ap} is the number of antiparallel-aligned nuclei per unit volume, N_p is the number of parallel-aligned nuclei per unit volume, ΔE is the energy difference, k is the Boltzmann constant and T is the temperature in Kelvin. The energy difference can be calculated from Equation(2.3).

$$\Delta E = \hbar\omega_0 = \hbar\gamma B_0 \tag{2.3}$$

Where $\hbar = \frac{h}{2\pi}$ is the reduced Planck's constant.

2.2.5 Resonance and relaxation

In order to change the populations of the energy states, an external source of radio frequency (RF) waves at the Larmor frequency is required. Some of the nuclei will resonate, absorbing energy to jump to the higher energy state (anti-parallel aligned). This causes an increase in the number of nuclei in the higher energy state compared to the number in the lower energy state. In the case of a 1.5 T clinical scanner used to image protons (hydrogen nuclei), the difference in populations is about 4 protons

in every million. When the RF excitation is switched off, the protons return to their thermal equilibrium distribution, emitting RF energy at the Larmor frequency.

In the classical interpretation, on the macroscopic scale the applied magnetic field B_0 induces a magnetisation in the sample which can be represented by the net magnetic vector (NMV). The NMV is disturbed from its equilibrium orientation when an RF pulse is applied at the Larmor frequency ω_0, and starts to precess about the direction of B_0 and at the Larmor frequency. One can consider two frames of motion. The first is the Laboratory frame, in which the NMV is seen to precess at ω_0. The second is the rotating frame, in which the the observer rotates at ω_0 and the precession of the NMV is frozen and the observed effect of the RF pulse is to increase the flip angle α (Figure.2.4). If a 90° pulse is applied, the flip angle increases from zero to 90° during the duration of the pulse. After the RF pulse, the NMV returns to its initial status pointing parallel to B_0.

The direction of the applied field B_0 is conventionally known as the longitudinal direction and lies perpendicular to the transverse plane (Fig.2.4).

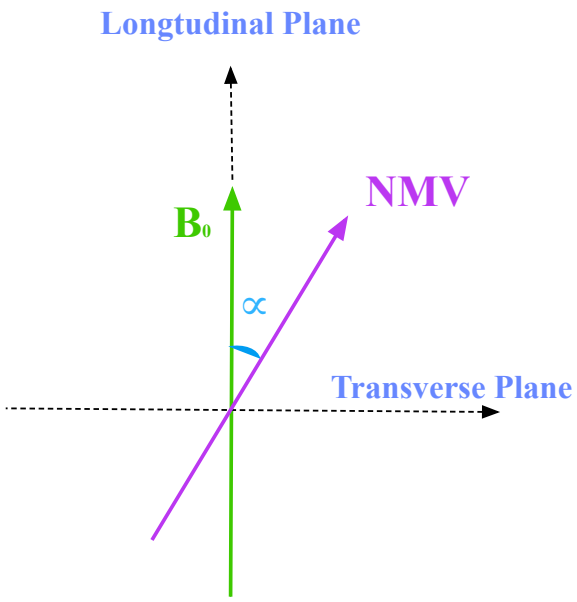

Figure 2.4: Illustration of the NMV, the longitudinal direction, the transverse plane, the flip angle and the direction of the static magnetic field B_0.

Hence the effect of a 90 pulse is to tip the NMV from the longitudinal direction into the transverse plane. It is important to emphasize that the transverse and longitudinal components of the NMV have different relaxation times. This results from the fact that the relaxation processes are different in each case. The recovery of the longitudinal component arises from nuclei in the higher-energy state (spin down) losing energy and returning to the lower-energy state (spin up). This phenomenon depends on interaction with the environment, known as the lattice. For this reason the associated time constant is known as the spin-lattice relaxation time given the symbol T_1. In contrast, the decay of the transverse component results from the dephasing of the nuclear spins. This phenomenon depends on magnetic interaction between the spins. Consequently, the associated time constant is called the spin-spin relaxation time given the symbol T_2. Both relaxations are exponential with time (Fig.2.5.).

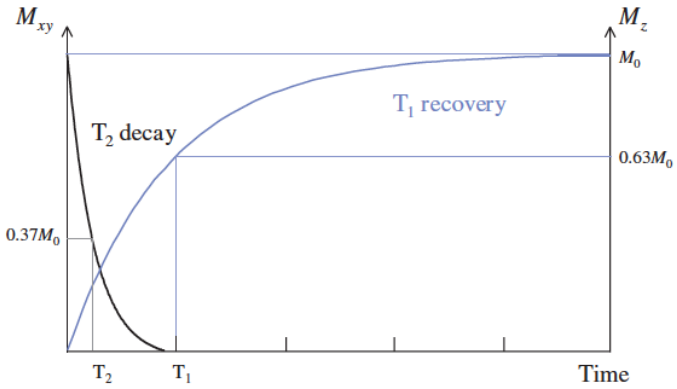

Figure 2.5: Longitudinal component recovery and transverse component decay curves (The figure was taken from reference [10]).

After a 90° pulse, the longitudinal component (M_z) recovers to 63% of its maximum in a time T_1. The decay in the transverse component (M_{xy}) reaches 37% of its maximum after a time T_2. These two time constants are intrinsic properties of the tissue being imaged. So, one cannot change their values by varying the settings of the MRI scanner. However, having knowledge about their estimated values allows the investigator to select the optimum imaging parameters.

2.2.6 Signal detection

After an RF excitation, in the Laboratory frame the NMV rotates (precesses) at the Larmor frequency ω_0. According to Faraday's law of induction, an electrical signal will be generated in a coil of wire with its axis in the transverse plane. (The magnetic field associated with the NMV is very small compared to the applied field: about 1 μT for the whole human body in a 1.5 T scanner.) The amplitude of the RF signal detected by such a coil is determined by the transverse magnetisation M_{xy} and hence varies as $\sin(\alpha)$ (Figure 2.4). This implies that the optimum flip angle for detecting the NMV is 90°.

The magnitude of the flip angle α depends on the amplitude and time duration of the RF pulse. This can be expressed mathematically by

$$\alpha = \gamma B_1 t_p \tag{2.4}$$

where α is the flip angle, B_1 is the amplitude of the magnetic component of the RF wave, and t_p is the duration of the pulse.

If a 90° pulse is applied, the NMV is tipped entirely into the transverse plane (Figure.2.6). The signal recorded after a 90° pulse will decay in a manner illustrated in Figure.2.7.

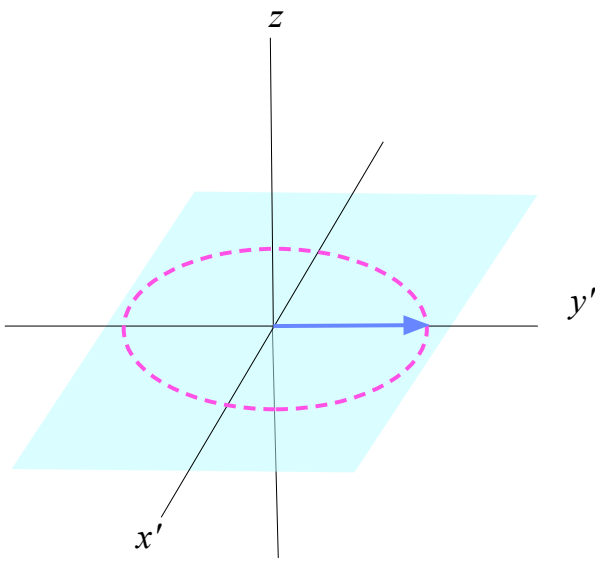

Figure 2.6: The NMV orientation in the rotating frame just after a 90° pulse

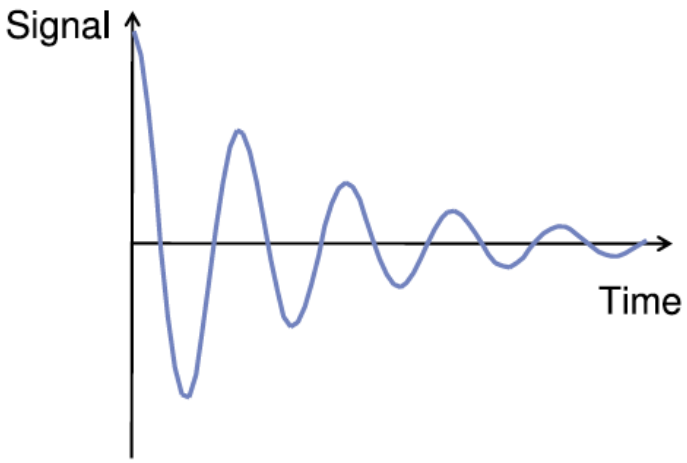

Figure 2.7: Free induction decay (FID)(The figure was taken from reference [10])

This type of signal is known as a free induction decay (FID). However, in imaging the signal received is of a different form; an "echo" is created using sequences such as spin echo and gradient echo which will be explained in the following section.

2.2.7 Imaging sequences

The two commonly used sequences in MRI are spin echo (SE) and gradient echo (GE). In the SE sequence (Fig.2.8), the initial 90° RF pulse is followed by a 180° pulse. Dephasing of spins that have accumulated during the period between the two RF pulses (Fig.2.8, c) is changed in sign by the 180° pulse (Fig.2.8, d). Hence phase changes over the following period (Fig.2.8, e) act to rephase the signal. After a time equal to the time between the 90° and 180° pulses, the spins will be in phase. The moment of spins being in phase (Fig.2.8, f) is known as the echo and the time from the 90° pulse to the echo is the echo time (TE). This process is repeated to obtain a complete image; the time between successive 90° pulses is known as the repetition time (TR).

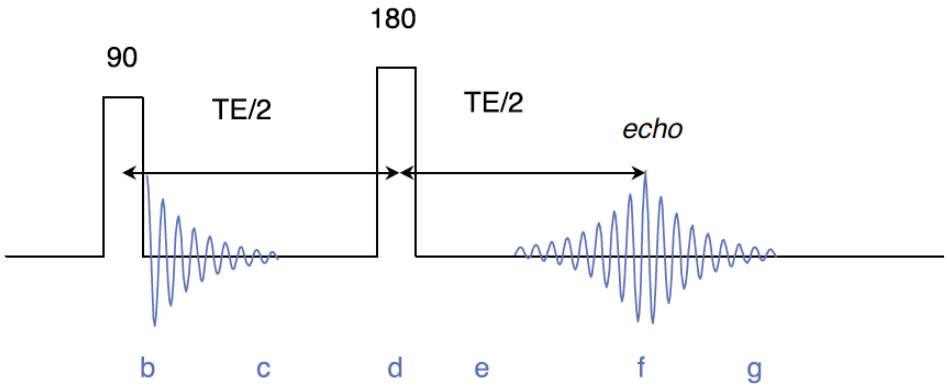

Figure 2.8: Spin-echo pulse sequence(reference [10])

When spin-echo sequence is utilised, the signal intensity is given by Equation(2.5) [10]

$$I^{SE} = c\left[1 - 2e^{-(\frac{TR-TE/2}{T_1})} + e^{-\frac{TR}{T_1}}\right] e^{-\frac{TE}{T_2}} \tag{2.5}$$

Where, c is a constant related to the MRI hardware properties, and, TE and TR are the echo and repetition times respectively. In Equation 2.5, T_1 and T_2 are intrinsic properties of the sample, whereas, TE and TR, are controlled imaging parameters. The sequence is T_1 weighted when these two parameters are chosen to highlight the variation in T_1 more than T_2 and vice versa. This actually requires previous knowledge about T_1 and T_2 of the sample, or, instead, one can rely on the fact that T_2 is always shorter than T_1.

In the GE sequence (Fig.2.9) an RF excitation pulse of 90° or less is followed by a negative gradient of magnetic field over the workspace. This produces significant additional dephasing of the nuclear spins and hence loss of the MR signal. However, application of a positive magnetic-field gradient then rephases the spins, producing an echo in a similar way to the SE sequence, described above. Again, the time from the 90° pulse to the echo is the echo time (TE), and the process is repeated to obtain a

complete image; the time between successive 90° pulses is known as the repetition time (TR).

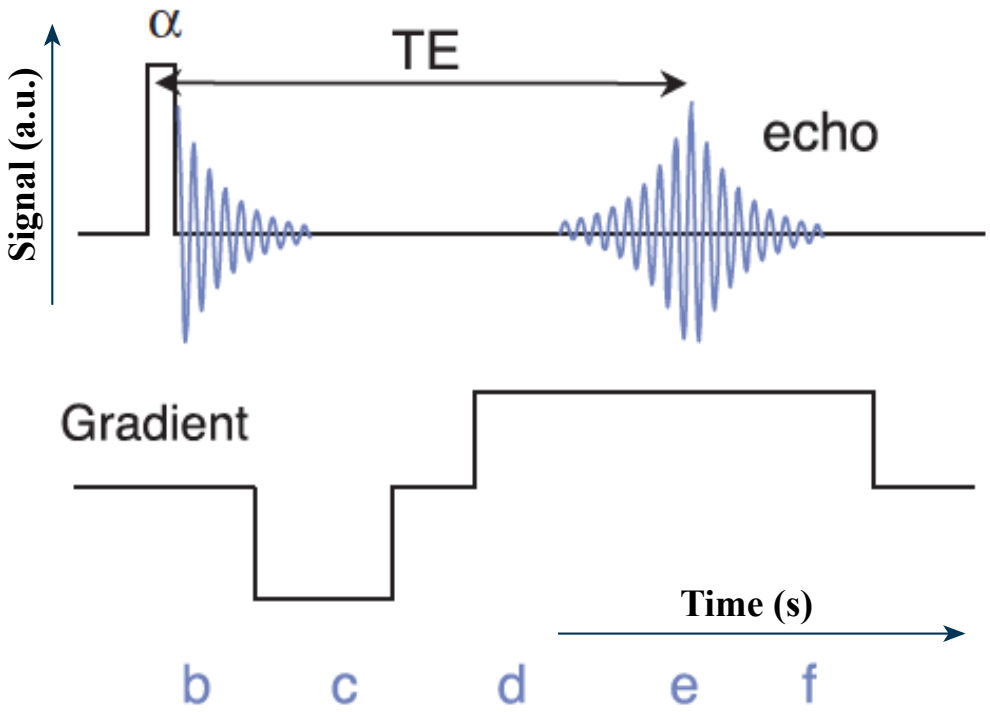

Figure 2.9: Gradient Echo pulse sequence(reference [10])

The signal intensity in a gradient echo sequence obeys the following equation

$$I^{SE} = c\left[1 - e^{-\frac{TR}{T_1}}\right] e^{-\frac{TE}{T_2}} \tag{2.6}$$

where, again, c is a constant associated to the MRI hardware, and, TE and TR are the echo and repetition times respectively.

2.2.8 The Bloch equations

In 1946, after discovering the phenomenon of magnetic resonance, a set of equations that describe the variation in the magnetisation components were derived by Felix Bloch [31]. From a classical mechanics paradigm, they describe the signal detected by the MRI receiver. Starting with

$$\frac{d\mathbf{M}}{dt} = \gamma \mathbf{M} \times \mathbf{B} = \gamma \begin{bmatrix} (M_x B_z - M_z B_y)\mathbf{i} \\ +(M_z B_x - M_x B_z)\mathbf{j} \\ +(M_x B_y - M_y B_x)\mathbf{k} \end{bmatrix} \tag{2.7}$$

Here $\mathbf{M}$ is the magnetisation induced in the bulk material, $\mathbf{B}$ the applied external magnetic field and γ is the gyromagnetic ratio. The magnetic field $\mathbf{B}$ is the vector summation of the static external magnetic field B_0 and the oscillating magnetic field produced by the RF where

$$B_x = B_1 \cos \omega t, B_y = B_1 \sin \omega t, B_z = B_0 \tag{2.8}$$

In a typical situation the frequency of the RF pulse will be chosen to be in resonance with the precession ($\omega = \omega_0 = \gamma B_0$). Observing that the relaxation processes in the z direction and the xy-plane occur at different rates, Bloch added relaxation terms to the component form of Equation(2.7) to obtain

$$\frac{dM_x}{dt} = \gamma(M_y B_0 + M_z B_1 \sin \omega t) - \frac{M_x}{T_2} \tag{2.9}$$

$$\frac{dM_y}{dt} = \gamma(M_x B_1 \cos \omega t + M_x B_0) - \frac{M_y}{T_2} \tag{2.10}$$

$$\frac{dM_z}{dt} = \gamma(M_x B_1 \sin\omega t + M_y B_1 \cos\omega t) - \frac{M_z - M_0}{T_1} \tag{2.11}$$

It can be seen that, when the RF pulse is switched off, $B_1 = 0$, the solution of the above differential equations will be given by

$$M_x(t) = [M_x(0)\cos\omega_0 t + M_y(0)\sin\omega_0 t] \cdot e^{-\frac{t}{T_2}} \tag{2.12}$$

$$M_y(t) = [M_y(0)\cos\omega_0 t + M_x(0)\sin\omega_0 t] \cdot e^{-\frac{t}{T_2}} \tag{2.13}$$

$$M_z(t) = M_z(0) \cdot e^{-\frac{t}{T_1}} + M_0\left[1 - e^{-\frac{t}{T_1}}\right] \tag{2.14}$$

The component of the NMV in the xy-plane, is simply given by

$$M_{xy}(t) = \sqrt{M_x(t)^2 + M_y(t)^2} \tag{2.15}$$

Substituting for $M_x(t)$ and $M_y(t)$ from Equations (2.12 and 2.13) in Equation (2.15), we get

$$M_{xy}(t) = e^{-\frac{t}{T_2}}\sqrt{M_x(0)^2 + M_y(0)^2} \tag{2.16}$$

Equations (2.12, 2.13, and 2.14) can be utilised to describe the relaxation process after an RF pulse. Let us assume a 90° pulse is applied. Accordingly the NMV will be flipped onto the xy-plane with its maximum magnitude M_0. Whatever the angle it makes with the coordinates x and y, the NMV is equal to M_{xy} at time t=0 (just after switching the RF off). This can be expressed mathematically by

$$M_{xy}(0) = M_{(0)} = \sqrt{M_x(0)^2 + M_y(0)^2} \tag{2.17}$$

Equation (2.17) gives us the initial condition just after the 90° pulse. Substituting this in Equation (2.16), the decay in the transverse component of the NMV can be given by

$$M_{xy}(t) = M_{(0)} e^{-\frac{t}{T_2}} \tag{2.18}$$

The recovery in the longitudinal component of the NMV is given by Equation (2.14). Just after a 90° RF pulse, the NMV will be totally flipped onto the xy-plane. If we chose this time to be our (t=0), then $M_z(0)$=0 and therefore, the first term of Equation (2.14) vanishes

$$M_z(t) = M_0 \left[1 - e^{-\frac{t}{T_1}}\right] \tag{2.19}$$

The magnitude of the NMV changes with time, so its components are independent of each other. To understand the independent variation of longitudinal and transverse components of the NMV, see Fig.2.10. It shows the relaxation process after a 90° RF pulse in the laboratory frame of reference. As illustrated, the NMV precesses around the z axis in at the Larmor frequency, with its component in the xy-plane decaying while its component in the z direction z axis is recovering. The recovering and decay occur with different relaxation times, $T_1$and T_2 respectively.

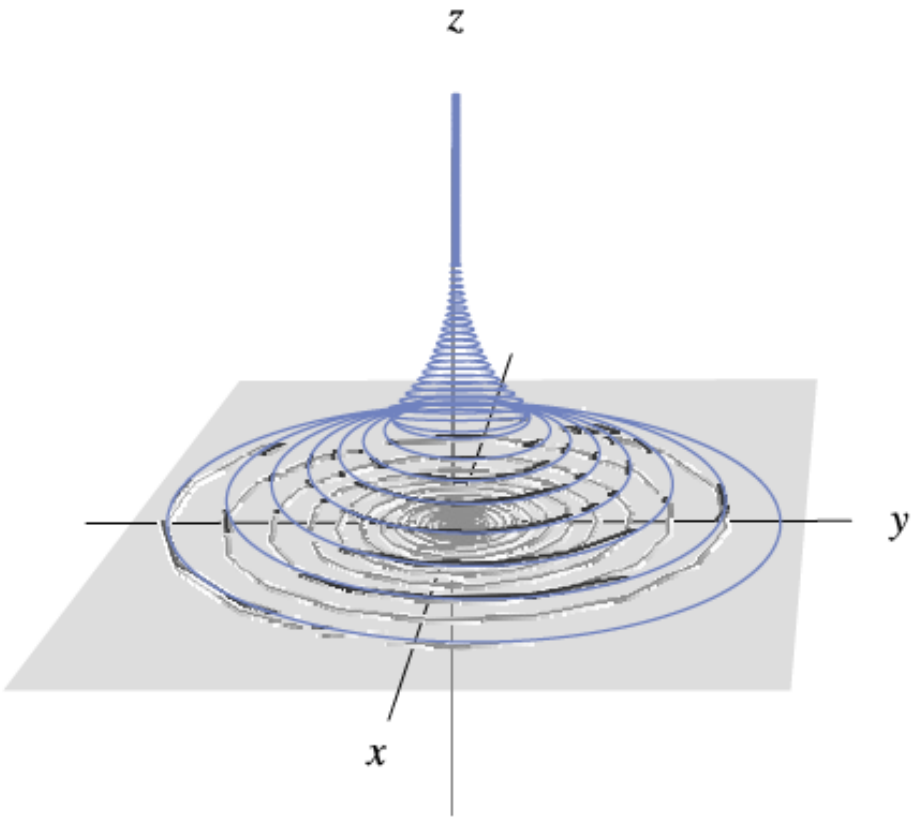

Figure 2.10: The relaxation as seen from the lab frame. The magnitude of the NMV does not always equal M_0(reference [10]).

2.2.9 Measuring relaxation time

As mentioned above, there are two different types of relaxation. The spin-spin relaxation time T_2 is less than the spin-lattice relaxation time T_1. In this section, we will explore the methods of measuring these relaxation times for a sample.

In order to measure T_2, a spin-echo sequence is applied with a range of different echo times. The signal intensity recorded in the receiver coil will obey Equation (2.18). So, a curve fit of the experimental data with this equation will provide us with the fitting parameters (M_0 and T_2).

For measuring T_1, one might suggest applying a similar method using Equation (2.19). However, it is not possible practically to measure the magnetisation component in the z direction. This is because the magnetic field associated with the NMV is much smaller than the static field which lies in the z direction. Instead, the so called inversion recovery sequence, is applied. It had actually been used before the days of MR imaging in NMR experiments for its applicability in measuring T_1 for bulk materials. In the inversion recovery sequence a 180° RF pulse is applied, flipping the NMV to the -z direction. Just after switching the RF pulse off, the recovery process will take place. This means the component of the NMV in the z direction will be increasing from -M_0 towards its equilibrium value of +M_0. After a certain time, known as the inversion time (TI), a 90° pulse is applied. This flips the z component of the NMV onto the xy-plane where it can be detected by the RF coil. This can be followed by a 180° pulse to refocus the signal and generate an echo, just as in the spin echo sequence. The signal intensity detected by the coil in the inversion recovery method is expressed by [10]

$$SI(TI) = M_{xy}(TI) = M_0 \left[1 - 2e^{-\frac{TI}{T_1}} + e^{-\frac{TR}{T_1}}\right] \tag{2.20}$$

In Equation (2.20), we chose the repetition time to be much longer than T_1 of the sample ($TR >> T_1$), to ensure full recovery. Figure(2.11) shows the time course of M_z in the inversion recovery experiment. So, a curve fit of the experimental data will provide us with the fitting parameters (M_0 and T_1).

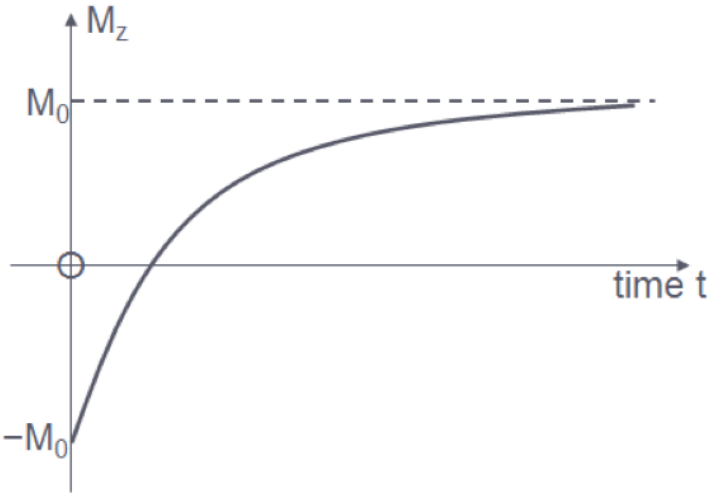

Figure 2.11: The time dependence of M_z in the inversion recovery experiment([32])

2.2.10 MRI contrast agents

The contrast in an MR image of a biological tissue is mainly due to the spatial variation in T_1 or T_2 values. The imaging sequence is said to be T_1 weighted if the principal image contrast relates to T_1 values, and T_2 weighted if the principal image contrast relates to T_2 values. The imaging parameters, TE and TR, are chosen in such a way that the image expresses the desired contrast. For instance, a long TE will give T_2 contrast (longer T2 appears brighter) and a short TR will give T_1 contrast (longer T_1 appears darker).

The variation in T_1 and T_2 are intrinsic properties that depend on the proton density, inhomogeneity of the magnetic field, and the chemical structure of the sample. However, magnetic material can be utilised in altering the sample relaxation properties. Such materials are known as contrast agents. The aim of this section is to understand how contrast agents work in MRI. This will be achieved by exploring the classification of magnetic materials, explaining the contrast mechanism, and the contrast agent relaxivity [33].

Magnetic material classification

Materials are classified into three main types for their response to an applied external magnetic field. The relationship between the magnetic field and the induced magnetisation is described by

$$\mathbf{M} = \chi \mathbf{B} \tag{2.21}$$

The classification is based on the proportionality constant, the magnetic susceptibility (χ), upon its magnitude, sign, and temperature dependence [34] . These types are diamagnetic, paramagnetic and ferromagnetic.

Diamagnetic materials do not have unpaired electrons in their outer atomic shell; so, their atoms do not exhibit any magnetisation when no magnetic field is applied. Their magnetic susceptibility is negative which means that the induced magnetisation is anti-parallel to the applied field. However, the magnitude of the magnetic susceptibility of diamagnetic materials is relatively small, 10^{-6} to 10^{-5} [35].

Paramagnetic atoms have unpaired electron in their outer shell. Each atom has a net magnetic dipole moment. However, the random orientations of the atoms moments cancel each other; so, the material has no magnetisation in the absence of an external magnetic field. When a magnetic field is applied, the magnetic moments of the atoms align parallel to its direction and the material develops net magnetisation. If a paramagnetic material placed in a non-uniform magnetic field it is attracted toward the stronger region. When the external field is removed the paramagnetic material loses its magnetisation.

Ferromagnetic materials are permanent magnets. They have unpaired electrons in their atoms outer shell, like paramagnet. However, the magnetic moments of atoms in ferromagnetic materials are arranged in domains due to a quantum effect known as

exchange coupling.

Contrast agents materials used in MRI belong to the second type, namely paramagnetic. The mechanism of how these materials enhance contrast of an MR image will be presented briefly in the following section.

Mechanism of contrast agents

As discussed in previous sections, contrast of an MR image depends on several factors such as proton density, relaxation times T_1 and T_2, and imaging sequence and parameters. Contrast agents shorten both relaxation times T_1 and T_2 (The detailed mathematical explanation is quite complicated and it is out of the scope of this thesis. For further details, the reader is referred to reference [36]). If the T_1 and T_2 values are altered by the contrast agents, the image contrast will be altered accordingly as stated by Equation(2.5) and Equation(2.7).

Relaxivity measurements

The relationship between the relaxation rates $1/T_1$ and $1/T_2$ and the concentration of a contrast agent is linear for relatively low concentration

$$\frac{1}{T_i} = \frac{1}{T_{i0}} + r_i\,[M] \qquad i = 1, 2 \tag{2.22}$$

where T_{i0} and T_i are the relaxation times of the sample before and after adding the contrast agent respectively, [M] is the concentration of the contrast agent, and r_i is known as relaxivity [36]. Here relaxation times are measured in seconds, the contrast agent concentration in mM, so the unit of relaxivity is $\mathrm{mM}^{-1}\mathrm{s}^{-1}$. Note that this equation is applicable for both T_1 and T_2 contrast agents.

In order to determine how a contrast agent is effective in MRI, its relaxivity is

calculated. Experimentally, this can be achieved by measuring the relaxation times for different concentrations of the contrast agent either by using the inversion recovery method for T_1, or by spin-echo sequence for T_2 as explained in section(2.2.9).

2.3 Optical spectroscopy and microscopy

2.3.1 Introduction

In this thesis, coherent Raman scattering (CRS) techniques are proposed to provide the complementary microscopic information about the 3D spatial distribution of the multi-scale nanoparticle contrast agents within a biological context. Also, optical spectroscopic methods are adopted to characterise optical properties of nanoparticles. Additionally, there are imaging techniques that can be used to image nanoparticles simultaneously with the same CRS laser excitations and experimental setup. The aim of this section is to explore the theoretical background of these spectroscopic and imaging techniques.

2.3.2 Confocal microscopy

Unlike a conventional optical microscope, the confocal microscope has the ability of optical sectioning. Only the signal from the excitation focal plane is collected using a pinhole detection scheme illustrated in Figure (2.12). This allows imaging at depth in 3D samples. The sample is stained with a fluorophore that absorbs at specific wavelength and emits light at longer (lower energy) wavelength. The excitation is typically achieved by employing a short-wavelength (400 -600 nm) visible laser.

The beam is raster scanned over the imaging plane with galvano mirrors and a dichroic mirror is utilised to isolate the emission beam by reflecting it to a photomulti-

plier tube. The image is recorded point-by-point with data read out with a computer and a matrix image constructed. Moreover, 3D imaging can be achieved by moving the objective lens to focus onto different planes. It is important to emphasize that the 3D confinement of the focal point is achieved by the pinhole setup as shown in Figure (2.12). The relationship between the emission and excitation is linear. This is important because another mechanism of the determination of the focal plane will be introduced later under nonlinear optical microscopes.

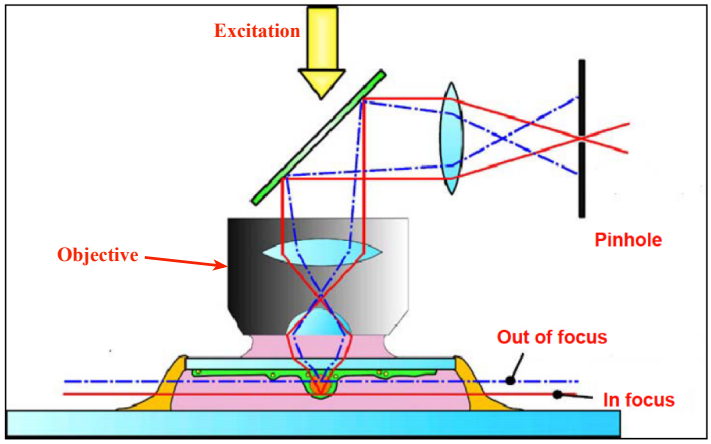

Figure 2.12: The principle of confocal microscopy(Figure was adapted from Leica TCS SP5 User Manual).

A significant limitation of confocal microscope is its inapplicability to scattering samples. In scattering media, light emitted from the focal plane undergoes scattering and is also rejected by the pinhole. This can severely reduce image sensitivity and can lead to high excitation power to obtain sufficient signal-to-noise. Another substantial limitation is that confocal microscopy relies on a single photon excitation. Accordingly,the excitation occurs in a large volume above and below the focal plane for the linear proportionality with laser power[see Figure(2.13)]. This results in bleaching of fluorescent dye even from out of focus lyers when scanning over the sample. Another limitation of the technique is the necessity to label sample molecules with fluorophores.

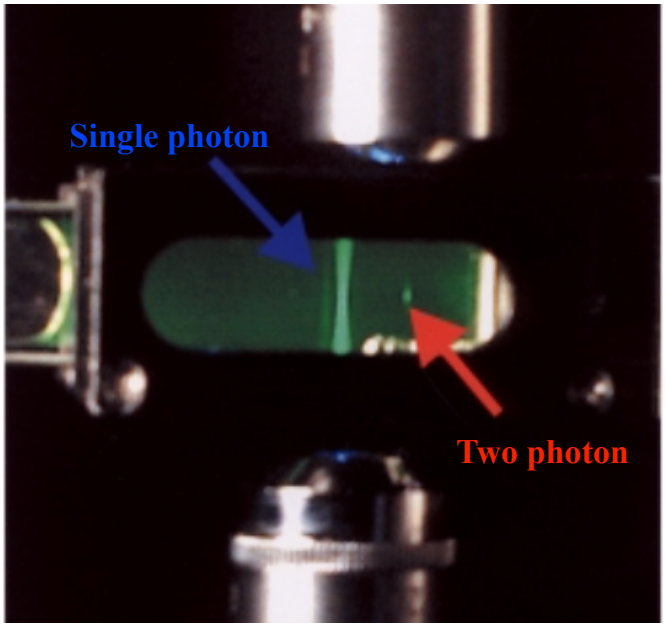

Figure 2.13: The excitation volume of single photon excitation versus two photon excitation(the figure was adapted from reference [37]). It can be seen that the excitation in a single photon process occurs below and above the focal plane whereas a point-like excitation in the focal plane is achieved by the two photon process.

2.3.3 Two photon fluorescence (TPF) microscopy

Two photon fluorescence (TPF) microscopy is based on the principle of nonlinear excitation where molecules are excited via simultaneous absorption of two near-infrared photons. This results in the emission of a higher energy photon (typically in the visible range) which is used for image contrast. This is not the case for confocal microscopy where single photon excitation is used [see Figure (2.14)]. The major advantage of using near-infrared excitation is reduction of the attenuation and scattering of the excitation light in biological tissue which enhances the optical penetration depth. This overcomes the major limitation of confocal microscopy. Also, the excitation of two photon fluorescence occurs only in the focal plane where the light is more intense for the nonlinear nature of the process. This reduces the photobleaching of the fluorophore [see

Figure(2.13)].

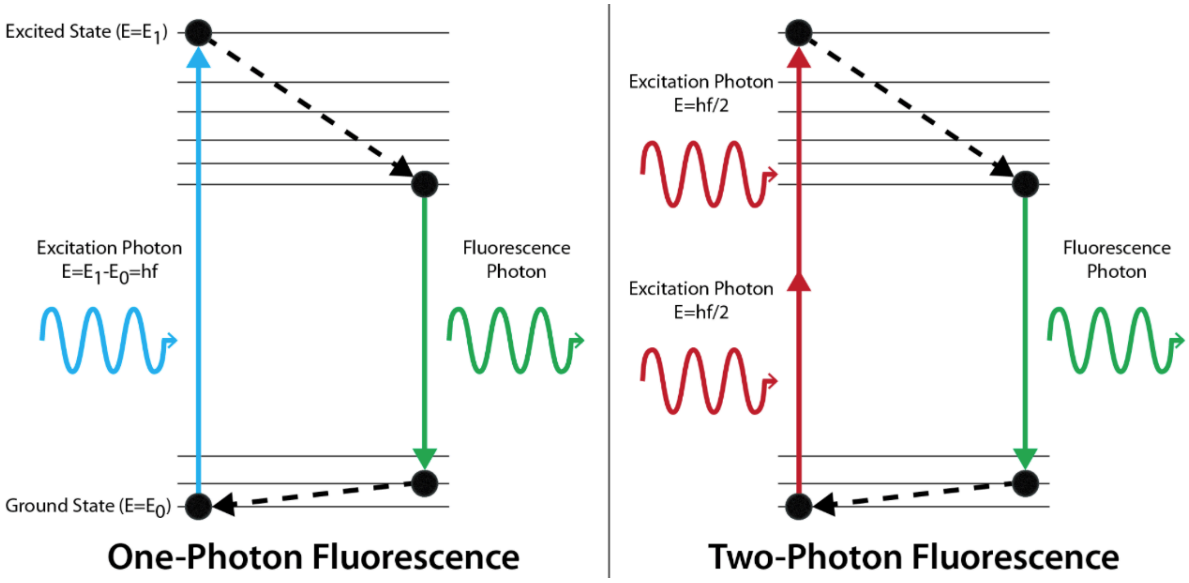

Figure 2.14: The energy digram of one photon and two photon fluorescence excitation (the figure was adapted from reference [37])

However, a significant disadvantage of two photon florescence (TPF) microscopy is the fact that it requires labelling the sample.

2.3.4 Spontaneous Raman scattering

Raman scattering is a type of interaction between light and matter at the molecular level. It was first reported by the Indian scientist Sir Chandrasekhara Venkata Raman in 1928 [38]. Photons of a monochromatic light beam experience inelastic collisions with the molecular bonds resulting in energy shifts either to a lower or a higher energy. The energy diagram (Fig.2.15)illustrates the interaction processes.

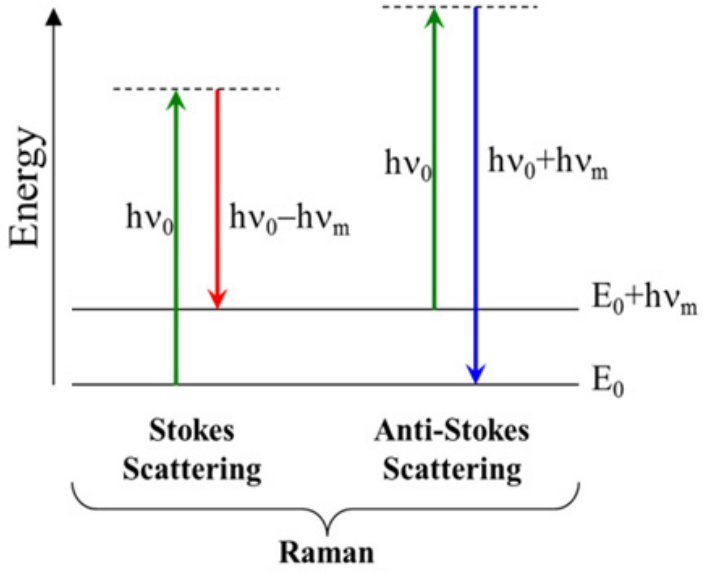

Figure 2.15: Energy diagram of Stokes and anti-Stokes Raman scattering (υ_0 is the frequency of the incident photon , υ_m is the molecular vibrational frequency and E_0 is the ground state energy of the molecule).

When a photon is absorb by a molecule in its ground state E_0, it is excited to a virtual electronic energy level and spontaneously relaxes to a vibrational state by emitting another photon with lower energy. The new photon is red shifted (has lower energy) with respect to the incident photon and this type of scattering is known as Raman Stokes scattering. In the second type of Raman scattering, anti-Stokes, a photon is absorbed by a molecule which is already in the vibrational energy level. Following excitation to the virtual electronic energy level, it spontaneously decays to the ground state emitting a photon with higher energy (blue shifted) with respect to the incident photon. However, anti-Stokes Raman scattering is less probable in thermal equilibrium (Boltzman distribution).

In both types, the Stokes and the anti-Stokes, the energy difference between the incident and emitted photons is equal to the vibrational energy of the specific chemical bond. It is conventional to measure the energy of a Raman shift using wave number

(cm^{-1}) according to Equation (2.23).

$$\Omega = \left| \frac{1}{\lambda_{in}} - \frac{1}{\lambda_{em}} \right| \tag{2.23}$$

where Ω is Raman shift and $\lambda_{in}$and λ_{em} are the wavelengths of incident and emitted photons respectively.

Raman scattering is a very powerful tool for chemical spectroscopy in biological applications, since the spectra of Raman scattered photon can be considered as a molecular fingerprint of a sample. Moreover, the direct proportionality of the signal to the bonds concentration allows quantitative analysis [39]. In microscopy, Raman scattering was utilised for imaging the distribution of bio-molecules with high resolution [40]. However, Raman scattering has a small cross section (typically 10^6 times weaker in biological tissue when compared to fluorescence) which means utilising it in microscopy requires long acquisition time of several hours to image biological cells [27].

2.3.5 Coherent anti-Stokes Raman Scattering (CARS)

CARS is a nonlinear optical technique based on the concept of Raman scattering that was first reported in the American Physical Society journal by Marker and Terhune in 1965 [41]. Instead of one incident laser beam, in CARS two laser beams are utilised to probe the molecular bond. The process of the energy transitions of the molecule under the two beams is illustrated in Figure(2.16). When the frequency difference between the two beams matches a Raman vibrational mode, they drive the molecules in the excitation volume to oscillate coherently. Three electromagnetic waves (2 of λ_p and λ_s) interact with the medium nonlinearly to induce a fourth wave via third order polarisation. This can be expressed mathematically by

$$P^{(3)}(\omega_{as}) \propto \chi^{(3)} E_p^2 E_s \tag{2.24}$$

where $P^{(3)}(\omega_{as})$ is the induced polarisation, $\chi^{(3)}$ is known as the third order electric susceptibility, and E_p and E_s are the electric field of the pump and Stokes respectively. The intensity of the anti-Stokes is given by [28]

$$I_{as} \propto \left|\chi^{(3)}\right|^2 I_p^2 I_s \left(\frac{\sin(\Delta k z/2)}{\Delta k/2}\right)^2 \tag{2.25}$$

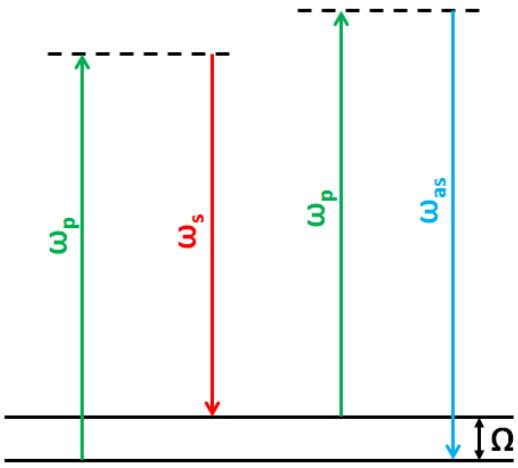

Figure 2.16: Energy diagram of CARS. Two pump photons of angular frequency (ω_p) and a Stokes photon of angular frequency of (ω_s) are involved in the generation of an anti-Stokes photon of angular frequency of (ω_{as}).

where I_{as} is the anti-Stokes signal intensity,$\chi^{(3)}$ is the third order electric susceptibility, I_p and I_s are the intensities of the pump and Stokes beams, respectively, z is the sample thickness, and Δk is the phase difference. It can be seen that the anti-Stokes signal is proportional directly to the square modulus of the third order susceptibility. This indicates that the CARS signal is proportional to N^2, where N is the number of oscillators in the excitation volume, since $\chi^{(3)} \propto N$. The signal is generated coherently from the oscillators and constructively interfere providing CARS with its higher sensitivity

when compared to spontaneous Raman scattering [28, 42, 43]. The non-linear dependence on excitation allows further enhancement by pulsed excitation. In Equation(2.25) Δk is given by

$$\Delta k = k_{as} - (2k_p - k_s) \tag{2.26}$$

In order to generate a maximum anti-Stokes signal from the excited volume Δk is required to be close to zero. This is known as phase matching condition(see Figure(2.17)). For CARS spectroscopy, the phase matching condition is obeyed by controlling the angle between the two incident beams in a 2D configuration. However, the phase matching condition was the challenging obstacle to employ CARS in imaging.

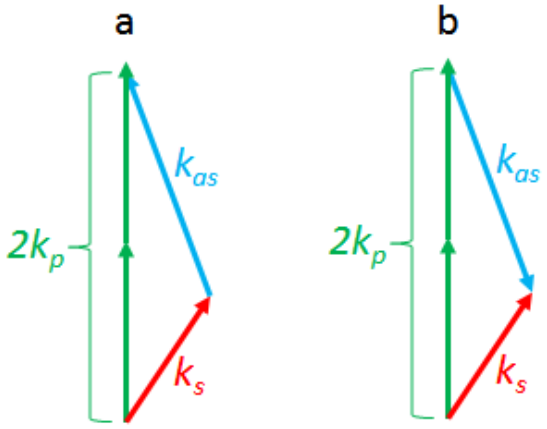

Figure 2.17: Phase matching condition in the (a)forward and (b)backward CARS.

It was not until 1999 that CARS was first implemented in microscopy [42]. This was achieved by tight focusing of collinear-aligned beams with high numerical aperture lenses to satisfy the phase matching condition. Since then, CARS microscopy has been utilised in biomedical applications [28].

Even if the difference between the two beams frequencies is chosen to be far from the Raman resonance frequency of a Raman active medium, there will be a signal generated

as a result of a response from the electrons. This contribution is independent of wavelength and known as the non-resonance background. When the frequency difference $(\omega_p - \omega_s)$ is tuned to match the Raman vibrational frequency, the anti-Stokes signal is enhanced by the resonance contribution. Accordingly, it can be assumed that $\chi^{(3)}$ consists of two components [28] stated by

$$\chi^{(3)} = \chi^{(3)}_{NR} + \frac{\chi^{(3)}_R}{\Delta - i\Gamma} \tag{2.27}$$

where $\chi^{(3)}_{NR}$ is the non-resonance component, $\chi^{(3)}_R$ is the resonance component, Δ is the detuning, and Γ is the bandwidth of a Raman peak. The detuning is given by

$$\Delta = (\omega_p - \omega_s) - \Omega_R \tag{2.28}$$

In Equation(2.28) Ω_R is the Raman shift and the value of Δ is zero at the resonance condition.

As mention above, the CARS signal intensity is proportional quadratically to $\chi^{(3)}$. Considering the resonance and non-resonance component Equation(2.27), the proportionality can be expressed as

$$I_{CARS}(\Delta) \propto \left|\chi^{(3)}_{NR}\right|^2 + \left|\chi^{(3)}_R(\Delta)\right|^2 + 2\chi^{(3)}_{NR} Re\chi^{(3)}_R(\Delta) \tag{2.29}$$

The physical concept of Equation(2.29) is illustrated in Figure(2.18). Each term of the equation is plotted as a function of Δ in Figure(2.18 **a**). The first term, $\left|\chi^{(3)}_{NR}\right|^2$, does not change when changing the detuning over a Raman vibrational mode, whereas the second term behaves like a spontaneous Raman peak. The third term is dispersive around $\Delta = 0$, which influences the addition of the three terms(Figure(2.18 **b**). Accordingly, the detected CARS signal peak is red shifted when compared to spontaneous

Raman. It also has a dip on the blue end of the peak which creates negative contrast of the active Raman medium(the black holes in Figure(2.18 **e**)).

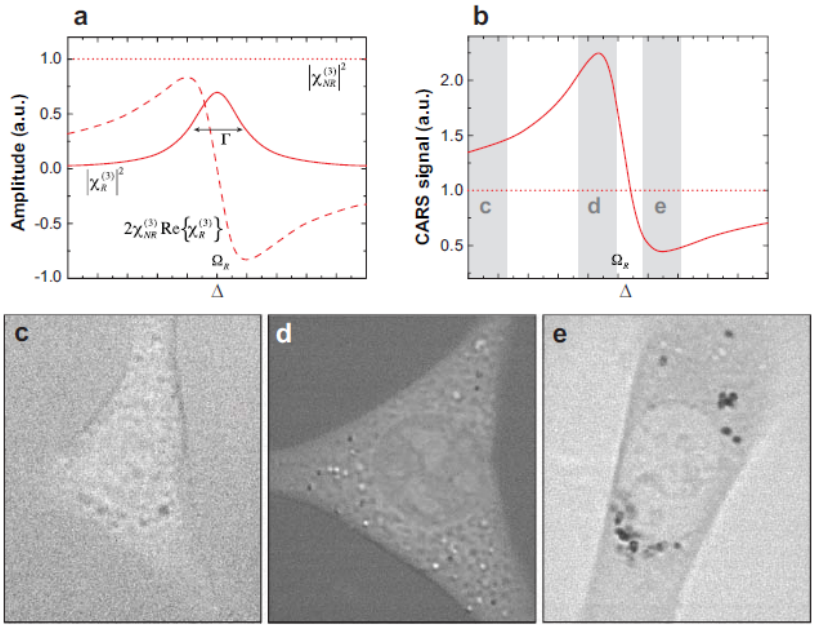

Figure 2.18: Resonance and nonresonance CARS (the image was taken from [28]). In image (a), the straight horizontal line represents the nonresonance term of Equation (2.29), the solid line peak-like curve corresponds to the second term of the equation, and the dashed curve represents the third term of the same equation. In image (b) the summation of the three terms of the equation is plotted and the images (c), (d) and (e) are CARS images of a biological cell with the correspondent detunings hilighted in image (b).

The signal of CARS microscopy can be detected in the forward and backward(epi) directions. Due to the coherent nature of signal generation unlike linear techniques such as Raman and fluorescence, CARS signal is directional. The strength of the signal in the forward and backward directions depends on different parameters. For a very thin object, the signal is equally generated in forward and backward directions. However, the forward signal gains more intensity for larger objects, whereas the backward signal decreases. This has special practical implication for epi CARS microscopy [44]. First,

objects in the size range of $\lambda/3$ generate backward signal because their size is not enough for the generated signal to interfere destructively [45]. Second, the sharp discontinuity in the third order susceptibility $\chi^{(3)}$in the focal volume permits higher backward signal. The third mechanism occurs in highly scattered medium, medium with continuous change in the refractive index, where the forward signal redirected toward the backward direction.

2.3.6 Four wave mixing (FWM)

As mentioned in the previous section there is a non-resonance signal generated in the focal volume (see Equation.2.27 and Figure.2.18). This signal is a result of a more general form of four wave mixing processes where three waves contributes in generating the fourth and it is independent of the Raman resonance mode. Nanoparticles of high third order susceptibility such as some metal oxides can be imaged with the FWM mechanism [46]. Moreover, the nanoparticles could be imaged in the biological tissue. The distinguishable contrast of the particles against the biological tissue is achieved by tuning the laser wavelength away from Raman resonance of CH bonds in lipids. The nanoparticles will still possess a strong FWM signal because of their high third order susceptibility and condensed nature.

To the best of the author's knowledge, there is only one study which investigated the possibility of imaging magnetic particles with the FWM process. In 2011, Rago and coworkers imaged iron oxide microparticles in biological cells [30]. Figure.2.19 shows three images of micro-sized iron oxide particles where (a) is a bright field image, (b) is an on-resonance CARS image where pump and Stokes tuned to target CH bonds and (c) is an off resonance image of the particles. As stated by the authors, the signal of (b) and (c) is due to different excitation power driven of the OPO, hence otherwise, both

on-resonance and off-resonance are physically expected to generate the same signals.

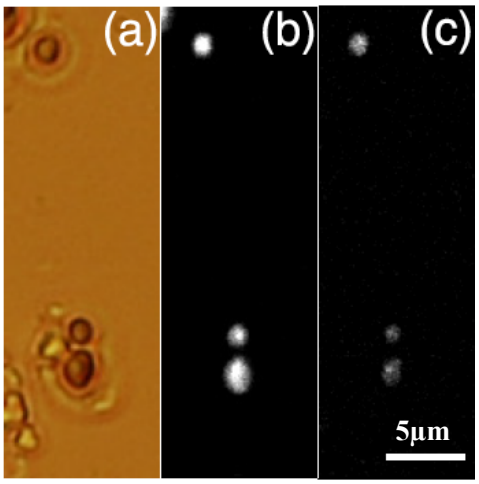

Figure 2.19: Imaging iron oxide micro-particles, a) transmission light, b) on resonance , and c) off resonance FWM.

However, it is more practical for drug targeted delivery for the particles to be of smaller size, namely, in the nanometer scale, especially in the case of solid tumours [47]. This is due to the diffusion process which was widely discussed in the literature as a way to deliver specific medicine and contrast agents to tumours where the vascular structure is leaky for such small particles. In this study the FWM will be considered as one of the available techniques for imaging magnetic nanoparticles.

2.3.7 Stimulated Raman Scattering (SRS)

When targeting a Raman vibrational mode using CARS, different processes occur simultaneously in the focal volume. One important process is the stimulated Raman scattering (SRS)(see the energy diagram Figure(2.20)). The molecules excited with the pump beam reach a virtual electronic state. If the sample is not subjected to another laser beam(the Stokes in this case), the molecules will spontaneously radiate photons in the Stokes frequency. This is exactly what occurs in the spontaneous Raman

process. However, in the presence of the Stokes beam the molecules are stimulated to radiate their energies resulting in a gain in the Stokes intensity(SRG) and a loss in the pump intensity(SRL). This process is known as stimulated Raman scattering.

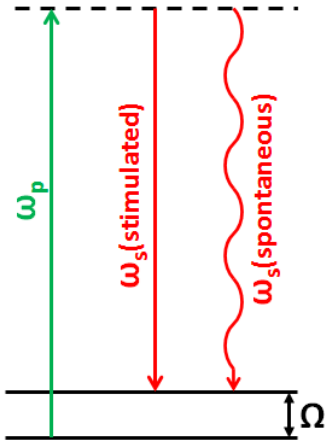

Figure 2.20: Stimulated and spontaneous Raman scattering

In order to detect this small change in the intensity, one of the beams is amplitude-modulated in a certain frequency and the intensity of the other is measured with a lock-in amplifier fitted after the sample. The Stokes will experience a loss that occurs in the same modulation frequency and a loss will be observed in the pump beam. Figure(2.21) illustrates the molecular transfer process for SRL detection when the Stokes beam is modulated.

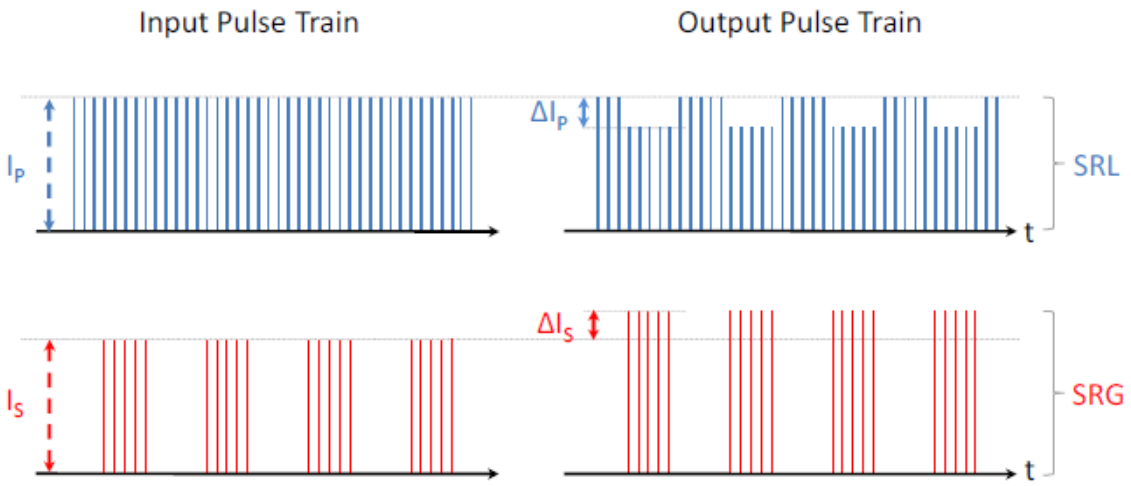

Figure 2.21: The loss and gain in the stimulated Raman scattering,adapted from [48].

The remarkable advantage of SRS comparing to CARS is the absence of the non-resonance background. Also, SRS is linearly proportional to the oscillators concentrations which permits utilising it in quantitative analysis.

2.3.8 Two Photon Photothermal lensing (TPPL)

Two photon Photothermal lensing microscopy is a method that maps the features of a sample via its nonlinear optical absorption. The sample is subjected to two beams focused with an objective lens. One of the beams (the pump) is absorbed nonlinearly by the sample in the focal point as an excitation of atoms to an electronic state. The absorption will generate heat that has gradient around the focal point causing a gradient in the refractive index. This causes the focal point to work as a lens. If the pump beam is modulated at certain frequency the lens effect will be modulated accordingly. The second beam experiences a lensing effect at the modulation frequency that causes its diameter at the detector to modulate. For a small aperture detector this changing in

diameter results in an intensity modulation in the probe signal [49]. Like SRS, the fluctuations of the probe signal intensity can be detected with a lock-in amplifier, and it can be given mathematically by [50]

$$S \propto \frac{I_{ex}^2 \cdot I_{pr} \cdot \sigma_{2-p} \cdot [c] \cdot \eta_H}{\lambda_{pr} \cdot \kappa} \left(\frac{dn}{dT}\right)_p \tag{2.30}$$

where S is the detected signal, I_{ex} and I_{pr} is the pump excitation and the probe intensities respectively, σ_{2-p} is the two photon absorption cross section, $[c]$ is the sample concentration, η_H is the yield of heat dissipation, λ_{pr} is the probe wavelength, κ is the thermal conductivity, and $\left(\frac{dn}{dT}\right)_p$ is the rate of change of refractive index with temperature at constant pressure.

2.3.9 Photoluminescence (PL)

Luminescence is an optical effect that generates light from a material via spontaneous emission. The emission is a result of an excitation that can occur in different ways. The excitation could be via a chemical reaction(chemiluminescence), electric field(electroluminescence), and so on. If the excitation occurs through light absorption, the process is known to be photoluminescence(PL). The term photoluminescence is conventionally used when an ultraviolet or visible photon excite the material to generate another photon of lower or equivalent energy. For solid state materials, there are two main categories in which the photoluminescence occurs: localised and delocalised systems. In the localised systems, the absorption and emission arise from quantum energy state centres within the material. Examples of the these active localised luminescent centres are rare earth ions and transition metal ions. Isolating materials or wide band gap semiconductors are doped with these ions and the luminescence properties depend on both the ions and the host materials. Another example of the localised centres systems is defects in solids.

In the second type, the delocalised materials, the luminescent properties are associated with the entire solid quantum states [51]. The photoluminescent materials investigated in this thesis belong to the localised luminescent centres systems type where a large band gap crystal is doped with rare earth ions.

The mechanism in which PL occurs in doped large-band-gap semiconductors is explained in detail by Belsky and Krupa [52]. In brief, doping such large band gap semiconductors with rare earth ions generates possible energy states within the band structure. The excitation occurs via a direct absorption either by the luminescence centres or by the host lattice. In both cases a portion of the absorbed energy is then re-emitted in the form of lower energy photons. The luminescence can be used as a fingerprint for the doping ions.

2.3.10 Upconversion Photoluminescence (UPL)

Upconversion Photoluminescence is a nonlinear optical process in which two or more infrared photons are involved in generating a photon in the visible spectrum. However, unlike other nonlinear processes, upconversion can occur even with low intensity excitation with the benefit of two or more metastable long-lived energy states. The mechanisms of upconversion can be classified into four main types: excited state absorption(ESA), cross relaxation(CR), energy transfer upconversion (ETU), and photon avalanche (PA) [53] (See Fig.2.22).

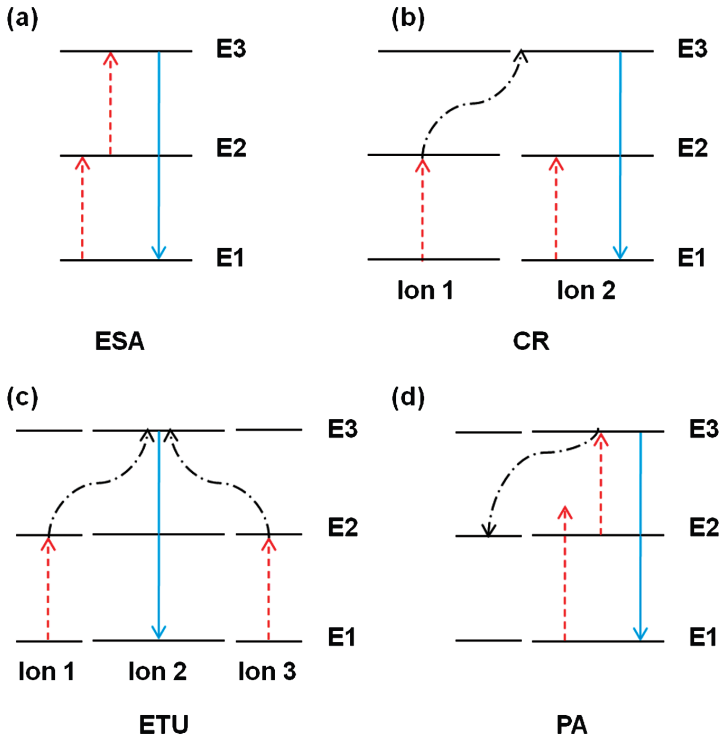

Figure 2.22: UC processes a) excited state absorption, b) cross relaxation, c) energy transfer upconversion and d) photon avalanche.(The figure is adapted from [53])

In ESA the ion is excited from its ground state E_1 to an energy state E_2 after absorbing an infrared photon. Because the new energy state has a long lifetime, there is a high probability for another photon to excite the ion to a higher energy state E_3. When the ion relaxes back to its ground state it emits a photon with the energy $(E_3 - E_1)$. In the cross relaxation process two ions are excited to an energy level E_2. Afterwards, one of the ions relaxes to its ground state through transferring energy to the other ion which absorbs the energy and is consequently excited to E_3. A photon is emitted with energy equivalent to $(E_3 - E_1)$. Three ions are involved in the ETU, where two ions(known as the sensitizers) are excited to $E2$ via absorbing infrared photons. They both transfer energy to a third ion (known as the activator) which is excited accordingly to E_3 and spontaneously emits a visible photon [54,55]. The last mechanism occurs when the intensity of the excitation reaches a threshold value, where many ions jump to E_2

through nonresonant excitations. Because a considerable number of ions are in the energy state E_2, a resonance ESA occurs for photons with energy $(E_3 - E_2)$ populating the energy level E_3. As more and more ESA events take place, ions exited to E_3 transfer energy to surrounding ground state ions resulting in a further increment in the E_2 population. A much stronger UC can be detected above the excitation intensity critical level [56].

Chapter 3

Method and Instrumentation

3.1 Introduction

Several spectroscopic and imaging techniques are utilised to achieve the goals of this thesis; label free imaging of the biological tissue and imaging magnetic nanoparticles on multiple scales. The theoretical backgrounds of these different techniques were covered in the previous chapter. In this chapter, the experimental techniques and methods used to implement them experimentally will be presented.

3.2 Magnetic Resonance Imaging

All the MRI data for this project was acquired at Exeter MR Research Centre. The center is equipped with a Philips 1.5 T clinical whole-body scanner. A head coil (SENSE Head coil 8 elements) was utilised to conduct the T1 and T2 measurements for the different MRI contrast agents. For the high resolution imaging, and detailed T1 and T2 mapping, a 23mm microscopy coil is used providing high signal-to-noise ratio.

3.3 Optical setup

3.3.1 Raman Spectroscopy and Photoluminescence

The Raman spectroscopy and the photoluminescence spectroscopy in this thesis were performed using a Renishaw RM1000 Raman micro-spectrometer Figure.3.1 (Renishaw, Wooton-Under-Edge, UK). The micro-spectrometer was modified between two available configurations. The first is achieved by utilising an infrared continuous laser source emitting at 785 nm and a 1200 line/mm grating, which provides spectral resolution of 1 cm^{-1}. In the second setup, a 532 nm green continuous laser is implemented with a 2400 line/mm providing approximately the same spectral resolution. The spectral acquisition parameters such as the illumination power, time of each scan and number of scans was controlled with Renishaw v.1.2 WiRE software. The microspectrometer was equipped with number of different objectives: 50x/0.75NA , 40x/0.55NA, 20x/0.40NA and 5x/0.12NA.

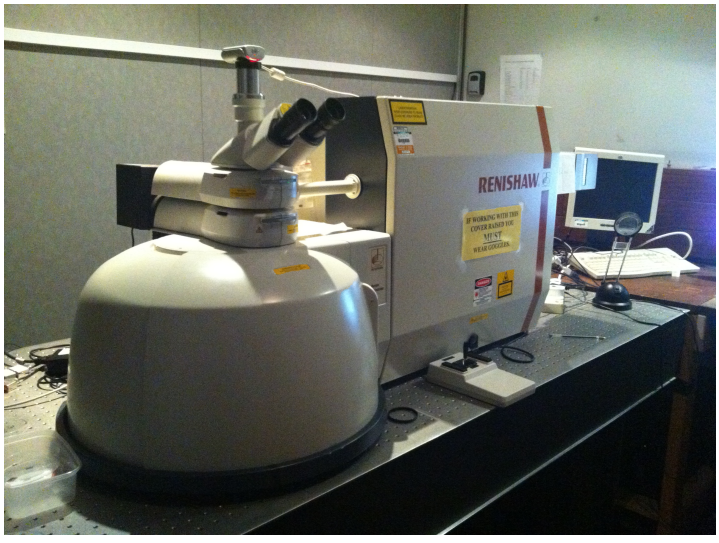

Figure 3.1: Image of the Raman spectrometer (RM1000).

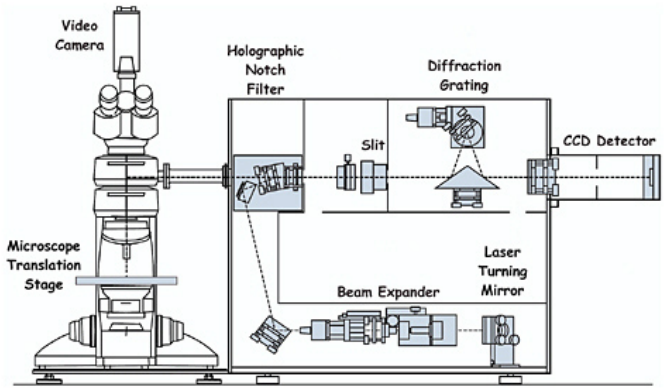

Figure 3.2: Sketch of the optical setup of the Raman spectrometer (RM1000).

The system is calibrated before each experiment using the well known strong silicon peak at 520 cm^{-1} as a reference.

3.3.2 Confocal microscope

The upconverting nanoparticles were imaged using a Leica TCS SP5 confocal microscope. The microscope is equipped with eight CW laser sources emitting from blue to green (Diode laser: 405 nm, Multiline Argon Laser: 458 nm, 476nm, 488 nm, 496 nm, 514 nm, 543 nm and HeNe Laser: 633 nm). Also, a tuneable acousto-optic filter provided flexibility of the emission. Three photomultiplier tubes are fitted in the optical setup of the microscope to provide three possible imaging channels. In a typical experiment, two channels are used to detect two tuneable ranges of the emission spectrum and the third detects the transmission light image.

In order to image the doped gadolinium oxide nanoparticles, two laser lines of the Argon laser are utilised (458 nm). A 63x oil immersion objective lens with numerical aperture of 1.4 was used. The detection spectrum of the two channels were determined according to the expected PL emission of the particles. All the imaging parameters were computer-controlled using the manufacturer software (Leica Application Suite Advanced

Fluorescence (LAS AF).

3.3.3 Coherent anti-Stokes Raman Scattering

Coherent anti-Stokes Raman scattering is a nonlinear optical mechanism that requires an ultra-fast pulsed laser. The laser source is a solid state Nd:Vanadium laser (High-Q Picotrain, Hohenems, Austria). An infrared 6 ps pulsed beam train is obtained at 1064 nm and frequency doubler generates green 532 nm light with output power 4 W. The system repetition rate is 76 MHz. The 1064 nm beam can be used directly from the source and the 532nm is used to pump an optical parametric oscillator (OPO) to produce two tuneable near infrared beams. These two beams are known conventionally as signal(the shorter wave length) and the idler. The range of wavelength of the signal and idler are from 690 nm to 990 nm and 1150 nm to 2300 nm, respectively. The output beams are steered on the optical bench with silver mirrors configured in such a way as to ensure that the beams are spatially overlapped in a colinear manner. The pulse trains of the two beams are temporally overlapped by changing the length of the optical path of one of them using a delay stage(see Fig.3.3), so that pump and Stokes arrive at the microscopy simultaneously.

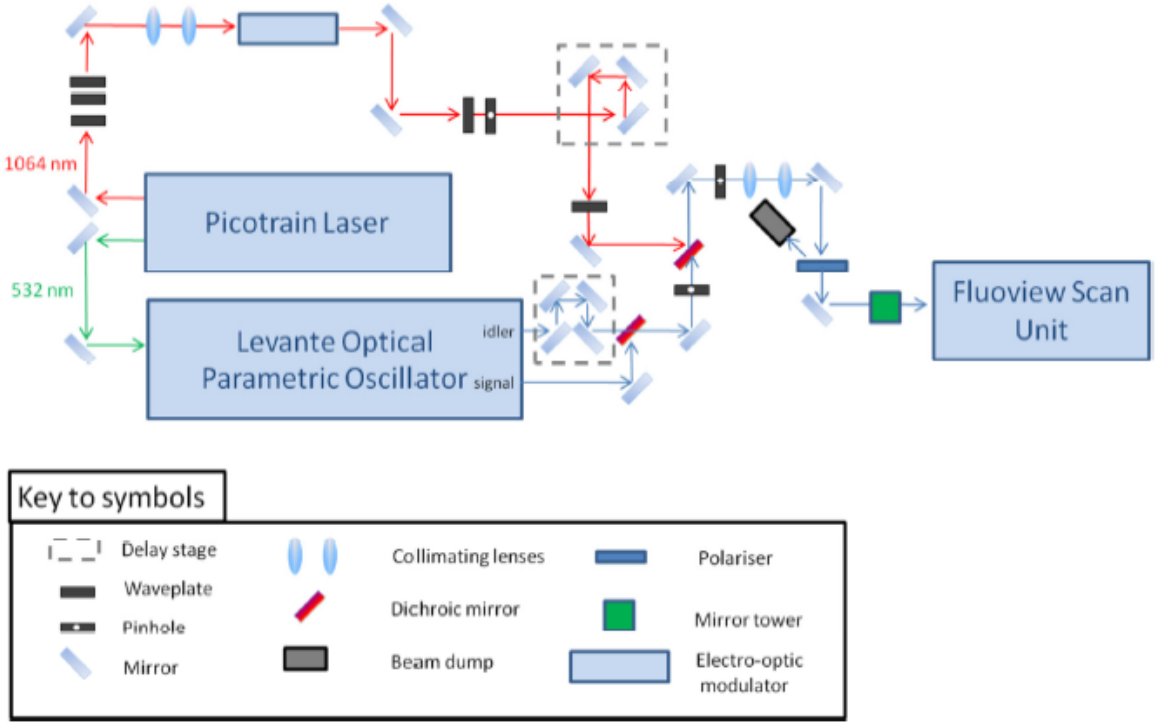

Figure 3.3: The optical setup of CARS microscopy [48]

The spatially and temporally overlapped beams are directed into a modified laser scanning microscope. (Olympus IX71 & FU300) which had silver galvanometric mirrors and MgF_2 coated lens to improve optical transmission in the near IR.

There are two available CARS setups to image biological structures by targeting the CH Raman vibrational mode at 2848 cm^{-1}. The first is by utilising signal and idler beams as pump at 924 nm and Stokes at 1254 nm respectively. For this configuration, a 850nm long wave pass diachronic mirror (z850rdc-xr, Chroma Technologies) is placed before the objective lens to allow epi-detection. The transparency profile (and hence oppositely the reflectivity) of the mirror is illustrated in Figure.3.4.

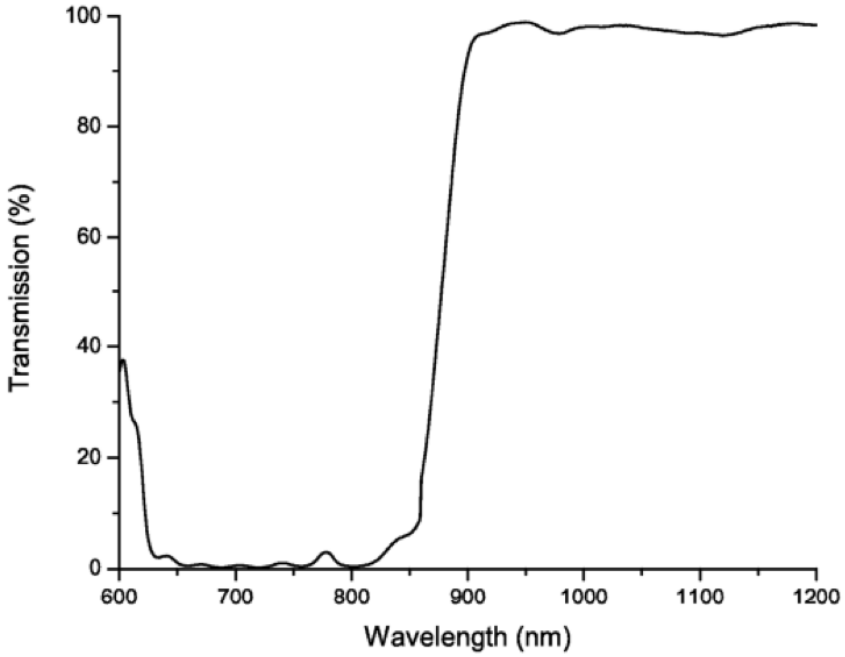

Figure 3.4: The transparency of the dichroic 850nm long-pass mirror (provided by the manufacturer)

For the forward detection, the signal is collected with an air condenser (NA=0.55), reflected with a mirror and filtered with a band pass filter (HQ750/210, Chroma Technologies). The transparency profile of the 750 nm band-pass filter is provided by the manufacturer in Fig.3.5.The signal is then collimated with a lens and detected with a red-sensitive photomultiplier tube (PMT) (R3896, Hamamatsu). Fig.3.6 shows the sensitivity profiles of two models of PMT from the same supplier. The sensitivity of the R3896 is considered when quantitative or qualitative comparison is required. The epi signal is collected by the objective lens and reflected with the 850nm long wave pass dichroic mirror into another R3896 PMT fitted in the back of the microscope. Another band pass filter (HQ750/210, Chroma Technologies) is used to isolate the anti-Stokes signal in the epi-direction.

The second available CARS setup for CH imaging at 2848 cm^{-1} is obtained by

employing the signal at around 816 nm and the 1064 nm beams as pump and Stokes respectively. For this choice, a 750 nm long wave pass dichroic mirror (Chroma) is placed before the objective lens. The epi-CARS is only collected with the objective lens and reflected with the dichroic mirror through two 660 nm band-pass filters (CVI). The signal is collimated with a lens and detected with the R3896 photomultiplier tube.

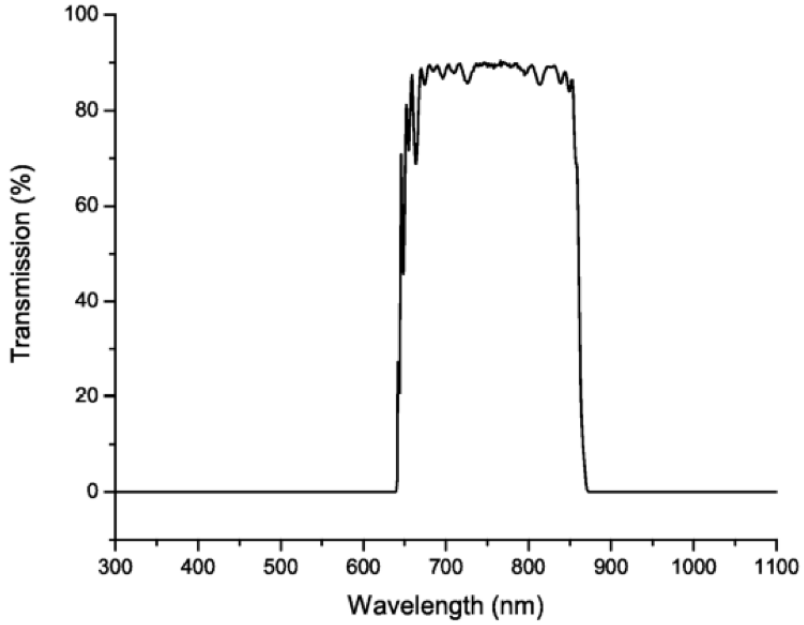

Figure 3.5: The transmission profile of the 750/210 nm band pass filter (provided by the manufacturer)

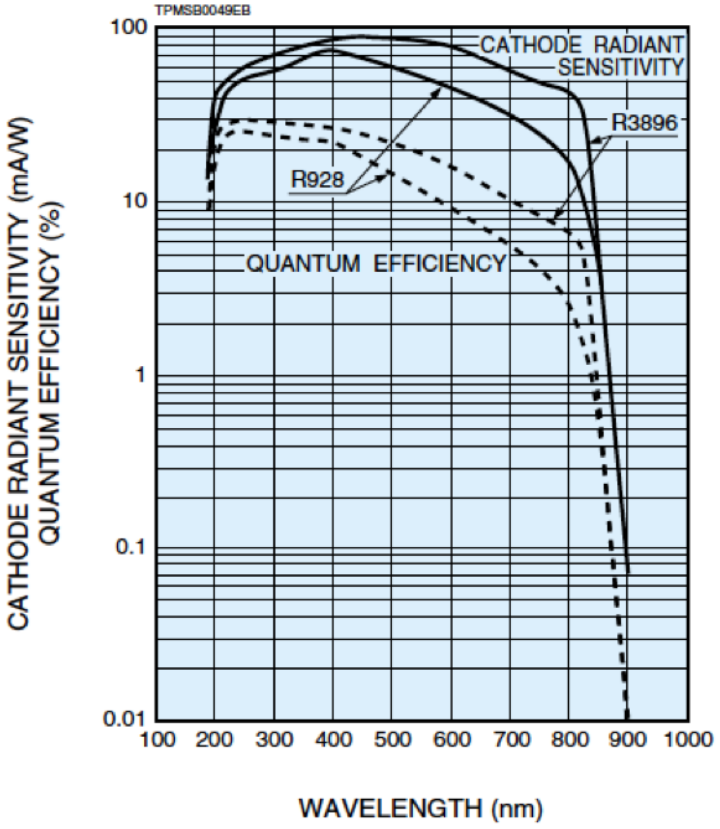

Figure 3.6: The cathode radiation sensitivity of the PMT (R3896, Hamamatsu) as a function of wavelength (provided by the manufacturer)

3.3.4 Stimulated Raman Scattering

Stimulated Raman scattering is detected with a similar optical configuration to the second CARS setup explained in the previous section. However, a Pockels cell (EM200, Leysop, UK) and a polariser are placed in the optical path of the 1064 nm beam to modulate its amplitude at 1.7 MHz importing the signal from a function generator(Agilent). The forward signals are collected using either the (0.55 NA) or another objective lens (Nikon Fluor 60 x, 1.0NA) for a higher sensitivity detection. Then a band-pass filter (Chroma, CARS 890/220 nm) is utilised to isolate the pump beam from the Stokes signal. The modulation of the pump signal intensity resulting from the SRL is detected

with a Si photodiode (Thorlabs, FDS1010). The electric current generated in the detector is filtered with a low-frequency pass filter (Mini-Circuits, BLP-1.9+) in order to suppress the strong signals generated due to the laser pulsing at the repetition rate 76 MHz. The signal is amplified with a lock-in amplifier (Stanford Research, SR844RF) referenced to the signal generator frequency 1.7 MHz. The modulation frequency is chosen to be far away from the laser relative intensity noise (RIN).

3.3.5 Two Photon Photothermal Lensing (TPPL)

The two photon photothermal imaging of the red blood cells and iron oxide nanoparticles was achieved by utilising the same setup used from SRS. However, as demonstrated in Section (2.3.8) the mechanism of TPPL is completely different form SRS. Consequently, different experimental parameters have been adjusted in order to enhance the quality of the background free image. This includes the modulation frequency, the temporal desynchronisation of pump and Stokes beams and aperture size of detection optics. The modulation frequency is controlled with the function generator and the delay stage of the 1064 nm beam is used to control the temporal overlapping of the two pulse trains. Finally, the aperture size of the detected beam is adjusted using a iris diaphragm.

3.3.6 Upconversion spectroscopy and imaging

For the upconversion spectroscopy, a single excitation picosecond or femtosecond (Coherent, MIRA) pulsed beam is used. The spectroscopy of the upconverting doped gadolinium oxide particles is performed by scanning them with the microscope. A polarising beam splitter is placed before the microscope to reflect portion of the backward collected signal to another optical path toward a spectrometer (Andor Technology, Shamrock sr-303i).

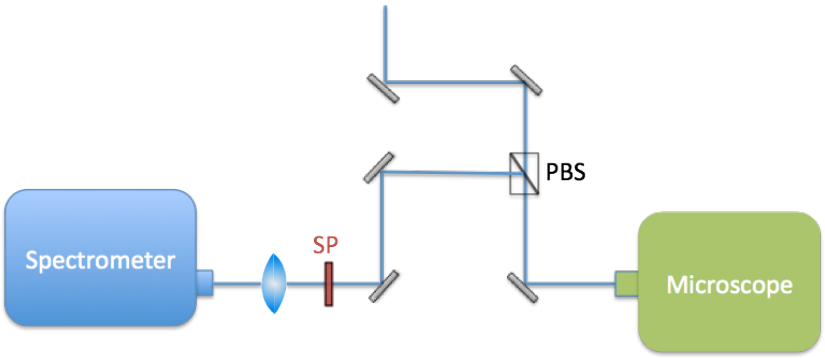

Figure 3.7: The additional setup required for UC spectroscopy and imaging of the doped gadolinium oxide particles

Before interesting the spectrometer the beam is filtered with a proper short-wavelength pass filter to suppress the excitation beams. Then a collimating lens is used to focus the light into the spectrometer aperture. The schematic of the optical setup is presented in Fig.3.7. The spectrometer is equipped with three gratings with different lines per mm providing three different resolutions and coverage ranges. Figure (3.8) shows the interior setup of the spectrometer.

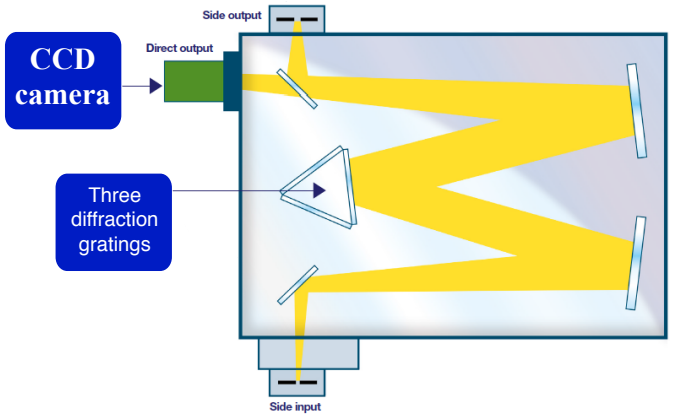

Figure 3.8: The interior setup of the Andor spectrometer.

3.4 Nanoparticles fabrication and Characterisation

3.4.1 Fabrication

Two main types of particles have been fabricated. A Precipitation method was used to synthesise gadolinium oxide doped nanoparticles, whereas iron oxide nanoparticles were fabricated by hydrothermal method. The detailed processes of both methods are explained in the two following sections.

Homogeneous precipitation method

Lanthanide doped gadolinium oxide nanoparticles were synthesised using the homogenous precipitation method. The raw material, Gadolinium(III) nitrate hexahydrate ($Gd_2(NO_3)_3{\cdot}6H_2O$, 99.9%), ytterbium(III) nitrate pentahydrate ($Yb_2(NO_3)_3{\cdot}\ 5H_2O$, 99.9%), Erbium(III) nitrate pentahydrate($Er_2(NO_3)_3{\cdot}5H_2O$, 99.9%) and Urea powder (BioReagent) were bought from Sigma-Aldrich (UK). An amount of 1.68 m mol(0.758 g) of gadolinium nitrate was added to 300 ml of distilled water in a beaker placed on a hot plate. Because erbium and ytterbium work as dopant ions, only minute quantities of their nitrate are added as molar percentages. For instance, when fabricating Gd_2O_3:1%Yb^{+3}, 1%Er^{+3}, about 0.0075g (0.0168 m mol) of the nitrate of each dopant is added. The solution is stirred vigorously at room temperature with a magnetic stirrer for 50 min to ensure a complete dissolving and homogeneous distribution of the different ions in the solution. Then, 9 g of urea is added while continuing the stirring for another 10 min at room temperature resulting in a transparent solution. The transparent solution is then heated with the hot plate at an average rate of 3 °C/min and then, maintained at 85 °c for 30 min. After reaching the nucleation temperature (85 °c), a lower transparency of the liquid is observed resulting in a milky colour, which suggests formation of nanoparticles. The nanoparticle powder is then isolated using centrefusion

with rotation speed of 600 r/m for 10 min. After centrefusion, the powder is left to dry overnight in an 80 °c oven. In order to enhance the crystalline structure of the nanoparticles, the powder was then annealed at 950° for 30 min.

The procedures mentioned above are similar to that reported by Hemmer et. al. [57]. However, here I have controlled the particle size by varying the nucleation time.

Hydrothermal method

In this method, 6.6 g of iron chloride (Sigma Aldrich, UK) was dissolved in 20 g of distilled water at room temperature resulting in 2.60 Molar yellowish iron chloride solution. This solution is kept in a tightly closed container to prevent altering the concentration via water evaporation and used later as starting solution for all the iron oxide synthesis experiments.

In order to achieve the high pressure and temperature required for the hydrothermal synthesis, Teflon-lined steel autoclaves were used Figure (3.9). The 2.6 Molar iron chloride was diluted to different lower concentrations in order to fabricate different size iron oxide nanoparticles. Then, 40 ml of the diluted solution was mechanically stirred inside the autoclave. Afterwards, the autoclave was sealed tightly and inserted into a furnace with a controlled temperature at 160° for 120 min. The autoclave was taken out of the furnace and left inside a fume hood to cool down naturally at room temperature. The nanoparticles were obtained from the resulting liquid by the centrefusion process mentioned in the previous section.

Figure 3.9: Teflonlined steel autoclaves used for hydrothermal synthesis method.

3.4.2 Characterisation

Scanning Electron Microscope (SEM)

In order to characterise the morphology and size of the nanoparticles a scanning electron microscope(Hitachi S-3200N SEM, Japan) was used. The instrument is capable of acquiring images with a resolution up to 3.5 nm in magnification range of 20-300,000 x. Because the nanoparticles used for this thesis are semiconductors, a carbon tape or conducting gold coating is applied.

The SEM is equipped with Energy Dispersive Spectroscopy (EDS). This was utilised to confirm the constituent material of the fabricated nanoparticles although, it only provides a semi-quantitative knowledge about the percentages of the dopant materials.

Transmission Electron Microscope (TEM)

For a higher resolution characterisation of the morphology and size of the nanoparticles a transmission electron microscope(JEM-2100 LaB6 200 kV TEM) was used. This was also used to confirm the crystallinity phase of the nanoparticle material.

X-ray Diffraction (XRD)

The X-ray diffraction was performed with a Bruker D8 Advance XRD (School of Engineering, University of Exeter). The measurements were taken of the particles in the powder form and the data was analysed with DiffracPlus EVA software combined with the PDF4+ database. This allowed the phase of the nanoparticles as well as the possible elements making up the crystal to be determined.

Chapter 4

Label-free Imaging of Tumours

4.1 Introduction

As stated in the introduction, one of the ultimate goals of this study is to suggest a practical method to investigate the distribution of anti-cancer nano-medicines in brain tumours. It is proposed to employ multi-contrast magnetic particles as tracking agents to understand the distribution of particles. This allows MRI to localise the particles distribution on the whole body scale and at the cellular level with nonlinear optical microscopy which could be used to provide new information on the bioavailability and accumulation of particles at multiple scales to aid the rational engineering of enhanced anti-cancer nano-medicines.

In this study, the role of the nanoparticles is not to enhance the contrast between healthy and diseased tissue, but to highlight the location of particles within tissue. Consequently, the contrast between the healthy and diseased tissue should be provided by the MRI and CARS in a label-free manner. Armed with this label-free contrast between the healthy and diseased tissue, the distribution of the nanoparticles can be assigned to the biological context, revealing valuable information. For instance, at the

MRI scale, one can tell if the nano-medicine is located in the targeted organ (the brain in this study) in appropriate concentrations, and whether or not the medicine has reached the tumour tissue. This can be achieved by imaging the animal before and after the administration of the nano-medicine. At the cellular level, CARS and other nonlinear optical microscopies can be used to determine whether particles crossed the blood-brain barrier and the cell type in which the particles reside.

The mouse is a common model animal in which to investigate tumour response to medicine [58]. One of the methods used to investigate the pharmacological effect in the literature is to assess tumour growth by measuring its volume. To be able to measure tumour volume accurately using MRI, it is necessary that tumour and healthy tissue can be clearly distinguished in the 3 D MR image, and that the edges of the tumour are sharp and well defined. To investigate this topic and contribute to the overall goals of the present study, a collaborative study with the London School of Pharmacy was undertaken, evaluating the effects of three different medicines on tumour growth.

This chapter explores the strengths and limitations of label-free imaging of mouse-brain tumours using MRI and CARS . The work includes optimisation of the imaging setup and parameters, to allow healthy and diseased brain tissue to be distinguished in both techniques. Also, a comparison of the high resolution MRI and conventional histology volume measurements is presented. Moreover, a novel method is proposed to correlate the images of the different-scale imaging modalities (MRI and CARS).

4.2 MRI of mouse brain tumour

4.2.1 Introduction

As discussed in Section (4.1), label-free imaging of the brain is required with contrast between healthy and diseased tissue. For this purpose, the MR imaging setup and parameters were optimised to enhance this contrast. Moreover, because tumours in mouse brain are relatively small in size, on the order of a few cubic millimetres, high-resolution imaging is required to achieve a reasonable error in volume measurements.

For MRI, there is a trade-off between image resolution and image noise, and it can be a major challenge to achieve both high-resolution images with high signal-to-noise ratio (SNR) [59]. In general, there are a number of parameters that affect the SNR. Firstly, SNR depends on the strength of the static magnetic field in the imaging hardware setup. As discussed in Section (2.2.4) in the background theory chapter, there is an advantage of having larger population inversion of the spin states, according to Equations (2.2 and 2.3). The relationship between the SNR and the static field is more than linear [60]. However, the disadvantages of utilising higher static field are the cost of magnets, the relatively high RF power required for imaging, the potential effects of the high RF power and strong field on biological subjects and the artefacts resulting from inhomogeneity [59]. As mentioned previously, a 1.5 T static field was available for the present study.

The second factor is the size of the receiver coil: SNR is inversely proportional to coil diameter [60]. Despite its small field of view and receptive volume, a smaller coil will be closer to the imaged voxel resulting in a stronger signal; the detected signal intensity is inversely proportional to the square of the distance from the voxel to the receiver [61]. The third factor affecting the SNR is the overall imaging time (signal averaging time), which affects SNR not only in MRI but also in other imaging techniques. In most in

vivo experiments, the overall time that an anaesthetised animal can be kept still inside the scanner is limited, but for ex-vivo studies longer acquisition time can be used.

Fourth, the imaging sequence and parameters, such as TE and TR, play an important role in the SNR. Finally, the fifth factor is the abundance of the targeted nucleus in voxels of interest and its T_1 and T_2 values. As a consequence of proton abundance, the voxel geometrical volume (i.e. the 3D resolution) affects the SNR in a linear proportionality. For instance, if the voxel dimensions in a 3D MRI image are reduced from $2 \times 2 \times 2mm^3$ to $1 \times 1 \times 1mm^3$ the signal intensity is reduced by a factor of 8 [61]. If a short-T_1 tissue is imaged with a T_1-weighted sequence the SNR is expected to be higher than for long-T_1 tissues. Similarly, if a short-T_2 tissue is imaged with a T_2-weighted sequence the SNR is expected to be lower than for long-T_2 tissues.

It can be seen that the parameters mentioned above can be classified into two categories. 1) Extrinsic parameters: hardware setup factors and imaging parameters. 2) Intrinsic parameters: properties of the sample that appear to be difficult to manipulate. However, by administration of contrast agents T_1 and T_2, (2) can be changed allowing more optimisation of SNR.

There are numerous studies in the literature which involve assessment of the tumour volume in response to different therapeutic remedies. One of the methods used is histology volume measurement: the tumorous brain is sliced and stained, then the largest tumour diameter is measured. Assuming that the tumour has a spherical shape, the volume is then calculated. For example, in 2009 Schauff et. al. [62] implemented this method to study the impact of gamma radiation and furegrelate on U78 tumour growth in mice. They claimed that a significant decrease in tumour volume was detectable for treated mice against those from a control group. However, the accuracy of this method is questionable since the tumour does not necessarily form a spherical shape (or even an ellipsoid), as illustrated later in this chapter.

In order to achieve the highest possible resolution with reasonable acquisition time for in vivo experiments, a range of different imaging setups have been investigated. In several of these studies, small-bore systems with high static magnetic fields (>3T) have been used to obtain high SNR. In 2012, Kerl et. al. [63] used a 9.4 T MRI scanner with a bore diameter of 20 cm to optimise a fast imaging sequence to measure a type of skin tumour. Without administration of contrast agent they could achieve edge detection for subcutaneous tumours in a 30 min scan with a spatial resolution of 120 × 100 × 375 μm^3. However, it is less challenging to determine the extent of an under-skin tumour than a brain tumour in its inhomogeneous context. In another study, McDaniel et.al. investigated the effect of ischaemia (shortages in blood supply to tissue) on the volume of different types of brain tissue using a 7 T scanner with a 15 cm bore [64]. Using diffusion contrast they could determine the interface surfaces between different brain parts and hence were able to measure volumes with a resolution of 58 × 58 × 469 μm^3. Sun et. al. [65] injected a mouse with contrast agent (Gado- pentetate dimeglumine (Gd-DTPA)). This was followed by T_1-weighted imaging of the brain with a 8.5 T scanner, 9 cm bore, combined with a 3 cm RF receiver coil. They could detect the U87 tumour boundaries with a resolution of 200 × 200 × 750 μm^3. Nelson and coworkers [66] used a gadolinium-based contrast agent to enhance tumour contrast in the mouse brain, imaged with a 8.45 T scanner and a 25.6 mm RF coil. Processing post-contrast T_1-weighted images, they measured tumour volume with a resolution of 200 × 200 × 750 μm^3. Similarly, using a 7 T scanner and custom-built solenoid coil, Holmes et al. [67] imaged contrast-enhanced flank tumour with high spatial resolution (60 × 60 × 60 μm^3)
.

Despite the advantages of small-bore high-field scanners for mouse brain imaging, whole-body clinical systems (commonly 1.5 or 3 T) are more available to researchers. Consequently, a number of researchers have reported the applicability and efficacy of

clinical scanners in small-rodent brain imaging. In 2011, Pillai and coworkers [68] developed a volume RF coil to image small-animal brains with a 3 T clinical scanner. They measured mouse tumour volume with a resolution of 200 × 200 × 1000 μm^3 from T_2-weighted images. In a similar study, a 3T clinical system was used with a 4 cm diameter RF coil to image rat brains after injecting the rat with contrast agents [69]. The tumour volume was calculated with in-plane resolution of 78 × 78 μm^2 and slice thickness of 1 mm.

In 2010, Matoba et. al. [70] monitored the effects of radiotherapy on tumour growth in rabbits using a 1.5 T clinical scanner and a 4.5 cm surface coil. Without contrast agent administration they acquired T_1- and T_2-weighted images of brains with a spin-echo sequence (with TE/TR=500/20 ms and TE/TR=2000/70 ms, respectively) with spatial resolution of (200 × 200 × 3000 μm^3). The tumour growth was analysed by measuring the diameter of the largest tumour slice from the T_2 weighted images (similar to the histology method described above). Although this resolution might be sufficient to detect the volume variations in the relatively larger rabbit tumours, it is not appropriate for mouse tumours where smaller volume errors are required. Moreover, the capability of MRI to reconstruct the full 3D shape of the tumour was not utilised.

In order to demonstrate the applicability of high resolution MRI to small animal studies, Brockmann et. al. utilised a 1.5 T clinical system with a small loop coil to measure mouse tumour volume after administration of contrast agent [71]. The tumour volume was measured by summing the areas of all tumour slices from the contrast enhanced MR images (the in-plane resolution was 160 × 160 μm^2 and the slice thickness was 1 mm). In a further study in 2011, Brockmann [72] analysed the influence of platelet count on U87 tumour growth with the same imaging method.

Linn et. al. [61] utilised a 1.5 T clinical scanner with a small loop coil and double array coil to optimise 3D imaging of tumour volume in rat brains. They used a 3D-

contrast interference steady-state (3D-CISS) sequence and a 3D magnetisation-prepared rapid gradient-echo (3D-MP-RAGE) sequence with resolutions of $600 \times 300 \times 500$ μm^3 and $800 \times 800 \times 800$ μm^3 respectively. The image processing was carried out manually and in a semi-automated segmentation to determine tumour boundaries. In another study, a simple solenoidal RF coil was developed in order to achieve multiple-mouse imaging using 1.5 T clinical system [73]. The largest tumour diameter was estimated from post-contrast 3D T_1-weighted spin-echo images with a resolution of $313 \times 417 \times 1500$ μm^3 and compared with histology. Similarly, Raila et. al. [74] employed a wrist coil and contrast media to study rat brain tumours in a 1.5 T clinical scanner. The tumour volume was measured from post-contrast T_1-weighted images by threshold segmentation.

A number of studies from those mentioned above have examined the reliability of MRI in measuring tumour volume by comparing the volumetry result with histology [66, 68, 70, 73]. In all cases, good statistical agreements between the two methods were reported. However, from a theoretical perspective, MRI data should provide more accurate volume measurements if the image sequence is optimised to allow accurate visualisation of tumour boundaries. This is a result of the approximation introduced in the histology measurement by assuming ellipsoidal or spherical shape for the tumour, whereas in MRI the actual tumour shape is obtained in 3D.

Cornelissen et. al. [75] investigated the reliability of MRI tumour volumetry by comparing it with a water-displacement measurement as a gold standard. The results confirmed the accuracy and reliability of MRI volumetry.

Most of the MRI studies mentioned above were carried out in vivo. The fact that MRI measurements of tumour volume can be made in vivo brings a number of advantages when studying animal tumours: In vivo experiments are conducted on the tissue while its biological function is ongoing, so fewer animals are required compared to end-

point histology or other ex-vivo volume measurements. That is because the same animal can be used at different time points in in-vivo MRI whereas only one time point can be investigated in methods where the animal is sacrificed. However, in-vivo MRI is limited by anaesthetisation time. According to Benveniste et. al. [59] the anaesthetisation time for in-vivo MRI of small animals is normally restricted to 4 hours (whereas in-vitro measurements can be much longer). Also, in-vivo experiments are challenging due to animal movements as a result of normal breathing and cardiac activity [59].

In order to achieve high accuracy MRI volumetry of rodent brain tumours, high resolution 3D imaging is required. As the voxel volume decreases, the error in measuring the volume of irregular tumours decreases. In most of the studies mentioned above, although a high in-plane resolution was utilised, the slice thickness was larger than 0.5 mm [61, 65, 66, 68, 70, 71, 74]. This level of resolution might be sufficient for the goals of previous studies where a large variation in volume was expected or a relatively large rodent was under investigation. In some studies [63, 64], the researchers achieved better 3D resolution by using slice thicknesses of 375 μm and 469 μm respectively. The best resolution ($60 \times 60 \times 60$ μm^3) was achieved by Holmes et. al. [67] utilising a small-bore system (30 cm) with a high static field (7T) and a custom-built coil.

In Section (4.2.4), a method for label-free imaging of mouse brain tumours with high spatial resolution($125 \times 125 \times 150$ μm^3)is demonstrated a using a 1.5 T whole-body MRI scanner and a commercially available surface coil. To the best of the author's knowledge, this is the best resolution that has been achieved to measure mouse brain tumour volume in a 1.5 T clinical scanner without the use of contrast agents. This will, first, meet the requirement of the present study for high MRI resolution in order to facilitate a qualitative comparison with the (far higher resolution) nonlinear optical microscopy. Second, the image MRI method allowed imaging of 83 mouse brains as part of a collaborative study with the London School of Pharmacy: tumour volume data was

compared to maximum diameter estimates, intended to replicate the results of histology measurements.

High resolution MRI was achieved by utilising a microscopy surface coil (23 mm diameter, Philips Healthcare) and long imaging times (i.e., averaging over multiple image acquisitions). The main limitation of time averaging in high resolution imaging is from movement artefacts. Despite some remarkable work towards minimising movement artefacts(i.e. [76]) by matching images within a sequence to each other, artefacts can still be a major obstacle specially when a spatial resolution on the order of 100 μm is required. Fortunately, movement artefacts were not a problem in the present study because the mouse-brain samples were fixed in an agarose-gel-formalin mixture which prevented movement over the imaging period. These measurements, described in Section (4.2.4), are preceded by some preliminary investigations (Sections (4.2.2) and (4.2.3)).

4.2.2 Whole animal MRI

This section demonstrates MR imaging of a whole animal at sufficient resolution to allow organ identification. (As mentioned in the introduction, identification of organs within the animal is required to facilitate drug localisation. If the animal is imaged before and after nano-medicine administration, enhanced signal will be detected in the organs where the drug is located.) In this case a euthanised rat was positioned securely inside an 8-channel RF coil designed for the human head (Philips Healthcare) so as to prevent movements during the scan. A T_1-weighted fast field echo (FFE) sequence with TR/TE = 50/6.87 ms and spatial resolution of 0.5 $\times$ 0.5 $\times$ 0.5 mm^3 was employed. The total scan time was 90 min for a 3D field of view of 60 $\times$ 180 $\times$ 180 mm^3. The two images below (Figure (4.1) and Figure (4.2)) show different coronal slices of the whole rat. In Figure (4.1) it can be seen that essential organs such as the heart (green arrow)

can be identified. Similarly, in Figure (4.2) the arrows indicate brain and liver.

For this preparatory study for the mouse imaging, the rat was chosen to be imaged because of its availability and low cost. The organs of the rat are relatively larger and and so do not require imaging at such a high resolution. However, the rat was imaged with a large field of view (FOV) for whole-mouse imaging a smaller FOV can be imaged at higher resolution within the same total scan time.

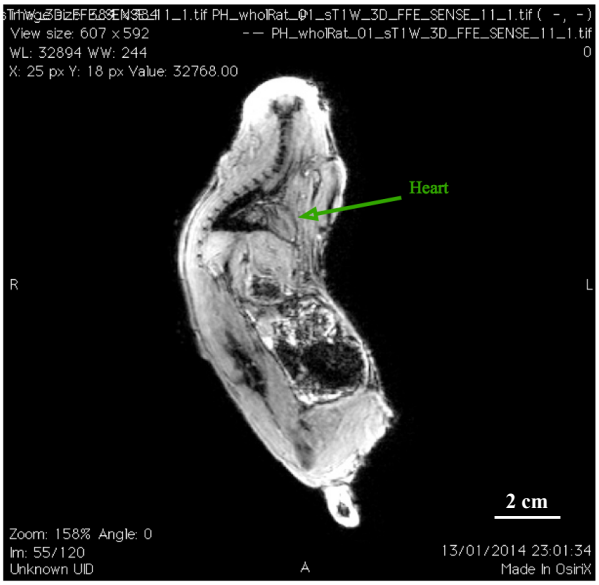

Figure 4.1: A slice of a 3D MRI image of a whole rat body showing anatomical details.The arrow indicates the heart.

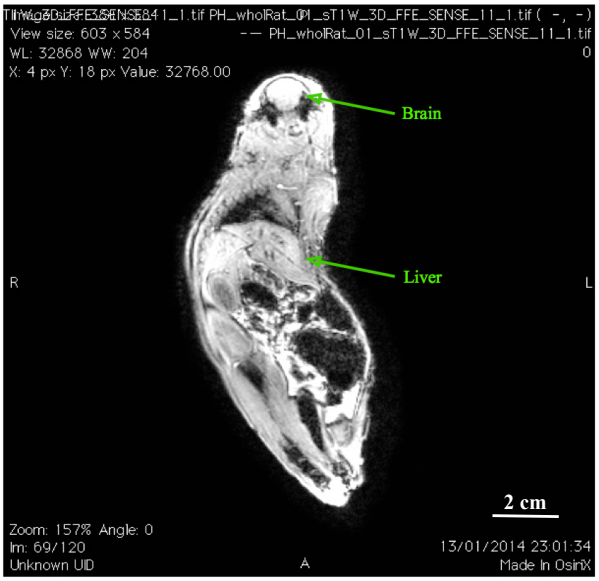

Figure 4.2: A slice of a 3D MRI image of a whole rat body showing anatomical details. The arrows indicate brain and liver.

4.2.3 T_1 and T_2 measurements of mouse brain

It is well established in the literature that T_2-weighted imaging sequences provide better contrast between tumour and normal brain tissue than T_1-weighted sequences (e.g. [77]). In order to achieve high SNR and good image contrast in MRI, the optimum imaging parameters (TR and TE) should be employed. This optimisation, however, requires previous knowledge of the intrinsic properties of the tissue of interest such as T_1 and T_2 values. Although T_1 and T_2 values for rodent tissues have been published in the MRI literature, there are a number of practical details that might affect their values in the present context, such as the formalin fixation protocol, time from animal sacrifice and tissue handling. In this section T_1 and T_2 measurements of normal and diseased tissue will be described.

A formalin-fixed mouse brain was mechanically fixed in 0.5% w/w agarose gel within a glass container and prepared for MRI scanning. The brain was close to the container

base inside the gel and, hence close to the surface coil which was positioned under the container, to ensure the highest possible SNR. The position of the brain was determined using survey sequences (a fast T_1-weighted spin-echo sequence followed by a low-resolution T_2-weighted spin-echo sequence) in order to locate the largest tumour slice. At this stage there was no interest in high-resolution detection of tumour edges, the surveys were intended to find a suitable slice for T_1 and T_2 measurements containing both normal and diseased tissues.

In order to map T_1 values an inversion recovery sequence was applied with inversion times of 50, 100, 200, 500, 1000, 1500 and 2000 ms. For accurate T_1 measurements, the repetition time was chosen (10^4 ms) to be much larger than the expected T_1 values of brain tissue (known to be not more than 10^3 ms). This is important to allow full recovery of the net magnetisation vector (NMV) between successive RF excitations [10]. The inversion recovery is described by Equation (2.20).

The outcome of the scanning process is seven images of the brain slice with the different inversion times mentioned above. The signal intensity of the tumour area was measure by selecting a region of interest inside the tumour and measuring the average grey scale value using ImageJ software. Also, in the same manner the signal intensity was measured for the normal brain tissue around the tumour. Figure 4.3 shows two plots of the inversion recovery data of normal brain tissue and tumour. The x-axes represents the inversion time (in ms) and the y-axes represents the signal intensity (in arbitrary units). The markers represent the experimental data and the lines represents the curve-fit generated by Easyplot software. It is important to mention that the standard deviations of grey scale values are ignorable when compared to the difference in signal intensity between the two different types of tissues. The curve-fits from both plots reveal the constants in Equation (2.20), namely, M_0 and T_1. However, we are interested only in T_1 values. The measured T_1 values of normal tissue and

tumour were 643 ms and 748 ms, respectively.

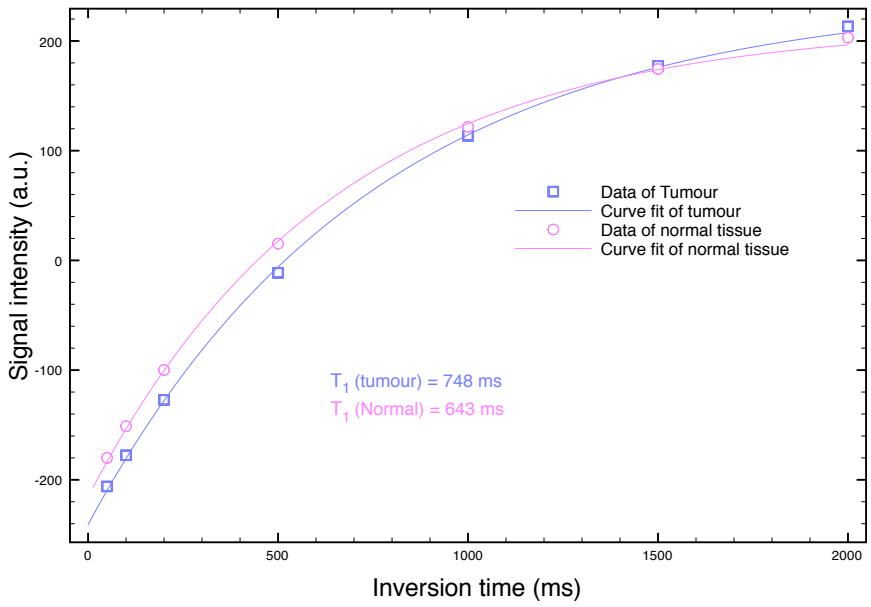

Figure 4.3: T_1 values for tumour and normal brain tissue measured with the inversion recovery method. Signal intensity is in arbitrary units.

Similarly, to measure T_2 values a spin-echo sequence was applied to the same slice with repetition time 3000 ms and echo times 16, 32, 48, .. 112 and 128 ms. The measured T_2 values of normal tissue and tumour (Figure 4.4) were 99.5 ms and 122 ms respectively.

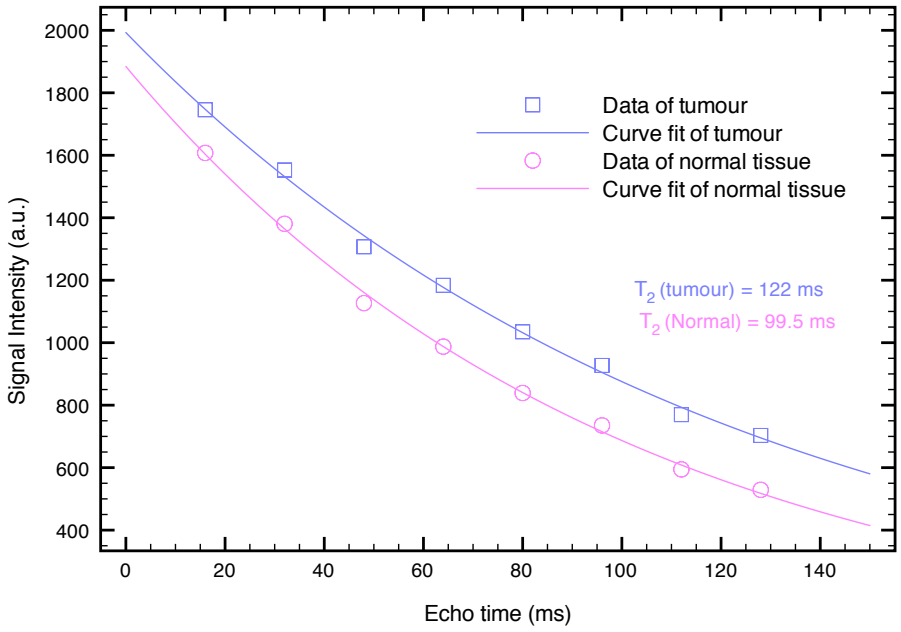

Figure 4.4: T_2 values for tumour and normal brain tissue measured by varying the echo time. Signal intensity is in arbitrary units.

Having the T_1 and T_2 values of both types of tissue we can theoretically study the contrast between them if a T_2-weighted sequence is used. The optimum contrast means mathematically that the difference between the signal intensity in the tumour and normal tissue is maximum. The signal intensity of each tissue can be calculated using Equation (2.5) substituting the T_1 and T_2 values measured above and choosing large TR (3000 ms). The difference between signal intensities in the two tissues is given by

$$\Delta I(TE) = I_{Tumour} - I_{Normal} \tag{4.1}$$

The plot of Equation(4.1) as a function of TE is shown in Figure 4.5. From the figure it can be seen that the optimum contrast between normal brain tissue and tumour can be achieved by setting TE to 110 ms. This optimised value for TE is used in the

high-resolution MR imaging described in the next section.

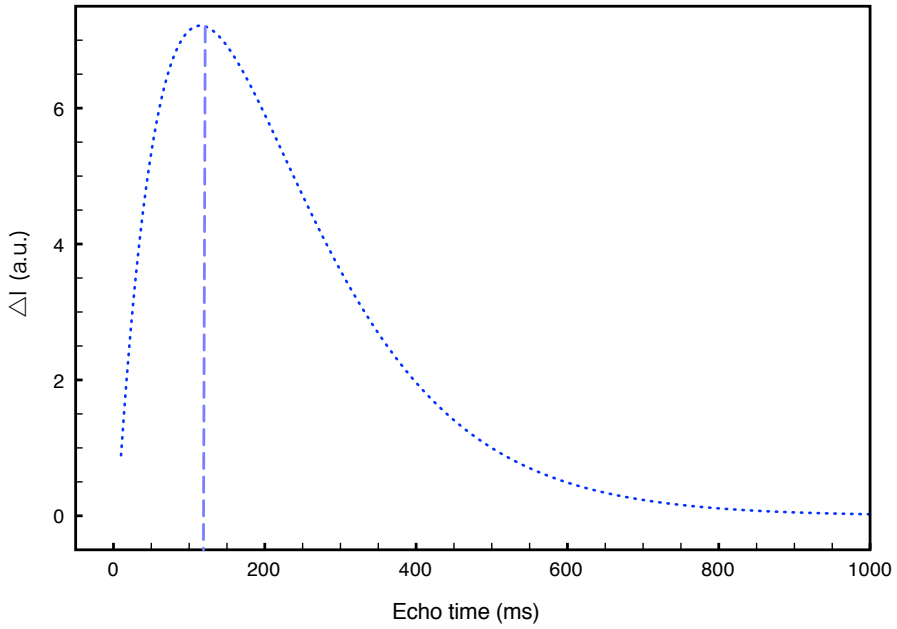

Figure 4.5: The curve shows the theoretical estimation of the contrast (difference in intensity, in arbitrary units) between normal brain tissue and tumour as a function of TE. The optimum contrast is achieved when TE = 110 ms.

4.2.4 High resolution MRI of tumour

The main aim of this chapter is to demonstrate the possibility of tumour detection with label free MRI and CARS. For MRI, as discussed above, the main obstacle for this is the limitation of SNR. However, utilising a commercially available surface coil, optimising imaging parameters (as shown in the previous section) and giving the scan time less priority, this obstacle can be overcome.

As mentioned above, movements of the sample during scanning result in motion artefacts. If the magnitude of movement during the scan time of an individual slice is much smaller than the voxel size, less movement artefacts are detected. However, in the high resolution MRI scheme adapted in this study, the imaging time has not

been restricted and the voxel size is relatively very small($125 \times 125 \times 150\ \mu m^3$). This implies that even very minor movements can significantly affect the image quality. For this reason, all the brain samples were embedded in 0.5% w/w agarose gel as preparation for MRI. Another advantage of using agarose gel when using it to mechanically fix the brain is that it facilitates image segmentation to determine the brain edges.

As mentioned in the previous section the parameters for imaging should be optimised, and using a T_2-weighted spin-echo sequence with TR = 3000 ms and TE = 110 ms provides the highest image contrast between normal brain tissue and tumour. Although the optimisation was based on T_1 and T_2 measurements of only one brain sample, it was found that these imaging parameters allowed identification of tumour edges for all the brains investigated. All brains were subject to similar animal and sample handling procedures and, most importantly, similar formalin fixation protocols and times between animal sacrifice and MR imaging.

A particular advantage of conducting MRI experiments ex-vivo is the possibility of using long imaging times. However, with the large number of brains involved a number of steps were carried out to maintain the imaging costs of the study within a reasonable limit. Unlike in-vivo scanning, where the researcher should monitor the experiment as part of the animal handling procedures, ex-vivo imaging can be carried out overnight without continuous monitoring. To be efficient in using out-of-hours scanner time, two brains were imaged simultaneously in each overnight scan. In order to ensure the images were assigned to the correct brains, the two brains were embedded in the gel in different orientations close to the container base. Moreover, the FOV of the high resolution MR image was kept as small as possible. This was achieved by utilising a fast 3D survey image to determine roughly the location of the tumour (fast field echo (FFE) T1-weighted sequence, TR/TE = 57/21 ms, typical matrix dimensions 148×97, slice thickness 0.6 mm, interslice gap -0.3 mm). Using this fast survey sequence, a 3D FOV

that includes the two brains ($9 \times 30 \times 30$ mm^3) could be imaged in 76.3 s. Figure (4.6, a) shows a slice of a typical 3DFFE survey where the two arrows indicate the tumours.

After locating the tumour with the survey, a high-resolution T_2-weighted sequence with the optimised parameters was applied (in-plane resolution 125×150 μm^2 and slice thickness 150 μm). Figure 4.6(b) shows the high-resolution image of the tumours in the two brains shown in Figure 4.6(a). In the high-resolution image the FOV is minimised as much as possible, to include the two tumours. This is done by reference to the survey image, as shown in Figure 4.6(a), where the new FOV is determined by the yellow rectangle. In this case the new FOV of the high resolution T_2-weighted image is $10.05 \times 18 \times 5.8$ mm^3. Using 10 signal averages, the total scan time is 4.28 hours, i.e., around two hours per brain.

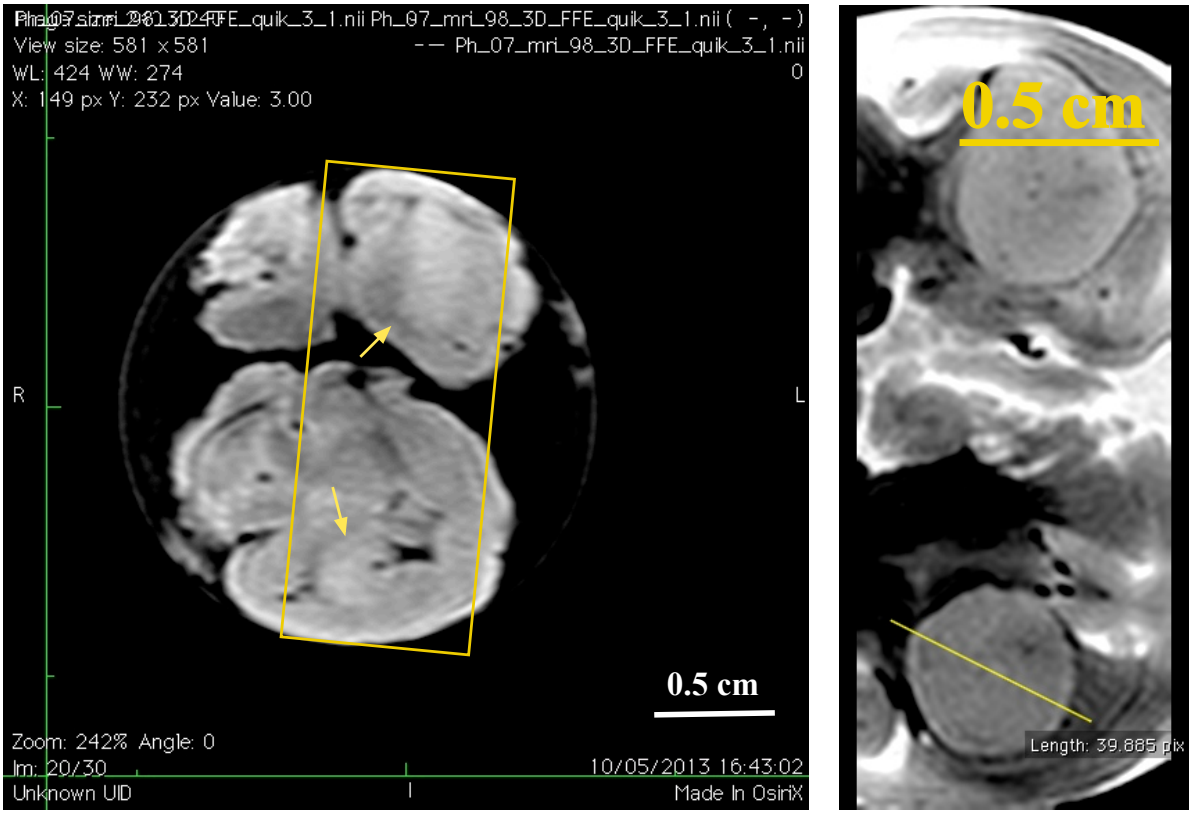

Figure 4.6: (a) T_1 weighted Low-resolution survey image of two typical brains embedded in agarose gel. The arrows show the tumour locations. The yellow rectangle shows the selected new FOV, as in (b).
(b) High-resolution T2-weighted image of two brains with FOV positioned around the tumours. The grey scale profile of the yellow line drawn across the lower tumour is plotted in Fig.4.7.

It can be seen that the tumour edges are much clearer in the optimised image in Figure 4.6(b) than in the survey image in Figure4.6(a). Figure4.7 shows a signal intensity profile for a line drawn across one of the tumours in the high-resolution image (the yellow line in Figure4.6(b)). The sudden change of grey scale value at the edges of the tumour is easily seen. Although there are other areas in the overall image that have a similar signal intensity to the tumorous tissue, with some knowledge of normal brain anatomy the tumours can be easily identified.

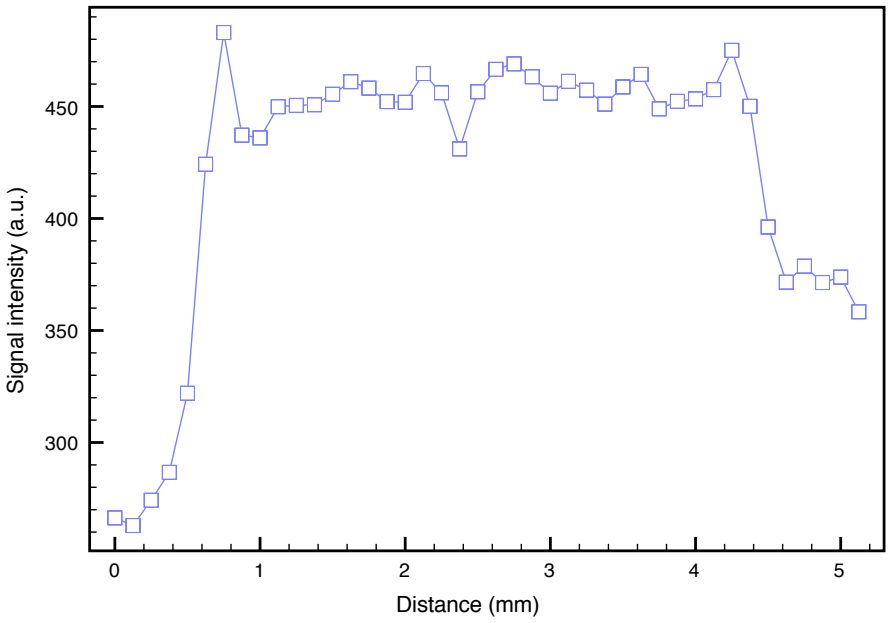

Figure 4.7: A plot of grey scale line profile across the tumour. The profile is for the yellow line in Fig 4.6(b). Signal intensity is in arbitrary units.

4.2.5 MR image processing

Having acquired a 3D stack of high-resolution images the tumour volume can be calculated with image processing. Previous studies have worked towards automated segmentation of brain tumours, but this is still challenging due to the brain's complicated anatomy. Even for the human brain, which is obviously much larger than a mouse brain, a recent article suggests semi-automatic rather than automated segmentation [78]. For mouse brains, a number of studies have adopted full manual processing by determination of the tumour area in each slice [63, 64, 71, 74]. The methods used in the present study for tumour boundary detection, tumour volume measurements and 3D tumour shape visualisation are described below.

MR Image normalisation

In typical MRI scanning the grey scale values of different slices are automatically normalised against the unavoidable signal intensity variation caused by the receiver coil geometry. For example, the signal detected by a surface coil varies as a function of the distance between the voxel source and the centre of the coil. For similar tissues, grey scale values from unnormalised slices close to the coil are higher than those at larger distance.

For the high-resolution sequence used for this study the automatic normalisation function ('Clear') provided by the Philips scanner did not work due to unknown technical problem. Both manual and automated segmentation are easier to carry out on normalised images, where equivalent slices have similar ranges of grey scale. For this reason, individual (slice) images were normalised against the distance from the surface coil by dividing each image by its mean grey scale value using an ImageJ macro that was developed for this purpose (Appendix.1). Fig.4.8 shows an example of two tumour slices at different distances from the coil, before and after normalisation (sample reference MRI3-83). The left-hand images are normalised and the right-hand images are unnormalised; images (a) are closer to the coil than images (b). It can be seen that, in the two normalised images, the brain anatomy details are observable (with clear tumour boundaries) without changing the image brightness or contrast. Whereas in the unnormalised images, if the brightness and contrast are left unchanged, only image (a) has clear details. This suggests that the normalised data set is appropriate for further image segmentation and processing, but the unnormalised data set is not.

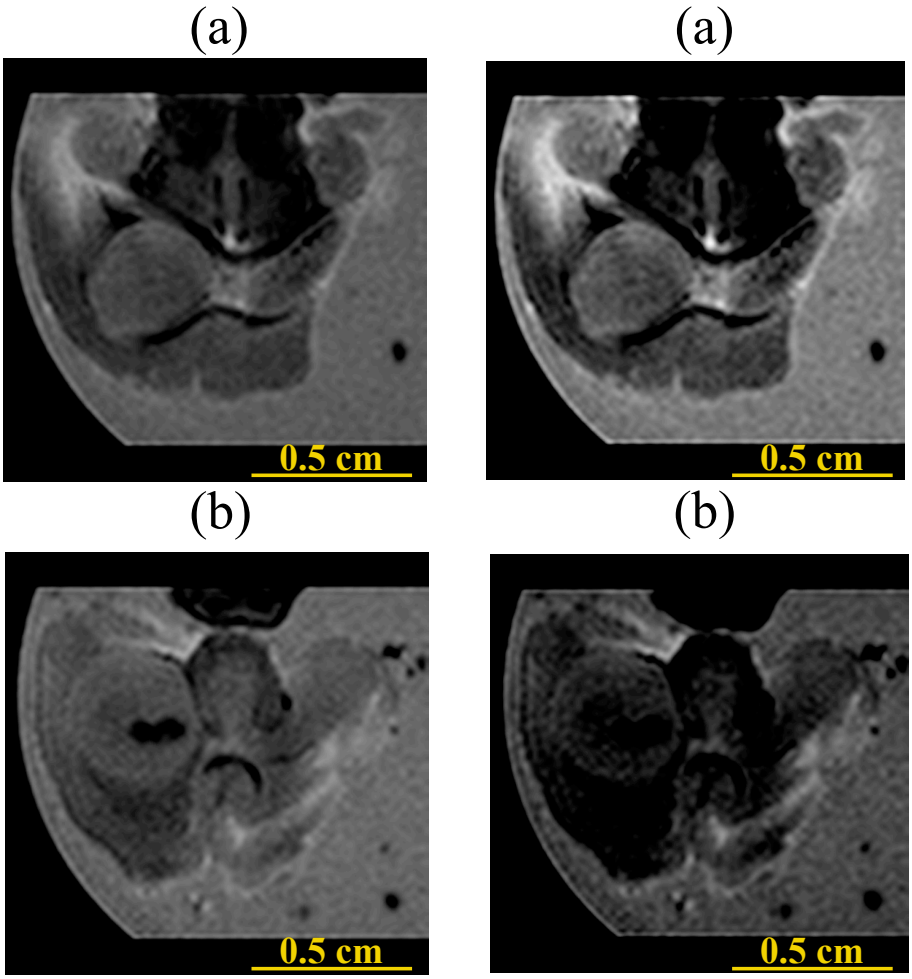

Figure 4.8: Images of two slices at different distance from the surface coil. The lefthand images are normalised and the right-hand images are unnormalised. The (a) images are closer to the coil than the (b) images.

Tumour volume measurements

All the images were obtained from the scanner and normalised against distance from coil with ImageJ as described in the previous section. To measure tumour volume, manual image processing was carried out using Osirix software installed on a MacBook Pro computer with OS X Lion (10.7) operating system. When opening the image in Osirix the 3D resolution of the image is checked to correspond to the known image

details. Then, using the available region of interest (ROI) tools, the tumour is manually determined as a region of interest in the image slice. Fig.4.9 illustrates three typical images of slices from different brains (sample references MRI3- 66, 70, 72) showing the slices before and after selecting the ROI. The images show clear tumour edges even when the signal intensity from tumour is similar to some areas in normal tissue.

After having selected the ROI slice by slice for the whole tumour, all the ROIs in the 3D data set are merged to a single ROI, whose volume is computed using the ROI volume command. The Osirix software computes the volume from the total number of voxels and the known resolution of the image.

The volumes of 83 mouse brain tumours were calculated using the MRI based methods explained above. Results are detailed in Appendix..2. The brains in the tables had been subjected to three different types of anti-cancer medications by our collaborators from the London School of Pharmacy.

One of the clear properties of brain tumours is that they do not form a spherical shape. Fig.4.10 shows a 3D model, generated by using Simpleware software with threshold segmentation and manual finishing, of an example tumour illustrating its irregular shape. An analysis of the effect of this irregularity in the tumour shape on conventional histology volumetry will be presented in the next section.

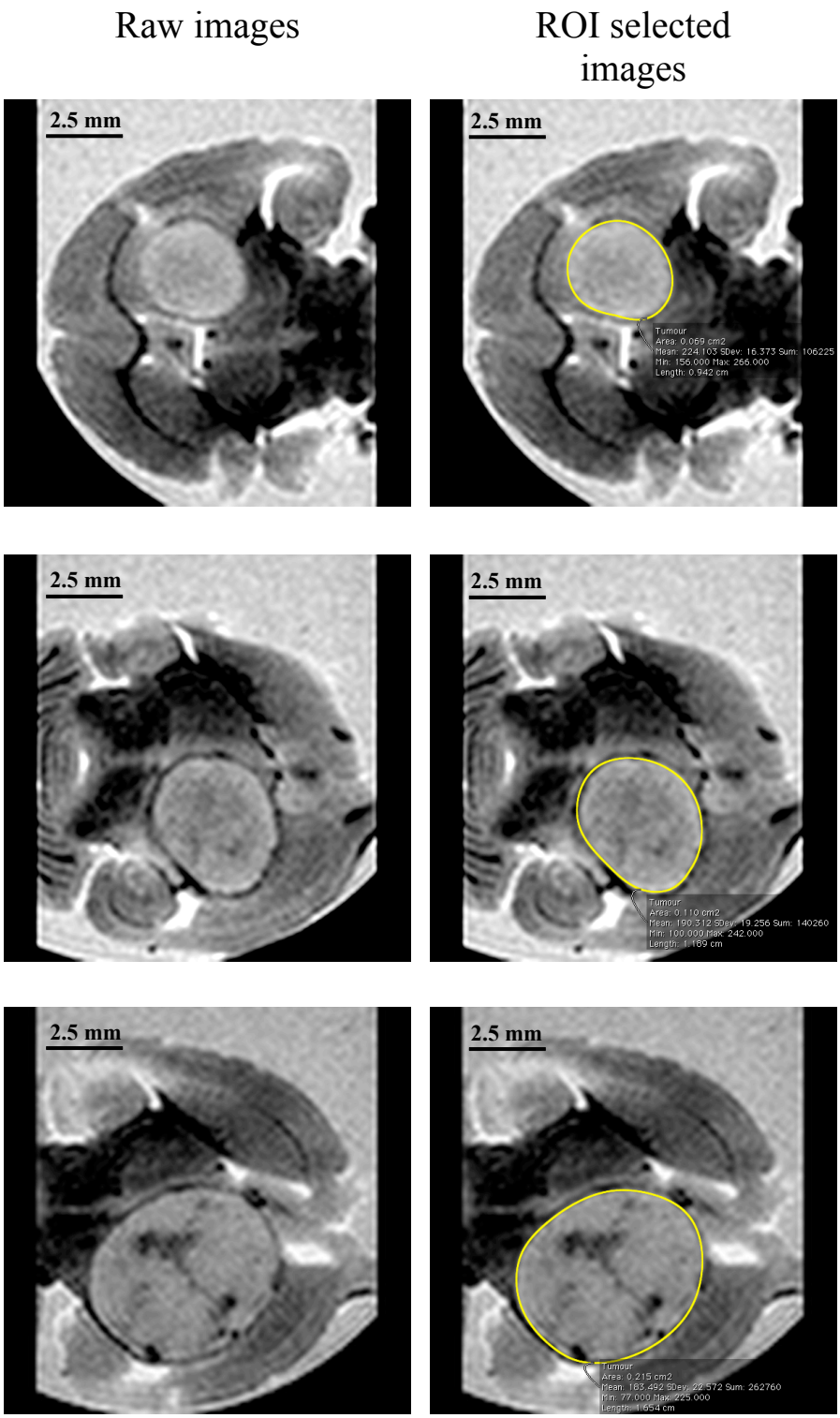

Figure 4.9: Three example images from different brains before and after ROI selection. Raw images are on the left and images with ROI selected are on the right.

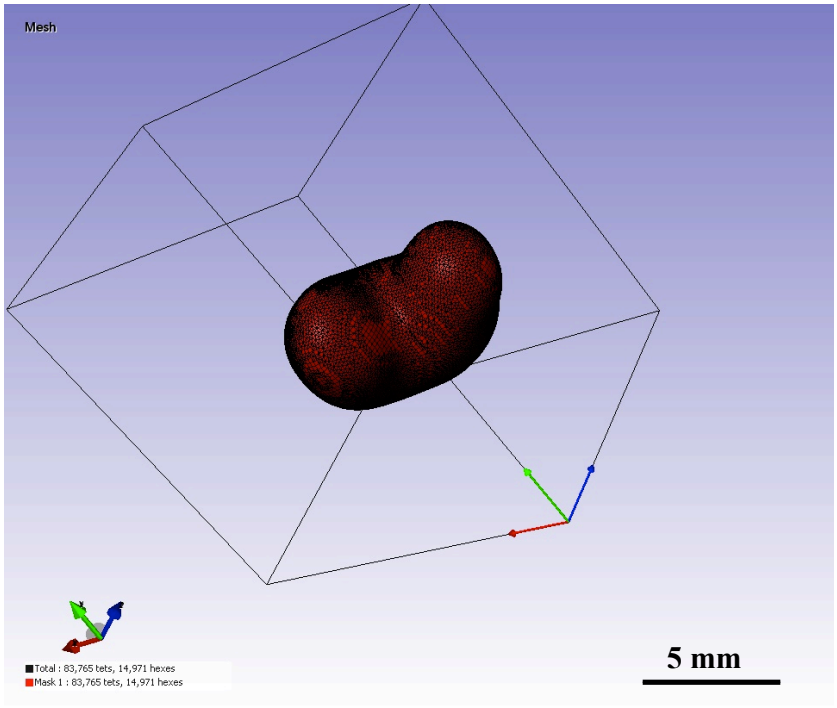

Figure 4.10: 3D model of a tumour showing its irregular shape. The model was generated with Simpleware software using semi-automated segmentation.

MRI vs semi-histology volumetry

The high-resolution label-free MRI of tumours presented in this chapter has allowed detection of well defined tumour edges and determination of tumour volumes. From a theoretical perspective, as explained in section(4.2.1), the high-resolution images should provide volume measurements with high accuracy. A number of studies have compared MRI volumetry to histology, assuming histology as the gold standard [66, 68, 70, 73]. However, in this section, MRI (3D ROI) is chosen to be the gold standard to which volume histology is compared. In fact, MRI volumetry is not here compared to true histology volumetry, but instead compared to simulated histology, using measurements from MRI image slices (see below) to mimic measurements from histology. The study is intended to provide some evidence of the effect of tumour shape on volume measurement.

As discussed in Section(4.2.1), histology is regularly used to measure tumour volume in mouse brains. The process is done by slicing the mouse brain in a coronal orientation, followed by choosing the largest tumour slice. The largest and smallest tumour diameters within this slice are determined, and an average diameter d is calculated, from which the tumour volume V is calculate using the formula $V = \pi\ d^3/6$ (i.e., as for a sphere of diameter d). In the present study this histology volumetry is simulated by making equivalent measurements on coronal slices from the 3D MRI data set. Two diameters (major and minor) are measured using Osirix as illustrated in Fig.4.11.

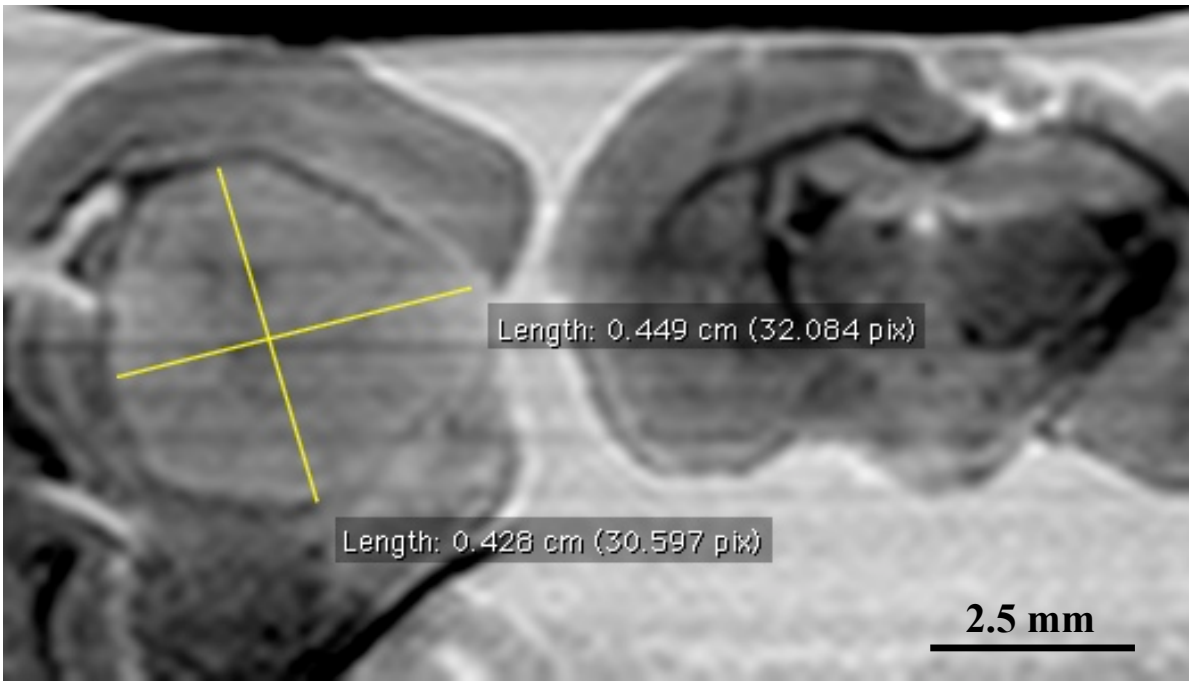

Figure 4.11: Tumour diameter measurements from a coronal cross- section of mouse brain, simulating histology measurements.

The volumes of all the tumours were measured with this simulated histology method (Appendix .2). In order to compare the outcome of both methods, MRI (3D ROI) and simulated histology, the two data sets have been used to generate the scatter plot in Fig.4.12. The horizontal axis is the tumour volume measured with MRI (3D ROI) and

the vertical axis is the tumour volume measured by simulated histology. If the two methods had perfect agreement, the data should fit exactly on a straight line through the origin, with unity gradient. However, it can be seen that in practice the data points are scattered around this line. Although the agreement looks satisfying, there are some significant discrepancies when considering individual differences. The differences as a percentage can be calculated using Equation ((4.2))

$$\Delta V\% = \frac{V_{MRI} - V_{sim-Histology}}{V_{MRI}} \times 100 \tag{4.2}$$

The percentage differences calculated from Equation(4.2) are plotted in Fig.4.13, with the sample number on the horizontal axis. Perfect agreement would give 0% differences. However, it is obvious that the data points are scattered with percentage differences up to 60%. The average percentage difference (magnitude) is found to be 20%, which is considerable. This discrepancy, as discussed before, derives from the spherical shape assumption used in histology volumetry.

It is suggested that MRI can be considered as a potentially more accurate alternative to histology when measuring the volume of mouse brain tumour for longitudinal pharmacological studies. Because of the suggested unreliability of the histology method, it may well be that using this method requires more animals to be sacrificed in order to obtain statistically significant results, so the MRI method may be preferable from an ethical perspective.

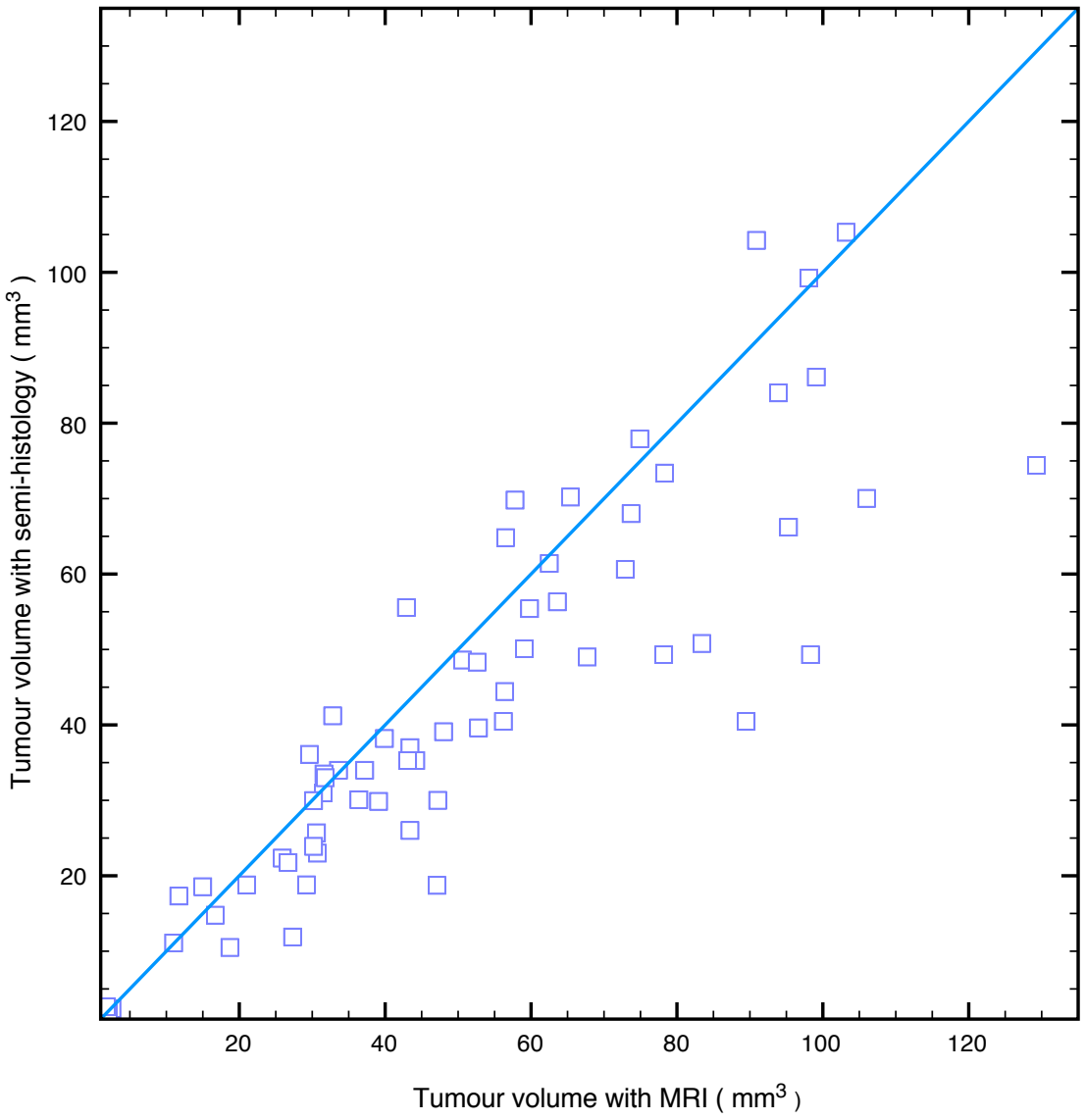

Figure 4.12: A plot of MRI (3D ROI) volume measurements vs simulated-histology measurements for 64 mouse brain tumours. The straight line indicates perfect agreement.

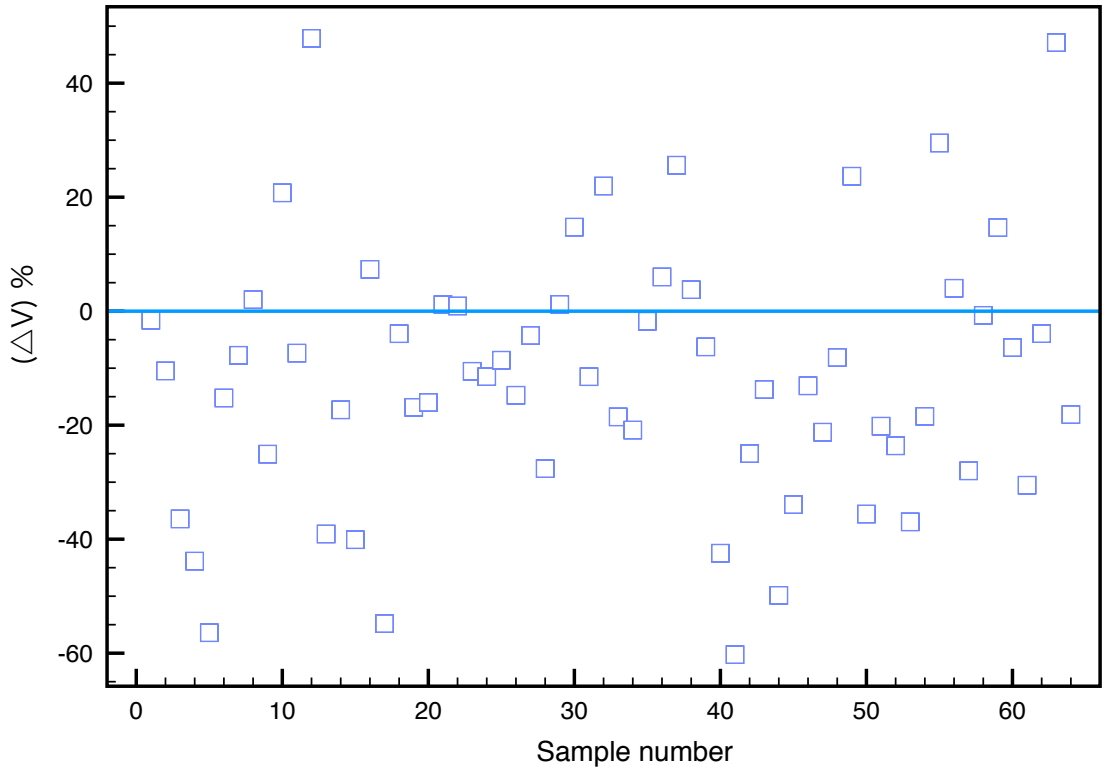

Figure 4.13: Percentage difference between MRI (3D ROI) volume measurements and simulated-histology measurements for 64 mouse brain tumours, plotted against sample number. The horizontal line represents perfect agreement ($\Delta V\% = 0$).

4.3 Nonlinear optical microscopy of mouse brain tumour

4.3.1 Introduction

As mention in Chapter.1, for this study, Coherent Raman Scattering CRS is more attractive as a microscopy modality than the conventional fluorescence confocal microscopy due its label free nature. In CRS the unlabelled tissue is imaged via the abundance of CH bonds in its biological membranes. For pharmacological studies, when using

nanoparticles as carriers and/or tracking markers for anti-cancer drugs, it is desirable to keep the biological system as normal as possible. CRS is able to show 3D images with sub micron resolution showing cells and their nuclei, blood vessels and red blood cells. Moreover, another particular advantage of using CRS against confocal fluorescent microscopy is its high contrast when imaging brain tissue to distinguish the type of tissue. This is applicable for the different shape and orientation of the micro structure of lipids and myeline and CH bond concentration. In case of nanoparticles contrast delivery, it is valuable if one is able to assign the particle distribution within this level of details of the biological context. Moreover, the laser sources used for CRS can generate the linear and nonlinear optical contrast from the proposed nanoparticles and also excite two-photon photo-thermal lensing(TPPL) of red blood cells which is an important technique that provides a 3D map of brain tissue vasculature. This technique is desirable to assign the distribution of nanoparticles as distance from blood vessels.

As a part of the technique development in this section CRS imaging of normal brain tissue and tumour will be presented. Also, acquiring a "mosaic" grid of images of brain slices will be demonstrated for a qualitative comparison with MRI.

4.3.2 CARS imaging of tumour

Imaging brain slices with CARS can be carried out with the two available optical setups mentioned in section(3.3.3). Both setups can generate forward and backward signals that can be detected and reconstructed into images with a desktop computer. However, it is very important to determine the optimum imaging choice depending on the tissue optical properties and sample thickness. Brain tissue in known to be highly scattering due to its non-uniform refractive index and relatively thick (0.5 mm) brain slices where used to avoid sample damage. Accordingly, it was found that forward detection setup

can yield low quality images comparing to the epi-CARS images which benefited from the strongly back-scattered F-CARS signal. For this reason a combination of 816.4 nm from the OPO as pump and the 1064 nm as Stokes was adopted to generate anti-Stokes signal at 660 nm to increase back scattered signal. Figure(4.14) shows an example of detailed epi-CARS image of mouse brain tissue obtained using this setup.

One of the main aims of this chapter is to find a method to qualitatively compare images acquired with MRI and CARS. This is made challenging by the different resolution and field of view (FOV) of the two modalities. The high resolution MR images of mouse brain presented in Figure (4.6(b)) are of in-plane resolution of 125 μm and a slice thickness of 150 μm with a FOV is capable of covering the whole brain in one 3D image. In contrast, the in-plane resolution of CARS images is 250 nm and the slice thickness is 1 μm with a FOV of 250 μm when using a 60$\times$ lens. If a 20$\times$ lens is used, the in-plane resolution is 750 nm with a FOV of 750 μm.

In order to overcome the FOV limitation in CARS images, the mosaic grid of images is adopted. The mosaic imaging was reported by Fu and coworkers as a powerful method to map brain structures over a large FOV with high spatial resolution [79]. In their work, mapping nerve fibres of the brain was ideal for imaging the anatomical structures where fine biological details were not important. However, in this study, it is very important to acquire high resolution images to reveal the fine detailed structure to compare a feature from the MR image and cellular location of a nanoparticle.

In this mosaic technique, the motorised stage (Prior, Proscan) is programmed and synchronised with the microscope to acquire images at different (x , y) coordinate positions. The coordinates of the images are in a grid built as an Excel file, converted into comma separated values(csv) format and uploaded to the motorised stage software according to a previous estimation of the brain slice dimensions. Another table containing the imaging parameters such as photomultiplier tube (PMT) voltage, gain,

scan speed, zoom and image dimensions is uploaded to the microscope software. The track number and the coordinate file name in the xy-stage file should match those in the microscope software file. Also, the most important step is to correctly chose the starting coordinates to match the brain slice location and the PMT voltage that gives the optimum image quality according to the imaging session parameters such as laser power and the depth of the imaging plane.

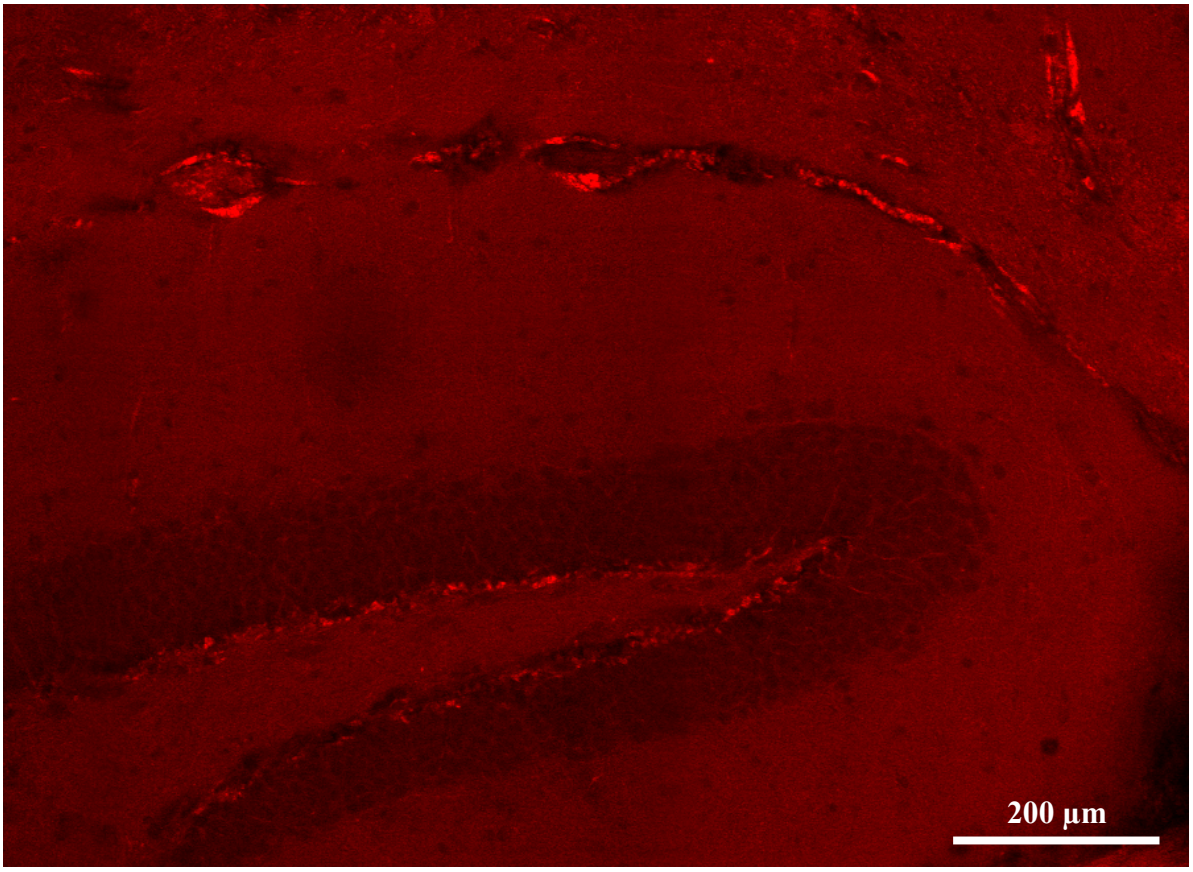

Figure 4.14: Detailed CARS image showing the different structures and features of brain tissue. This is a zoomed-in image determined by the yellow rectangle in the large mosaic presented in Fig.4.15.

After having acquired the images, the stitching is carried out using ImageJ software and Plugins (Stitching - Stitch sequence of grids of images). To use this image stitching plugin the images should be saved in the form of (Tile_zzz_yyy_xxx) where zzz, yyy and

xxx are three digits numbers that determine the image as an element in a 3D matrix. However, in this special case the zzz values are always 001 because there is only one imaging plane. The xxx and yyy rage from 001 to the maximum number of images in each of x and y axes.

It is very difficult and time consuming to rename the large number of images required for the mosaic manually. Accordingly, an ImageJ macro was built to accomplish this automatically (Appendix.1.2). When running the ImageJ macro the user is asked to determine two directories of two folders by browsing, the first where the row images are saved and the other where the Tile images should be saved. Also, the user has to determine values for the parameters "ymax" and "xmax" within the macro that indicate the y and x dimensions of the grid matrix respectively.

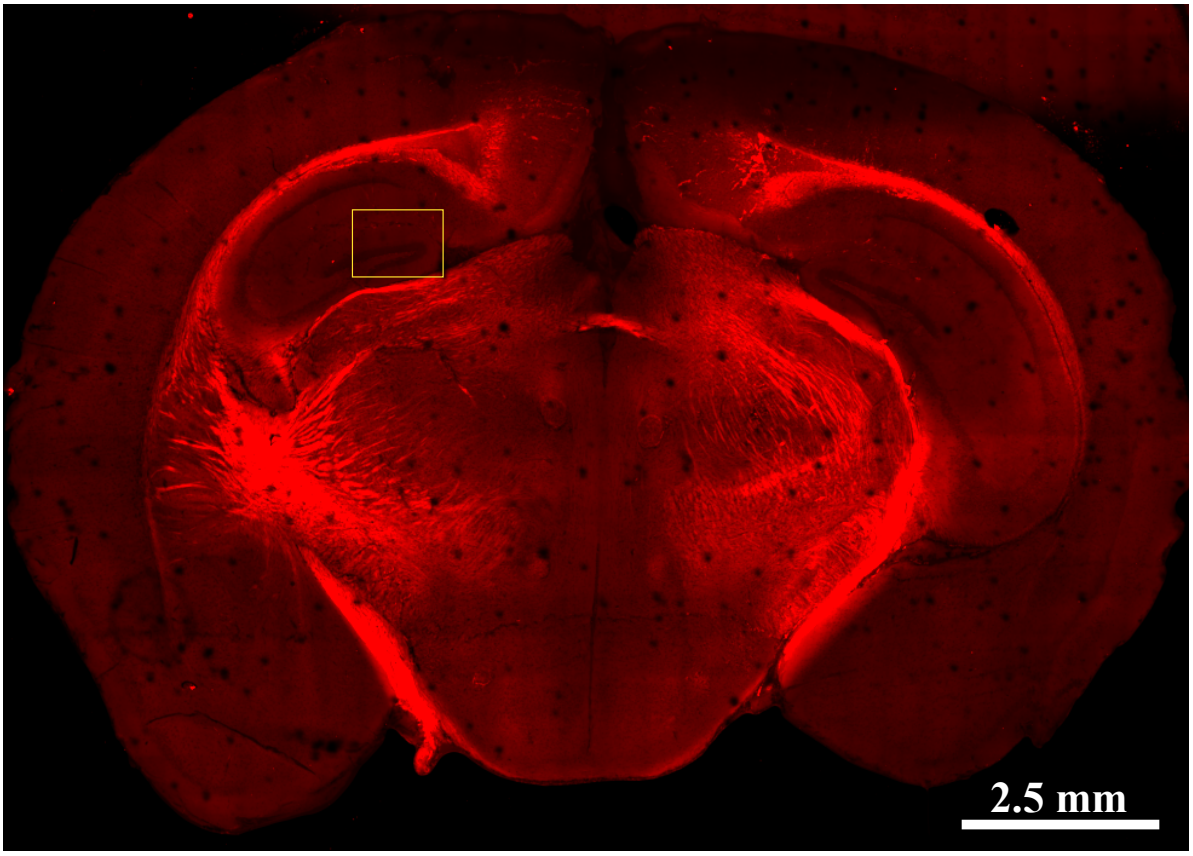

Figure 4.15: Large scale mosaic of CARS images of a whole brain slice. The mosaic is obtained by stitching 750 CARS images acquired by a 20 times objective lens. The yellow rectangle corresponds to Fig.4.14

There are two major experimental issues that must be taken into consideration when creating large area scan with CARS. First, the coverslip spacers thickness should match the brain slice within the two coverslips. Even small difference causes microscopic curvature of the coverslips from one or both sides. This curvature causes the imaging plane to be within the biological tissue in one place and in the coverslip in another. To be able to image a whole slice with such a curvature the imaging plane should be sufficiently deep into the tissue to prevent the image plane from leaving the brain tissue. This usually results in a low quality image. Even if a sufficiently deep mosaic image is obtained, the individual images will correspond to different actual plane of the biological

tissue because of the curvature. Fig.4.16 illustrates the coverslip curvature effect of the imaging plane focussing.

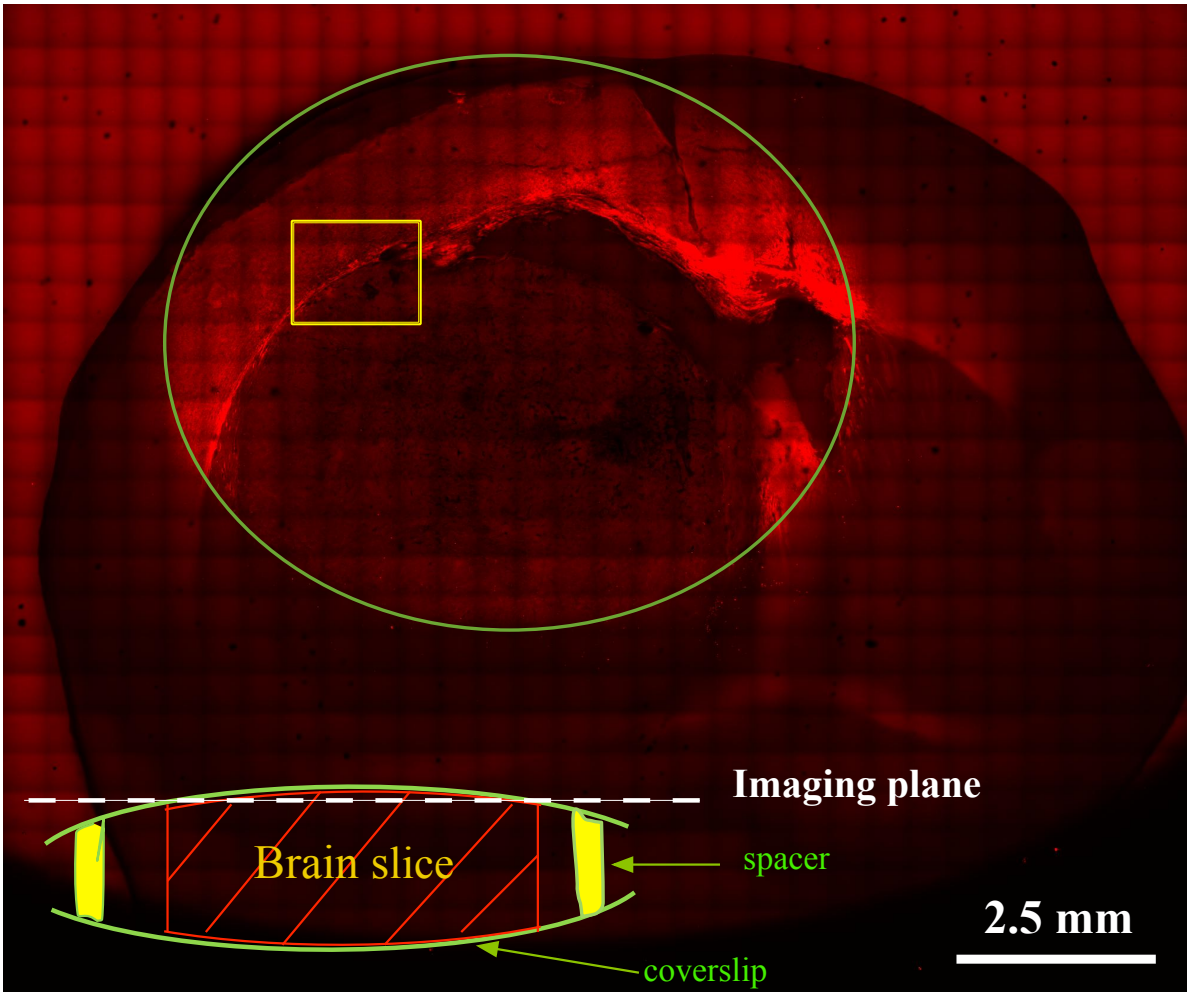

Figure 4.16: The effect of coverslip curvature on CARS mosaic images. The green ellipse determined the in-focus while the rest is out of focus of imaging plane. The lower sketch is an illustration of the curvature resulting from the thinner coverslips spacers. The yellow rectangle shows the power of CARS in sharply determining tumour edges(This image is not intensity normalised).

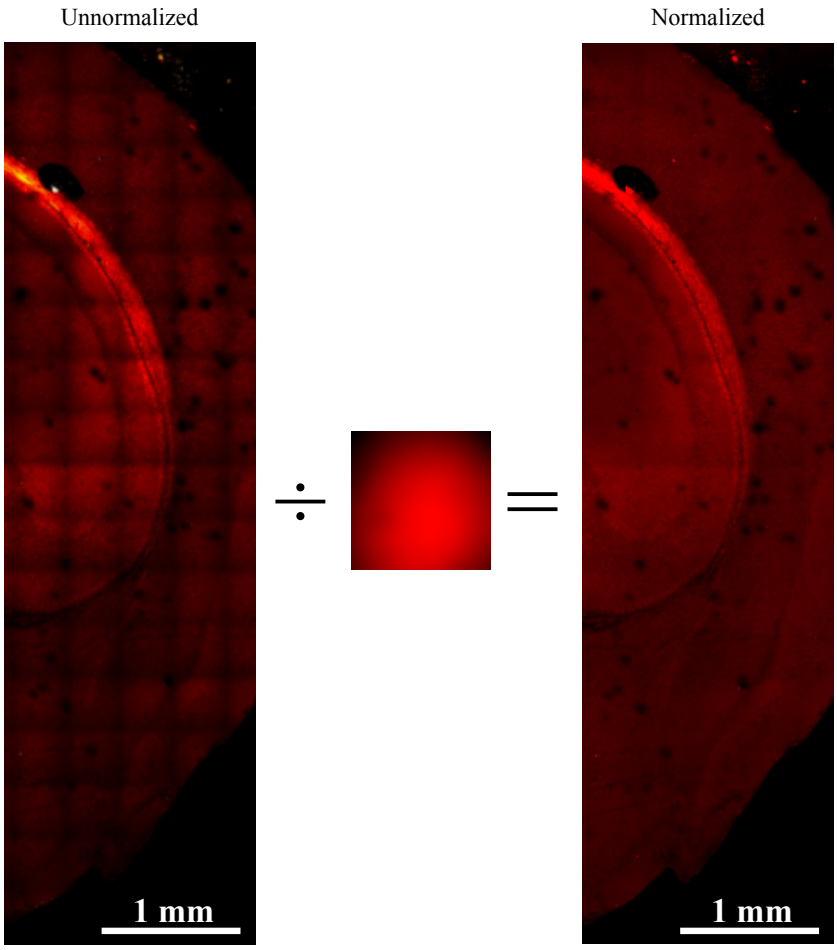

Figure 4.17: Image normalisation of CARS mosaic of mouse brain tissue. The unnormalised image (left) has unwanted dark sides of individual images. Each individual image was divided by an averaged FWM image of glass coverslip surface to generate the uniform intensity normalised mosaic (right).

The second experimental obstacle toward high quality mosaic CARS imaging arises from the geometry of the objective lens combined with the scanning nature of multiphoton microscopy. The intensity of a CARS image follow a Gaussian profile resulting in lower signal in the image periphery. This Gaussian profile is due to what is conventionally known as phase curvature. CARS based originally on two laser beams that geometrically setup to satisfy phase matching condition (an important condition to generate CARS, see Section(2.3.5)) [41]. To satisfy this condition for microscopy, two

collinear beams are focused with a high numerical aperture lens [42]. However, when scanning the beams over the field of view, the beams deflect larger angles to excite points in the image periphery and spherical aberration degrades the phase matching. This issue was tackled during the experiment by optimising imaging setup and after experiment by postacquisition image processing. During this experiment a 20 times lens was used to minimise this effect. Also, 2× zoom was used in the microscope software to limit the scan to the most uniform area (475.5 × 475.5 μm^2). Post image processing normalised the image intensity by dividing each image in the mosaic by an average image of the non-resonance signal from the coverslip. However, dealing with a such large number of images manually is time consuming. for this reason, an ImageJ macro was built to carry out the process automatically. Figure (4.17) illustrates the image normalisation process showing a mosaic image of a mouse brain before and after normalisation. The intensity of each individual image in the unnormalised mosaic (left) is dimmer at the edges of each tile, which results in unwanted artefacts. However, after normalisation of the mosaic image (right) this effect is almost unnoticeable. The small image in the centre is the averaged non-resonance CARS image of a glass coverslip surface that each individual image is normalised by.

4.4 Summery

In this chapter, the label-free imaging of mouse brain tumour using MRI and CARS was explored. The main aim was to investigate the capability of both techniques in detecting tumour with a distinguishable contrast between healthy and diseased tissues. To achieve this goal for MRI, preliminarily experiments were conducted to optimise the MR imaging sequences and parameters. A 1.5 T clinical MRI scanner was used with a micro surface coil to achieve a high spatial resolution (125 × 125 × 150 μm^3)

within a reasonable imaging time (2 hours per brain). The data was used to measure tumour volume using Osirix software after a manual slice-by-slice tumour boundaries determination by the user. Moreover, the data was used to simulate the conventional histology measurements of mouse brain tumour by choosing the largest coronal tumour slice, measuring its diameter, and calculating the tumour volume assuming a spherical shape. The 3D MR images were also used to simulate histological volumetry. The two sets of data were compared and it was found that histology volumetry suffers from an average of 20% error as a result of irregular tumour shape. This suggests that MRI is a powerful alternative and requires less number of animals when compared to histology to achieve significant statistics which is an important finding from ethical point of view.

A CARS microscope with 1064 nm and 816 nm laser excitations combination was used to image mouse brain tumour. It was found that sharp contrast between healthy tissue and tumour is achievable when imaging in the backward direction benefiting from the scattering nature of the brain and the relatively short wavelength anti-Stokes CARS signal generated by the laser excitations mentioned above. The FOV limitation of CARS images which disallows comparing with MR images was tackled via proposing mosaic of images that covers a whole brain slice. Moreover, image processing technique was developed to compensate for the phase curvature in the CARS images.

Chapter 5

Nanoparticle characterisation

5.1 Introduction

The biomedical applications of nanoparticles are currently of great interest and there has been remarkable efforts toward fabricating and characterising their magnetic and optical properties. The paramagnetic property is of interest to be able to use particles as MRI contrast agents and the optical properties are desirable for light microscopy. Iron oxide and gadolinium oxide nanoparticles are well stablished as MRI contrast agents [80]. It has been reported that their longitudinal and transverse relaxivities are higher than the clinically used gadolinium complexes because of the condensed nature of the particles [81, 82].

This chapter describes the characterisation of the particles used in this thesis. The characterisation includes investigation of the shape and particle size, crystalline structure, optical properties and MR relaxivity. A novel technique is presented to measure particles photoluminescence (PL) properties using a Raman microspectrometer over an extended spectral range. Also, to the best of the author's knowledge, upconversion photoluminescence (UCPL) of doped Gd_2O_3 is investigated under a focused pulsed laser

excitation for the first time.

5.2 Composition materials

Table(5.1) shows the gadolinium oxide nanoparticles (GONPs) samples that were fabricated and investigated throughout this study. The particles were doped or co-doped with different lanthanide ions in different molar percentages for different investigation purposes which will be illustrated later in this chapter and in the next chapter.

Although the chemical reaction in the precipitation method adopted in this study was reported by Hemmer et. al. [57], it is important to know the composition materials in order to ensure that right nanoparticles with the doping elements have been made. For this purpose, energy dispersed X-ray spectroscopy (EDS) has been employed. Fig.5.1 is an SEM image of GONPs doped with 5% Er^{3+}. Three dispersive energy spectra were acquired on three relatively large scale regions for the sake of significant averaging. In order to illustrate the patterns of the obtained spectra, an example spectrum (spectrum1) is shown in Figure (5.2). As illustrated in Table(5.2) all three spectra were analysed automatically with a fitting software into weight percentages. It is important to mention that there are two obstacles towards accurate quantitative EDS. Firstly, having the particles in oxides form. Oxygen is light element that possesses relatively low energy characteristic X-ray with a very low quantum yield. Also, even if a sensitive detector is used this low energy X-ray is more probable to be absorbed by the material itself with low portion escaping the sample surface to reach the detector. The second practical difficulty toward quantitative EDS is having the material in particle form. Relatively large, flat and polished surfaces are required to achieve accurate quantitative analysis [83].

However, it is still valuable for this study to employ EDS in order to obtain quali-

Table 5.1: Lanthanide doping percentages of Gd_2O_3 nanoparticles

Sample	**Doping percentage (mol%)**		
	Yb^{3+}	**Er^{3+}**	**Tm^{3+}**
S1	1	1	0
S2	20	5	0
S3a	0	5	0
S3b	5	0	0
22	0	0.5	0
23a	0.5	0	0
24	10	0	2
29	10	0	4
30	0	5	2
31	10	0	1
32	10	0	0.5

tative data to confirm the degree of doping which is vital for the optical properties. In Table(5.2) we can ignore the carbon percentage because it is the composition martial of the conductive tape. The qualitative data in the spectra and the table prove the existence of the doping element ion Er^{3+} within the particle material (Sample 3a). EDS of sample 3a was presented in this section as an example.

This section confirms that the fabricated gadolinium oxide particles were successfully doped/co-doped with the lanthanide ions. This is necessary for the particles to possess the optical properties required for optical microscopy.

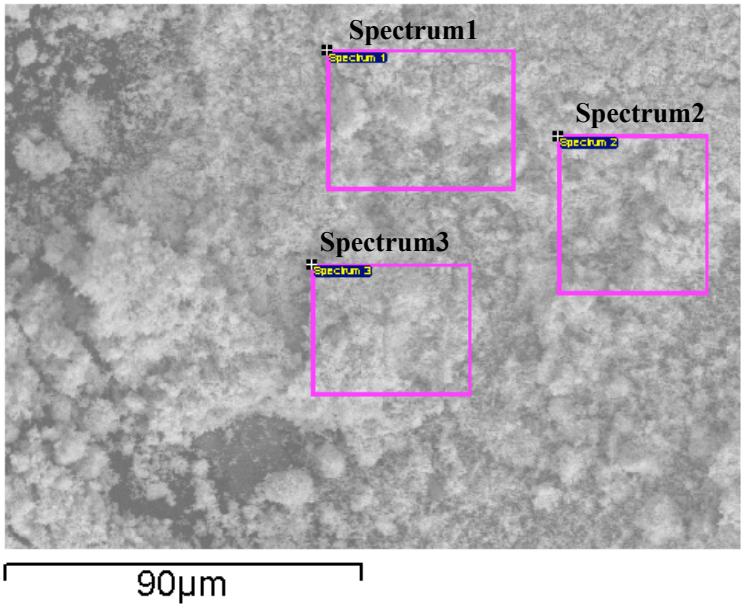

Figure 5.1: SEM image of Gd_2O_3: 5% Er^3+ nanoparticles with three rectangles indicating three areas where the three EDS spectra in Table(5.2) were acquired.

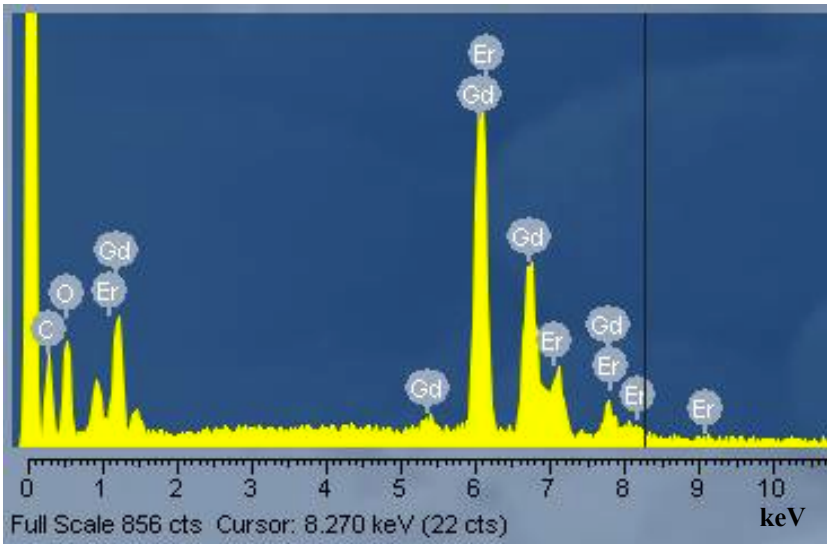

Figure 5.2: The dispersive energy spectroscopy of of Gd_2O_3: 5% Er^3+ nanoparticles. The spectrum corresponds to the upper rectangle labeled (spectrum1) in Fig.5.1.

Table 5.2: The EDS data of Gd_2O_3: 5% Er^{3+} nanoparticles. The three spectra in the table correspond to the three rectangular areas in Fig.5.1. All results are in weight%.

Spectrum	**In stats.**	**C**	**O**	**Gd**	**Er**	**Total**
Spectrum 1	Yes	21.24	15.99	58.64	4.13	100.00
Spectrum 2	Yes	22.70	15.42	58.07	3.81	100.00
Spectrum 3	Yes	19.44	15.35	60.82	4.39	100.00
Mean		**21.13**	**15.59**	**59.18**	**4.11**	**100.00**
Std. deviation		1.63	0.35	1.45	0.29	
Max.		22.70	15.99	60.82	4.39	
Min.		19.44	15.35	58.07	3.81	

5.3 Morphology and size

The morphology and size of the nanoparticles are important factors when using them for MR and CARS imaging contrast. Moreover, the monodispersity of the particle size is significantly important in the case of targeted drug delivery where the same pathway within the body is desirable [84]. For instance, nanoparticles of the same size are expected to diffuse into the tumour in the same manner whereas particles with a different size would be expected to behave differently. Accordingly, size and morphology of nanoparticles were inspected before they were used experimentally.

Scanning Electron Microscope (SEM) and Transmission Electron microscope were utilised for this purpose. However, for SEM imaging, because the doped GONPs are semiconductors with a wide band gap (5.2 eV) [85], they have been spread on a conductive carbon tape to eliminate any electrical charging of particles that may result in unwanted artefacts and hence low quality image. In Figure (5.3) two example SEM images of doped Gd_2O_3 particles (Sample1) are presented. In image (a) the single particle size (diameter = 257.7 nm) is determined with the size tool available in the SEM software. To show the monodispersity of the particles, larger field of view (FOV) image was acquired for the same sample(image b).

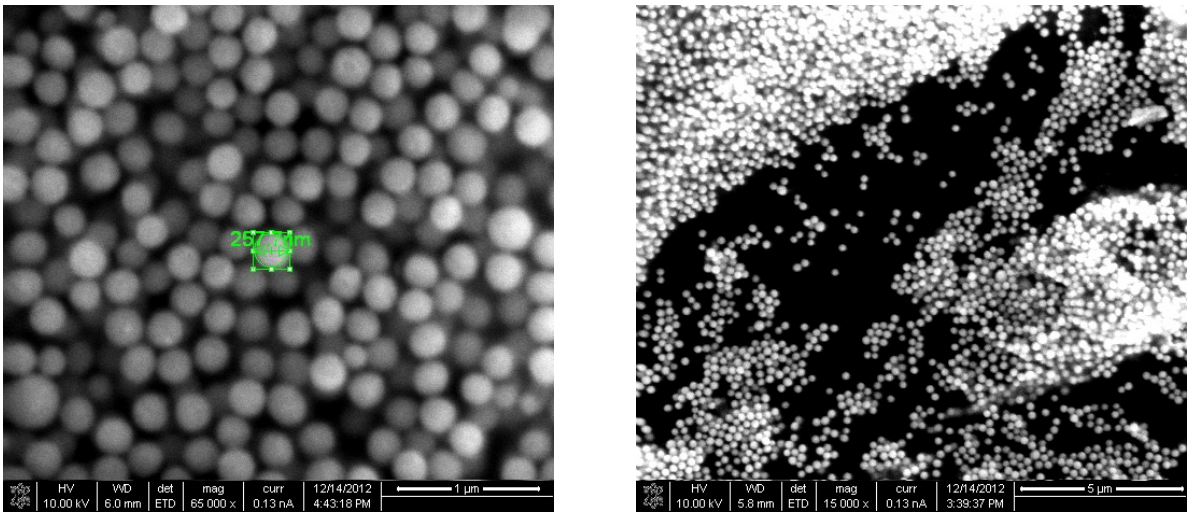

a **b**

Figure 5.3: SEM image of doped Gd_2O_3 nanoparticles (Sample1). Image (a) shows the spherical particle shape with diameter of about 260 nm) whereas image (b) is a large scale image that shows the size monodispersity of the particles.

Because these particles are proposed to be used as biomedicine contrast agents, controlling their size is desirable for medical investigation purpose as mentioned above. Hemmer et. al. have utilised surfactants to obtain different sizes of doped Gd_2O_3 nanoparticles [57]. However, in this study a simpler approach for controlling size was achieved by changing the nucleation time of the particles. Figure (5.4) shows two images of doped gadolinium oxides particles of different sizes. The nucleation time was 30 min for the particles in image (a) resulting in particle size of (230 - 265 nm). Only by changing the nucleation time to 15 min, the particle size could been reduced to 85 nm.

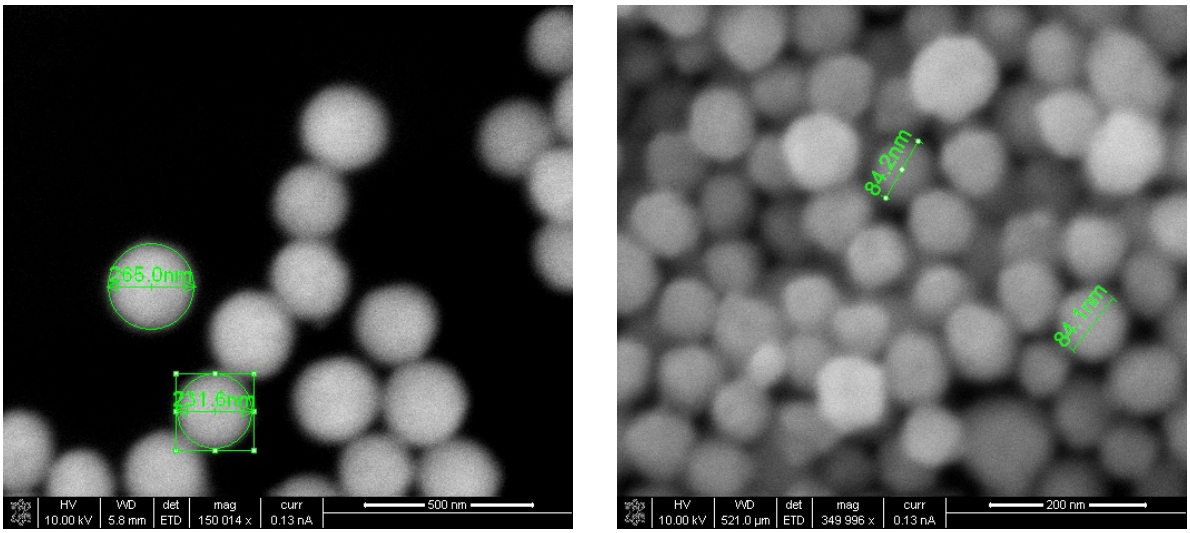

a **b**

Figure 5.4: SEM image of doped Gd_2O_3 nanoparticles. Image (a) shows particles with size of (230-265 nm) obtained with 30 min nucleation time. Image (b) corresponds to 85 nm particles fabricated with 15 min nucleation time.

In order to estimate the monodispersity of the particles statistically, they were first distributed uniformly in 2D on a glass coverslip. This was achieved by washing the glass with soap and water, then cleaning with acetone and followed by rinsing with propanol. Nanoparticles suspension was prepared by adding 0.5 mg of the particle powder to 1 mL propanol then sonicating for 30 minutes. A droplet of the suspension was then spin coated onto the coverslips. It was found that a rotation speed of 200 revolutions/min was optimum for this purpose. Slides were then coated with a 3 nm gold film in order to overcome the charging artefacts caused by their large gap instead of placing them on carbon tape. Fig.5.5 (a) is an SEM image of 2D distributed doped gadolinium particles. In image (b) the particles where selected by brightness threshold using ImageJ followed by particle size analysing using the "Analyse Particles" plugin. The largest feature included in the analysis was limited to 10 pixels, to avoid inclusion of particle aggregations (c). Finally, the particles selected and analysed are presented by

small circles in image (d). The sizes of the particles was measured by assigning the area in pixels to the actual image dimensions assuming circular appearance of particles in the image. The size distribution histogram is plotted in Fig.5.6. The same procedure was executed to statistically inspect the size distribution of iron oxide particles fabricated by the hydrothermal method (S21). The particles form in cubic shape, and, accordingly, they appear as squares in the SEM image. Therefore, side length is measured and cubic volume is considered. The result is shown in Fig.5.7.

In both size distribution histograms it is obvious that both fabrication methods produce particles with a good degree of monodispersity for this preliminary study (the particles were not injected to live animals throughout the study) . Moreover, adding surfactants potentially enhances the size monodispersity as reported in the literature (e.g. [86] and [87]). It can be concluded from this section that the two fabrication methods adopted in this study are capable of producing monodispersed nanoparticles applicable for biomedical investigations. Moreover, the particle size is easily tuneable in both methods either by changing nucleation time in the homogeneous precipitation method or by changing the starting solution concentration in the hydrothermal method.

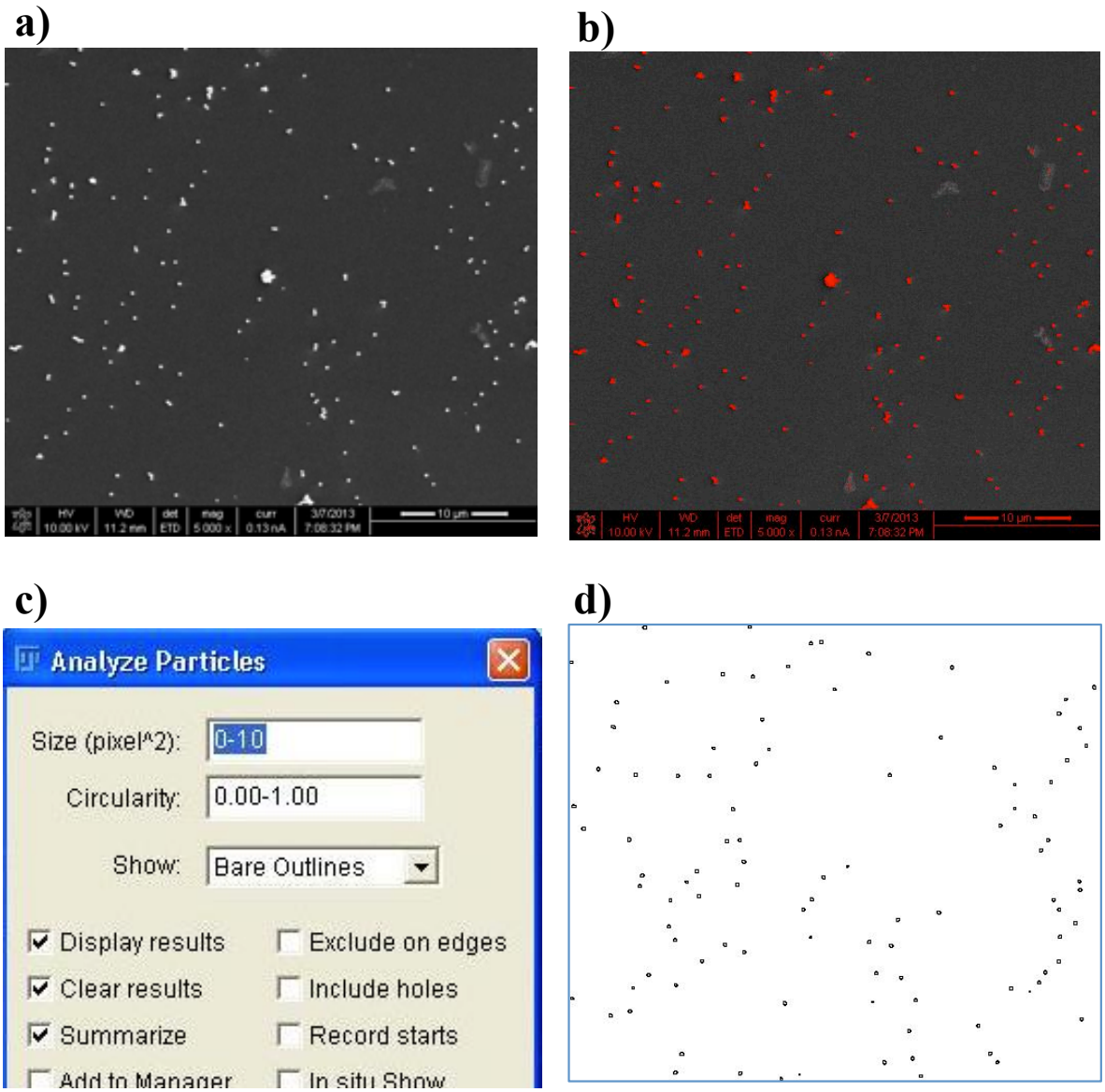

Figure 5.5: An illustration of the process of the statistical analysis of particle size monodispersity. The SEM image (a) was intensity threshold to select particles (b). Image (c) shows the parameters chosen in "Analyse Particles" ImageJ plugin, and (d) shows the selected particles.

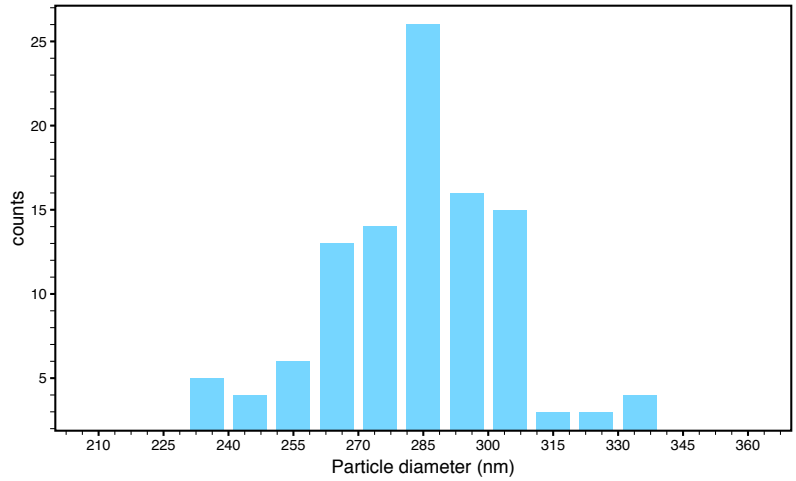

Figure 5.6: Histogram of size distribution of doped gadolinium oxide nanoparticles (S3a). The x-axis represents particle diameter obtained from the circular appearance of the particle in the SEM image in (nm)

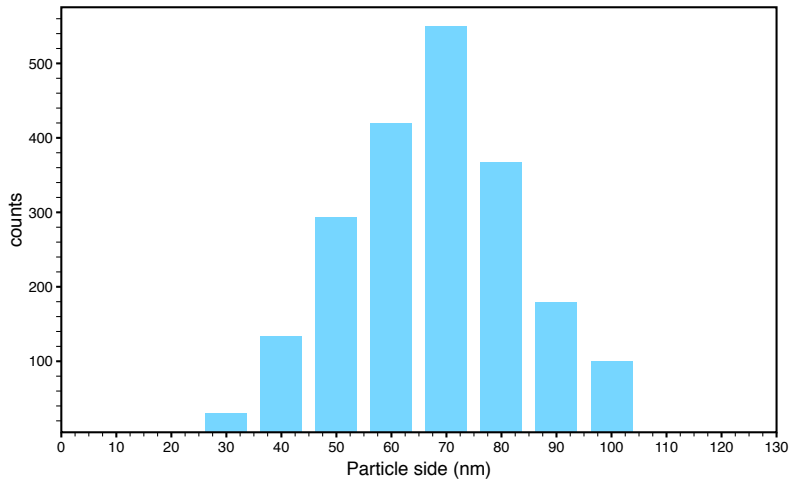

Figure 5.7: Histogram of size distribution of Iron oxides nanoparticles (S21). The rectangular particle appearance in the image is assumed to be square and hence the side length is considered in (nm)

5.4 Crystalline structure

The crystalline structure of doped gadolinium oxide nanoparticles is vital for photoluminescence (PL) and upconversion photoluminescence (UCPL) [88]. For this reason the crystalline phase of the doped gadolinium particles was inspected before and after annealing at 950° for 30 min using an X-ray diffractometer (XRD). The process of diffraction was carried out with what is conventionally known as powder diffraction setup. A powder of a material oriented randomly in all possible directions is equivalent to rotating a single crystal in all possible angles in front of an X-ray beam. However, an ideal powder with small enough particle size and complete randomness with no preferable direction is required to reach statistically significant pattern. These conditions are satisfied with the nanoparticles under investigation where the size is relatively small and no known factor acts on the particles externally to alter the orientation degree of freedom. In Figure(5.8) it can be seen that the XRD pattern before and after annealing is completely different. The annealed particles powder possesses strong peaks which indicates that they are in the crystalline form. Moreover, the detected XRD pattern matches that reported by Chen and coworkers an erbium doped gadolinium oxide crystals [89]. Also, the pattern matches the JCPDS database entry for the same material.

For the sake of reducing the cost of the XRD characterisation process, only one patch of the early-fabricated particles was investigated. However, there are two reasons to be confident that the other particles would develop the same crystalline structure. Firstly, all the doped gadolinium oxide particles were fabricated with the same homogenous method. Moreover, the same starting chemical compound groups (Nitrates) of different lanthanide ions were utilised. Secondly, possessing strong photoluminescence properties is another indication of the crystalline phase as illustrated in more detail in the following section.

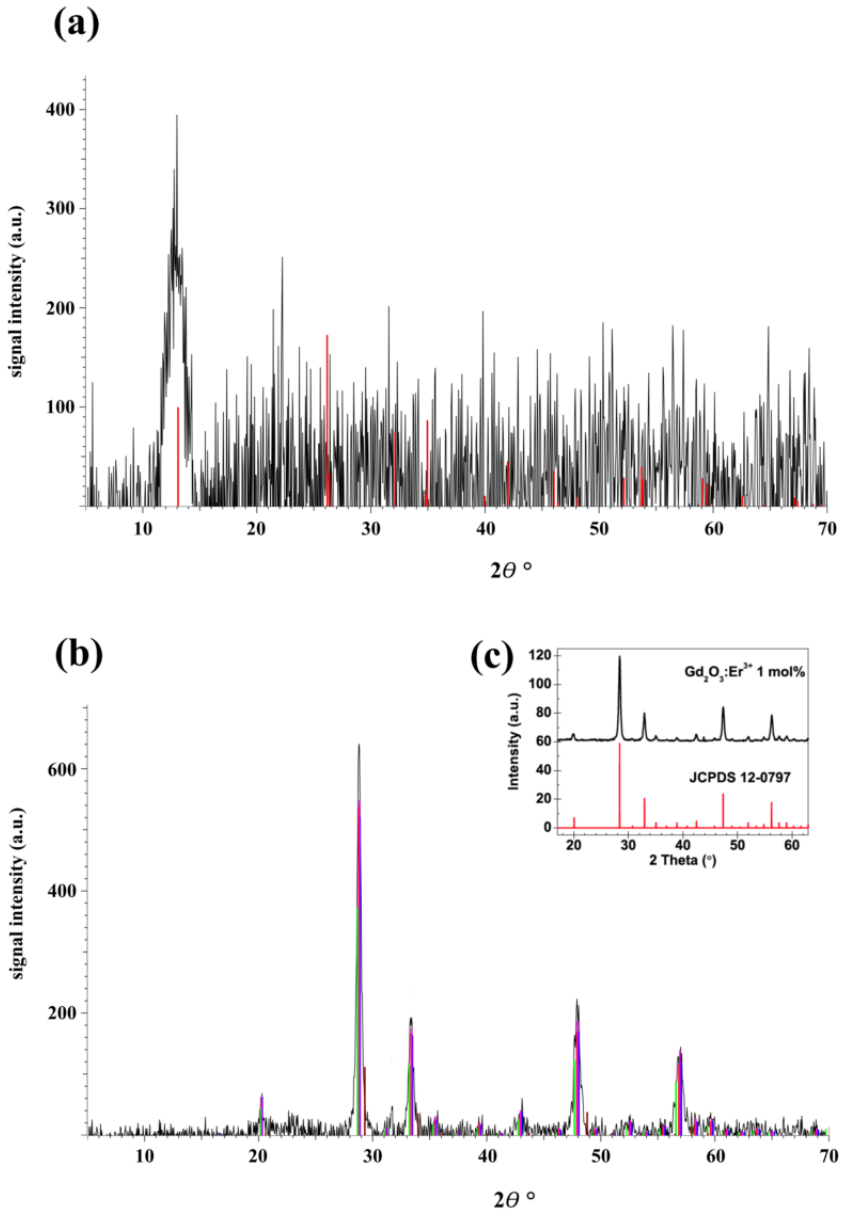

Figure 5.8: XRD of doped gadolinium particles (sample 3a) (a) as prepared and (b) annealed at 950° for 30 min. The pattern matches XRD of Er doped gadolinium oxide (C) as reported in reference [89].

5.5 Photoluminescence

Photoluminescence of rare-earth-ion doped organic and inorganic materials has been investigated in a number of previous studies [90, 91]. Among those materials, magnetic nanoparticles are attractive for the multi-modal imaging capability. Doped Gadolinium oxide in particular received noticeable attention for their high relaxivity in MRI compared to the clinically used complexes.

Photoluminescence properties of doped gadolinium oxides particles are interesting for medical imaging. Before imaging these particles, it is necessary to characterise their photoluminescence with a spectroscopic setup for several reasons. First, some of the important material structural properties such as crystallite can be inspected. As mentioned in section 5.5, XRD was carried out for only one sample and photoluminescence strength depends on the crystalline structure (an experimental evidence is given below). Secondly, photoluminescence is a fingerprint of the dopant ions. Using this fingerprint signature, the doping of gadolinium oxide crystals can be confirmed qualitatively. Thirdly, the strength of photoluminescence is an indication of the efficiency of using these particles for imaging purposes where strong signal results in acceptable imaging averaging. Finally, although the mechanism of upconversion photoluminescence is completely different from photoluminescence, particles with strong photoluminescence pose efficient upconversion photoluminescence. For these reasons, the photoluminescence spectroscopy for doped gadolinium oxide was performed.

The process in which photoluminescence occurs in lanthanide doped gadolinium oxide nanoparticles is explained in section (2.3.9). In summary, a visible or ultraviolet photon is absorbed by the material and a lower energy photon is emitted at the characteristic wavelength. In a typical photoluminescence spectroscopy measurement an ultraviolet excitation is utilised (as examples see references [92–94]). This is to generate

emissions from all the possible energy levels in the visible and infrared regions because only levels with energies lower than the excitation photon are emitted. In this study, a commercial compact Raman spectrometer equipped with 532nm green and 785 nm infrared lasers was used. The limitation of using such excitation lasers is the inability to detect any emission with wavelength shorter than 535 nm. Also, there is another limitation in the detection spectrum range of the microscope for the diffraction gratings and the detector arrangements. When using the 532 nm laser, the maximum detectable wavelength is 750 nm and it is 1050 nm when utilising the 785 nm infrared laser. These detection ranges are enough to detect the photon energy shift caused by the relatively low energy Raman shift from molecular vibrations. However, for photoluminescence spectroscopy, the detection range is desired to be large to detect all the possible peaks which include the visible and infrared part of the spectrum.

Nevertheless, despite limitations with the Raman spectrometer it was found to be acceptable for the purposes of this study. Firstly, there is more interest in the relatively longer wavelength for biological imaging application. Short wavelengths are more scattered in the biological tissue which results in low quality image and short imaging depth. Accordingly, it is sufficient to investigate peaks longer than 532 nm. Moreover, any missed short peak will be investigated in the upconversion photoluminescence spectroscopy in the following section. Secondly, regarding the spectrum range, having two excitation lasers (532 nm and 785 nm) allow for full spectrum detection in two separate acquisitions.

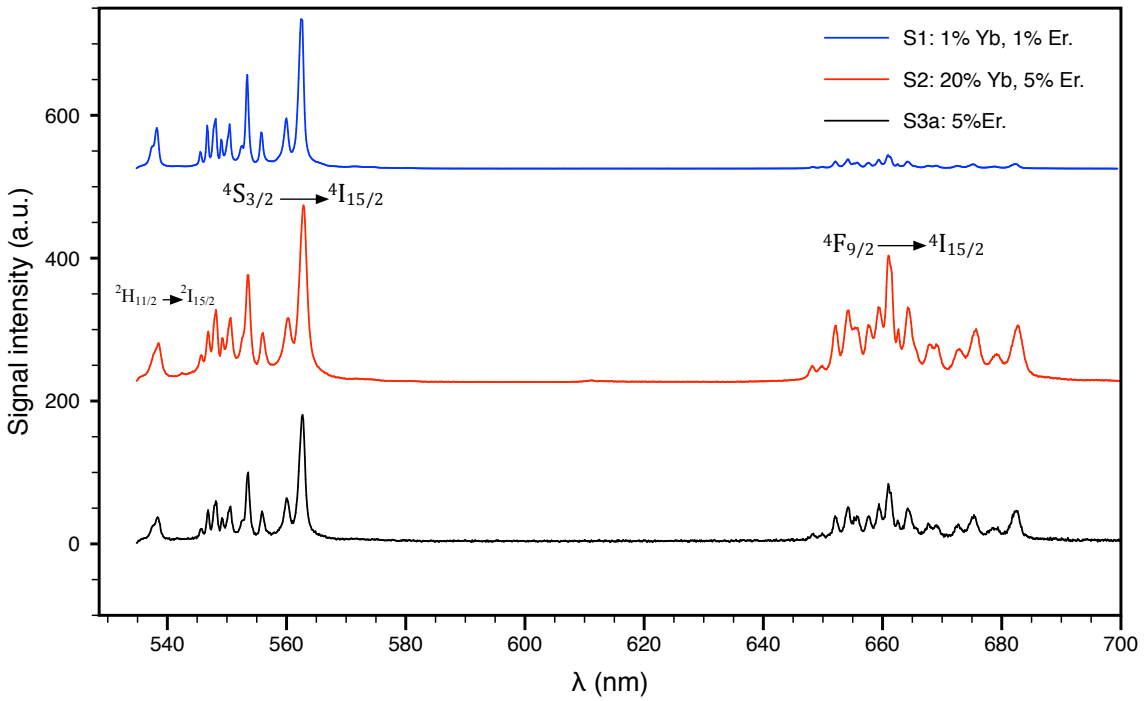

Figure 5.9: PL spectrum of different percentages doped/co-doped gadolinium oxide particles excited with a 532 nm green laser. The figure shows the effect of varying the doping percentages on the ratio of red/green photoluminescence.

There are three different doping rare earth ions investigated in this study: ytterbium (Yb), erbium (Er) and thulium (Tm). Doping Gd_2O_3 with each element generates a band of emissions with a specific pattern that corresponds to the energy levels created within the relatively large band gap crystal. Figure (5.9) shows photoluminescence spectra of three samples (S1, S2, and S3a) under 532 nm excitation with a 1 mW power and 5x lens. The three samples are either doped or co-doped with ytterbium and erbium in different percentages as mentioned in Table(5.1). All the peaks in this range of wavelengths corresponds to the transitions in the Er ions. The red photoluminescence is generated via the transitions between $^4F_{9/2}$ and $^4I_{15/2}$ whereas the green results from the emissions from $^4S_{3/2}$ and $^2H_{11/2}$ to $^4I_{15/2}$ [95]. It can be seen from the same figure that the ratio of the red/green emissions is tuneable by changing the percentages of the

doping ions.

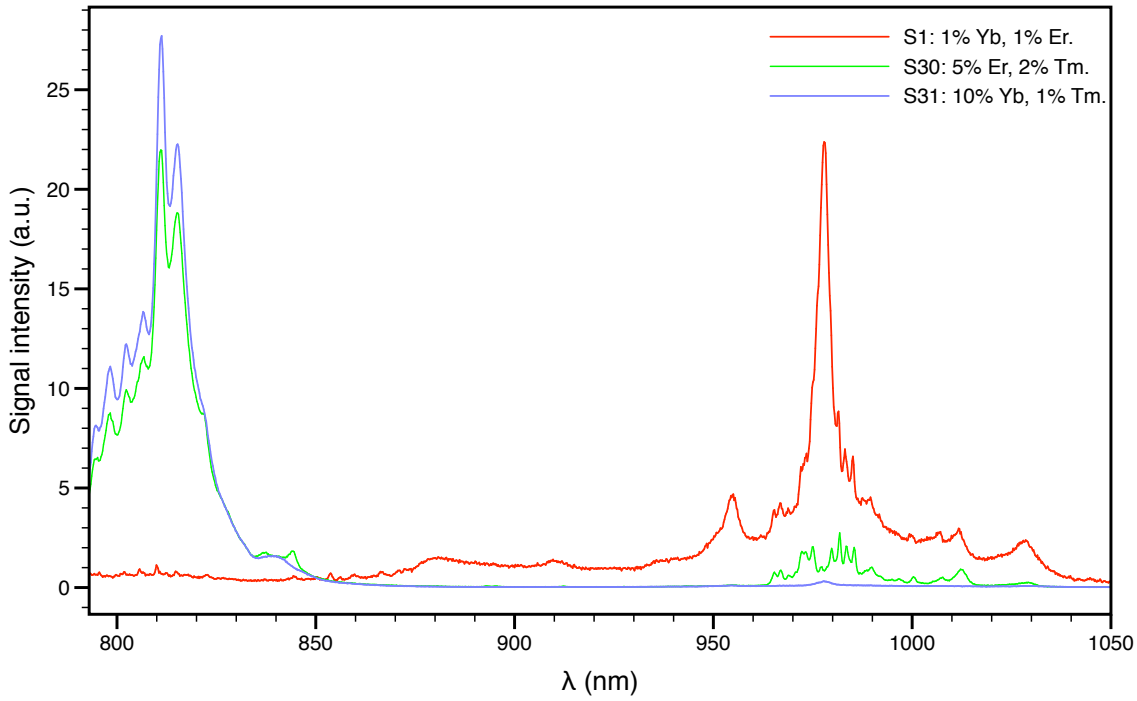

Figure 5.10: PL spectrum of gadolinium oxide particles (S1, S30, and S31) excited with 785 nm CW laser.

As mentioned before, when using the 532 nm green laser the maximum detectable wavelength is limited to about 750 nm. Accordingly, the infrared 785 nm laser was used to detect longer-wavelength peaks. Figure(5.10) shows the resulting spectrum of S1(1% Yb, 1% Er), S30(5% Er, 2% Tm) and S31(10% Yb, 1% Tm) indicated with the different colours in the legends. Before any further discussion and analysis it is important to mention that the different spectra are normalised to put them in the same figure.

There are strong bands of emissions at the ranges (790 - 850 nm) and (950 - 1040 nm). The peaks of the blue and green lines spectrum at 811 nm are due to the transitions from $^3H_4$ to $^3H_6$ that is generated by the Tm ions [96]. The peaks in the other range

(950 - 1040 nm) are either from the $^2F_{5/2}$-$^2F_{7/2}$ transitions in Yb ions or $^4I_{11/2}$-$^4I_{15/2}$ in the Er ions. The Yb emission at 978 nm has also a strong absorption cross section that has been utilised to generate efficient upconversion photoluminescence (see the following section). One of the attracting observation of this spectrum is the relatively stronger 811 nm illuminated from Tm ions comparing to the Yb 978 nm emission. This can be confirmed from the spectrum of S31.

To confirm that photoluminescence is a finger print of doping element, a closeup look at the range (950-1040 nm) is taken (Fig.5.11). The spectra were taken under different excitation powers, objective lenses and focus situations to avoid detector saturation, therefore, the intensities were normalised to allow qualitative comparisons and analysis. In Fig.5.11 (a) and (b) Tm ions do not have active transitions in this range which suggest that the peaks correspond to Er and Yb ions. The addition of spectra (a) and (b) is presented in Figure (5.11 (c)). The resultant pattern is similar to the spectrum of a third sample containing the two types of ions Fig.5.11(d), indicating that the doping of a specific ion can be confirmed from the spectra pattern even if the hosting crystal is doped with several ions.

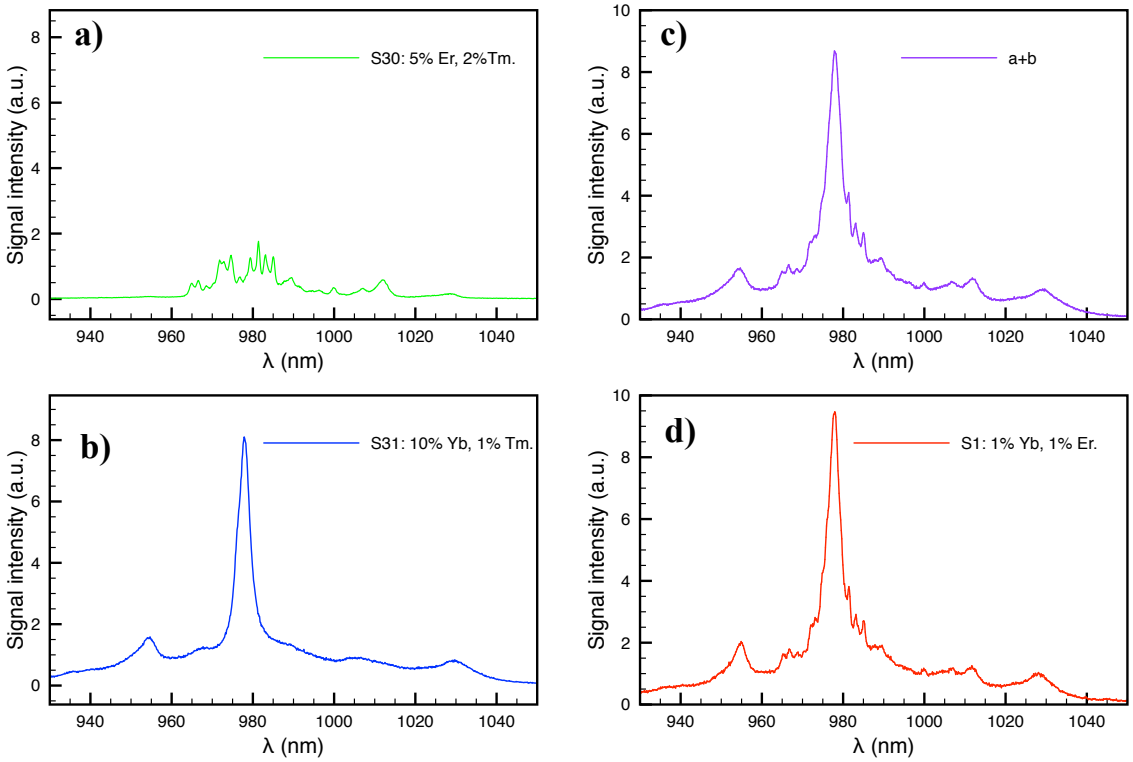

Figure 5.11: PL spectrum of gadolinium oxide particles under 785 nm CW laser excitation, a) doped with Er and Tm and the peaks correspond to the $^4I_{11/2}$-$^4I_{15/2}$ transitions in the Er ions. b) doped with Yb and Tm and the peaks correspond to the $^2F_{5/2}$-$^2F_{7/2}$ transitions in Yb ions. c) is the addition of (a and b). d) doped with Yb and Er.

In order to emphasise the importance of the annealing process which provide the particles with the crystalline form, a photoluminescence spectrum was acquired for S2 before and after annealing (Figure (5.12)). It is obvious that flat spectrum with no sharp peaks results from the un-annealed particles whereas strong emissions detected from the annealed particles, hence confirming the crystalline structure of the annealed particles.

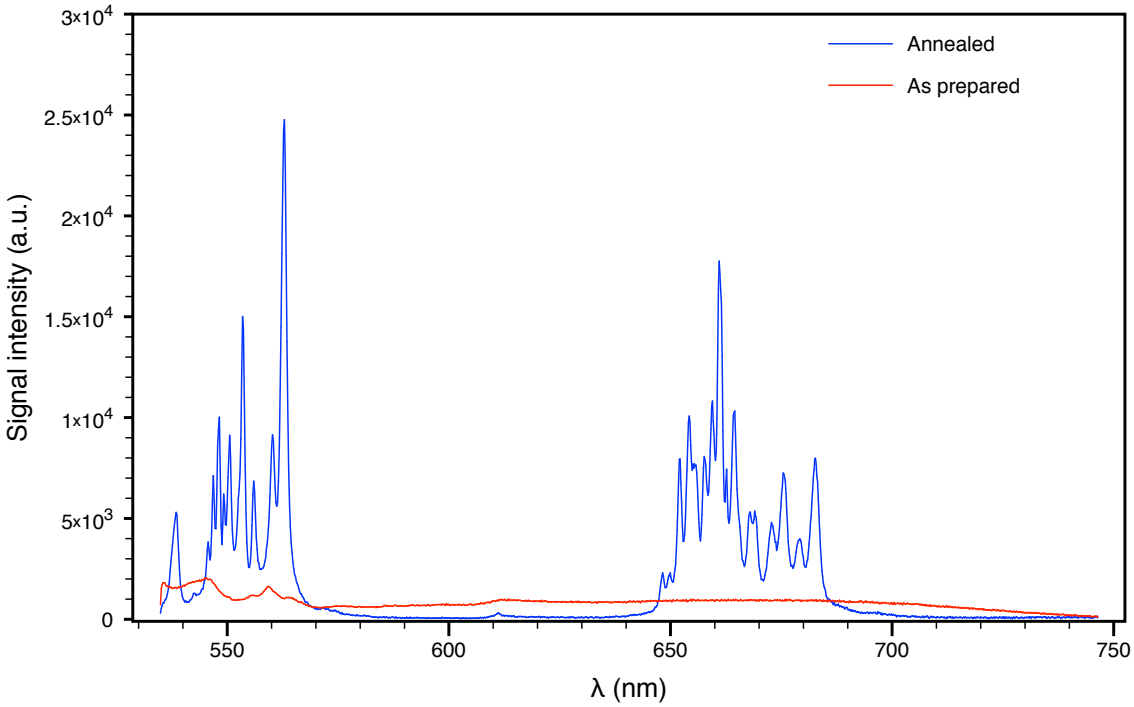

Figure 5.12: PL spectrum of doped gadolinium oxide particles(Sample2) as prepared (red) and annealed at 950° for 30min (blue). The figure demonstrates the importance of annealing for optimum optical properties.

5.6 Upconversion Photoluminescence Spectroscopy

Upconversion photoluminescence is an attractive optical property of crystals doped with optically active rare earth ions, which offers several novel advantages. Firstly, upcoversion emission is relatively strong and proved to be efficient for imaging even with a CW laser if tuned to the Yb absorption band at 980 nm [57, 97, 98]. Secondly, the emissions peaks are sharp and well defined with multi-colour availability depending on the doping choice. This is of great importance when applying the nannoparticles as contrast agents for CRS imaging systems where different excitations and, hence, detected signal are available. This allows one to find applicable nanoparicles with a contrast that does not overlap with the biological signal generated with the available

laser system. Thirdly, the power dependence of the emissions is nonlinear [89,95,99–101] which offers the same advantages for deep tissue image offered by conventional multi-photon microscopy. Finally, the conversion of infrared excitation into visible emission further enhances depth penetration in scattering biological tissues.

All reported techniques in the literature have implemented a CW laser with a wavelength of about 980 nm. This is to take the advantage of the strong absorption cross section of ytterbium which, consequently, allows for efficient emission. In this section, for the first time, the upconversion spectroscopy of doped Gd_2O_3 nanoparticles will be investigated under an ultrafast pulsed laser combined with a high numerical aperture lens. Moreover, for this study, it is essential to explore the spectroscopic properties of the particles before utilising them in imaging in order to specify the approperiate band-pass filters. Also, the power dependence of the upconversion emission under the pulsed laser excitation will be investigated. Finally, the upconversion emission dependency on the excitation wavelength will be explored for the different types of dopants.

The particles were spin coated on a glass coverslip and sealed with another glass coverslip with parafilm spacer. The sandwiched coverslips were then placed in the microscope with the coverslip marked "down"(the coverslip on which the particles have been coated) facing the objective lens. Then the optical setup described in Section (3.3.6) was used to collect generated emission in the backward direction under a picosecond excitation generated by the signal output from the OPO. The filter used to suppress the excitation beams is either a 900 nm or 750 nm short pass filter depending on the excitation wavelength. The upconversion emission is collected by the objective lens and reflected with a dichroic mirror (750nm - long pass) to pass through a 660 nm-band-pass filter. The filtered light is then focused with a lens onto a photo multiplier tube. This imaging setup allows for particle localisation whatever the dopant since all the particles have UCP emissions in this range. After focusing the scan on aggregations

of the particles, the dichroic mirror was removed from the optical path allowing all the backward generated UCP emission and reflected portion of the excitation beam to travel back to the beam splitter polariser then to the spectrometer as explained above. A 150 l/mm gratings was used providing a maximum of 600 nm bandpass range and a spectral resolution of 0.88 nm.

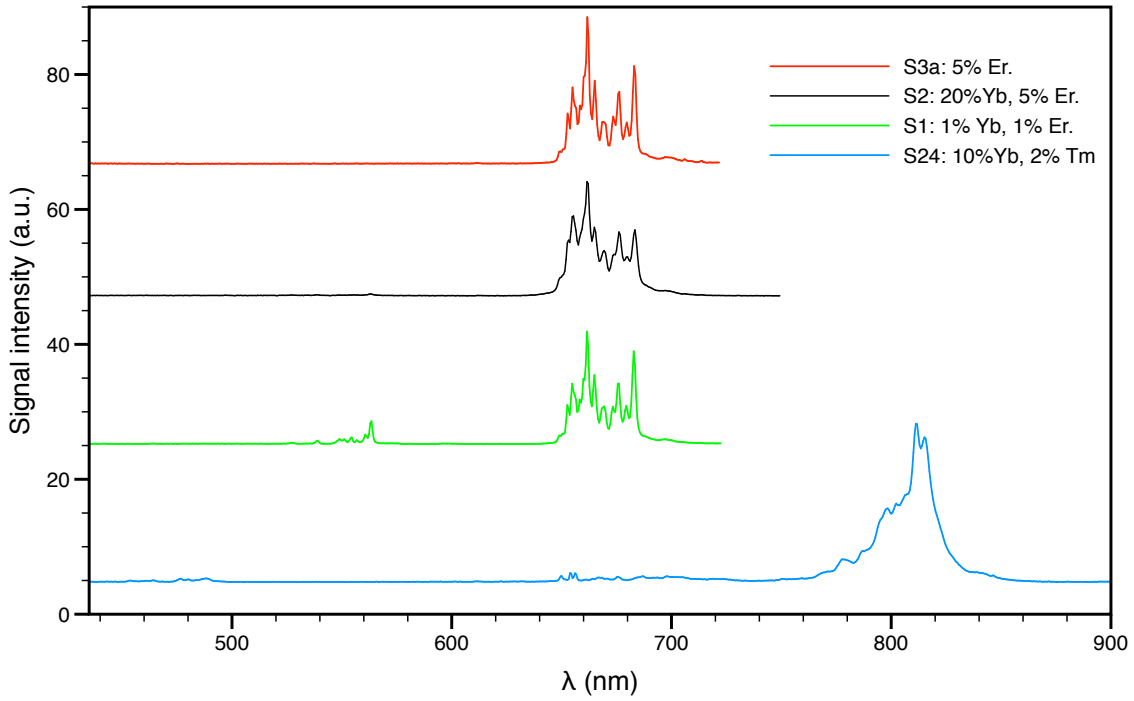

Figure 5.13: UCP of different doped/co-doped gadolinium oxide particles. The figure illustrates the emissions in arbitrary units.

The upconversion photoluminescence spectrum of doped Gd_2O_3 nanoprticles are shown in Figure (5.13). Three samples, each doped or co-doped with one or two of the different doping elements (Yb,Er,Tm), were investigated with different laser excitations and filters. S3a, S2 and S1 were excited with the 816 nm picosecond pulsed laser and a 750nm short-wavelength-pass filter was used. It can be seen from the figure that the three samples exhibit similar red upconversion spectrum. For S3a, which doped with

5% Er, only pure red emission is detected. The other two convert a portion of the near infrared photons into green emission. However, the relative red/green intensities are different.

S24, which is co-doped with 10% Yb and 2% Tm, exhibits efficient upconversion photoluminescence only when excited at the Yb absorption band at 978 nm (shown in Figure.5.21). A 900 nm short-wavelength-pass filter was used to suppress the excitation and a wider range of spectrum was detected. It can be seen that a different spectrum corresponding to the thulium ions was collected. A similar spectrum was reported in previous studies with different host crystals [96, 102, 103]. Only one article reported the upconversion photoluminescence of thulium in a gadolinium oxide host crystal [104]. However, the detected spectrum range was limited to the blue emission (430 nm -510 nm).

It is interesting to study the upconversion spectrum of the particles under the two picosecond excitation beams which are used to acquire CRS images of the biological samples. This is to see how the spectrum would look like in a real imaging experiment where the two excitations are required to obtain CRS images. For this reason the spectrum of all the types of particles were collected under the standard CRS imaging setup (816nm and 1064nm). It was expected that two types of optical emissions would be generated in the focal volume: namely, four wave mixing (FWM) and UC photoluminescence.

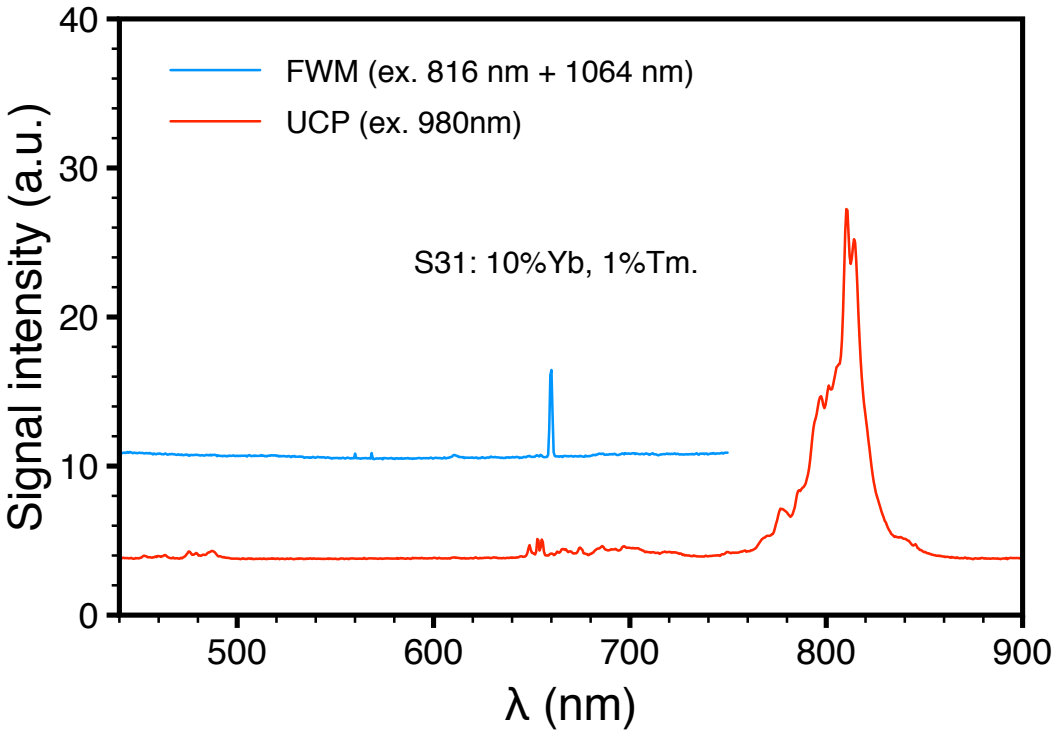

Figure 5.14: The UCP and FWM spectrum of S31. The UCP recorded under 980 nm excitation whereas the FWM was generated by two collinear excitations (816 nm and 1064 nm).

For Er doped particles, the UC photoluminescence was overwhelming and no FWM was detectable. However, for Tm doped particles the FWM process was more noticeable than any upconversion emission (see Figure.5.14). If the 816 nm beam is blocked and only the 1064 nm is used for excitation, there is no detectable upconversion photoluminescence in the Yb,Tm co-doped gadolinium oxide particles whereas if a longer acquisition time (60 seconds) is allowed and an average power of 100 mW is used the red emission can be detected of the Er doped particles(see Figure.5.15). However, this might not be efficient for imaging purposes where a faster scanning rate is required (order of microseconds for one point).

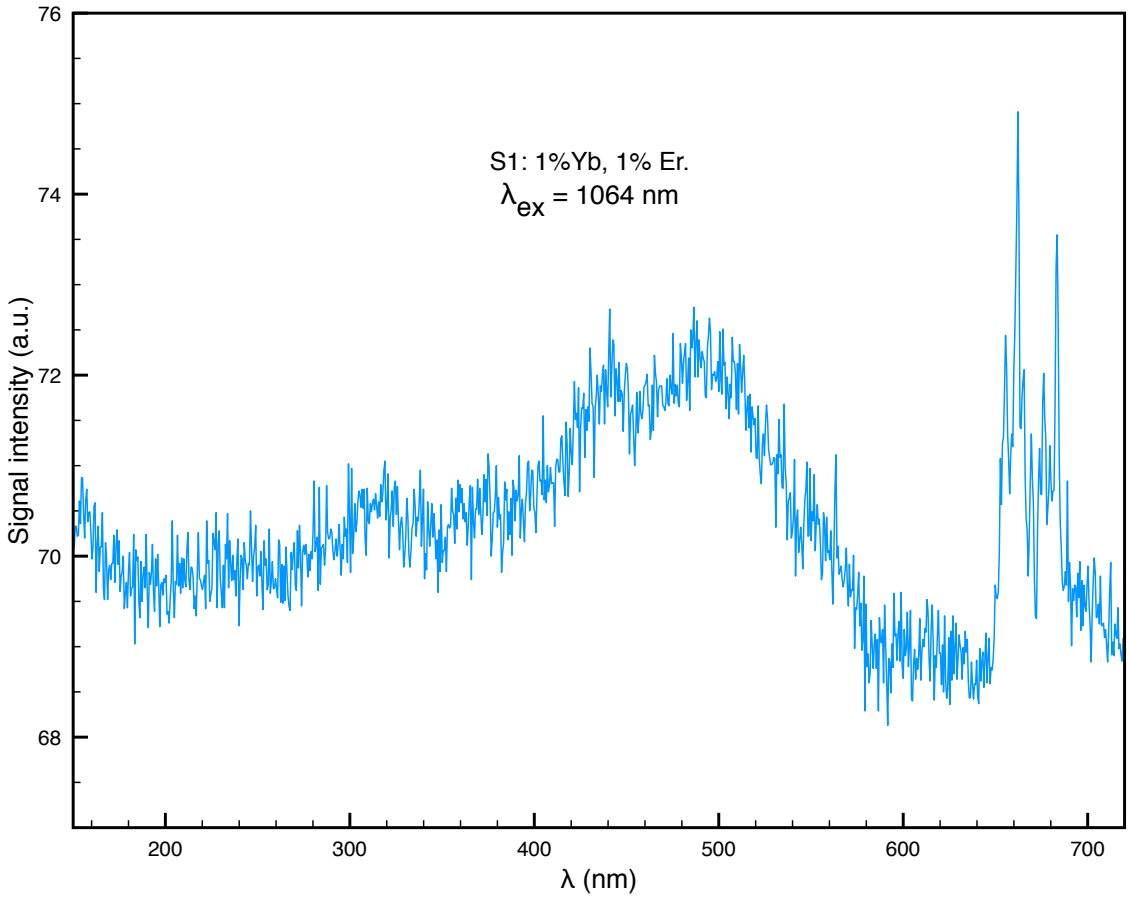

Figure 5.15: UCP of S1 under the 1064 nm excitation at 100 mW. The spectrum was collected over 60 sec.

Also, the spectra were acquired with single excitation either 816 nm or 976 nm for those particles doped with erbium which generate upconversion photoluminescence with the different excitation wavelength. Figure.5.16 shows the spectrum of S30 under the two excitation wavelengths. It can be seen that a change in the relative intensities of the red and green photoluminescence is detected.

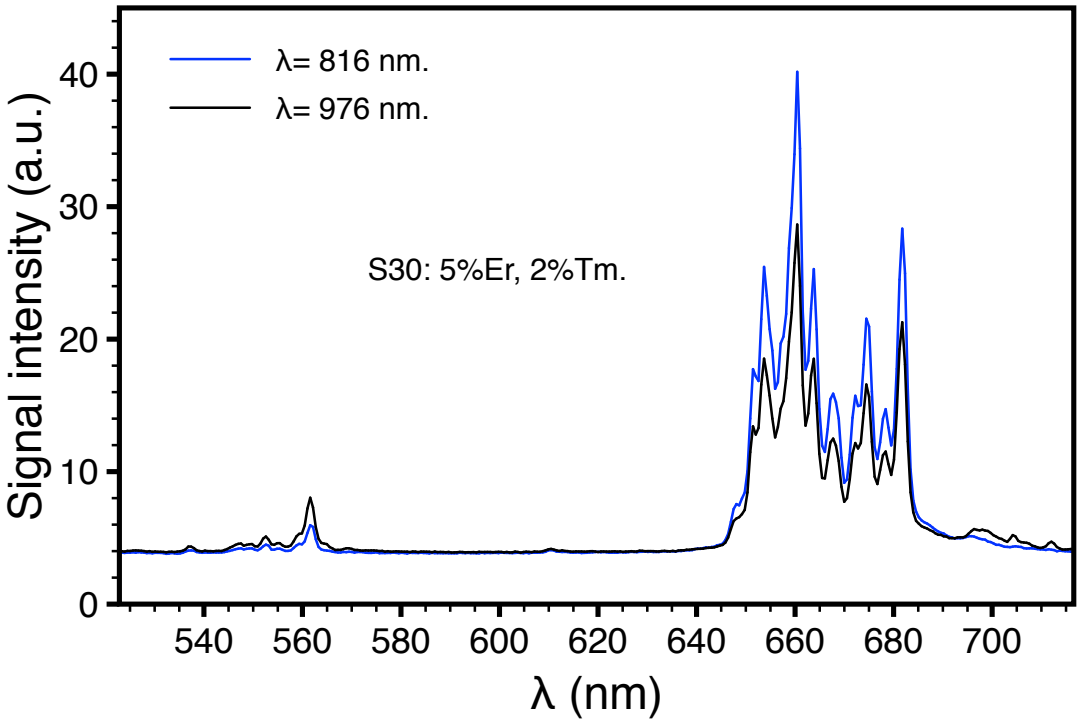

Figure 5.16: The effect of changing excitation wavelength on UC photoluminescence. S30 was illuminated with 816 nm and 976 nm. The relative intensity of the red/green emission are slightly different.

As mentioned above, the relationship between upconversion photoluminescence and excitation power is nonlinear [89, 95, 99–101]. This is a result of the low of conservation of energy since two or more photons are required to generate a higher energy visible photons. However, all the reported techniques used a CW laser. It is of great interest to investigate the power dependency of the UCP in a typical CRS optical system where picosecond pulsed laser combined with high numerical aperture lenses are used.

In order to achieve this, the optical setup mentioned above to collect the UC spectrum was used. However, more considerations were taken into account regarding power. First, the power of the excitation beam was attenuated using a neutral density filter

and measured using a power meter. Second, in order to consider the fluctuations of the power during a scan, the spectral range was extended to cover the excitation peak (a portion of the excitation passes through the filter). Then the intensity of the spectrum was normalised against the intensity of the excitation peak.

Figures.(5.17,5.18,5.19 and 5.22) show the power dependance of the UCP of particles with different dopant types, concentrations and different excitation wavelengths. In Figure.5.17 gadolinium oxide particles doped with 1% Yb and 1% Er were illuminated with a 978 nm picosecond pulse train driven from the signal output of the OPO. The average power of the laser was attenuated and measured as mentioned above to cover the range from 20 mW to 200 mW where the power is measured before the microscope. Although this does not reflect the actual power when the beam is focused by the lens onto the particles, the relation between the two values(power before the microscope and in the focal point) is linear. This is theoretically well established because the percentages of mirror reflectivity and transmission through the lens are independent of power. The strongest peak of each transition band was chosen to study the power dependence. Among the red transition peaks the 662 nm peak was investigated and the 564 nm peak was chosen for the green transitions. It can be seen that for this range of power the relationship between UCP and excitation power is linear. For the same particles a different wavelength (816 nm) was used by changing temperature of the optical parametric crystal of the OPO. Although the 816 nm wavelength is far away from the absorption band of ytterbium, it produces efficient UCP as mentioned above. Figure.5.18 illustrates the behaviour of UCP spectra of S1 under 816 nm excitation of different powers (20 mW to 100 mW). The relation is linear as can be seen in the power Vs intensities plot of the two strongest peaks (564 nm and 662 nm). The same experiment was replicated for S2 which was co-doped with 20% Yb and 5% Er revealing the same linear behaviour (Figure.5.19). Also, particles co-doped with Yb and Tm

were subjected to the power dependence experiment. However, because these particles exhibit less efficient visible UCP when compared to Er doped particles, two preliminary experiments were conducted. The first experiment aimed to find the optimum Tm doping concentration that provides the most efficient UCP. Figure (5.20) shows the spectra of four gadolinium oxide particles samples doped with 10% Yb and different Tm doping concentrations (0.5% , 1% , 2% and 4%). The power was tuned to 100 mW and checked by the power meter before every scan and the spectrum was collected in 1 sec for each sample. Additionally, the spectra were divided by the excitation peak intensities recorded by the spectrometer to consider any possible power fluctuations during the scan. It can be seen that 0.5% Tm is the optimum concentration for the most efficient UCP emission. The second preliminary experiment was conducted to determine the most absorbed wavelength which leads to the strongest UCP. This was done by tuning the excitation wavelength across the range (971 nm - 984 nm) as illustrated in Figure (5.21). The intensity of the 811 nm peak was plotted as a function of wavelength. It can be seen that the UCP efficiency is very sensitive to the excitation wavelength with a maximum emission at 978 nm. According to these two experiments, S24 (10% Yb, 0.5% Tm) was illuminated with 978 nm and the spectrum of the particles was recorded at different laser powers (see Figure.5.22). The intensities of the strongest peaks (486 nm and 689 nm) from the blue and the red transmissions were plotted as a function of power. Also, it can be seen that the intensity is linearly proportional to laser power.

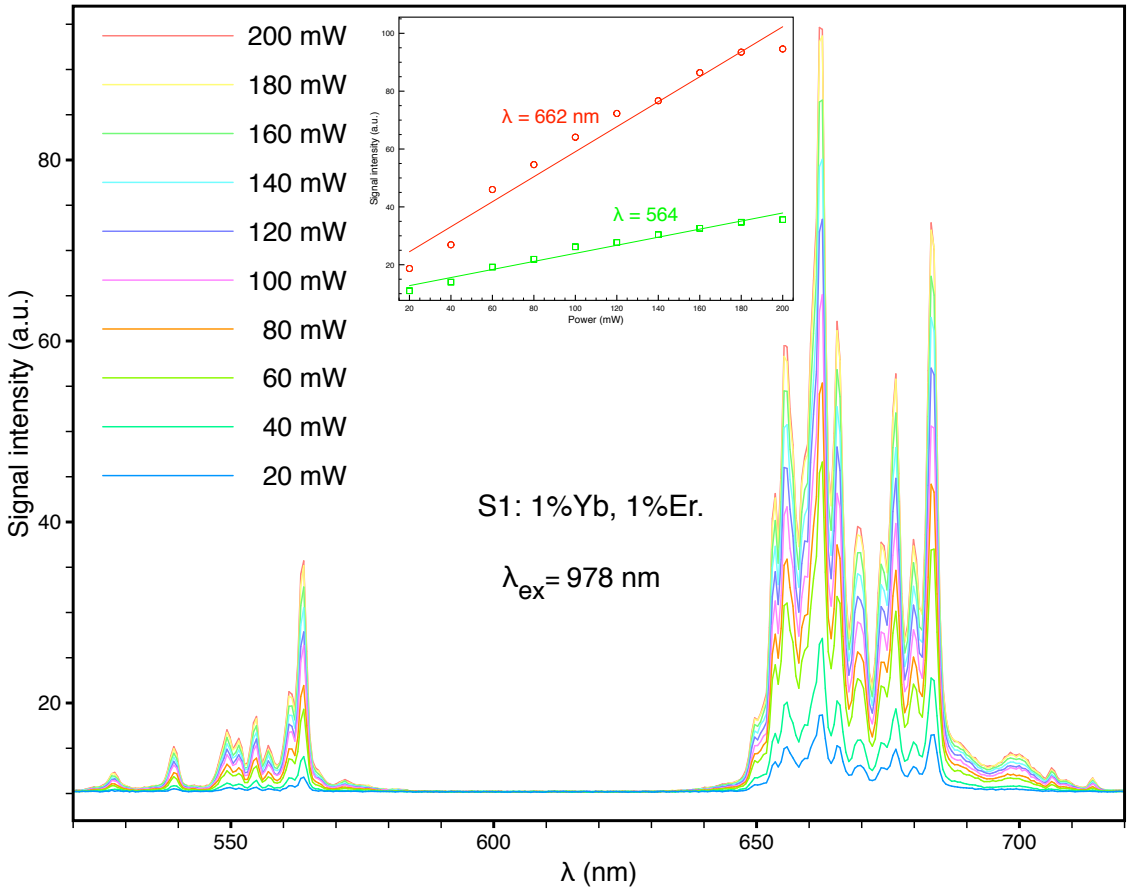

Figure 5.17: UCP power dependence of S1 under the 978 nm excitation of the range of powers (20 - 200 mW). The plot of power Vs intensities of the two peaks (662 nm and 564 nm) shows linear relation.

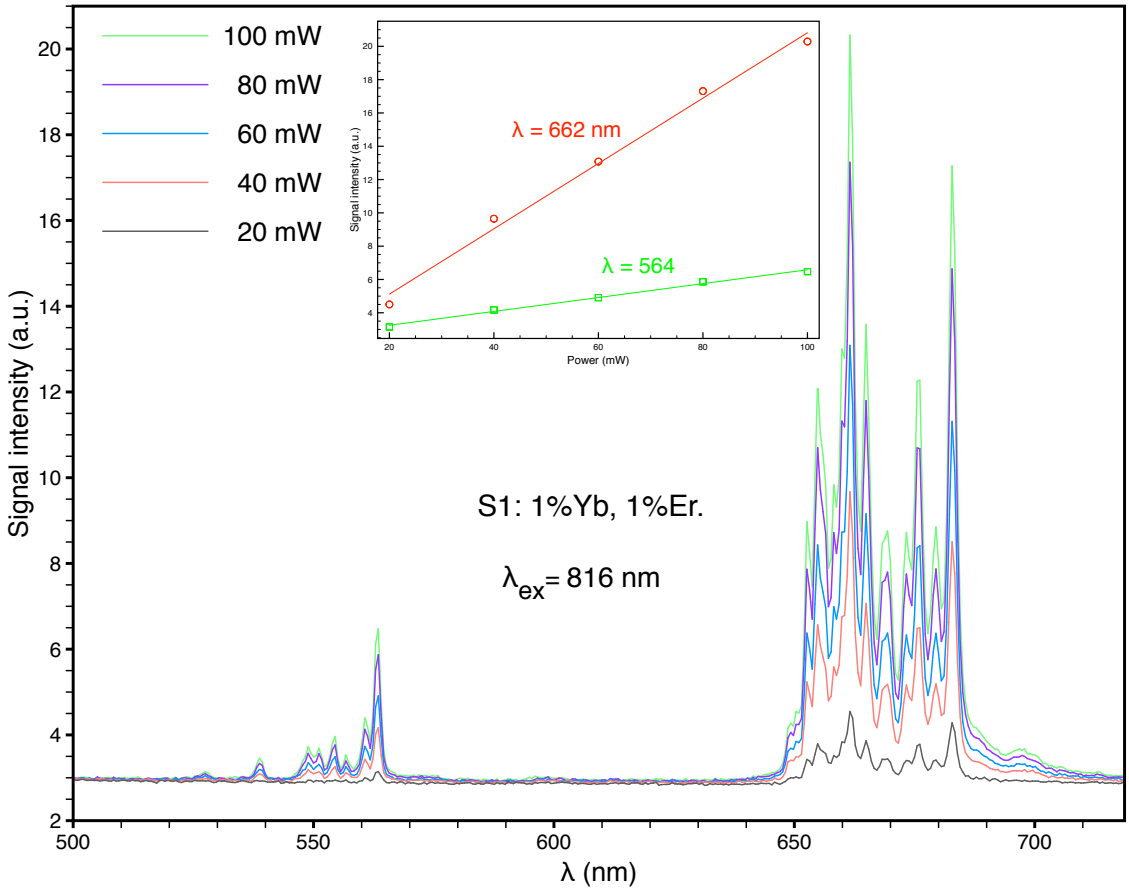

Figure 5.18: UCP power dependence of S1 under the 816 nm excitation of the range of powers (20 - 100 mW). The plot of power Vs intensities of the two peaks (662 nm and 564 nm) shows linear relation.

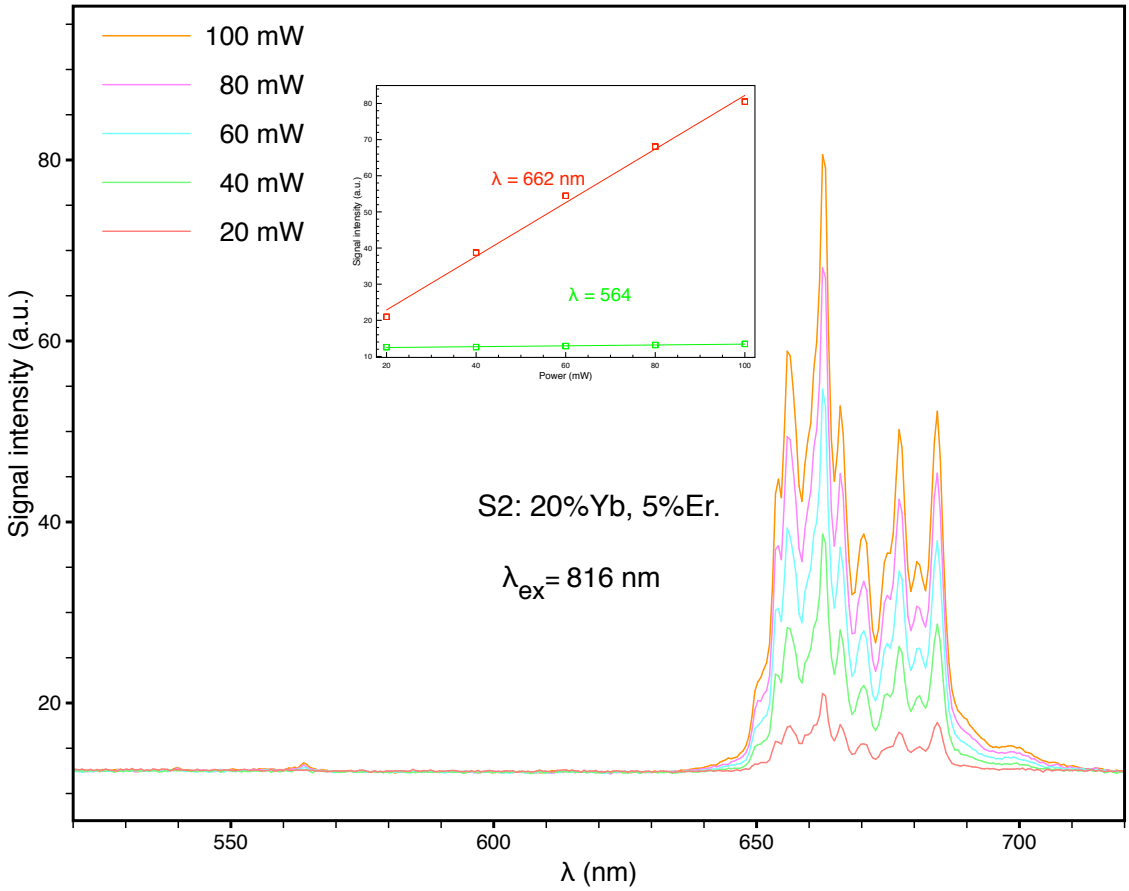

Figure 5.19: UCP power dependence of S2 under the 816 nm excitation of the range of powers (20 - 100 mW). The plot of power Vs intensities of the two peaks (662 nm and 564 nm) shows linear relation.

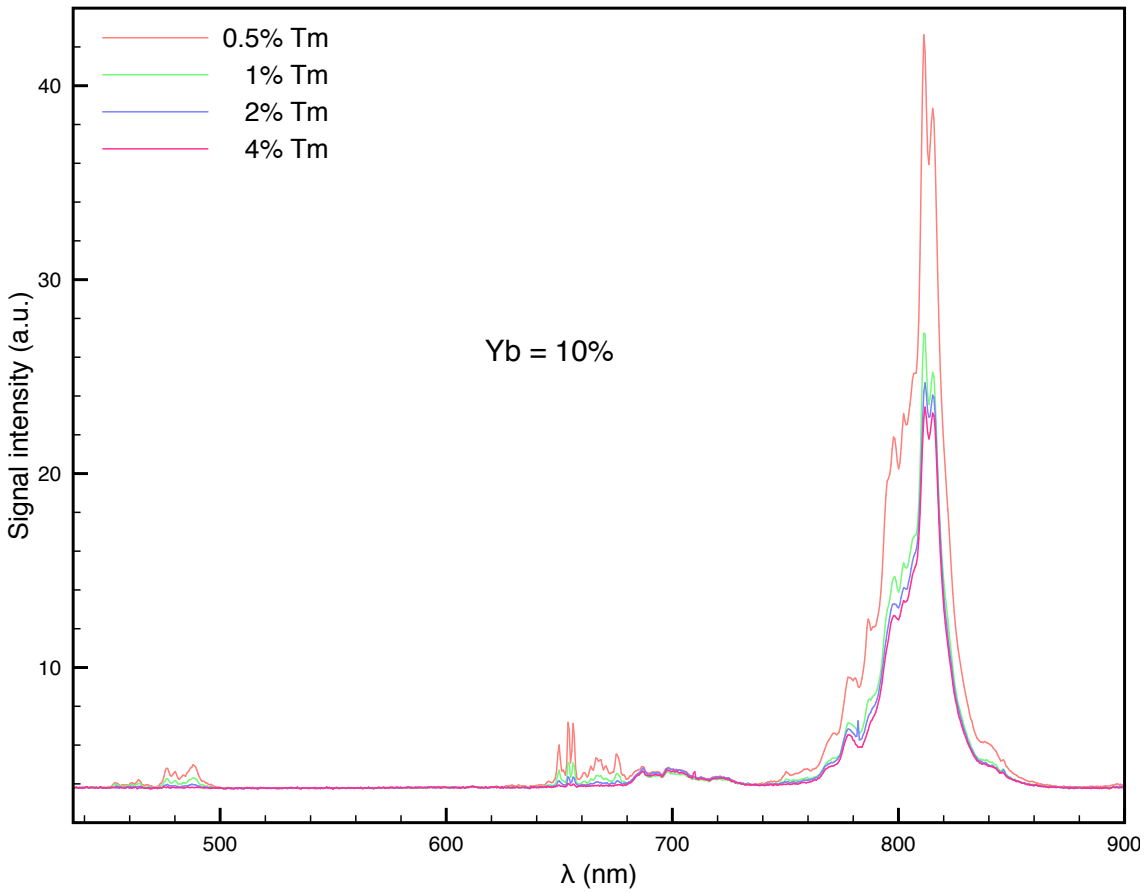

Figure 5.20: UCP of gadolinium oxide particles co-doped with 10% Yb and different Tm concentrations (0.5%, 1%, 2% and 4%) under a 980 nm picosecond pulsed laser excitation.

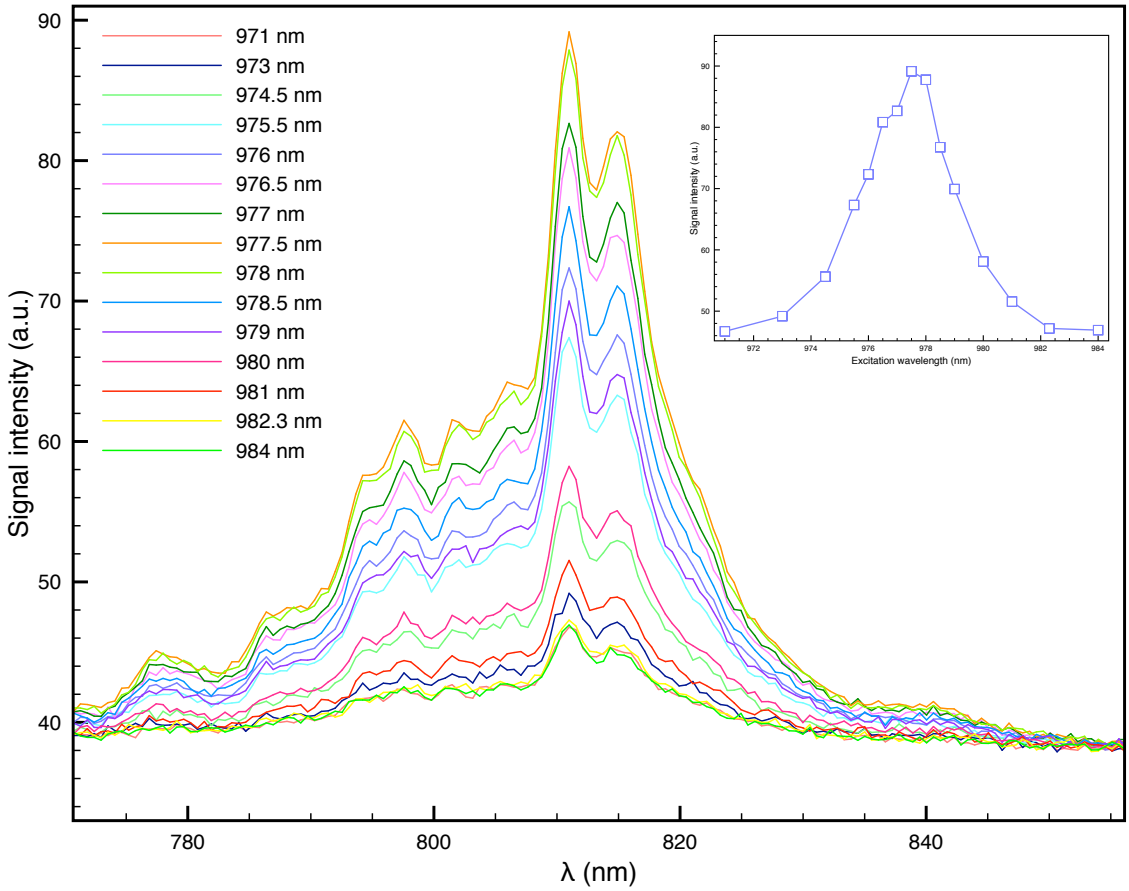

Figure 5.21: The 811 nm UCP of S24 under constant 100 mW power and range of excitation wavelengths (971 nm - 984 nm). The plot of wavelength vs normalised intensity shows an optimum excitation wavelength of 978 nm.

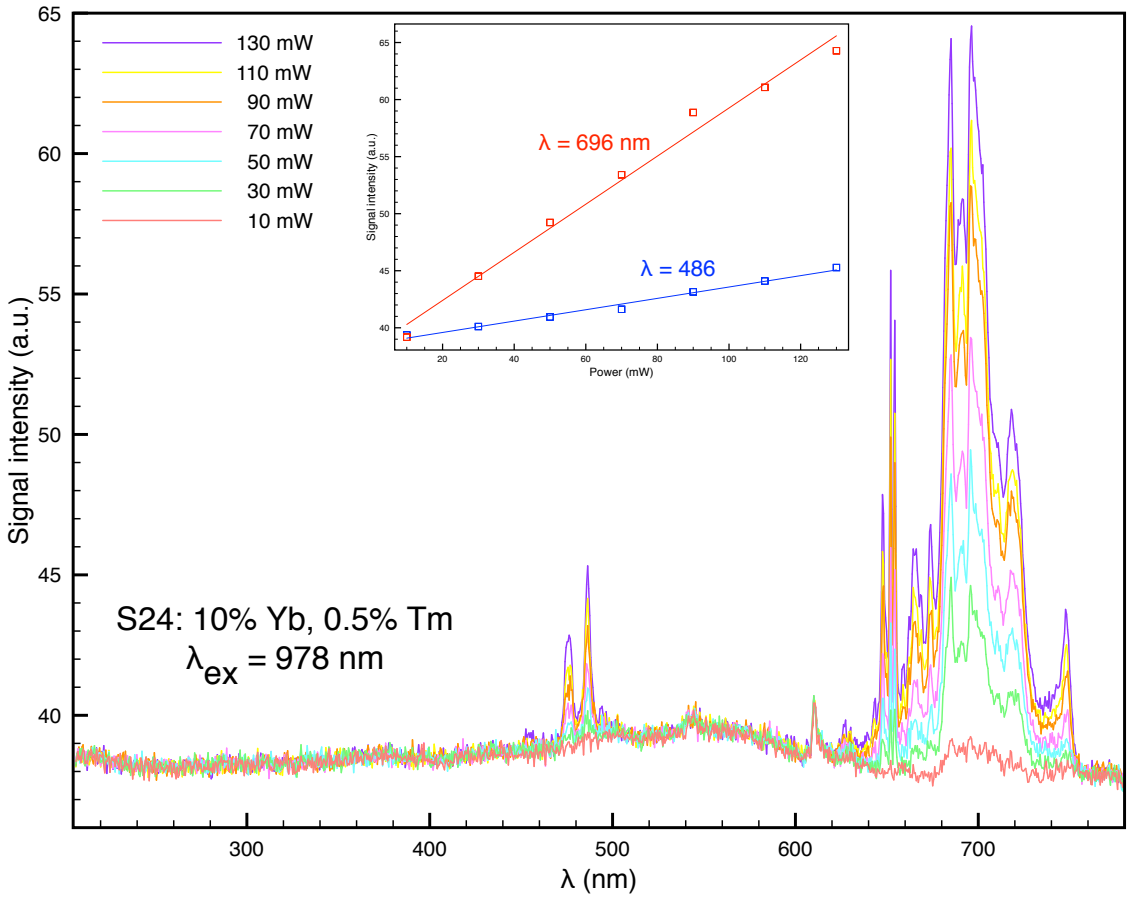

Figure 5.22: UCP power dependence of S24 under the 978 nm excitation of the range of powers (10 - 130 mW). The plot of power Vs intensities of the two peaks (696 nm and 486 nm) shows linear relation.

It has been found from the experiments that gadolinium oxide particles doped with erbium (Er) generate efficient upconversion emission even if the excitation is tuned to a wavelength far from the absorption band of the ytterbium at 980 nm. This is an interesting observation for CRS imaging purposes where an 816 nm laser beam is used as a pump. Also, the upconversion emission for this type of particle is not sensitive to the excitation wavelength. This is beneficial when using other laser setups or when conducting CRS spectral experiment where the excitation beam is tuned over a range of wavelengths, hence particle can be imaged simultaneously.

5.7 Magnetic relaxivity

As mentioned in Chapter1, well established MRI contrast elements (namely gadolinium and iron) were used in this study. In fact, Gadolinium is used clinically and administered to humans in the form of diethylene triamine pentaacetic acid (DTPA) complexes [105]. However, such a solution is not appropriate for optical contrast where more condensed matter is required for high sensitivity detection. The nanoparticle forms of gadolinium oxide and iron oxide have been used widely in the literature as MRI contrast agents [80]. In most of these studies, small particle size (not larger than 30 nm) was adopted to enhance both longitudinal and transverse relaxivities as a result of maximising the surface to volume ratio. However, the particles used for this study are chosen to be much larger than this range to be optically detectable. This raises concerns about the effect of the particle size on its relaxivity. Fortunately, for iron oxide nanoparticles, Hinds and coworkers proved that micro-sized iron oxide particles are even more efficient than those of nano-size [106]. This reduces the particle size investigation to gadolinium oxide nanoparticles because there is no previous study in which longitudinal relaxivity of these particles of 100 nm size-range was measured. Accordingly, the aim of this section is to measure the relaxivity of our relatively large gadolinium oxide particles to ensure that the size is still providing appropriate relaxivity even with their small surface to volume ratio.

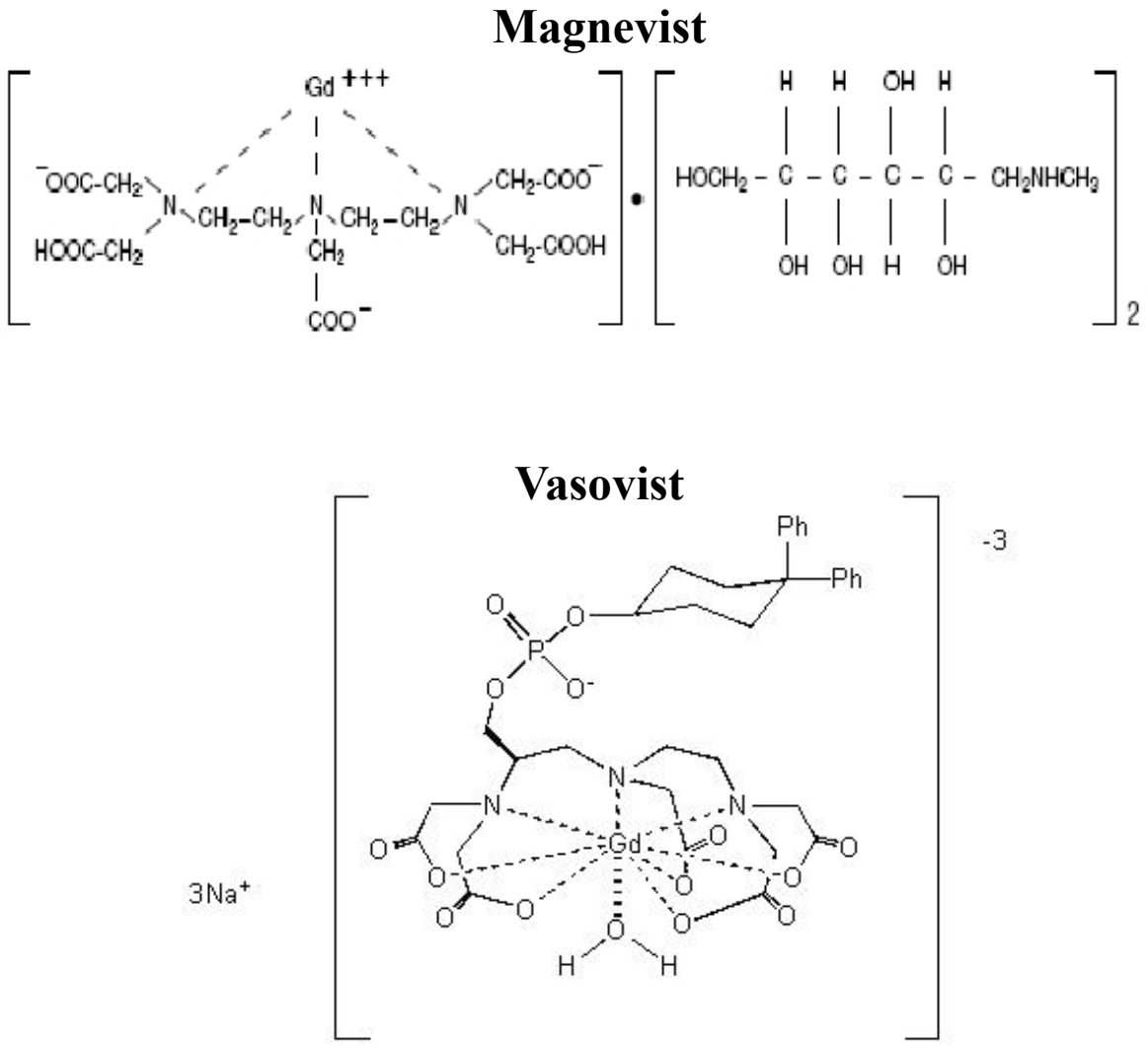

Figure 5.23: The molecular structures of Magnevist and Vasovist.

In seeking to develop the technique of measuring longitudinal relaxivities for an MRI contrast agent well known gadolinium based complexes Magnevist and Vasovist were used as test agents. They are water soluble complexes with the molocular structures illustrated in Fig.5.23. Magnevist and Vasovist are available with gadolinium concentration of 0.5 mol/L and 1.0 mol/L respectively. The original solutions were diluted to lower concentrations by adding distilled water. The concentrations used for these experiments are 0.2, 0.4, 0.6, 0.8, 1.0, 1.2, 1.4, 1.6, 1.8 and 2.0 mM. The different con-

centrations of the two contrast agent solutions were transferred into glass containers and placed in the center of the MRI coil. A fast T_1 imaging sequence was used to localised the samples in the scanner. This was followed by applying inversion recovery sequence with a relatively long repetition time (10^4 ms) and different inversion times (50,100,200, 500, 1000, 1500, and 2000 ms). Seven images of the samples were acquired as shown in Fig.5.24 (b-h) with a sketch illustrating the arrangements of the samples(a). The images were collected in one stack in the order of the inversion time using ImageJ software, then, a z-profile was generated for each concentration. The z-profile corresponds to the grey scale value of each concentration in the image at different inversion time. However, it is important to mention that although the magnetisation is a vector quantity which might take positive or negative directions, the image grey scale value is always positive. Accordingly, negative signs were added to some grey scale values so the curves patterns are matched the theory (see Section (2.2.9)). The signal intensity was plotted versus inversion time for each concentration and curve fitted to Equation2.20 as shown in Figure5.25. The constants in the equation (M_0 and T_1 were retrieved from the curve fitting calculations. Plotting concentrations vs $1/T_1$, the longitudinal relaxivity can be obtained by curve fitting the data to Equation2.22 where the slope is the relaxivity. The relaxivities of Magnevist and Vasovist were found to be 4.56 $s^{-1}mM^{-1}$ and 6.80 $s^{-1}mM^{-1}$ respectively. For the same conditions, the relaxivity values match those reported in the literature for both Magnevist [81] and Vasovist [105].

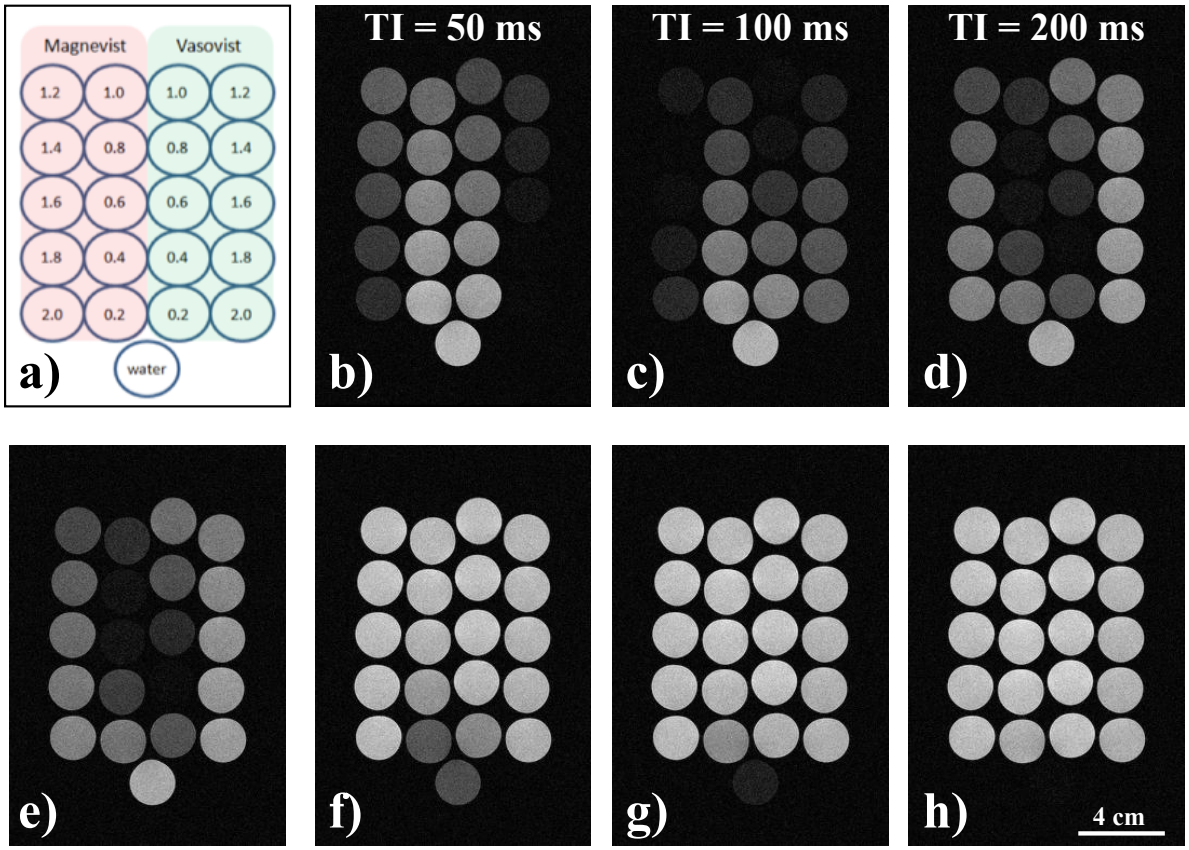

Figure 5.24: The samples arrangements (a) and inversion recovery images (b-h) of different concentrations of the clinically used contrast agents Magnevist and Vasovist at different inversion times as illustrated on the images.

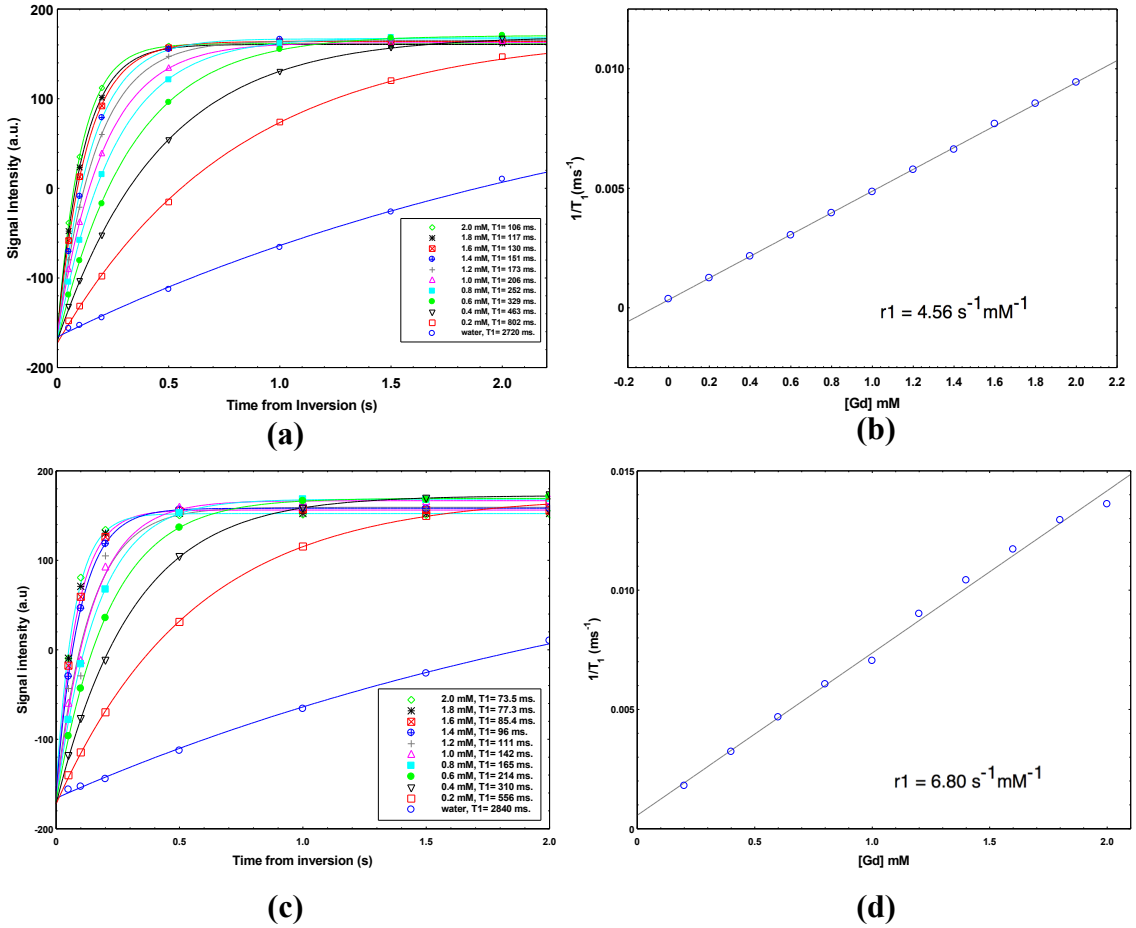

Figure 5.25: The longitudinal relaxivity measurements of Magnevist (a and b) and Vasovist (c and d). The plots of signal intensity versus inversion recovery time are shown in figures (a and c), where the symbols represent the data points and the solid lines are the curve fits of the different concentrations as illustrated in the legends. The plots of $1/T_1$ as a function of gadolinium ions concentrations are shown in figures (b and d).

The above measurements were carried out using water as a solvent for the water soluble Gd-based contrast agents. However, the large nanoparticles used for this study do not suspend in water. It was noticed that they gradually settle at the bottom of the container which makes the concentration change with time. The proposed alternative was to use agarose gel to maintain constant concentration of the particles during the

MRI experiment. However, it was necessary to insure that replacing water with gel did not significantly affect the T_1. Accordingly, Magnevist samples were prepared with different concentrations (0, 0.2, 0.4, 0.6, 0.8, 1.0, and 1.2 mM) in water and 0.5 w/w agarose gel. The samples were placed in the MRI scanner and a T_1-weighted imaging sequence with TR/TE = 20/16 ms was applied. The head coil was used to achieve better signal to noise ratio. The resultant image was then opened in ImageJ software where the signal intensity and standard deviation of each sample were obtained.

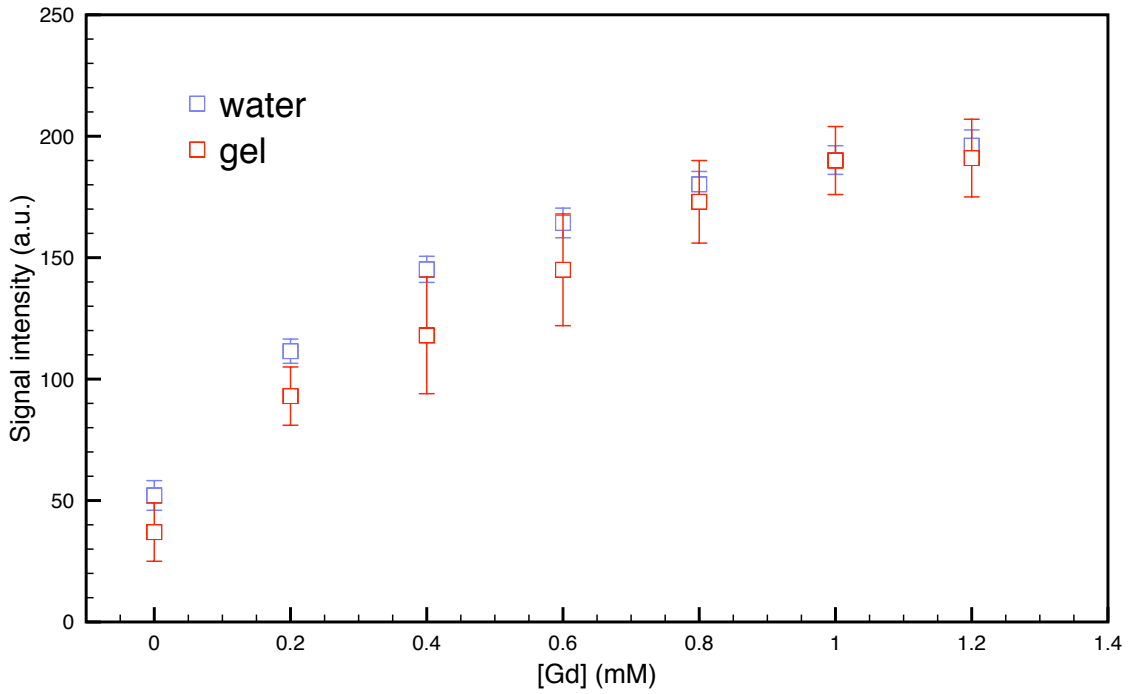

Figure 5.26: The signal intensity of a T_1-weighted image of different concentrations of gadolinium ions (Magnevist) in water and gel.

Figure5.26 shows the plot of gadolinium ions concentrations vs signal intensity of water and gel samples. The error bars are the standard deviation values and they are greater in gel samples than those of water because of the inhomogeneity of the gel. It can be seen that the two sets of data have no remarkable difference and with overlapping

error bars. This suggest that it is possible to compare relaxivity measurements of particles in gel with the reported relaxivity of other contrast material in water.

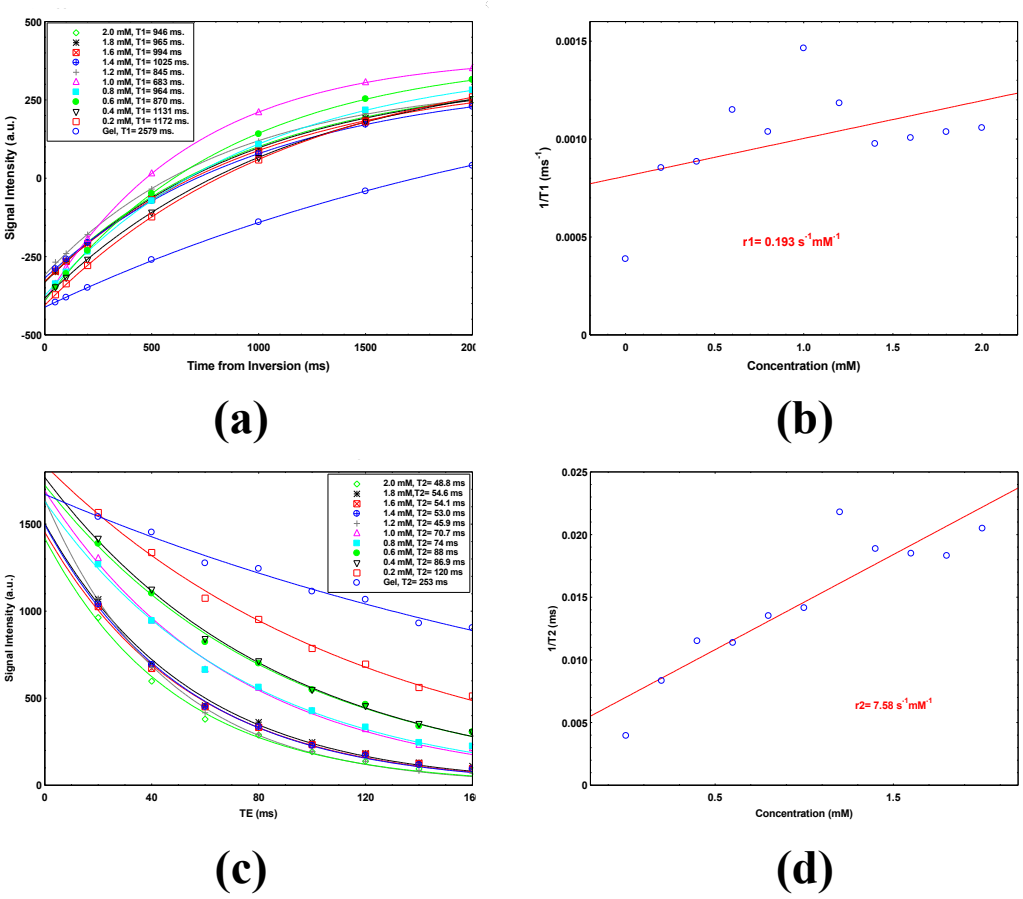

Figure 5.27: Relaxivity measurements of 100 nm gadolinium oxide particles in gel. a) is the inversion recovery curves and (b) is the longitudinal relaxivity of the particles. Figure (c) is the decay curves at different TE and (d) is the transverse rlaxivity.

The gadolinium oxide nanoparticles (100 nm) were purchased from Sigma Aldrich,UK. In order to prepare different concentrations of the particles, 29 mg of powder was added to 20 mL of distilled water which results in 4 mM of the gadolinium ions. The mixture was then sonicated for 30 min and diluted into smaller concentrations by adding (1 mL, 900 μL, 800 μL, 700 μL, 600 μL, ...,100 μL) of the original mixture to (0 mL, 100

μL, 200 μL, 300 μL, 400 μL, ...,900 μL) respectively. The resultant mixtures are 1 mL each with gadolinium concentrations of (4 mM, 3.6 mM, 3.2 mM, 2.8 mM, 2.4 mM, ..., 0.4 mM). Then, 1 mL of 1 % gel was added to each container and mixed until white foggy colour is achieved, then the containers are cooled down in an ice bath to conserve the uniform particle distribution. The longitudinal relaxivity measurements were acquired using the same inversion recovery sequence and ImageJ software procedures described above. The results are showed in Figure(5.27,a and b). It can be seen that the data points are widely scattered around the fitting straight line and a very low longitudinal relaxivity was obtained. To understand the possible reason the transverse measurements were also acquired for the same samples. A set of T_2-weighted spin echo images were acquired with a TR= 3000 ms and different echoes at (20, 40, 60, ..., 140, and 160 ms). The eight images were collected in a stack and z-profile of the signal intensity for each concentration. The z-profile data represent the signal intensities at the different echoes. In Figure(5.27,c) the data points are the experimental data of the signal intensity as a function of echo time whereas the solid lines are the curve fits of the data to Equation2.18. From the curve fit, the T_2 of each concentration is obtained as marked in the legends. Figure(5.27,d) shows the plot of $1/T_2$ as a function of concentration from which the transverse relaxivity was calculated by curve fitting the data to Equation2.20. It can be noticed that the data points of the transverse relaxivity in Figure(5.27,d) seem to obey the straight line better that those in the longitudinal relaxivity data points in Figure(5.27,b). Also, the transverse relaxivity is more significant than the longitudinal one. This might be a result of particle aggregation. The aggregation seems to affect r1 (longitudinal relaxivity) more than r2 (transverse rlaxivity) because T_2 can be altered by the magnetic contrast agents in a long range manner [10] whereas direct contact between the protons and the paramagnetic material is required if T_1 contrast is desired [21] . That explains also why in shell-core particles T_2 based contrast material

is placed inside the core and for the shell a T_1 based contrast material is chosen [107].

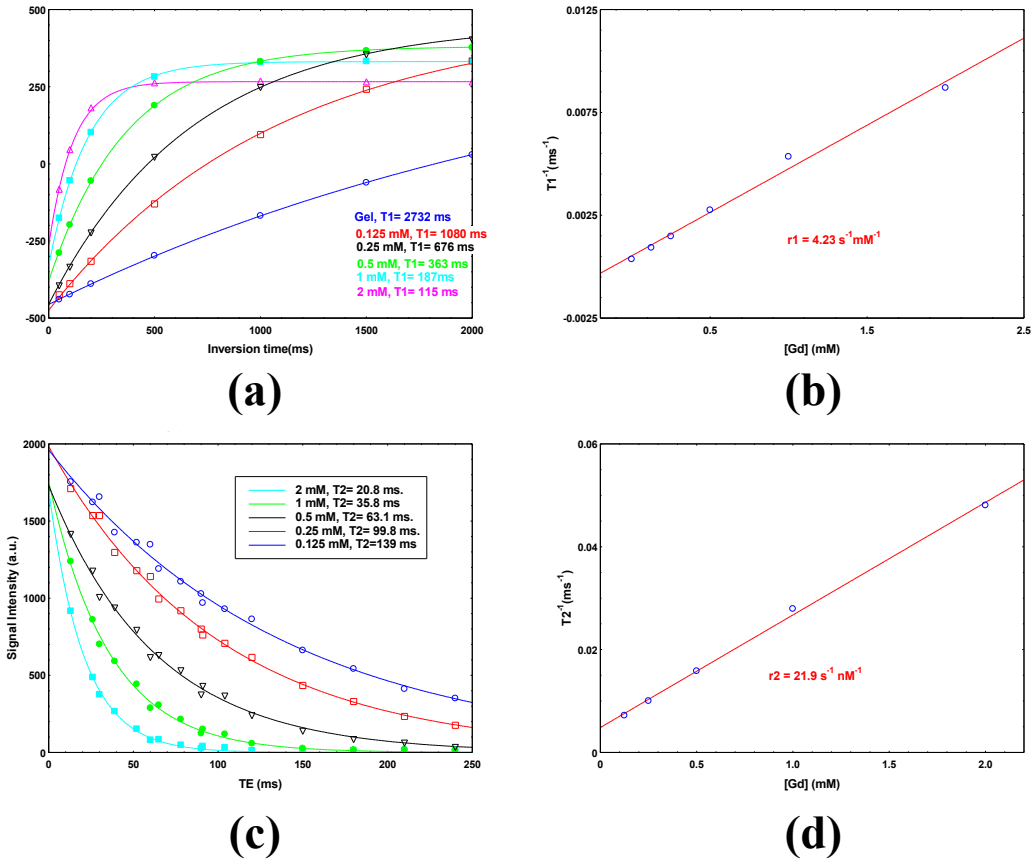

Figure 5.28: A replication of the data in Figure.5.27 with a better particle distribution and less aggregations.

In order to overcome the aggregation problem, a commercially available dispersing agent (DISPERBYK-190) was used in 1 % w/w concentration as described in reference [108]. The samples were prepared again in a similar way to the method mentioned above except that the dispersing agent was added to the Gd_2O_3-water mixture before sonication. Also, only five concentrations of gadolinium ions were prepared this time (2, 1, 0.5, 0.25, 0.125 mM). The same MRI sequences and ImageJ analysis were applied to obtain the relaxivity measurements of the laterally prepared samples (See Figure5.28).

It can be seen that the exponential recovery and decay curves of different concentrations in the inversion recovery (Fig.5.28,a) and spin echo (Fig.5.28,c) have different gradient which are the theoretically expected behaviour (as in Eq.2.20 and Eq.2.18). Consequently, better straight line fit was achieve for both longitudinal(Fig.5.28,b) and transverse (Fig.5.28,d) relaxivities. Moreover, and most importantly, the longitudinal relaxivity of the relatively large gadolinium oxide nanoparticles (100 nm) is found to be similar to those calculated for clinically used complexes. This result allow us to confidently propose these particles for the multi-modal imaging approach suggested in this study. Also, for the scientific community, it might be interesting to know for the first time that this size of gadolinium oxide nanoparticles work efficiently as T_1 contrast agents in the widely available 1.5 T clinical scanner.

5.8 Summary

In this chapter the structural, morphological, optical, and magnetic properties of the nanoparticles were characterised. The composition materials and doping of gadolinium oxide nanoparticles were confirmed by X-ray energy dispersive spectroscopy. Also, XRD spectrum confirmed the crystalline structure which is vital for the particles to expose photoluminescence properties and provided another evidence confirming the composition of the materials. The morphology of the particles were inspected using SEM and TEM. It was found that Gd_2O_3 nanoparticles form in a spherical shape whereas a cubic shape is obtained when synthesising iron oxide nanoparticles with a tuneable particle-size for both types. Both synthesising methods, homogenous precipitation and hydrothermal, provided acceptable level of size monodispersity which cloud potentially improved if surfactants are used. The photoluminescence properties of the particles were studied using a compact Raman micro-spectrometer equipped with two excitation

CW lasers (532 nm and 785 nm). An extended range of PL spectrum was recorded for particles doped or co-doped with different rare earth ions (Yb, Er, Tm). It was found that efficient photoluminescence is detected even when using low power, minute particle concentration and less magnification lens. The efficient photoluminescence emission also confirms the successful doping and the crystalline structure. The UC photoluminescence spectrum of doped gadolinium oxide nanoparticles were investigated for the first time under a pulsed laser excitation and high numerical aperture lenses, a typical optical setup of acquiring CRS images of biological structures. The UCP dependence upon laser power, excitation wavelength, and doping concentration was investigated. The most interesting observation is that gadolinium oxide nanoparticles doped with Er provide a strong UCP in the whole available range of excitation wavelength. Although UCP is recognised as a nonlinear process the relationship between the laser power and signal intensity was found to be linear due to a saturation effect. To ensure that gadolinium oxide particles exhibit acceptable longitudinal relaxivity with their relatively large size (100 nm), they were subjected to MRI relaxivity measurements in a 1.5 T scanner. It was found that the relaxivity of the particles is comparable to clinically used contrast agents.

Chapter 6

Nanoparticle optical imaging

6.1 Introduction

Multi-functional nanoparticles have been used widely in recent years for multi-modal imaging, targeted drug delivery, gene therapy and photodynamic therapy (the reader is referred to articles [109–112]). Multi-modal imaging is desirable for its capability in assisting the efficiency and credibility of the under-investigation therapeutic methods in different imaging scales and contrasts. The multi-modal nanoparticles investigated in this study are required to possess optical and magnetic properties that allow the combination of the advantages of large scale 3D MR imaging and the high resolution CARS microscopy to image particles in biological tissue at the cellular scale. In MRI there are two main types of contrast particles, longitudinal (T_1 based contrast agents) and transverse (T_2 based contrast agent). Each type has its own advantages and applications to target specific kinds of organs and tissue. For this reason two types of particles with T_1 and T_2 contrast are investigated.

Among the multi-modal imaging nanostructures, fluorescent dye-coated iron oxide nanoparticles and lanthanide doped gadolinium oxide particles have been imaged with

MRI and optical imaging techniques for their magnetic and optical properties [113] [114]. Both types of particles have unpaired electrons in their outer shell of iron and gadolinium providing them with the paramagnetic properties that alter both T_1 and T_2 of the biological tissue. However, iron oxide nanoparticles and gadolinium oxide nanoparticles are considered as T_2 and T_1 based contrast agents respectively for the ratios of their longitudinal and transverse relaxivities.

The optical contrast of iron oxide nanoparticles is gained by a dye coating material which allows fluorescent imaging with conventional laser scanning confocal microscopy [113] [114] [20] [15]. In these studies the contrast of the living cells was achieved with different fluorescent dye staining, transmitted light or labeled with the particles themselves.

The doped gadolinium oxides nano-structures pose optical properties for the 4f transitions that occur in doping lanthanide ions either with normal photoluminescence or up-conversion photoluminescence. A number of previous studies utilised the photoluminescence properties of doped gadolinium oxide nanoparticles for confocal microscopy imaging. This was demonstrated using blue or ultra violet excitation and detecting longer wavelength light emitted by the nano-structures [19] [115]. The upconversion process was adopted in imaging in two different methods, whole animal infrared imaging and confocal microscopy. The whole animal infrared imaging was carried out using 980 nm excitation laser and a filter fitted to a CCD camera to detect the shorter wave length emitted by the nanoparticles in a dark room. The image is merged with another white light image of the animal taken with the same camera from the same position to assign the particle location to the animal body [116] [8]. The upconversion photoluminescence (UCL) confocal microscopy was developed by utilising the same excitation laser in a confocal microscopy setup to image the particles in a high resolution 3D manner in the biological context [110, 112].

As mentioned before, CARS microscopy has several key advantages when compared to the conventional confocal microscopy. For this reason there is interest to develop a technique that images these magnetic particles with CARS microscopy systems. This imaging technique should provide different contrast of the particles so they can be imaged and localised in 3D within the biological contents of the tissue at cellular resolution. There is only one previous study that payed attention to this demand. This was carried by Rago and coworkers in 2011 who studied the possibility of visualising micrometer-sized iron oxide particles with FWM [30], however, such particle size is not suitable for drug delivery applications.

In this Chapter, armed with the spectroscopic data from the previous chapter, the possible imaging techniques that can be used to image iron oxide and lanthanide doped gadolinium oxide nanoparticles in CRS microscopy systems are explored. Moreover, the particles will be imaged within a stable biological model sample (starch) to show the possibility of obtaining distinguishable contrast. Starch is an appropriate biological model sample for its strong CH_2 Raman signal which is similar to lipids in living cells.

6.2 Confocal imaging

The novel optical properties of doped gadolinium oxide nanoparticles allow imaging them with a conventional confocal microscope. Several groups have already investigated this. The imaging is carried out in two different methods either using photouminescenc or upconversion photoluminescence. The former is achieved by detecting the visible emissions after exciting the particles with a shorter wavelength laser, whereas, an infrared excitation is used in the latter. However, there was no evidence in these studies that single particles can be detected. When particles suspended in solution they usually aggregate and form larger structures. The aim of this section is to explore the applicabil-

ity of the particles when imaged with confocal microscope via their photoluminescence properties.

As mentioned earlier, a uniform 2D distribution of the nanoparticles was achieved by spin coating them on glass coverslips. This was confirmed with scanning electron microscope(SEM) and example images are given in Figure (6.1). Four images of different magnifications of S3a are presented (scale bars provided). It can be seen from the images that, although there are aggregations of the particles, the overwhelming number of the particles are found singles and separated by more than 300 nm in 2D distribution. Also, similar 2D distributions were achieved repeatedly with different types of particles with high reproducibility.

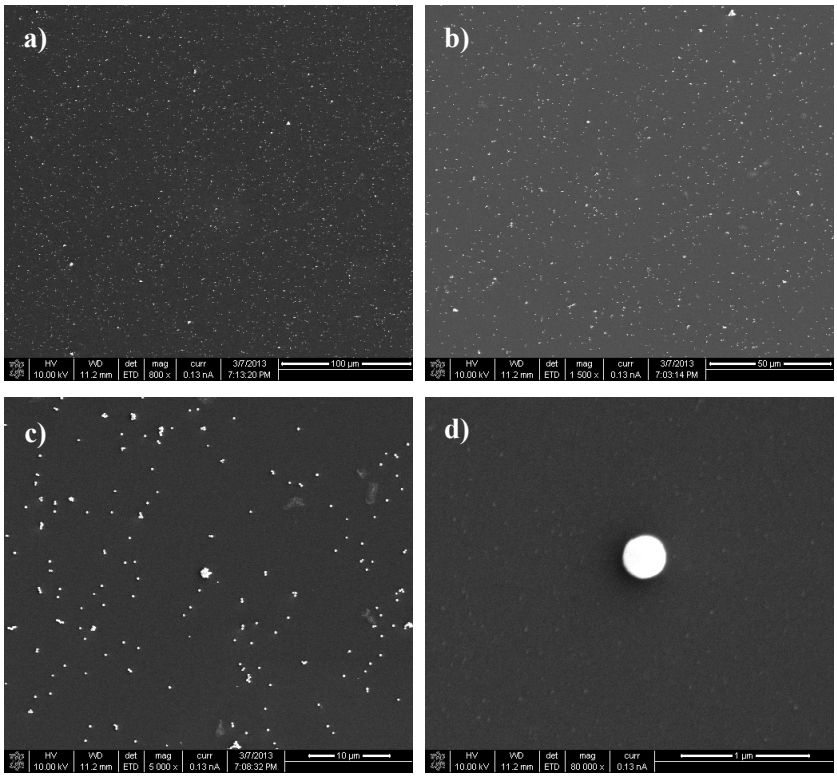

Figure 6.1: SEM of sample 3a.

In the confocal microscope, an excitation of blue argon CW laser was used. The objective was a 63X oil immersion lens and two magnifications of the images were

used. Three channels recorded the images with different contrasts, two for detecting the photoluminescence spectrum in which tuneable filters was set up to cover specific ranges and the third channel used to acquire the transmission light. Figure(6.2) shows six images of the nanoparticles(S2). The images on the right hand side are of 10x magnification whereas the images on the left correspond to 2x magnification. Images (a and b) are acquired with the first channel covering a spectral range of 500-600 nm. The spectral range 600-700 nm, was acquired and presented with images (c and d). Finally, images (e and f) recorded the transmitted light.

These images of the doped gadolinium oxide particles were acquired by detecting the photoluminescence emissions as illustrated in Figure(6.3). The emissions detected by CH1 are due to the transitions from $^4S_{3/2}$ and $^2H_{11/2}$ to $^4I_{15/2}$ whereas CH2 recorded the red emissions between $^4F_{9/2}$ and $^4I_{15/2}$ [95]. It is clear that the intensity of the particles in Figure(6.2 a and b) are brighter than those of Figure(6.2 c and d). This is a result of the relative difference of the intensities of the two spectra (see Figure(6.3)) as well as the wavelength detection dependence of the PMTs.

In Figure(6.4) three images of S22b are presented. The first image was acquired by detecting the green emission (500-600nm) and the second image is the transmitted light. The third image is an image of merging the two channels. It is clear that the signal of the particles located in the centres of the circular patterns observed from the transmission channel. Combining this with our previous knowledge about particles distribution formed by spin coating and confirmed by SEM, it can be concluded that imaging single particle was achieved.

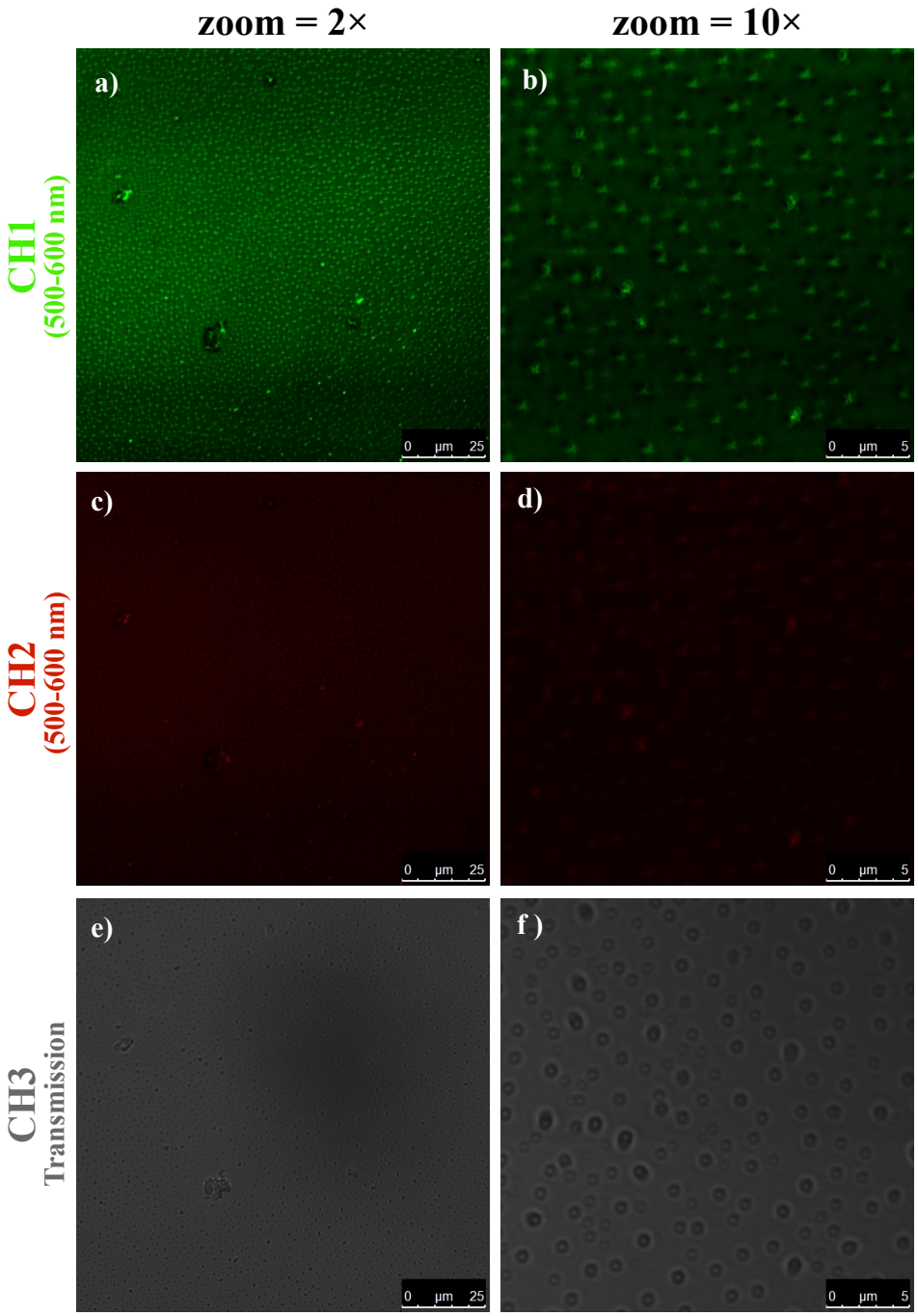

Figure 6.2: Confocal microscopy images of S2 particles at different zoom and detection spectra as labeled on the images.

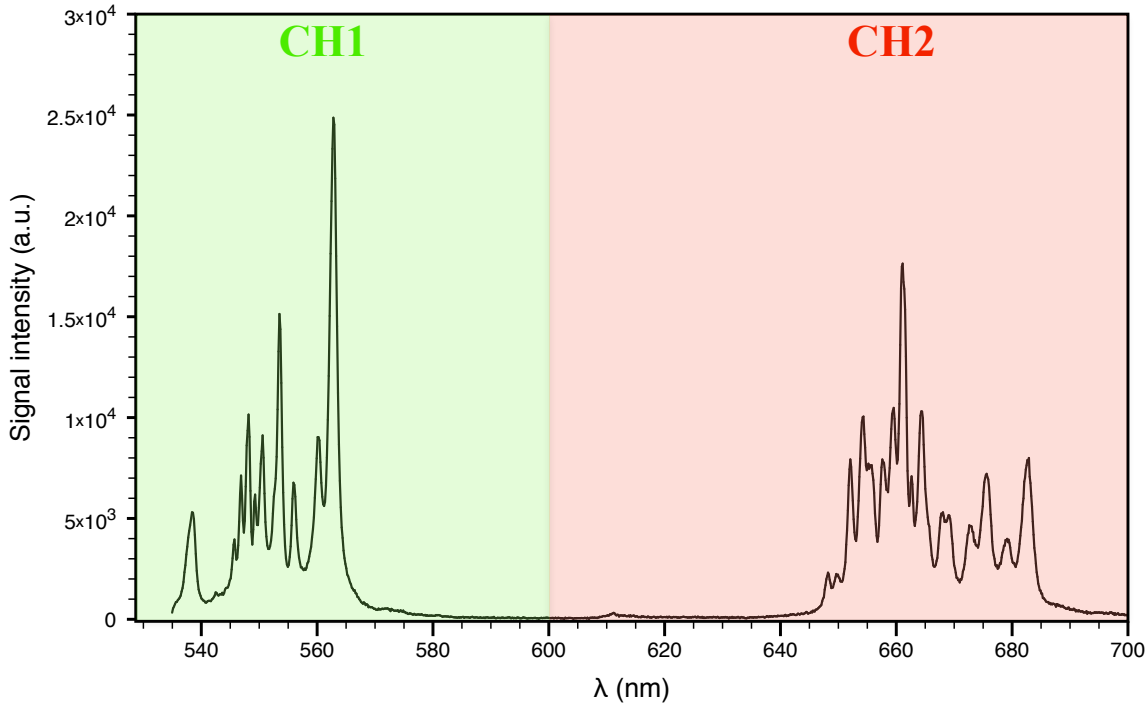

Figure 6.3: The spectral ranges covered by the red and green channels of the Confocal microscope.

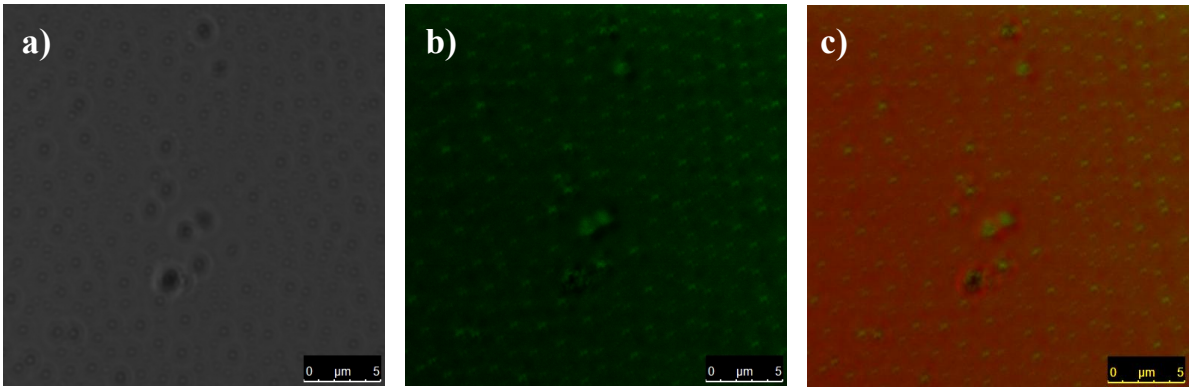

Figure 6.4: Confocal imaging of sample 22b: a) recording the transmission light b) detecting the green spectrum, and c) merging a and b images.

In this section the photoluminescent properties of our particles are proved to be efficient for confocal imaging which bring them to the standard of those reported in the literature. Moreover, unlike particles reported before, conclusive result show single

particle detection. However, although confocal microscopy is widely used in biology, it has several weaknesses that make it not appropriate for the purpose of this study. First, biological tissue should be stained with specific dyes to gain cellular contrast under the microscope, which complicates the biological system in which the nanoparticles distribution is investigated. The second drawback is the fact that confocal microscopy relies on a pinhole to achieve the imaging plane confinement, which significantly limits optical penetration depth in scattering tissue such as brain.

6.3 FWM imaging

Four wave mixing (FWM) has proved to be a powerful technique to image inorganic nanoparticles in a biological context [46, 117]. However, as mentioned in section 2.3.6 there was only one study where this process was utilised to image magnetic particles [30]. The particles investigated in that study were in the micro-size range. In this section, four wave mixing process will be applied to image magnetic nanoparticles (iron oxide and gadolinium oxide) dried on microscope glass coverslips, embedded in agarose gel, and mixed with starch as a model CH content.

The optical setup used here for FWM imaging was described in Section(3.3.3). Two co-aligned pulsed laser beams (816 nm and 1064 nm) were used to produce the FWM in the magnetic particles in the focal point. The wavelengths of the two beams were chosen to be a set of the typical combinations used to achieve C-H vibrational contrast of the biological structures. Moreover, this combination of wavelengths is more desirable for imaging scattering tissue such as brain as explained before in Section(4.3.2). Therefore, it is appropriate to apply the same excitation beams to image the magnetic particles.

In order to investigate the possibility of imaging gadolinium oxide nanoparticles (bought from Sigma Aldrich) with FWM, a droplet of the particle-water mixture was

dried on a microscope glass coverslip by placing the coverslip on a hot plate at 50° c. The coverslip was then sealed and placed in the microscope and imaged with the CARS setup and wavelengths mentioned above. Figure(6.5, a) shows a 512 × 512 image of aggregations of the Gd_2O_3 nanoparticles. In Figure(6.5, b) same setup was applied to image the particle aggregation. However, the 816 nm and the 1064 nm beams were blocked while scanning the particle as illustrated in the image. The red horizontal lines represent closing and opening shutters. It can be seen that the signal comes from the particles only if the two beams are applied. This confirms that this signal results from four wave mixing, since, according to our previous knowledge of the FWM spectrum generated by gadolinium oxide nanoparticles(see Section(5.6)), the signal fits within the spectrum band detected by the filter 660/40 nm; the particles are not doped which indicates that they do not generate an UCP signal; even if the UCP signal is generated it could be generated by the 816 nm only which did not occur as when the 1064 nm was blocked no signal was detected.

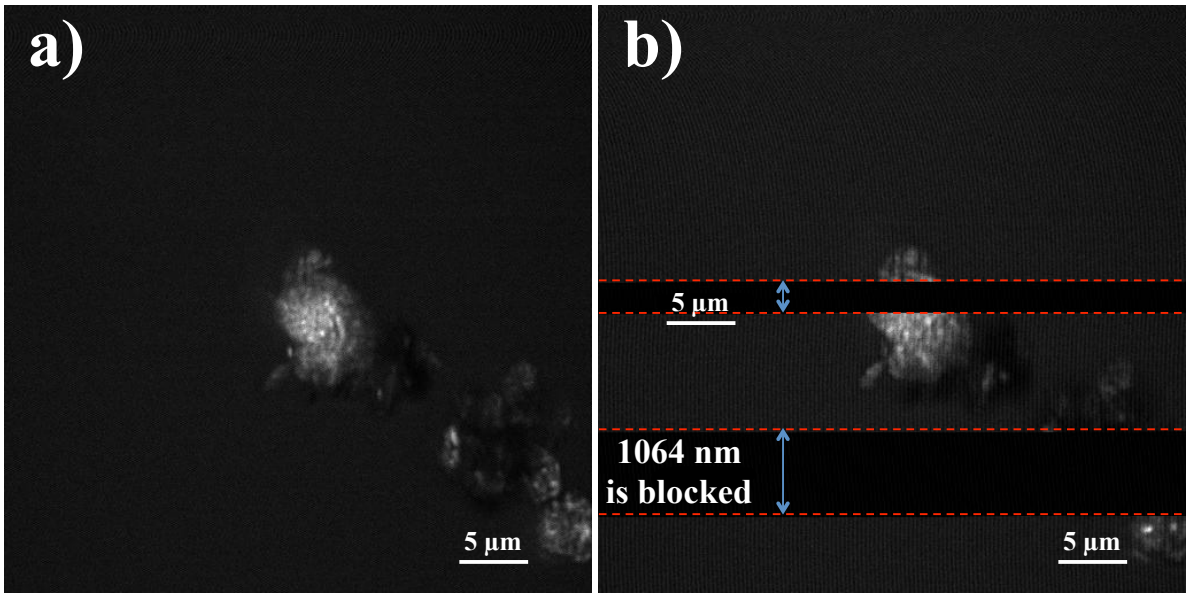

Figure 6.5: A FWM image of aggregation of gadolinium oxide nanoparticles, a) with continuous scanning with both beams (816 nm and 1064 nm) whereas in b) one of beams was blocked as labeled and determined with the red dashed lines.

In order to investigate the FWM of iron oxide particles, commercially available 200 nm particles were purchased from microParticles GmbH. The particles were suspended in 0.03 % of the original concentration in 1% w/w agarose gel. A droplet of the resultant particle-gel suspension was dropped on a microscope glass coverslip and sandwiched with another glass coverslip and sealed with parafilm spacer as described before. A z-stack of 40 images were taken of field of view of ($157 \times 157\ \mu m^2$) and with a 0.5 μm step in the z-direction which covers a volume of $157 \times 157 \times 20\ \mu m^3$.

Z-stacks were opened in ImageJ software and a z-projection was taken Figure(6.6, a). Also, to see the confinement of the particle in the z-axes, the stack was resliced using the same software in the xz-direction and y-projection was taken and shown in Figure(6.6, b). The bright dots in the images show the locations of the particles, however there is no conclusive evidence that single particle imaging was achieved. Nevertheless, qualitatively, a relatively stronger signal was achieved. Moreover, from Figure(6.6, b) it can be seen that small dots which are not spreading in the z-direction confirm that sharp z-confinement was achieved as a result of the nonlinear FWM process. If the relationship between the laser power and emission was linear the particles would appear unconfined in the z-axes similar to those in Figure (6.8, b).

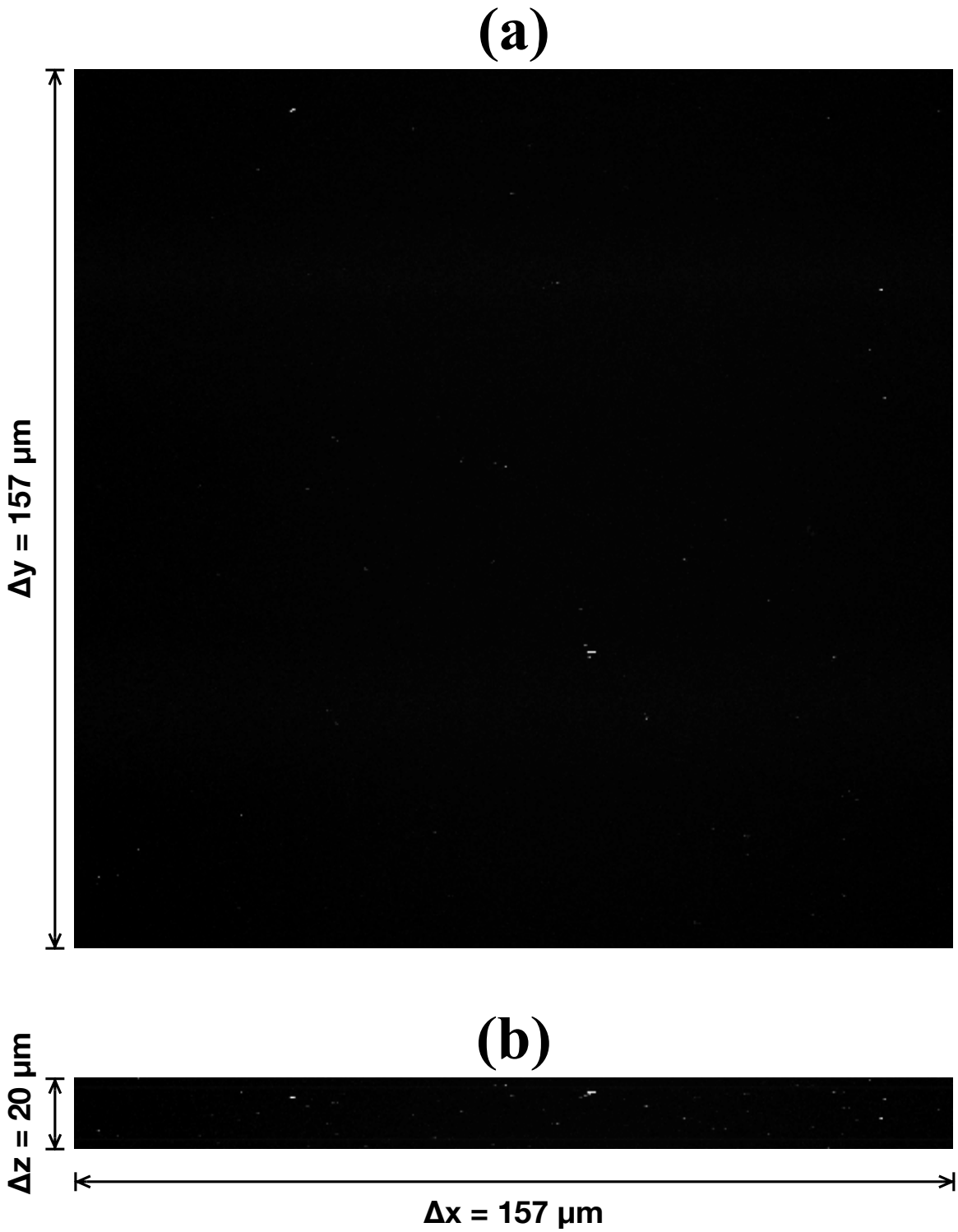

Figure 6.6: A FWM image of iron oxide particles suspended in agarose gel, a) a z-projection with FOV in xy-plane of ($157 \times 157\ \mu m^2$) and b) a y-projection with FOV in the xz-plane of ($157 \times 20\ \mu m^2$). The bright spots indicate the particles.

In the previous paragraph an efficient nonlinear FWM signal was achieved using commercially available iron oxide microparticles. Here, the iron oxide nanoparticles(S21) were spin-coated on a glass coverslip as described before. The particles were imaged using the CARS setup (λ_{pump} =816 nm ,λ_{stokes} = 1064 nm). The image is shown in Figure (6.7) with Field of view of (157 × 157 μm^2). This experiment was conducted to confirm that same efficient signal can be generated from the fabricated nanoparticles (S21, 70 nm).

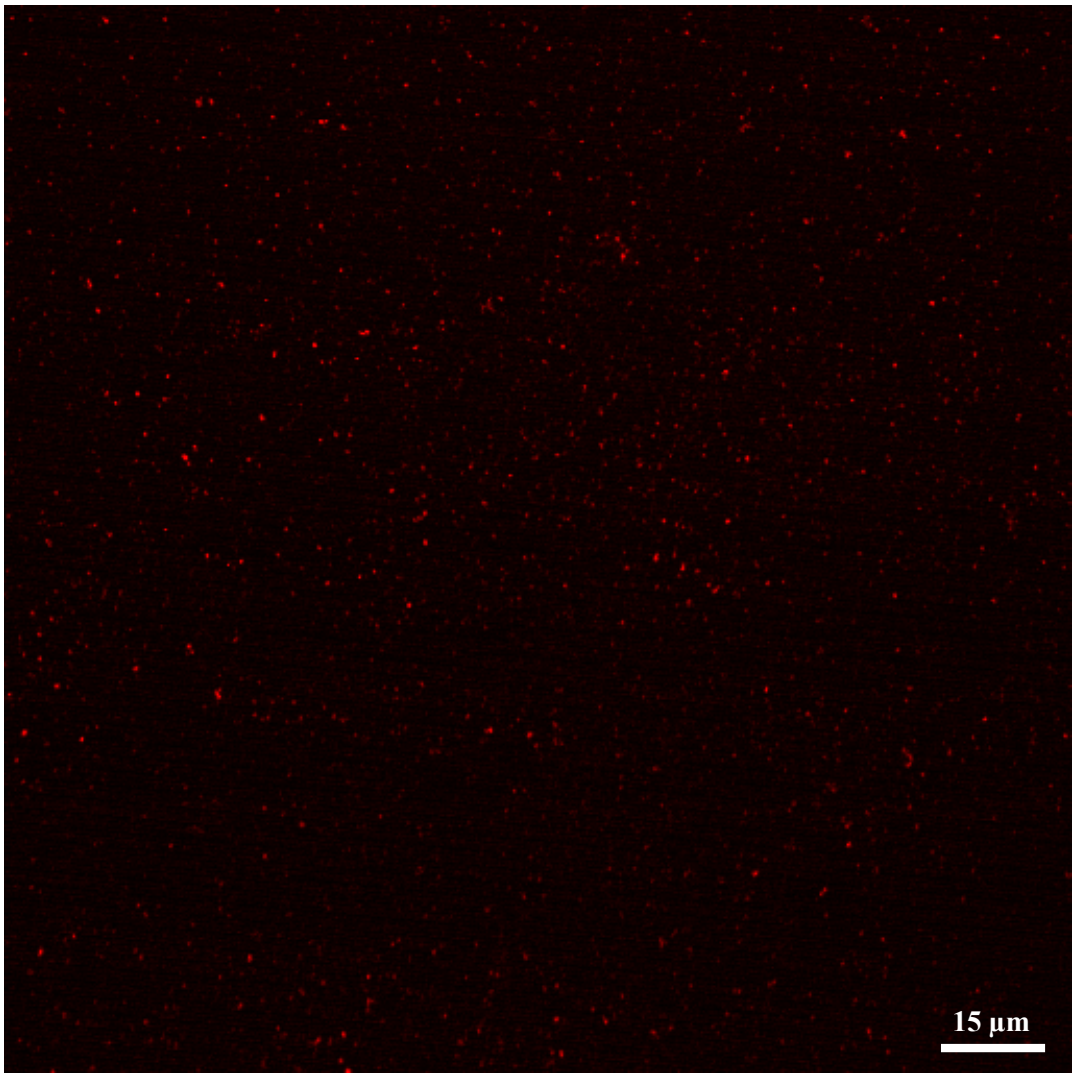

Figure 6.7: A FWM image of iron oxide nanoparticles (S21) spin coated on a glass coverslip. The image size is (512 × 512 pixels) with field of view of (157 × 157 μm^2).

6.4 Upconversion imaging

Despite the large number of works in the literature to applying gadolinium doped particles in biomedical imaging, there has been no work toward utilising them in a pulsed laser system combined with high numerical aperture lenses. Such systems are required to acquire CARS images of biological tissue in a label free manner which is suggested by this study as a powerful modality for monitoring targeted drug delivery and contrast agents. In this section doped gadolinium oxide nanoparticles will be investigated under typical laser excitations. The investigations will deal with signal strength, optimum scan time, and nonlinearity of the signal.

Doped gadolinium oxide particles (S1) were spin coated on a glass coverslip and prepared for imaging as detailed earlier. The CARS setup used to image the particle utilised the excitation wavelengths 816 nm and 1064 nm. The filter used for detection scheme is also the filter used for CARS for this excitations combination (660 nm bandpass filter). Sample (S1) was chosen for this experiment as it is one of the samples with erbium dopant which is vital for the particles to exhibit efficient upconversion photoluminescence under the 816 nm excitation as concluded in Section(5.6).

Figure(6.8, a) shows an UCP image of the particles which was acquired using CARS setup and excitation power with typical PMT voltage used to image CARS and a reasonable scan time 10 sec/frame. The detected signal is efficient to the standard of sensitivity of the detection scheme. In Figure(6.8, b) a line scan was acquired with the microscope to investigate the ability of z-confinement of the particle signal. As mentioned in section(6.2) the spin coated particles form a uniform 2D distribution as confirmed by SEM images. On one hand, this 2D layer is of particle diameter thickens (in this case with sample particles it is 280 nm). On the other hand, the microscope is capable of acquiring z-step of $0.5\mu m$. It is an effective method to examine the z-confinment of the

microscope using UCP of the particles. If the UCP signal is generated in a nonlinear manner, the signal will be orders of magnitude higher when the focal point scans on the particles layer. When the focal point scans above or beneath the particles layer the produced signal should be much lower and undetectable with that same PMT voltage used to detect the in-focus signal. This is the main concept of nonlinear (or multi-photon) microscopy which is explained in Section(2.3.3). However, it can be seen in Figure(6.8, b) that UCP signal is generated efficiently even if the particle layer is out of focus. This is a result of the linear behaviour of the UCP discussed in section(5.6). Although UCP is a nonlinear process, it suffers from saturation which drives the relationship with laser power to a linear manner at relatively high power. It seems that the saturation limit is far below the sensitivity of the CARS detection setup. Also, the pico second pulsed laser is not the correct choice for producing efficient nonlinear UCP signal at low powers. The pulse peak intensity is above the saturation limit even if the average power is lower than the saturation limit. If the average power is attenuated so that the peak power is below the saturation limit, the generated signal is not efficient for imaging.

Although the loss of z-confinement of the particles is considered as a disadvantage, it might be a novel advantage for the purpose of multi-modal drug tracking in brain tumours with MRI and CARS. As mentioned in Section(4.3.2), one of the main obstacles of comparing MRI and CARS images is the different scale image dimensions and resolution. A CARS mosaic image is just 0.5 μm thick, whereas, a high resolution MRI image can be 100 μm. The unconfined signal of the particles will be detected from a slice with a thickness of about $20\mu m$ above and underneath the CARS image. This will help to locate particles in the thick brain slice as a first step, and a z-stack can be applied to any region of interest accordingly.

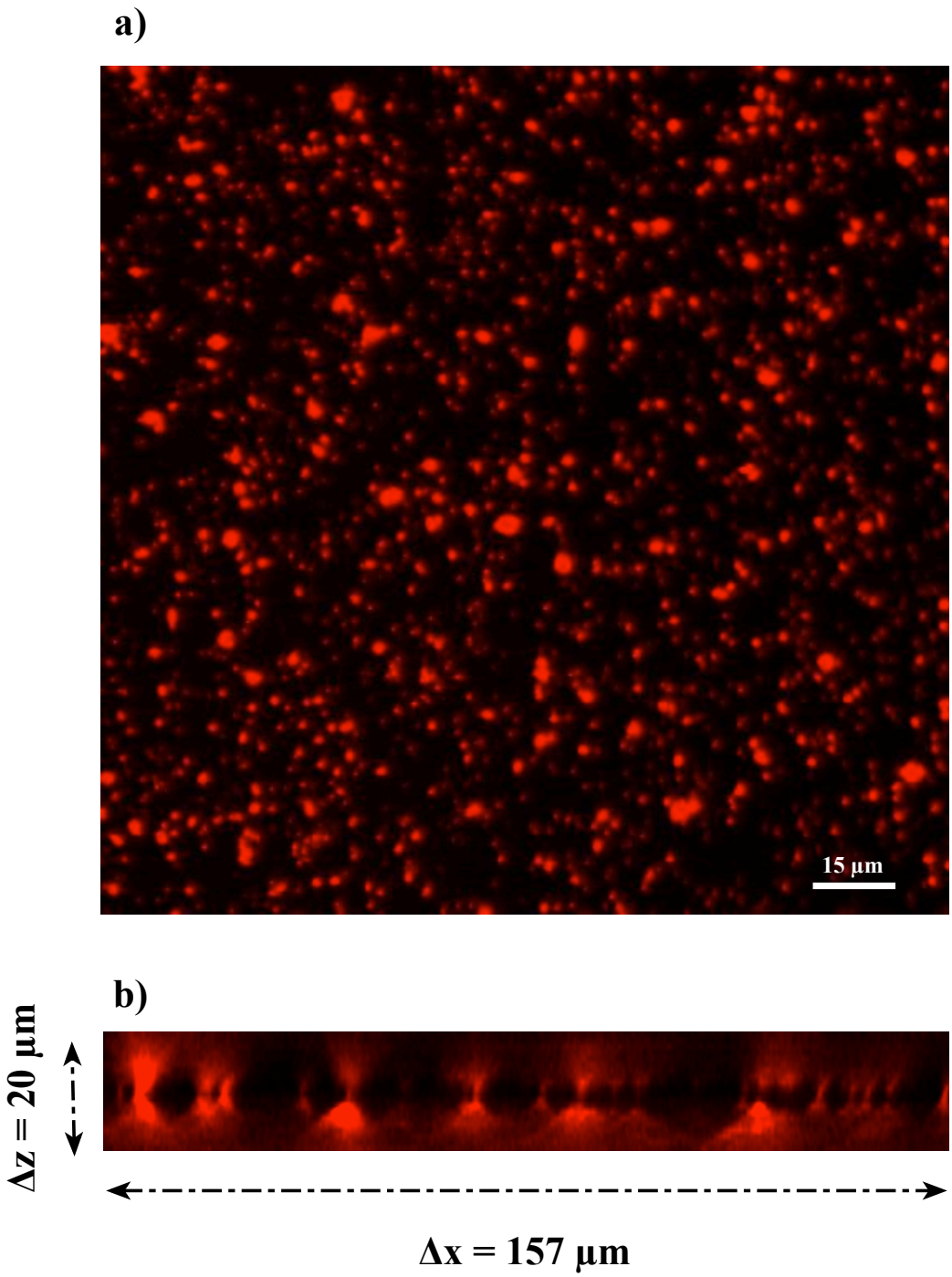

Figure 6.8: a) In focus UCP 512 × 512 image with 157 × 157 μm^2 FOV of Gd_2O_3:1 % Yb, 1% Er particles taken with 816 nm excitation and 660/40 nm detection filter and typical CARS PMT voltage. b) A line scan generated with the microscope software allowing xz-plane imaging with FOV illustrated in the figure.

Another important characteristic of UCP is the relatively long lifetime of the emission. In order to address this, Figure(6.9, a) is a 250 × 250 image of doped gadolinium oxide nanoparticles (S2) acquired under 816 nm excitation with scan speed of 2010 ms/frame (or 32 μs/pixel). Because the UCP lifetime is longer than the pixel dwell time, a decaying blurry edge is produced in the image towards the scan direction. An estimation of the decay time was undertaken to consider its effect in any further UCP imaging. In Figure(6.9, a) a yellow line and its grey scale value profile in terms of pixel distance was produced with ImageJ software. The line profile (Figure(6.9, b)) corresponds to signal decay as a function of time after replacing distance in pixels with the corresponding scan time. The data points were then fitted to the equation $I_{(t)} = I_0 e^{(-t/\tau)}$ revealing the value of τ to be 200 μs.

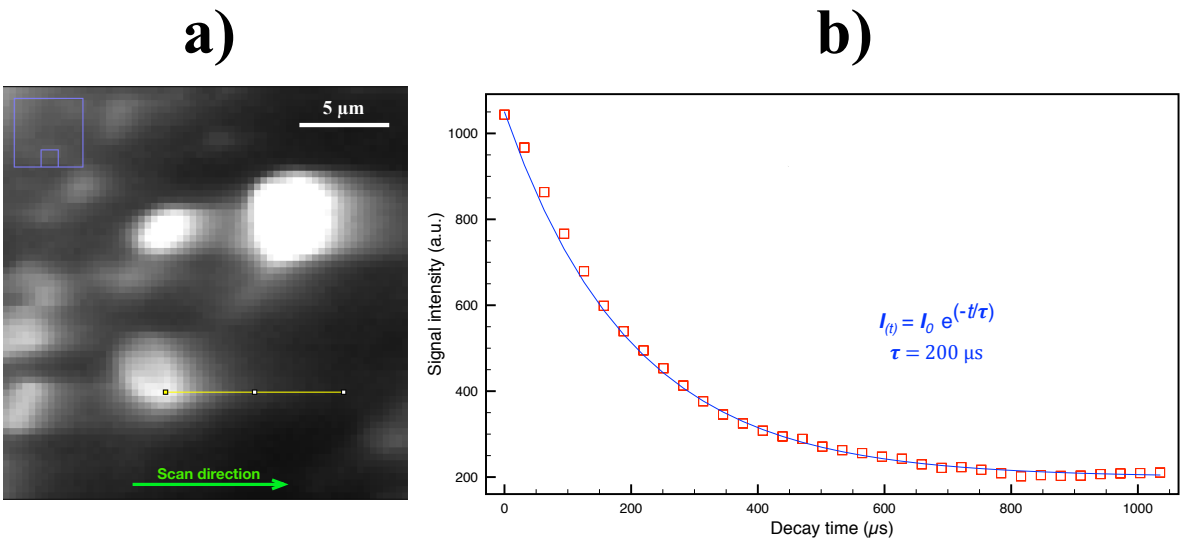

Figure 6.9: This is an illustration of the decay time effect on the image. On the left (a) is a (250 × 250) image of aggregations of doped particles(Sample 2) excited at 816 nm at scan speed of 2010 ms/frame. The plot in (b) is the intensity profile of the yellow line drawn in image (a).

Although the decay lifetime is close to that previously reported [88], it is important to mention that the aim of this experiment was not to accurately measure decay lifetime,

but to estimate the decay lifetime and consider its effect on the imaging process.

Figure(6.10) shows three 512 × 512 UCP images (a, b, and c) of doped gadolinium oxide particles acquired at different imaging speed (3.8 μs/pixel or 1 s/frame, 42 μs/pixel or 11 s/frame, and 191μs/pixel or 50 s/frame, respectively). To understand the effect of the scan time on the image the line profile of the grey scale value of the white lines drawn on the images were generated using ImageJ software and plotted in Figure(6.10, d). The intensity profiles are shown in different colours and labeled in the legends. It can be seen that that the red profile is shifted with a large number of pixels with disappearing of some small peaks under the decay of more intense peaks. However, the other two intensity profiles corresponding to images (b) and (c) are showing similar behaviour with excising of all the peaks and an ignorable minor shift. It can be concluded that UCP particles can be imaged with reasonable scan time of 42 μs/pixel. This time is required anyway when imaging highly scattering tissue such as brain.

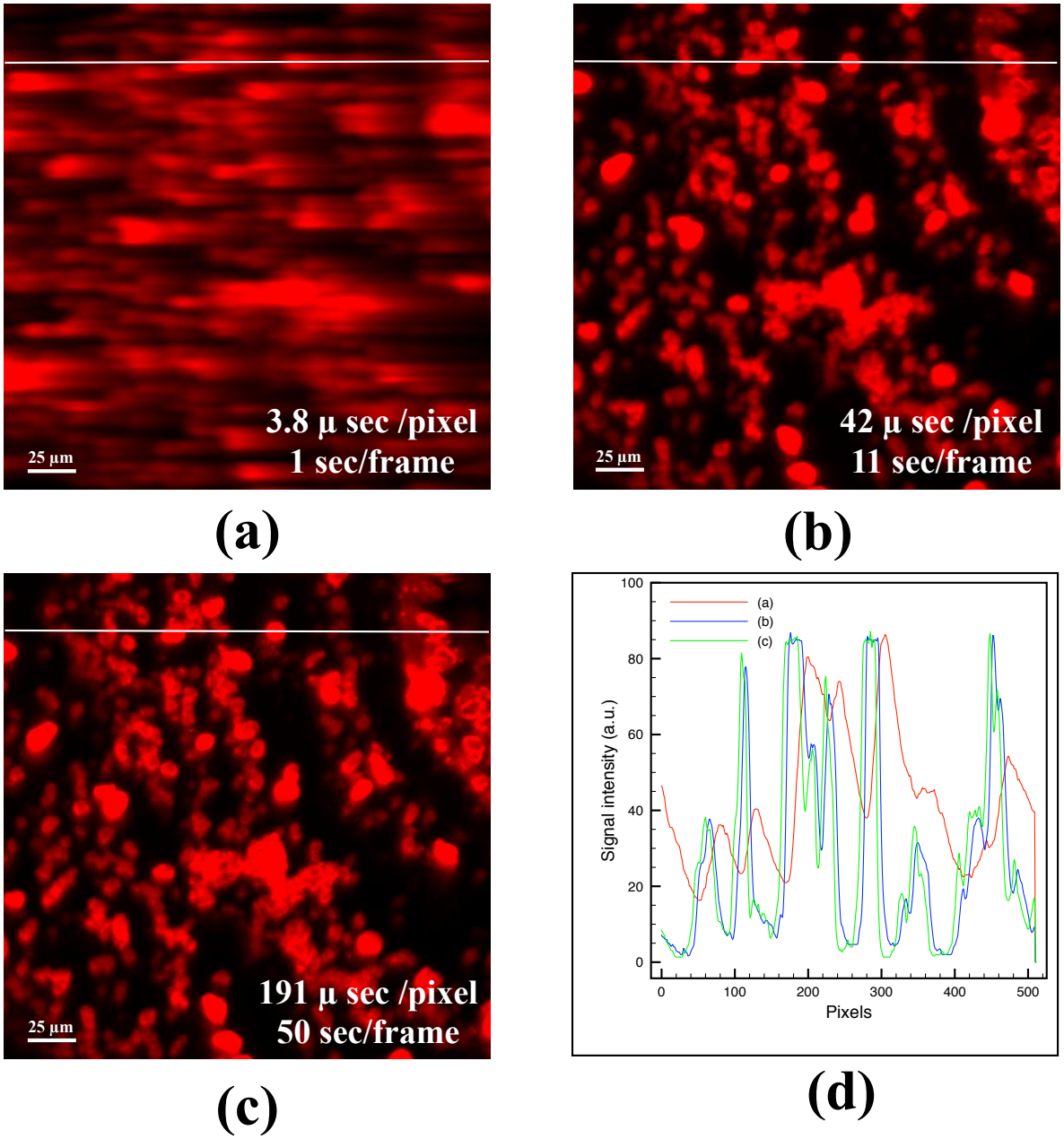

Figure 6.10: The effect of imaging speed on the upconverting nanoparticles image. Three images of the same sample (a,b and c) were acquired with the same laser power (100 mW) and different scanning time where a 660/40 nm wavelength-bandpass filter was used. The scanning time is shown on each image in microsecond/pixel and seconds/frame. The profiles of the three white lines drawn on the images are plotted in (c).

As mentioned in the introduction starch was used as a model to investigate the

possibility of imaging doped gadolinium oxide nanoparticles in biological structures. Nanoparticles from sample (S3a) were mixed with starch and two images were acquired with different excitations and same typical CARS detection bandpass filter 660/40 nm (see Figure. 6.11, a and b). Image (a) was taken with single beam excitation (816 nm) and the detected signal is the UCP of (S3a) at this range of the spectrum as illustrated in Figure(6.12). In Figure(6.11, b) two synchronised pulse excitations (816 nm and 1064 nm) were applied resulting in generating both CARS from starch, FWM and UCP from the particles. However, in particles, UCP is the overwhelming as illustrated previously in section(5.6). Using ImageJ the two images were composed in one image using the merge colour function. The resultant composite image shows the structure of starch and the distribution of the particles in a distinguishable contrast. These two images were acquired in two different scans to enable the researcher to change excitation setups which might be considered as a drawback. However, simultaneous imaging of the two types of signal (UCP and CARS) can be achieved by using different emission filters. As illustrated in Figure(6.12), the UCP signal of the particles covers a wider range of spectrum (650 nm - 685 nm) whereas FWM is a narrow peak located at 660 nm. If, for instance, two wavelength-bandpass filters (660/20 nm and 680/20 nm) with two PMT detectors are used, simultaneous imaging is possible. Also, different doping can be used to detect different colour of UCP emission, however, due to cost implications, the work in this thesis is limited to the available CARS setup.

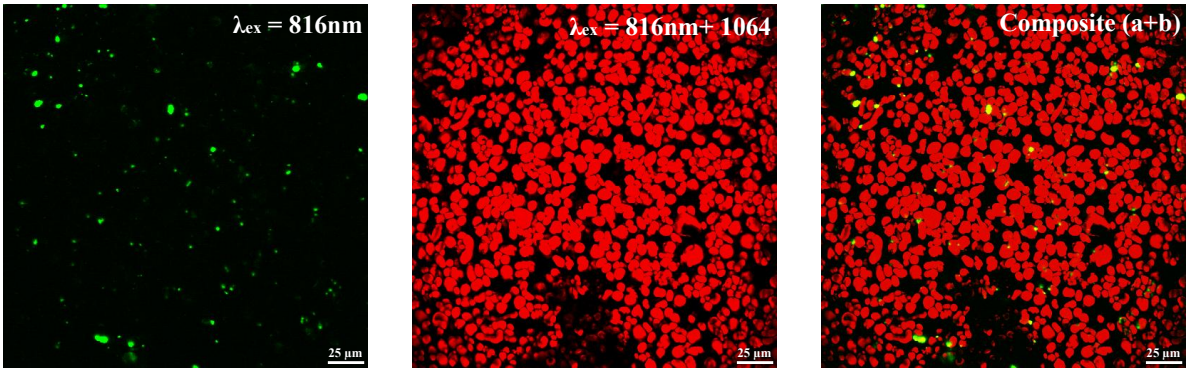

Figure 6.11: Imaging the upconversion nanoparticles in a biological context model(starch). In image (a) the upconversion photoluminescence was detected after a single beam excitation (816 nm) whereas two beams were used to generate the epi-CARS of starch (b). The composite of the two images (a and b) is presented in image (c) showing the localisation of the doped gadolinium oxide particles within the biological context model.

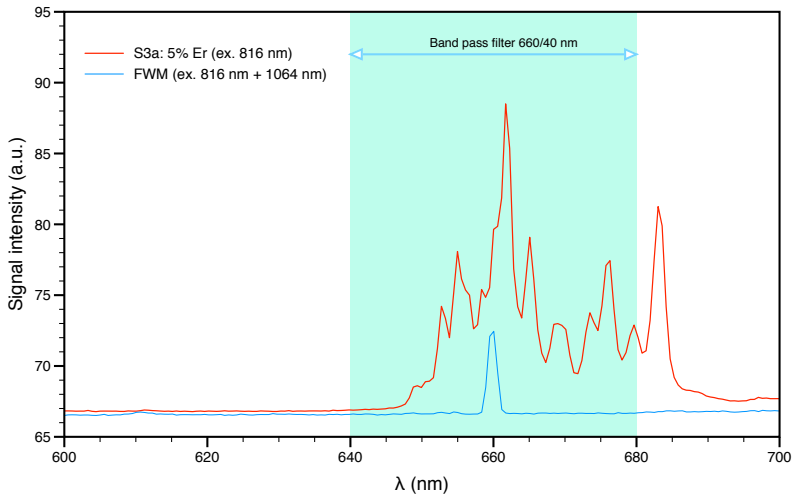

Figure 6.12: The spectra range covered by the 660/40 nm band pass filter of the UCP and FWM.

6.5 Two photon photothermal lensing (TPPL) imaging

As mentioned in Section(2.3.8), two photon photo-thermal lensing is an imaging process that relies on detecting the modulated defocusing of a laser beam as a result of local thermal gradient in the focal volume caused by another. This process was used to image heme proteins with a conventional SRS setup [49]. As an emerging application in biological tissue imaging TPPL process was used to gain contrast of red blood cells and, hence, measure the blood vessels density in 3D [118]. However, in terms of nanostructure spectroscopy, Gold nanoparticles were detected via their surface plasmonic resonance absorbing properties [119]. Moreover, single nanoparticle was detected using same thermal properties of metallic nanoparticles in another previous study [120]. In this section, we show for the first time that iron oxide nanoparticles can be imaged using TPPL with the picosecond-laser SRS setup. Also, a possible physical explanation of how this process occurs in such semi-conducting material will be discussed.

The SRS setup used in this section was presented in Section(3.3.4). Briefly, two collinearly alined picosecond pulsed laser beams (1064 nm and 816 nm) were temporally overlapped and directed to pass through the objective lens of the microscope. The 1064 nm pulse train was modulated at 1.7 MHz and a lock-in amplifier was set to detect variations in signal at the same reference frequency. Two different sized iron oxide nanoparticles (S20, S21) were synthesised using hydrothermal method described in Section(3.4.1). Samples were prepared by distributing the particles on a glass coverslip (single layer) as illustrated before then placed in the microscope for imaging. From the first trial and without changing any of the typical setup used for lipids SRS imaging a strong signal was detected in the lock-in amplifier resulting in a relatively high intensity signal in the grey scale image. FWM was recorded simultaneously in the backward

direction as illustrated in Section(6.3) to confirm the detection of iron oxide particles.

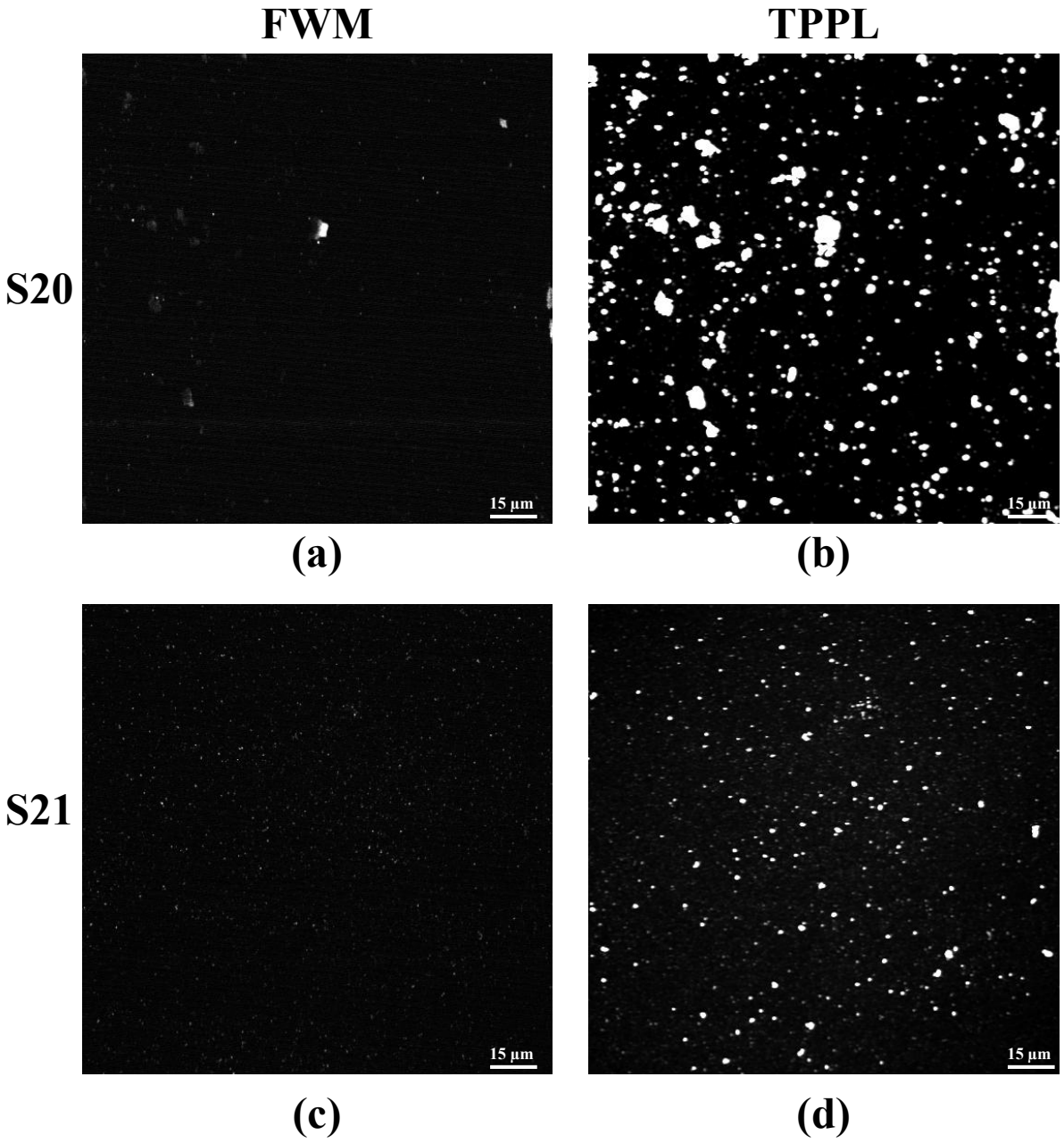

Figure 6.13: FWM and TPPL of iron oxide nanoparticles (S20 and S21).

Figure(6.13) shows both FWM (a,c) and TPPL (b,d) images of S20 and S21. The overwhelming observation is the relatively stronger signal recorded in the TPPL channel compared to CRS suggesting enhanced sensitivity of the thermal lens process. Moreover,

particles can be seen at full image FOV edges without loss of signal which confirms that the process does not require phase matching as in FWM and CRS.

Another experiment was conducted to investigate the z-confinement of the particles in a TPPL image and hence the nonlinearity of the power-signal dependency. A z-stack of 40 images of (157 $\times$ 157 μm^2) with a z-step of 0.5 μm was acquired using the 60x lens. The resultant z-stack image was opened with ImageJ and was re-sliced in the x-z plane direction (x is one arbitrary axes of the two in-plane axes of the original image). Then, a projection of the x-z images was produced (see 6.14). The resultant image dimensions are labeled on the image(20μm $\times$ 157μm). A series of bright dots that lay on approximately a straight and horizontal line can be seen in the middle of the image. These bright spots indicate a projection of the particles on the glass coverslip. The z-confinement of the particles proves that nonlinear dependency between laser power and generated TPPL signal is achieved.

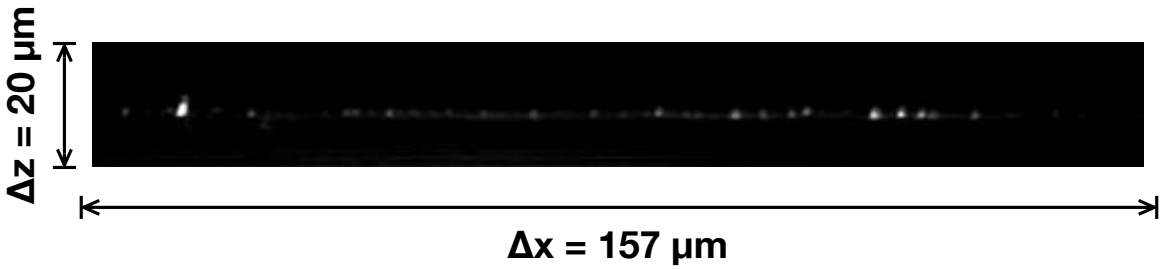

Figure 6.14: The z-confinement of the TPPL signal detected from iron oxide nanoparticles (S21).

After having achieve a clear z-confinement of the particles with TPPL, it is interesting to see how these particles would appear in a biological context and if the contrast will be distinguishable. For this purpose a mixture of the particles and starch was prepared as described earlier. Figure(6.14) shows images of the mixture with recorded in the forward (SRS and TPPL) and in the backward (CARS andFWM) directions using the

same Stoke beam and different pump beam wavelength. When using C-H vibrational resonance set of beams (816 nm and 1064 nm), starch appear bright for the anti-Stokes CARS signal detected in the epi-direction (Figure6.15,a). Also, particles in specific size and locations can be seen in (Figure6.15,a) for the FWM process which was explained before in section(6.3). A simultaneous image was acquired in the forward direction and presented in (Figure6.15,b) showing SRS of the starch and TPPL of the particles. The particles show relatively stronger TPPL signal and larger spots than those detected of them with FWM. This might be a result of the nature of epi-detected signal, since only small aggregations of the particles (smaller than 1/3 of the wave length), or, those located in an interface allowing them to reflected signal generated by starch or glass coverslip, will show up in the image [28]. It is interesting to investigate the effect of changing the wavelength of the pump beam driven from the OPO to a value close to the off resonance frequency. This will exclude any doubts that the signal might be originating from starch since CH bonds would appear dark in the image. Hence providing additional evidence since we already imaged the particles without mixing them with a biological material before, see Figures(6.13 and 6.14). As expected, when tuning the wavelength of the OPO beam to 810 nm, signals from starch in both e-CARS and SRS is reduced (Figure6.15, c and d). Also, the pump wave length was tuned to 807 nm (Figure6.15, e and f) where in image(e) no CH signal is detected of starch, and only non-resonant signal of the glass is recorded. In image (f) only TPPL signal of the particles is detected which is considered as a distinguishable contrast from the biological model context.

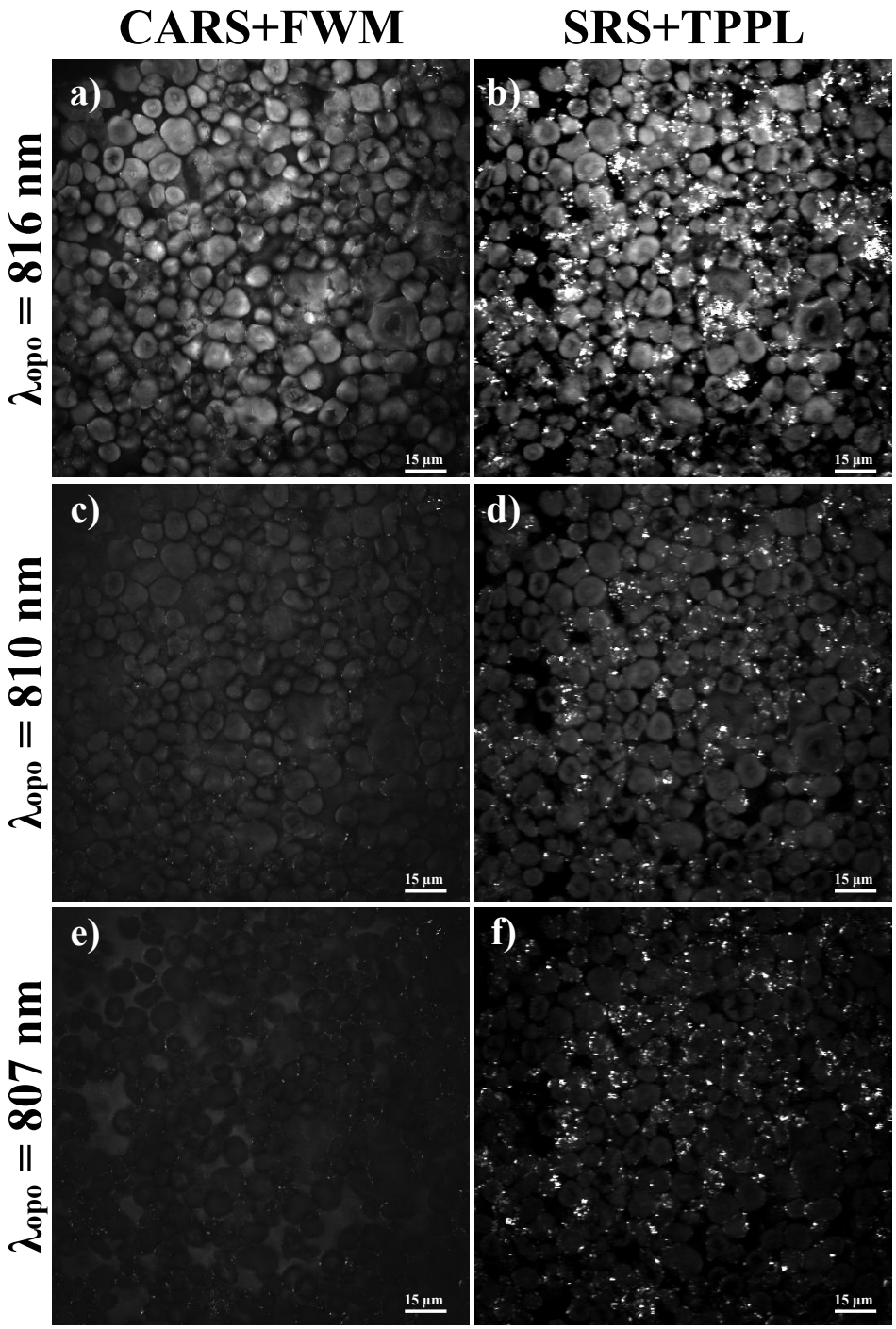

Figure 6.15: The figure shows 6 images, (a,c and e) acquired at different pump wave lengths of Epi-CARS of starch and FWM of iron oxide particles detected in the backward direction, and (b, d and f) recorded SRS of starch and TPPL of the particles.

Another technique that can be used to provide contrast between particles and biological structure is desynchronising the two excitation pulse trains. Unlike CRS processes, TPPL does not require temporal overlap of the pulse trains. Figure (6.16) shows images where the two excitation pulse trains were synchronised (a,b) and where pulse trains were desynchronised until no epi CARS signal was detected (c,d). It can be seen that TPPL signal of the particles is detected in image (d).

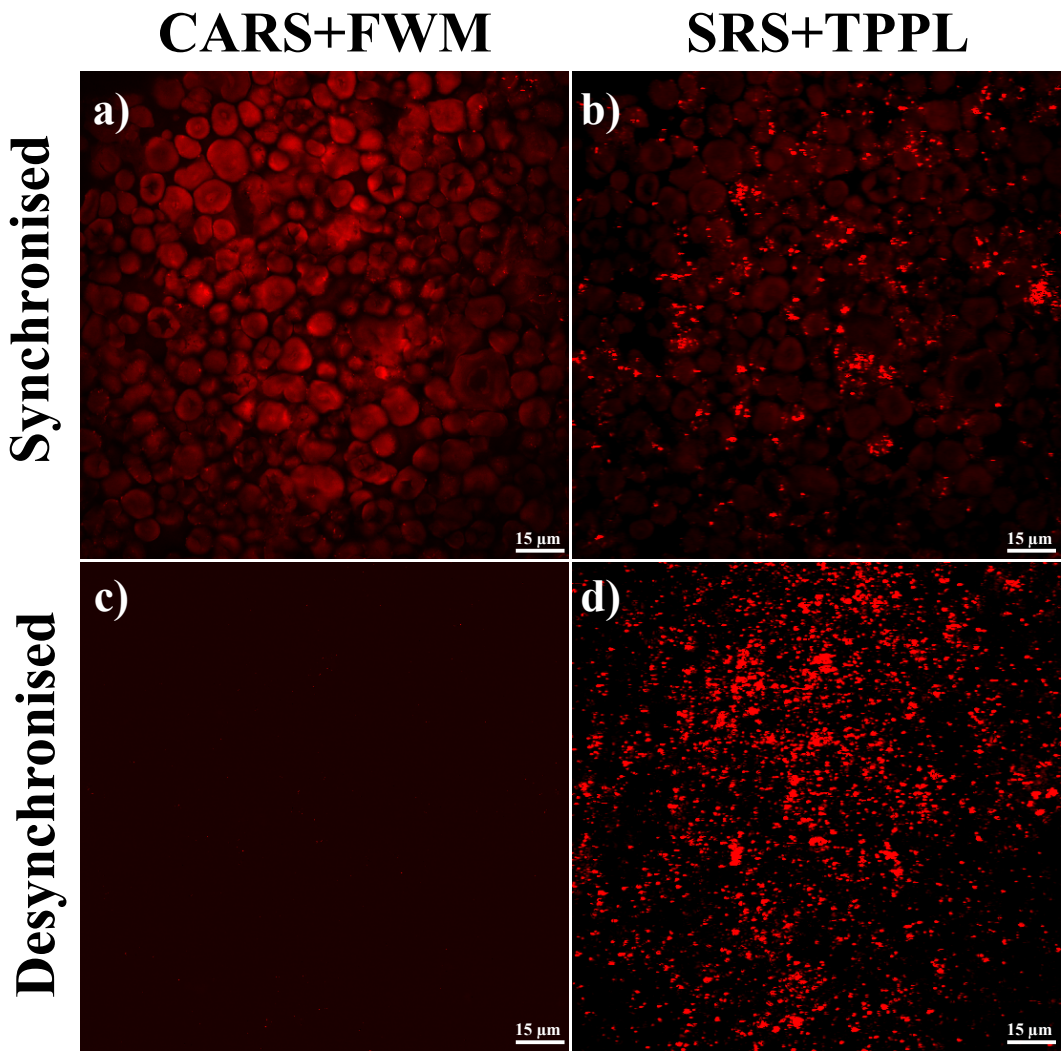

Figure 6.16: The figure shows 4 images, (a and c) acquired of Epi-CARS of starch and FWM of iron oxide particles detected in the backward direction, and (b and d) recorded SRS of starch and TPPL of the particles, with the pump and Stokes pulse train either synchronised (a and b) or desynchronised (c and d).

Changing the wavelength of the pump excitation and desynchronising the two pulse trains are available techniques to differentiate between particles and biological context as mentioned above. However, this requires the investigator to acquire images in two separate sessions which is considered as a limitation. Fortunately, as reported in previous studies TPPL signal does not arrive at the detector simultaneously with the SRS of an active vibrational bond. It has previously been shown [118] that the difference in phase (with respect to pump modulation) of SRS and TPPL processes can be exploited to separate the two processes using phase-sensitive lock-in detection. Similar technique can be used to differentiate between particles and biological structures. This, however, should be proceeded by inspecting the phase difference between TPPL of particles and SRS of CH bonds in starch. For this reason, ten images of the starch particles mixture were acquired for different phases (0°,20°,40°,60°,...,160°,180°) with respect to pump modulation. The images were normalised against laser fluctuation and the variation in signal intensity of two spots in the image that represent particle aggregation and starch were measured in arbitrary units using ImageJ. The particles and starch spots were confirmed by FWM detected in the backward direction at a nonresonace wavelength. Figure (6.17) shows the variation in signal intensities of SRS of starch and TPPL of the particles as a function of detected phase.

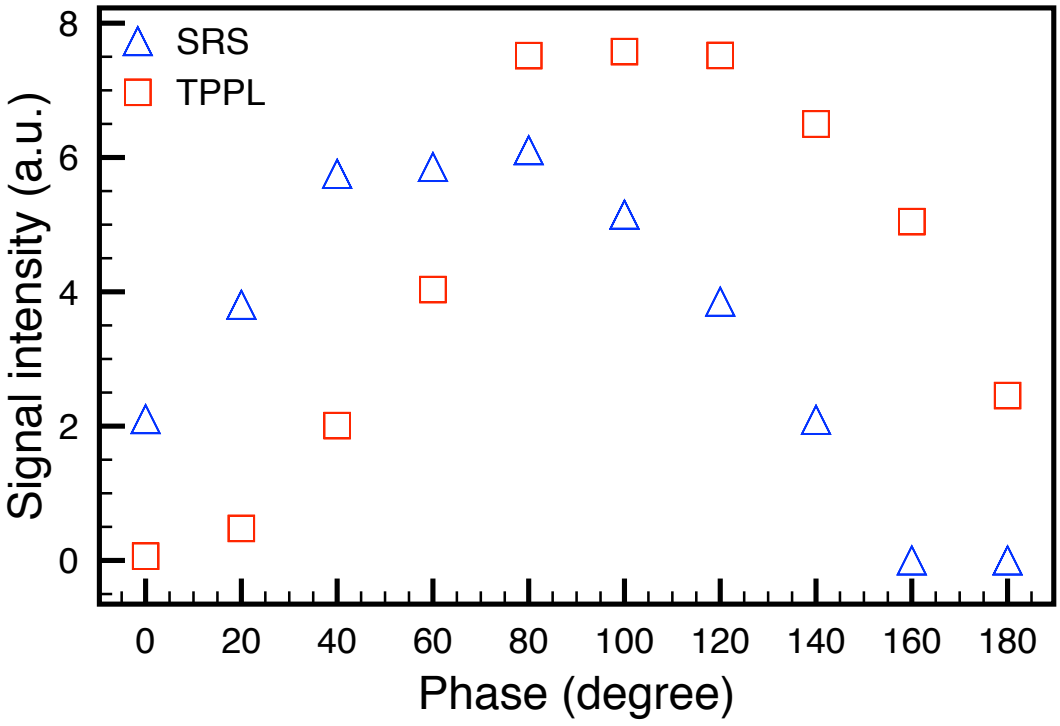

Figure 6.17: The signal intensities of SRS of starch and TPPL of iron oxide particles as functions in phase.

In Figure(6.17) it can be seen that the signal of the particles can be isolated by choosing the 160° phase image. Baring that an available epi-CARS image showing starch was acquired simultaneously with this image, the two images were merged in two different colours to display the distribution of the particles within the biological model(see Figure(6.18)). In the figure TPPL signal of particles is shown in green and the epi-CARS of the starch appears in red.

In this experiment the backward direction was available to detect a simultaneous epi-CARS image of starch, however, in other experiments another imaging technique is used to image different biological structure for a specific purpose (for instance Second Harmonic Generation to image collagens). In such experiments the forward direction

is enough to detect both SRS of starch and TPPL of iron oxide particles. This can be achieved by detecting amplitude and phase of the signal and post image processing can be carried out to produce distinguishable contrast of particles and starch.

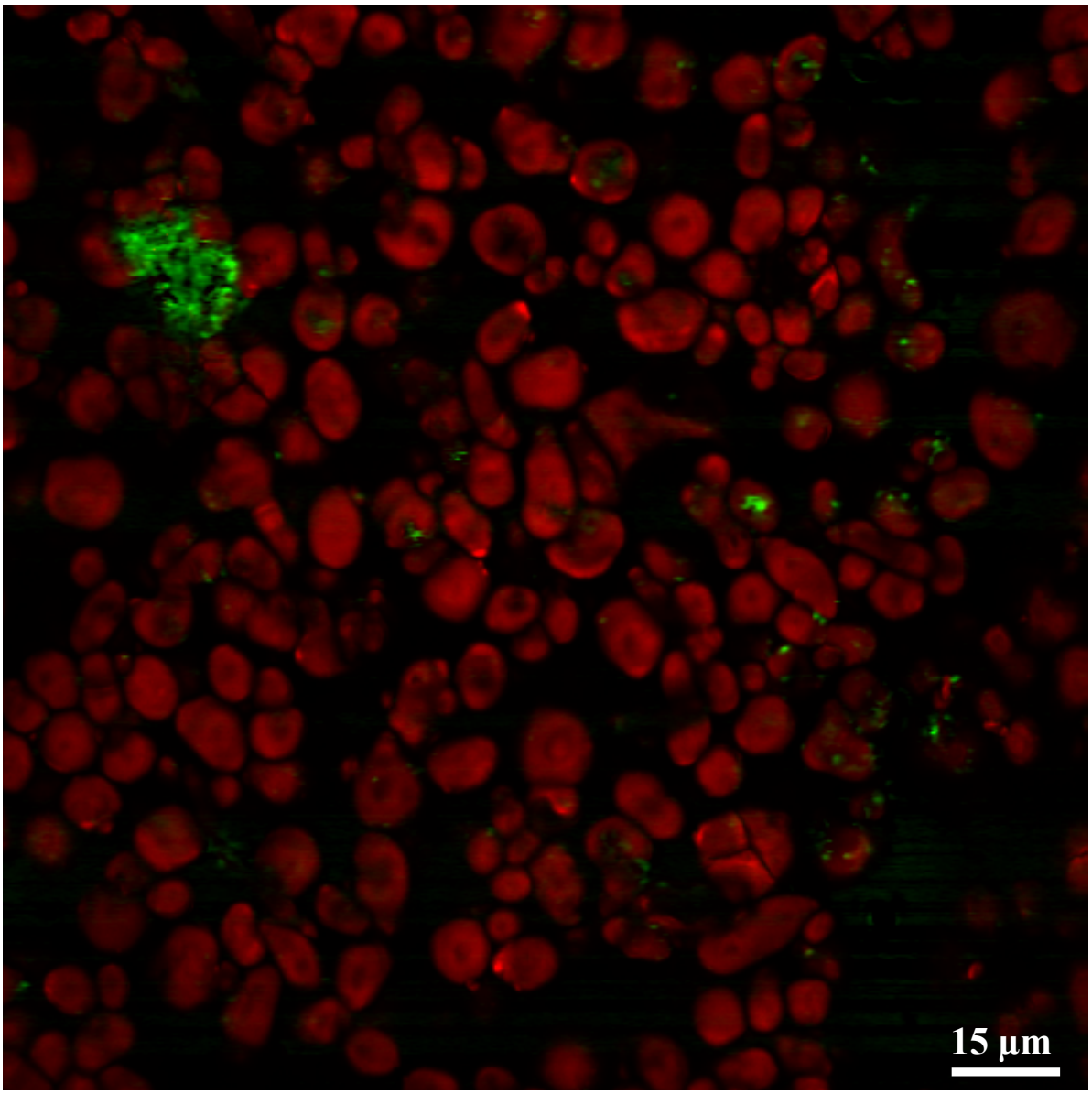

Figure 6.18: A composite of two images epi-CARS of starch (red) and TPPL of iron oxide nanoparticles (green) recorded at phase of 160°.

From the above experiments it can be concluded that the signal detected of the

particles is a result of two photon photothermal lensing (TPPL) that occurs in the particles material. It is two photon process because of the nonlinear z-confinement of the signal(see Figure(6.14)) and it is photothermal lensing because it poses similar properties to TPPL technique reported in previous studies. This conclusion is supported by evidence from the literature showing that iron oxide nanparticles have an absorption band at the green spectrum [121, 122]. The broad absorption range covers the 532 nm which is equivalent to doubling the energy of the 1064 nm beam. So, two 1064 nm are absorbed nonlinearly benefiting from the high peak intensity of the picosecond pulse. Given that the 1064 nm beam is intensity modulated, this results in the modulated heat gradient in the focal point that leads to modulated focussing of the 816 nm beam.

6.6 Summary

This chapter investigated the possible 3D imaging techniques of magnetic nanoparticles using a typical coherent Raman scattering (CRS) imaging system. This, however, was proceeded by preliminary experiments to assess the capability of imaging doped gadolinium oxide particles in a conventional confocal microscope. It was found that the particles provide an enhanced signal with a possibility of single particles detection. Four waves mixing (FWM) was used to image both gadolinium oxide and iron oxide nanoparticles in biological contexts. The backward of this technique is that, in order to obtain distinguishable contrast of the particles, the investigator is required to acquire two set of images in two different imaging sessions to allow changing the excitation wavelength. Upconversion photoluminescence was used for the first time to image magnetic nanoparticles with CRS setup. These particles can be imaged simultaneously in a distinguishable contrast within biological structures with unconfined signal in the z direction. The lack of confinement, however, can be considered as an advantage that

help finding nanoparticles location in the relatively thick tissue. Two photon photothermal lensing was used for the first time to images iron oxide nanoparticles in biological structures. Simultaneous imaging with distinguishable contrast was achieved by a phase separation technique.

Chapter 7

Conclusion and future work

This thesis described the development of nanoparticles contrast agents that can be used in both MRI and CRS to provide multi-scale imaging of biological tissues. The main motivation for this is the need of multi-modal imaging technique to understand the mechanism of anti-cancer nano-medicines.

The label-free MRI and CRS imaging of mouse brain were explored. In MRI, an enhanced SNR was achieved using a surface coil within a clinical whole body scanner. The MRI imaging parameters that provide optimal contrast between tumour and healthy tissue were explored. It was found that a spin-echo sequence with TR/TE (3000/110 ms) is efficient for tumour edge detection of the formalin fixed mouse brains. The tumour volume of 83 brains were measured from the high resolution MR images (0.125 $\times$ 0.125 $\times$ 0.150 mm^3) as part of a collaboration study aiming to investigate three different anti-cancer drugs on tumour volume as therapeutic response. The MR images were also used to investigate the accuracy of histology tumour volumetry by assuming MRI as a gold standard and obtaining semi-histology measurement from the same MRI data. It was found that histology volume measurements suffer from up to 60% error with an average of 20%. MRI volumetry is suggested as a higher level alternative tool

that requires less number of animals to achieve significant statistics, which is desirable from the ethical prospective. To be able to carry out qualitative comparison between the two different scale modalities (MRI and CARS), a mosaic of CARS images was proposed and a technique was developed to compensate for plane-curvature and produce uniform intensity CARS mosaic images.

The particle size was controlled either by changing nucleation time for doped Gd_2O_3 nanoparticles or by varying the starting FeCl solution with a good degree of size monodispersity. The crystalline structure was investigated using XRD and it was found that annealing is an important process to achieve efficient PL and UCP of the doped gadolinium oxide nanoparticles. Regarding the PL properties of the Er doped gadolinium oxide it was demonstrated that the green/red emissions ratio is tuneable via changing doping percentages. Moreover, the fingerprint feature of PL as a signature for the doping element was shown. The upconversion photoluminescence spectroscopy of doped gadolinium oxide was acquired for the first time in a typical CRS system under a picosecond pulsed laser excitation. It was found that upconversion photoluminescence of the Er doped Gd_2O_3 can be generated efficiently even with the excitation wavelength tuned away from the Yb absorption at 980 nm. For the Tm doped particles the UC spectrum was recorded in the near infrared range detecting a strong peak at 811 nm.

Potential NLO imaging techniques to image magnetic nanoparticles in biological tissue were explored. Doped gadolinium oxide nanoparticles were imaged using confocal microscopy and conclusive data showed efficiency of the PL signal to detect single particles. FWM was used to image both gadolinium oxide and iron oxide nanoparticles. Although the later provide relatively strong signal, the drawback of FWM is that it requires changing wave length and two separate imaging acquisitions are necessary to achieve distinguishable contrast between tissue and particles. Upconversion photoluminescence was used to image Er doped gadolinium oxide particles because they provide

efficient emission with the laser of 816 nm, unlike the Tm doped particles which only emit UC when excited with 980 nm beam. The particle signal however was not confined in the z-axes due to the linear relationship between signal and laser power resulting from UC saturation effect which was found to be far below the sensitivity of the CRS system. Although this is considered as a drawback, it is useful for the purpose of this study when images from the different scale modalities MRI and CRS are compared. The signal of the particles is generated even if the plane of imaging is above or below the particles in 20 μm range which helps locating the particles easily within the 500 μm thick brain slice. Also, it was demonstrated that the decay lifetime of the UC photoluminescence is much shorter than a typical pixel dwell time of CRS when imaging scattering tissue, which allows for clear and sharp edges of the particle aggregations in the image with no blurring effect in the xy-plane towards scan direction. Although the UC and CARS images were acquired in two different imaging sessions due to limited financial resources, it was demonstrated that, in principle, a simultaneous distinguishable contrast image of starch and particles is possible. TPPL was utilised to image iron oxide nanoparticles with a sharp z-confinment and relatively strong signal when compared to SRS of starch at the same detection setup. The distinguishable contrast between TPPL of iron oxide particles and SRS of starch was achieved by changing wavelength of pump beam, desynchronising pulse trains of the 816 nm and 1064 nm beams, and detecting signal at different phase. The first two techniques require imaging in different sessions, which is not desirable specially when imaging nanoparticles in a biological tissue. For the third technique, it was possible to record simultaneous images of particles by detecting TPPL at a specific phase, that was determined by conducting a preliminary experiment, and epi-CARS of starch. The two images were merged in two different colours to show particles distribution in the biological model. For experiments where the backward direction is dedicated for another imaging modality the phase and amplitude can be recorded and

post-image processing can be carried out to obtain the distinguishable contrast.

The main conclusion of this thesis is that MRI can be combined with CRS to image multi-scale magnetic nanoparticles in biological context. In a label-free manner, MRI and CRS are capable of distinguishing healthy tissue and tumour as well as registering the 3D nanoparticles distribution to the tumour microenvironment and the whole body.

Ideally this thesis would have shown the ability of the technique administered to ex-vivo mouse brain tumours and MRI and CRS combined with other optical techniques would be utilised to image particles distribution in the biological tissue. However, due to time and cost limitations this could not be achieved and it is one of the top priorities of future work. Additionally, the compatibility of the particles to the biological tissue will be investigated via coating with different surfactants. The impact of these surfactants and particle size on targeting specific organ or tumour could be examined.

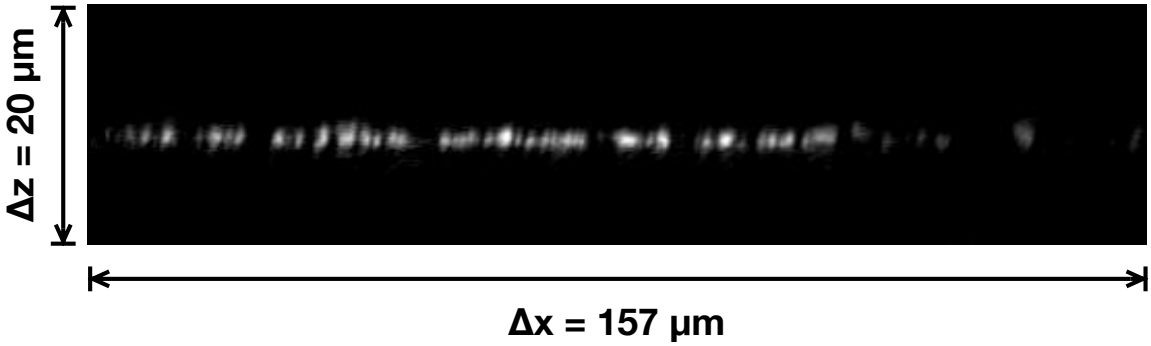

Figure 7.1: An xz-projection image of Gd_2O_3 nanoparticles coated on a glass coverslip using SRS setup and detecting what might be a stimulated emission.

One of the interesting properties of doped gadolinium oxide nanoparticles that they provide weak signal in the lock-in amplifier when using SRS setup. This signal is not due to two-photon photothermal lensing because it vanishes if the two excitation beams are desynchronised. Moreover, it is surely nonlinear process because it is confined in the z-direction. Fig.7.1 shows an xz projection of the particles spin coated on a

glass coverslip confirming the z-confinement . This signal might be due to stimulated emission that occurs within the possible energy levels of the doped particles when excited simultaneously with the two excitation beams. Because one of the beam is modulated, a modulated gain or loss process is detected accordingly. However, further investigations are required to confirm the origin of this signal and additional optimisation of the particle doping could be carried out subsequently.

Appendices

.1 Image processing

.1.1 3D MRI image normalisation against distance from coil

```
stacksize = nSlices();
width= getWidth();
length= getHeight();
run("32-bit");
setBatchMode(true);
for(k=0;k<stacksize;k++)
{m=0; for(i=0;i<width;i++)
{
for(j=0;j<length;j++){
a=getPixel(i,j);
m=m+a;
}
}
d= width * length;
m=m/d;
run("Divide...", "value=m slice");
run("Next Slice [>]");
}
setBatchMode(false);
```

.1.2 Rename images as Tile grid of images

```
dir1 = getDirectory("Choose the Directory of your images");
dir2 = getDirectory("Choose the Directory where you want to safe the images as Tile ");

    list=getFileList(dir1);
print(list.length);
ymax=25;
xmax=30;
f=-1;

    for (y=1; y<=ymax; y++) {
for (x=xmax; x>=1; x–){
f=f+1;
path1 = dir1+list[f];
name="Tile_001";
//Zero fill if(y<10)u2="_00";
else{ if(y<100) u2="_0"; else u2="_";}
if(x<10)u3="_00";
else{ if(x<100) u3="_0"; else u3="_";}
d=name+u2+y+u3+x;
    path2 = dir2+d;
open(path1);
saveAs("Tiff", path2);
close();
}}
```

.2 Tumour volumetry data

Table 1: Tumour volume measured with MRI and semi-histology, Table(1 of 3).

N	**Image code**	**Tumour Volume (mm^3)**	**Average radius (mm)**	**Semi-histology volume (mm^3)**
1	MRI2-48-15	31.50	1.96	31.00
2	MRI2-48-26	21.00	1.65	18.80
3	MRI2-48-31	47.20	1.93	30.00
4	MRI2-48-36	undetectable	undetectable	undetectable
5	MRI2-48-41	18.70	1.36	10.50
6	MRI2-48-46	27.30	1.42	11.90
7	MRI2-48-51	59.10	2.29	50.10
8	MRI2-48-57	73.70	2.53	68.00
9	MRI2-48-62	undetectable	undetectable	undetectable
10	MRI2-48-67	103.20	2.93	105.30
11	MRI2-48-72	30.70	1.76	23.00
12	MRI2-48-77	57.80	2.55	69.80
13	MRI2-48-82	59.80	2.37	55.40
14	MRI2-48-87	11.70	1.60	17.30
15	MRI2-48-92	83.40	2.30	50.80
16	MRI2-48-97	36.40	1.93	30.10
17	MRI2-48-102	43.40	1.84	26.00
18	MRI2-48-107	65.40	2.56	70.20
19	MRI2-48-112	undetectable	undetectable	undetectable
20	MRI2-49-07	undetectable	undetectable	undetectable
21	MRI2-49-11	undetectable	undetectable	undetectable
22	MRI2-49-15	89.50	2.13	40.45
23	MRI3-60	50.60	2.26	48.60
24	MRI3-55	72.90	2.44	60.60
25	MRI3-51	30.60	1.83	25.70
26	MRI3-74	98.10	2.87	99.23
27	MRI3-77	11.00	1.38	11.10

Table 2: Tumour volume measured with MRI and semi-histology, Table(2 of 3).

N	**Image code**	**Tumour Volume (mm^3)**	**Average radius (mm)**	**Semi-histology volume (mm^3)**
28	MRI3-52	93.90	2.72	84.00
29	MRI3-72	63.60	2.38	56.30
30	MRI3-69	37.20	2.01	34.00
31	MRI3-56	43.40	2.07	37.00
32	MRI3-71	undetectable	undetectable	undetectable
33	MRI3-57	39.90	2.09	38.20
34	MRI3-54	67.70	2.27	49.00
35	MRI3-65	33.60	2.01	34.00
36	MRI3-61	undetectable	undetectable	undetectable
37	MRI3-63	56.50	2.49	64.83
38	MRI3-80	16.70	1.52	14.78
39	MRI3-70	29.60	2.05	36.10
40	MRI3-83	48.00	2.11	39.10
41	MRI3-62	30.20	1.79	23.90
42	MRI3-81	62.50	2.45	61.40
43	MRI3-66	31.60	2.00	33.50
44	MRI3-64	32.80	2.14	41.20
45	MRI3-67	31.80	1.99	33.00
46	MRI3-76	undetectable	undetectable	undetectable
47	MRI3-73	78.30	2.60	73.40
48	MRI3-78	129.30	2.61	74.40
49	MRI4-84-C1N5	47.10	1.65	18.72
50	MRI4-84-C5N2	undetectable	undetectable	undetectable
51	MRI4-85-C2N4	52.80	2.12	39.61
52	MRI4-85-C3N4	undetectable	undetectable	undetectable
53	MRI4-87-C2N2	25.90	1.75	22.34
54	MRI4-87-C3N3	98.30	2.28	49.30

Table 3: Tumour volume measured with MRI and semi-histology, Table(3 of 3).

N	**Image code**	**Tumour Volume (mm^3)**	**Average radius (mm)**	**Semi-histology volume (mm^3)**
55	MRI4-88-C1N1	106.00	2.56	70.04
56	MRI4-88-C3N1	99.10	2.74	86.12
57	MRI4-90-C3N5	undetectable	undetectable	undetectable
58	MRI4-90-C6N4	56.40	2.20	44.43
59	MRI4-91-C2N3	52.60	2.26	48.33
60	MRI4-91-C5N5	undetectable	undetectable	undetectable
61	MRI4-92-C1N4	15.00	1.64	18.55
62	MRI4-92-C3N2	undetectable	undetectable	undetectable
63	MRI4-94-C4N2	undetectable	undetectable	undetectable
64	MRI4-94-C6N5	29.20	1.65	18.81
65	MRI4-95-C1N2	44.20	2.04	35.28
66	MRI4-95-C6N3	39.10	1.93	29.86
67	MRI4-96-C5N4	undetectable	undetectable	undetectable
68	MRI4-96-C6N2	78.20	2.28	49.30
69	MRI4-97-C5N1	undetectable	undetectable	undetectable
70	MRI4-97-C6N1	undetectable	undetectable	undetectable
71	MRI4-98-C1N3	26.70	1.73	21.77
72	MRI4-98-C4N4	42.90	2.37	55.56
73	MRI4-99-C4N1	74.90	2.65	77.91
74	MRI4-100-C4N5	56.20	2.13	40.46
75	MRI4-100-C5N3	undetectable	undetectable	undetectable
76	MRI4-101-C2N5	30.20	1.93	29.98
77	MRI4-101-C4N3	90.90	2.92	104.24
78	MRI-5-202-C1N1	2.53	0.83	2.37
79	MRI-5-202-C2N2	95.30	2.51	66.20
80	MRI-5-201-C1N3	undetectable	undetectable	undetectable
81	MRI-5-201-C1N4	2.03	0.77	1.91
82	MRI-5-203-C1N5	1.81	0.86	2.66
83	MRI-5-203-C2N1	43.10	2.04	35.28

References

[1] Andrew I Minchinton and Ian F Tannock. Drug penetration in solid tumours. *Nature Reviews Cancer*, 6(8):583–592, 2006.

[2] Olivier Trédan, Carlos M Galmarini, Krupa Patel, and Ian F Tannock. Drug resistance and the solid tumor microenvironment. *Journal of the National Cancer Institute*, 99(19):1441–1454, 2007.

[3] Lara S Jabr-Milane, Lilian E van Vlerken, Sunita Yadav, and Mansoor M Amiji. Multi-functional nanocarriers to overcome tumor drug resistance. *Cancer treatment reviews*, 34(7):592–602, 2008.

[4] Janet L Markman, Arthur Rekechenetskiy, Eggehard Holler, and Julia Y Ljubimova. Nanomedicine therapeutic approaches to overcome cancer drug resistance. *Advanced drug delivery reviews*, 65(13):1866–1879, 2013.

[5] Quentin A Pankhurst, J Connolly, SK Jones, and J Dobson. Applications of magnetic nanoparticles in biomedicine. *Journal of physics D: Applied physics*, 36(13):R167, 2003.

[6] Jason R McCarthy and Ralph Weissleder. Multifunctional magnetic nanoparticles for targeted imaging and therapy. *Advanced drug delivery reviews*, 60(11):1241–1251, 2008.

[7] Jon Dobson. Magnetic nanoparticles for drug delivery. *Drug development research*, 67(1):55–60, 2006.

[8] Gan Tian, Zhanjun Gu, Xiaoxiao Liu, Liangjun Zhou, Wenyan Yin, Liang Yan, Shan Jin, Wenlu Ren, Gengmei Xing, Shoujian Li, et al. Facile fabrication of rare-earth-doped gd_2o_3 hollow spheres with upconversion luminescence, magnetic resonance, and drug delivery properties. *The Journal of Physical Chemistry C*, 115(48):23790–23796, 2011.

[9] Yuran Huang, Sha He, Weipeng Cao, Kaiyong Cai, and Xing-Jie Liang. Biomedical nanomaterials for imaging-guided cancer therapy. *Nanoscale*, 4(20):6135–6149, 2012.

[10] Donald W McRobbie. *MRI from Picture to Proton*. Cambridge University Press, 2007.

[11] Jiang Hsieh. Computed tomography: principles, design, artifacts, and recent advances. SPIE Bellingham, WA, 2009.

[12] Brian Herman and John J Lemasters. *Optical microscopy: emerging methods and applications*. Elsevier, 2012.

[13] Jaeyun Kim, Yuanzhe Piao, and Taeghwan Hyeon. Multifunctional nanostructured materials for multimodal imaging, and simultaneous imaging and therapy. *Chemical Society Reviews*, 38(2):372–390, 2009.

[14] Alex M Aisen, William Martel, Ethan M Braunstein, Kim I McMillin, William A Phillips, and TF Kling. Mri and ct evaluation of primary bone and soft-tissue tumors. *American journal of Roentgenology*, 146(4):749–756, 1986.

[15] Omid Veiseh, Conroy Sun, Jonathan Gunn, Nathan Kohler, Patrik Gabikian, Donghoon Lee, Narayan Bhattarai, Richard Ellenbogen, Raymond Sze, Andrew Hallahan, et al. Optical and mri multifunctional nanoprobe for targeting gliomas. *Nano Letters*, 5(6):1003–1008, 2005.

[16] Kimberly A Kelly, Jennifer R Allport, Andrew Tsourkas, Vivek R Shinde-Patil, Lee Josephson, and Ralph Weissleder. Detection of vascular adhesion molecule-1 expression using a novel multimodal nanoparticle. *Circulation research*, 96(3):327–336, 2005.

[17] Ali S Arbab, Victor Frenkel, Sunil D Pandit, Stasia A Anderson, Gene T Yocum, Monica Bur, Hanh M Khuu, Elizabeth J Read, and Joseph A Frank. Magnetic resonance imaging and confocal microscopy studies of magnetically labeled endothelial progenitor cells trafficking to sites of tumor angiogenesis. *Stem Cells*, 24(3):671–678, 2006.

[18] Chris Heyn, John A Ronald, Lisa T Mackenzie, Ian C MacDonald, Ann F Chambers, Brian K Rutt, and Paula J Foster. In vivo magnetic resonance imaging of single cells in mouse brain with optical validation. *Magnetic Resonance in Medicine*, 55(1):23–29, 2006.

[19] Rodrigo M Petoral Jr, Fredrik Soderlind, Anna Klasson, Anke Suska, Marc A Fortin, Natalia Abrikossova, Linnéa Selegård, Per-Olov Kall, Maria Engstrom, and Kajsa Uvdal. Synthesis and characterization of tb^{3+}-doped gd_2o_3 nanocrystals: a bifunctional material with combined fluorescent labeling and mri contrast agent properties. *The Journal of Physical Chemistry C*, 113(17):6913–6920, 2009.

[20] Yu Chen, Hangrong Chen, Deping Zeng, Yunbo Tian, Feng Chen, Jingwei Feng, and Jianlin Shi. Core/shell structured hollow mesoporous nanocapsules: a po-

tential platform for simultaneous cell imaging and anticancer drug delivery. *ACS nano*, 4(10):6001–6013, 2010.

[21] David P Cormode, Brenda L Sanchez-Gaytan, Aneta J Mieszawska, Zahi A Fayad, and Willem JM Mulder. Inorganic nanocrystals as contrast agents in mri: synthesis, coating and introduction of multifunctionality. *NMR in Biomedicine*, 26(7):766–780, 2013.

[22] Victoria E Centonze and John G White. Multiphoton excitation provides optical sections from deeper within scattering specimens than confocal imaging. *Biophysical journal*, 75(4):2015–2024, 1998.

[23] Chuqiao Tu, Xuchu Ma, Periklis Pantazis, Susan M Kauzlarich, and Angelique Y Louie. Paramagnetic, silicon quantum dots for magnetic resonance and two-photon imaging of macrophages. *Journal of the American Chemical Society*, 132(6):2016–2023, 2010.

[24] Yu-Mei Zhou, Hai-Bao Wang, Ming Gong, Zhi-Yuan Sun, Kai Cheng, Xiang-kai Kong, Zhen Guo, and Qian-Wang Chen. Yolk-type au@ fe 3 o 4@ c nanospheres for drug delivery, mri and two-photon fluorescence imaging. *Dalton Transactions*, 42(27):9906–9913, 2013.

[25] Yimin Huang, Lin Hu, Tingting Zhang, Hao Zhong, Jiajia Zhou, Zhenbang Liu, Haibao Wang, Zhen Guo, and Qianwang Chen. Mn3 [co (cn) 6] 2@ sio2 core-shell nanocubes: Novel bimodal contrast agents for mri and optical imaging. *Scientific reports*, 3, 2013.

[26] Jian Chen, Zhen Guo, Hai-Bao Wang, Ming Gong, Xiang-Kai Kong, Peng Xia, and Qian-Wang Chen. Multifunctional fe 3 o 4@ c@ ag hybrid nanoparticles

as dual modal imaging probes and near-infrared light-responsive drug delivery platform. *Biomaterials*, 34(2):571–581, 2013.

[27] Karen E Shafer-Peltier, Abigail S Haka, Jason T Motz, Maryann Fitzmaurice, Ramachandra R Dasari, and Michael S Feld. Model-based biological raman spectral imaging. *Journal of Cellular Biochemistry*, 87(S39):125–137, 2002.

[28] Conor L Evans and X Sunney Xie. Coherent anti-stokes raman scattering microscopy: chemical imaging for biology and medicine. *Annu. Rev. Anal. Chem.*, 1:883–909, 2008.

[29] Christian W Freudiger, Wei Min, Brian G Saar, Sijia Lu, Gary R Holtom, Chengwei He, Jason C Tsai, Jing X Kang, and X Sunney Xie. Label-free biomedical imaging with high sensitivity by stimulated raman scattering microscopy. *Science*, 322(5909):1857–1861, 2008.

[30] Gianluca Rago, Carolin M Langer, Christian Brackman, James PR Day, Katrin F Domke, Nathanael Raschzok, Christian Schmidt, Igor M Sauer, Annika Enejder, Martina T Mogl, et al. Cars microscopy for the visualization of micrometer-sized iron oxide mri contrast agents in living cells. *Biomedical optics express*, 2(9):2470–2483, 2011.

[31] Felix Bloch. Nuclear induction. *Physical review*, 70(7-8):460, 1946.

[32] Mark A Brown and Richard C Semelka. *MRI: basic principles and applications*. John Wiley & Sons, 2011.

[33] Peter Caravan. Strategies for increasing the sensitivity of gadolinium based mri contrast agents. *Chemical Society Reviews*, 35(6):512–523, 2006.

[34] David C Jiles. *Introduction to magnetism and magnetic materials*. CRC press, 1998.

[35] Robert C O'handley. Modern magnetic materials: principles and applications. *Modern Magnetic Materials: Principles and Applications, by Robert C. O'Handley, pp. 768. ISBN 0-471-15566-7. Wiley-VCH, November 1999.*, 1, 1999.

[36] Alan Jasanoff. *Cancer Imaging: Lung and Breast Carcinomas*, volume 1, chapter Contrast Agents for Magnetic Resonance Imaging : An Overview. Academic Press, 2007.

[37] Peter TC So, Chen Y Dong, Barry R Masters, and Keith M Berland. Two-photon excitation fluorescence microscopy. *Annual review of biomedical engineering*, 2(1):399–429, 2000.

[38] Chandrasekhara Venkata Raman and Kariamanikkam Srinivasa Krishnan. A new type of secondary radiation. *Nature*, 121(3048):501–502, 1928.

[39] MJ Pelletier et al. Quantitative analysis using raman spectrometry. *Applied spectroscopy*, 57(1):20A–20A, 2003.

[40] C Otto, de CJ Grauw, JJ Duindam, NM Sijtsema, and J Greve. Applications of micro-raman imaging in biomedical research. *Journal of Raman spectroscopy*, 28(2-3):143–150, 1997.

[41] PD Maker and RW Terhune. Study of optical effects due to an induced polarization third order in the electric field strength. *Physical Review*, 137(3A):A801, 1965.

[42] Andreas Zumbusch, Gary R Holtom, and X Sunney Xie. Three-dimensional vibrational imaging by coherent anti-stokes raman scattering. *Physical Review Letters*, 82(20):4142–4145, 1999.

[43] Ji-Xin Cheng and X Sunney Xie. Coherent anti-stokes raman scattering microscopy: instrumentation, theory, and applications. *The Journal of Physical Chemistry B*, 108(3):827–840, 2004.

[44] Ji-xin Cheng, Andreas Volkmer, Lewis D Book, and X Sunney Xie. An epi-detected coherent anti-stokes raman scattering (e-cars) microscope with high spectral resolution and high sensitivity. *The Journal of Physical Chemistry B*, 105(7):1277–1280, 2001.

[45] Ji-Xin Cheng, Andreas Volkmer, and X Sunney Xie. Theoretical and experimental characterization of coherent anti-stokes raman scattering microscopy. *JOSA B*, 19(6):1363–1375, 2002.

[46] Julian Moger, Blair D Johnston, and Charles R Tyler. Imaging metal oxide nanoparticles in biological structures with cars microscopy. *Optics express*, 16(5):3408–3419, 2008.

[47] Patrick M Winter, Shelton D Caruthers, Andrea Kassner, Thomas D Harris, Lori K Chinen, John S Allen, Elizabeth K Lacy, Huiying Zhang, J David Robertson, Samuel A Wickline, et al. Molecular imaging of angiogenesis in nascent vx-2 rabbit tumors using a novel $\alpha\nu\beta 3$-targeted nanoparticle and 1.5 tesla magnetic resonance imaging. *Cancer research*, 63(18):5838–5843, 2003.

[48] Natalie Garrett. *Nano-Biophotonics*. PhD thesis, University of Exeter, 2010.

[49] Sijia Lu, Wei Min, Shasha Chong, Gary R Holtom, and X Sunney Xie. Label-free imaging of heme proteins with two-photon excited photothermal lens microscopy. *Applied Physics Letters*, 96(11):113701, 2010.

[50] Stephen E Bialkowski. *Photothermal spectroscopy methods for chemical analysis*, volume 134. Wiley New York, 1996.

[51] Leah Bergman and Jeanne L McHale. *Handbook of luminescent semiconductor materials*. CRC Press, 2011.

[52] AN Belsky and JC Krupa. Luminescence excitation mechanisms of rare earth doped phosphors in the vuv range. *Displays*, 19(4):185–196, 1999.

[53] Danny Vennerberg and Zhiqun Lin. Upconversion nanocrystals: synthesis, properties, assembly and applications. *Science of Advanced Materials*, 3(1):26–40, 2011.

[54] Markus Haase and Helmut Schäfer. Upconverting nanoparticles. *Angewandte Chemie International Edition*, 50(26):5808–5829, 2011.

[55] Feng Wang and Xiaogang Liu. Recent advances in the chemistry of lanthanide-doped upconversion nanocrystals. *Chemical Society Reviews*, 38(4):976–989, 2009.

[56] Marie-France Joubert. Photon avalanche upconversion in rare earth laser materials. *Optical materials*, 11(2):181–203, 1999.

[57] Eva Hemmer, Hiroyuki Takeshita, Tomoyoshi Yamano, Takanori Fujiki, Yvonne Kohl, Karin Löw, Nallusamy Venkatachalam, Hiroshi Hyodo, Hidehiro Kishimoto, and Kohei Soga. In vitro and in vivo investigations of upconversion and nir emitting gd2o3: Er3+, yb3+ nanostructures for biomedical applications. *Journal of Materials Science: Materials in Medicine*, 23(10):2399–2412, 2012.

[58] Jason A Koutcher, Xiaoyi Hux, Su Xu, Terence PF Gade, Norman Leeds, Xiaohong Joe Zhou, David Zagzag, and Eric C Holland. Mri of mouse models for

gliomas shows similarities to humans and can be used to identify mice for preclinical trials. *Neoplasia (New York, NY)*, 4(6):480, 2002.

[59] Helene Benveniste and Steve Blackband. Mr microscopy and high resolution small animal mri: applications in neuroscience research. *Progress in neurobiology*, 67(5):393–420, 2002.

[60] Peter Mansfield. *Nmr imaging in biomedicine: Supplement 2 advances in magnetic resonance*, volume 2. Elsevier, 1982.

[61] Jennifer Linn, Friederike Schwarz, Christian Schichor, and Martin Wiesmann. Cranial mri of small rodents using a clinical mr scanner. *Methods*, 43(1):2–11, 2007.

[62] Anne Katrin Schauff, Ella L Kim, Jan Leppert, Roger Nadrowitz, Robin Wuestenberg, Mark Alexander Brockmann, and Alf Giese. Inhibition of invasion-associated thromboxane synthase sensitizes experimental gliomas to γ-radiation. *Journal of neuro-oncology*, 91(3):241–249, 2009.

[63] Hans U Kerl, Hanne Boll, Marcel Ramacher, Melanie Heilmann, Christoph Groden, Martin Kramer, Viktor Umansky, and Marc A Brockmann. Characterization and longitudinal monitoring of melanoma growth in ret-transgenic mice using a single-sequence mri protocol. *Experimental dermatology*, 21(11):837–841, 2012.

[64] Benjamin McDaniel, Huaxin Sheng, David S Warner, Laurence W Hedlund, and Helene Benveniste. Tracking brain volume changes in c57bl/6j and apoe-deficient mice in a model of neurodegeneration: a 5-week longitudinal micro-mri study. *Neuroimage*, 14(6):1244–1255, 2001.

[65] Yanping Sun, Nils O Schmidt, Karl Schmidt, Sameer Doshi, Joshua B Rubin, Robert V Mulkern, Rona Carroll, Mateo Ziu, Kadir Erkmen, Tina Y Poussaint, et al. Perfusion mri of u87 brain tumors in a mouse model. *Magnetic resonance in medicine*, 51(5):893–899, 2004.

[66] Aaron L Nelson, Sibel A Algon, Jeeva Munasinghe, Ondrea Graves, Liliana Goumnerova, Deborah Burstein, Scott L Pomeroy, and John YH Kim. Magnetic resonance imaging of patched heterozygous and xenografted mouse brain tumors. *Journal of neuro-oncology*, 62(3):259–267, 2003.

[67] WM Holmes, S Maclellan, B Condon, Christine Dufès, TRJ Evans, IF Uchegbu, and AG Schätzlein. High-resolution 3d isotropic mr imaging of mouse flank tumours obtained in vivo with solenoid rf micro-coil. *Physics in medicine and biology*, 53(2):505, 2008.

[68] Deepu R Pillai, Robin M Heidemann, Praveen Kumar, Nagesh Shanbhag, Titus Lanz, Michael S Dittmar, Beatrice Sandner, Christoph P Beier, Norbert Weidner, Mark W Greenlee, et al. Comprehensive small animal imaging strategies on a clinical 3 t dedicated head mr-scanner; adapted methods and sequence protocols in cns pathologies. *PloS one*, 6(2):e16091, 2011.

[69] Tobias Engelhorn, Ilker Y Eyupoglu, Marc A Schwarz, Marek Karolczak, Holger Bruenner, Tobias Struffert, Willi Kalender, and Arnd Doerfler. In vivo micro-ct imaging of rat brain glioma: a comparison with 3t mri and histology. *Neuroscience letters*, 458(1):28–31, 2009.

[70] Munetaka Matoba, Tamaki Kondou, Takuji Tanaka, Masataka Kitadate, Kiyotaka Oota, and Hisao Tonami. Noninvasive monitoring of radiation-induced early ther-

apeutic response using high-resolution mr imaging and proton mr spectroscopy in vx2 carcinoma. *Journal of radiation research*, 51(6):699–705, 2010.

[71] M-A Brockmann, S Ulmer, J Leppert, R Nadrowitz, R Wuestenberg, I Nolte, D Petersen, C Groden, A Giese, and S Gottschalk. Analysis of mouse brain using a clinical 1.5 t scanner and a standard small loop surface coil. *Brain research*, 1068(1):138–142, 2006.

[72] Marc A Brockmann, Birte Bender, Elena Plaxina, Ingo Nolte, Ralf Erber, Katrin Lamszus, Christoph Groden, and Lothar Schilling. Differential effects of tumor–platelet interaction in vitro and in vivo in glioblastoma. *Journal of neuro-oncology*, 105(1):45–56, 2011.

[73] S Xu, TPF Gade, C Matei, K Zakian, AA Alfieri, X Hu, EC Holland, S Soghomonian, J Tjuvajev, D Ballon, et al. In vivo multiple-mouse imaging at 1.5 t. *Magnetic resonance in medicine*, 49(3):551–557, 2003.

[74] Frank A Raila, Alfred P Bowles, Eddie Perkins, and Allen Terrell. Sequential imaging and volumetric analysis of an intracerebral c6 glioma by means of a clinical mri system. *Journal of neuro-oncology*, 43(1):11–17, 1999.

[75] Bart Cornelissen, Veerle Kersemans, LENNART Jans, Ludovicus Staelens, RUTH Oltenfreiter, T Thonissen, Eric Achten, and Guido Slegers. Comparison between 1 t mri and non-mri based volumetry in inoculated tumours in mice. *British journal of radiology*, 78(928):338–342, 2005.

[76] Shuzhou Jiang, Hui Xue, Alan Glover, Mary Rutherford, Daniel Rueckert, and Joseph V Hajnal. Mri of moving subjects using multislice snapshot images with volume reconstruction (svr): application to fetal, neonatal, and adult brain studies. *Medical Imaging, IEEE Transactions on*, 26(7):967–980, 2007.

[77] Mikael Montelius, Maria Ljungberg, Michael Horn, and Eva Forssell-Aronsson. Tumour size measurement in a mouse model using high resolution mri. *BMC medical imaging*, 12(1):12, 2012.

[78] Yao Wu, Wei Yang, Jun Jiang, Shuanqian Li, Qianjin Feng, and Wufan Chen. Semi-automatic segmentation of brain tumors using population and individual information. *Journal of digital imaging*, 26(4):786–796, 2013.

[79] Yan Fu, T Brandon Huff, Han-Wei Wang, Ji-Xin Cheng, and Haifeng Wang. Ex vivo and in vivo imaging of myelin fibers in mouse brain by coherent anti-stokes raman scattering microscopy. *Optics express*, 16(24):19396–19409, 2008.

[80] Hyon Bin Na, In Chan Song, and Taeghwan Hyeon. Inorganic nanoparticles for mri contrast agents. *Advanced Materials*, 21(21):2133–2148, 2009.

[81] Maria Engström, Anna Klasson, Henrik Pedersen, Cecilia Vahlberg, Per-Olov Käll, and Kajsa Uvdal. High proton relaxivity for gadolinium oxide nanoparticles. *Magnetic Resonance Materials in Physics, Biology and Medicine*, 19(4):180–186, 2006.

[82] Beata Chertok, Bradford A Moffat, Allan E David, Faquan Yu, Christian Bergemann, Brian D Ross, and Victor C Yang. Iron oxide nanoparticles as a drug delivery vehicle for mri monitored magnetic targeting of brain tumors. *Biomaterials*, 29(4):487–496, 2008.

[83] Joseph Goldstein, Dale E Newbury, David C Joy, Charles E Lyman, Patrick Echlin, Eric Lifshin, Linda Sawyer, and Joseph R Michael. *Scanning electron microscopy and X-ray microanalysis*. Springer, 2003.

[84] Marie Gaumet, Angelica Vargas, Robert Gurny, and Florence Delie. Nanoparticles for drug delivery: the need for precision in reporting particle size parameters. *European Journal of Pharmaceutics and Biopharmaceutics*, 69(1):1–9, 2008.

[85] D Jia, L Lu, and WM Yen. Erbium energy levels relative to the band gap of gadolinium oxide. *Optics communications*, 212(1):97–100, 2002.

[86] Albert Figuerola, Riccardo Di Corato, Liberato Manna, and Teresa Pellegrino. From iron oxide nanoparticles towards advanced iron-based inorganic materials designed for biomedical applications. *Pharmacological Research*, 62(2):126–143, 2010.

[87] Xingchen Ye, Joshua E Collins, Yijin Kang, Jun Chen, Daniel TN Chen, Arjun G Yodh, and Christopher B Murray. Morphologically controlled synthesis of colloidal upconversion nanophosphors and their shape-directed self-assembly. *Proceedings of the National Academy of Sciences*, 107(52):22430–22435, 2010.

[88] Gagandeep Kaur, SK Singh, and SB Rai. Eu 3+ and yb 3+ codoped gd 2 o 3 single phase nanophosphor: An enhanced monochromatic red emission through cooperative upconversion and downconversion. *Journal of Applied Physics*, 107(7):073514–073514, 2010.

[89] GY Chen, HJ Liang, HC Liu, G Somesfalean, and ZG Zhang. Anomalous power dependence of upconversion emissions in gd2o3: Er3+ nanocrystals under diode laser excitation of 970 nm. *Journal of Applied Physics*, 105(11):114315, 2009.

[90] Purificación Escribano, Beatriz Julián-López, José Planelles-Aragó, Eloisa Cordoncillo, Bruno Viana, and Clément Sanchez. Photonic and nanobiophotonic properties of luminescent lanthanide-doped hybrid organic–inorganic materials. *Journal of Materials Chemistry*, 18(1):23–40, 2008.

[91] Koen Binnemans. Lanthanide-based luminescent hybrid materials. *Chemical reviews*, 109(9):4283–4374, 2009.

[92] Qinghai Xu, Bingchen Lin, and Yanli Mao. Photoluminescence characteristics of energy transfer between er 3+ and bi 3+ in gd 2 o 3: Er 3+, bi 3+. *Journal of Luminescence*, 128(12):1965–1968, 2008.

[93] N Dhananjaya, H Nagabhushana, BM Nagabhushana, B Rudraswamy, SC Sharma, DV Sunitha, C Shivakumara, and RPS Chakradhar. Effect of different fuels on structural, thermo and photoluminescent properties of gd 2 o 3 nanoparticles. *Spectrochimica Acta Part A: Molecular and Biomolecular Spectroscopy*, 96:532–540, 2012.

[94] N Dhananjaya, H Nagabhushana, BM Nagabhushana, B Rudraswamy, C Shivakumara, and RPS Chakradhar. Spherical and rod-like gd 2 o 3: Eu 3+ nanophosphorsstructural and luminescent properties. *Bulletin of Materials Science*, 35(4):519–527, 2012.

[95] Hai Guo, Ning Dong, Min Yin, Weiping Zhang, Liren Lou, and Shangda Xia. Visible upconversion in rare earth ion-doped gd2o3 nanocrystals. *The Journal of Physical Chemistry B*, 108(50):19205–19209, 2004.

[96] Ao Xia, Yuan Gao, Jing Zhou, CY Li, TS Yang, DM Wu, Limin Wu, and Fuyou Li. Coreeshell nayf4: Yb3ž, tm3ž@ fexoy nanocrystals for dual-modality t2-enhanced magnetic resonance and nir-to-nir upconversion luminescent imaging of small-animal lymphatic node. *Biomaterials*, 32(29):7200e8, 2011.

[97] Chao Wang, Liang Cheng, and Zhuang Liu. Drug delivery with upconversion nanoparticles for multi-functional targeted cancer cell imaging and therapy. *Biomaterials*, 32(4):1110–1120, 2011.

[98] Dev K Chatterjee, Abdul J Rufaihah, and Yong Zhang. Upconversion fluorescence imaging of cells and small animals using lanthanide doped nanocrystals. *Biomaterials*, 29(7):937–943, 2008.

[99] Timur Sh Atabaev, Zhonglie Piao, Yoon-Hwae Hwang, Hyung-Kook Kim, and Nguyen Hoa Hong. Bifunctional gd 2 o 3: Er 3+ particles with enhanced visible upconversion luminescence. *Journal of Alloys and Compounds*, 572:113–117, 2013.

[100] Lingling Xu, Yingning Yu, Xiaoguang Li, Gabriel Somesfalean, Yungang Zhang, Hong Gao, and Zhiguo Zhang. Synthesis and upconversion properties of monoclinic gd 2 o 3: Er 3+ nanocrystals. *Optical Materials*, 30(8):1284–1288, 2008.

[101] SK Singh, K Kumar, and SB Rai. Synthesis and spectroscopy of transparent colloidal solution of gd 2 o 3: Er 3+, yb 3+ spherical nanocrystals by pulsed laser ablation. *Materials Science and Engineering: B*, 166(2):180–184, 2010.

[102] Fiorenzo Vetrone, Venkataramanan Mahalingam, and John A Capobianco. Near-infrared-to-blue upconversion in colloidal bayf5: Tm3+, yb3+ nanocrystals. *Chemistry of Materials*, 21(9):1847–1851, 2009.

[103] Jing Zhou, Yun Sun, Xiaoxia Du, Liqin Xiong, He Hu, and Fuyou Li. Dual-modality in vivo imaging using rare-earth nanocrystals with near-infrared to near-infrared (nir-to-nir) upconversion luminescence and magnetic resonance properties. *Biomaterials*, 31(12):3287–3295, 2010.

[104] Qiu Sun, Hua Zhao, Xiangqun Chen, Fuping Wang, Wei Cai, and Zhaohua Jiang. Upconversion emission enhancement in silica-coated gd2o3: Tm3+, yb3+ nanocrystals by incorporation of li+ ion. *Materials chemistry and physics*, 123(2-3):806–810, 2010.

[105] Peter Caravan, Jeffrey J Ellison, Thomas J McMurry, and Randall B Lauffer. Gadolinium (iii) chelates as mri contrast agents: structure, dynamics, and applications. *Chemical reviews*, 99(9):2293–2352, 1999.

[106] Kathleen A Hinds, Jonathan M Hill, Erik M Shapiro, Mikko O Laukkanen, Alfonso C Silva, Christian A Combs, Timothy R Varney, Robert S Balaban, Alan P Koretsky, and Cynthia E Dunbar. Highly efficient endosomal labeling of progenitor and stem cells with large magnetic particles allows magnetic resonance imaging of single cells. *Blood*, 102(3):867–872, 2003.

[107] Jin-sil Choi, Jae-Hyun Lee, Tae-Hyun Shin, Ho-Taek Song, Eung Yeop Kim, and Jinwoo Cheon. Self-confirming and logic nanoparticles for fault-free mri. *Journal of the American Chemical Society*, 132(32):11015–11017, 2010.

[108] Quoc Lam Vuong, Sabine Van Doorslaer, Jean-Luc Bridot, Corradina Argante, Gabriela Alejandro, Raphaël Hermann, Sabrina Disch, Carlos Mattea, Siegfried Stapf, and Yves Gossuin. Paramagnetic nanoparticles as potential mri contrast agents: characterization, nmr relaxation, simulations and theory. *Magnetic Resonance Materials in Physics, Biology and Medicine*, 25(6):467–478, 2012.

[109] Rui Hao, Ruijun Xing, Zhichuan Xu, Yanglong Hou, Song Gao, and Shouheng Sun. Synthesis, functionalization, and biomedical applications of multifunctional magnetic nanoparticles. *Advanced Materials*, 22(25):2729–2742, 2010.

[110] Chao Wang, Liang Cheng, and Zhuang Liu. Upconversion nanoparticles for photodynamic therapy and other cancer therapeutics. *Theranostics*, 3(5):317, 2013.

[111] Anna Gnach and Artur Bednarkiewicz. Lanthanide-doped up-converting nanoparticles: merits and challenges. *Nano Today*, 7(6):532–563, 2012.

[112] Liang Cheng, Chao Wang, and Zhuang Liu. Upconversion nanoparticles and their composite nanostructures for biomedical imaging and cancer therapy. *Nanoscale*, 5(1):23–37, 2013.

[113] Santimukul Santra, Charalambos Kaittanis, Jan Grimm, and J Manuel Perez. Drug/dye-loaded, multifunctional iron oxide nanoparticles for combined targeted cancer therapy and dual optical/magnetic resonance imaging. *small*, 5(16):1862–1868, 2009.

[114] Yufang Zhu, Ying Fang, and Stefan Kaskel. Folate-conjugated fe3o4@ sio2 hollow mesoporous spheres for targeted anticancer drug delivery. *The Journal of Physical Chemistry C*, 114(39):16382–16388, 2010.

[115] Xiaojiao Kang, Ziyong Cheng, Dongmei Yang, Ping'an Ma, Mengmeng Shang, Chong Peng, Yunlu Dai, and Jun Lin. Design and synthesis of multifunctional drug carriers based on luminescent rattle-type mesoporous silica microspheres with a thermosensitive hydrogel as a controlled switch. *Advanced Functional Materials*, 22(7):1470–1481, 2012.

[116] Zhen Liu, Fang Pu, Sa Huang, Qinghai Yuan, Jinsong Ren, Xiaogang Qu, et al. Long-circulating gd (2) o (3): Yb (3+), er (3+) up-conversion nanoprobes as high-performance contrast agents for multi-modality imaging. *Biomaterials*, 34(6):1712–1721, 2013.

[117] Ling Tong and Ji-Xin Cheng. Label-free imaging through nonlinear optical signals. *Materials Today*, 14(6):264–273, 2011.

[118] Julian Moger, Natalie Garrett, David Begley, Larisa Mihoreanu, Aikaterini Lalatsa, Maria Victoria Lozano, Mariarosa Mazza, Andreas Schatzlein, Ijeoma

Uchegbu, et al. Imaging cortical vasculature with stimulated raman scattering and two-photon photothermal lensing microscopy. *Journal of Raman Spectroscopy*, 43(5):668–674, 2012.

[119] Anton V Brusnichkin, Dmitry A Nedosekin, Mikhail A Proskurnin, and Vladimir P Zharov. Photothermal lens detection of gold nanoparticles: Theory and experiments. *Applied spectroscopy*, 61(11):1191–1201, 2007.

[120] Kazuma Mawatari, Takehiko Kitamori, and Tsuguo Sawada. Individual detection of single-nanometer-sized particles in liquid by photothermal microscope. *Analytical chemistry*, 70(23):5037–5041, 1998.

[121] B.K. Pandey, a.K. Shahi, Jyoti Shah, R.K. Kotnala, and Ram Gopal. Optical and magnetic properties of Fe2O3 nanoparticles synthesized by laser ablation/fragmentation technique in different liquid media. *Applied Surface Science*, 289:462–471, January 2014.

[122] Subarna Mitra, Soumen Das, Kalyan Mandal, and Subhadra Chaudhuri. Synthesis of a α-fe2o3 nanocrystal in its different morphological attributes: growth mechanism, optical and magnetic properties. *Nanotechnology*, 18(27):275608, 2007.